

Design Rules for Statistical Copolymer Surfactants for Foam-Forming Applications



The
University
Of
Sheffield.

by

Andi Xie

Submitted to the University of Sheffield
in fulfillment of the requirements for the award of
Doctor of Philosophy

June 2025

Declaration

The work described in this thesis was undertaken at the University of Sheffield under the supervision of Professor Steven P. Armes, FRS and Professor Anthony J. Ryan, OBE between October 2021 and June 2025 and has not been submitted, either wholly or in part, for this or any other degree. All the work is the original work of the author, except where acknowledged.

Andi Xie

June 2025

Acknowledgements

Firstly, I would like to express my sincere gratitude to my two supervisors, Prof. Steve Armes FRS and Prof. Tony Ryan OBE, for the opportunity to join their research teams. I am deeply thankful for their academic guidance, insightful discussions and timely feedback throughout my doctoral studies. I also greatly appreciate the training and conference opportunities they provided.

I would like to acknowledge Dr. James Jennings and Dr. Niall Ward-O'Brien for their initial conception of this project, as well as Dr. Deborah Beattie for her valuable advice and support at the outset. I am particularly indebted to Dr. Oleksandr Mykhaylyk (Sasha) and Prof. Jan Skov Pedersen for their irreplaceable support throughout the course of this thesis. Their deep understanding of SAXS enabled me to handle the substantial volume of data. I would also like to thank all members of the Armes and RyMyk groups for their support and encouragement throughout my PhD journey. Special thanks go to Derck, Csilla, Rory and Priyanka for generously sharing their experience in polymer synthesis and characterisation; to Sasha, Rachel, Courtney, Ellen, Anna and Max for their assistance with XEUSS; and to the synchrotron trip teams (Matt, Priyanka, Max, Mark, Josh, Ben) who collected data on my behalf. I am sincerely grateful to the entire technical team for their outstanding support. In particular, I thank Alan and Rory for their help in assembling the GPC-MALLS system, Sharon for the MS, and Khalid for the NMR. I would also like to thank Denise and Louise from the administration and finance office, as well as Nick and Sharon from the chemstore, whose efforts ensure the department runs smoothly. I am also thankful to MSc student Nikita and summer

student Fred for their hard work.

I gratefully acknowledge the financial support from EPSRC and the University of Sheffield. I am also thankful to Tony for securing additional funding during the writing stage of my thesis. I would also like to thank Dr. Julie Hyde. Without her guidance and advice I would not have stayed in Sheffield and had the privilege of working with so many people.

I would like to thank Tony and Sasha for organising the research retreat (ski trip). Who would have thought that one of the most daunting challenges of my PhD would be skiing downhill? I also appreciate the members of our badminton group (especially Sasha, Rory and Hubert!), whose participation clearly helped to ease the tension in my neck and back. I sincerely thank Tony for preparing my first gravel bike and inviting me on his birthday ride. As a professor, Tony clearly possesses expertise far beyond academia.

Over the past four years, pursuing a PhD more than 10,000 kilometres from home has been a challenging journey. In addition to my academic colleagues, I would like to thank my family and friends. I am especially grateful for the company of my two cats, Colin and Nana. While they may not have understood what I was saying, I did practise my presentations in front of them. Thank you to Shaoyan for patiently listening to my complaints. Thank you to Fangyi for your support and encouragement during the writing process. Without you, my anxiety would have been far worse. I am deeply thankful to my parents for their understanding and support over the years.

It has been a pleasure to work in the Armes and RyMyk groups. I dedicate this work to all of you, thank you!

Abstract

As an inherently unstable dispersed system, liquid foam requires surfactant for effective formation and stabilisation. However, the performance of conventional hydrocarbon-based small-molecule surfactants has now reached its design limit. Amphiphilic copolymers have emerged as promising alternatives, offering both superior foamability and a broader range of tuneable structural parameters. Nevertheless, their fundamental macromolecular nature poses significant challenges for their rigorous characterisation and the underlying structure-performance relationships remain unclear.

Copolymer compositions with optimal surface activity were identified through Design of Experiment (DoE) analysis of published data. In particular, statistical copolymers containing the 3,5,5-trimethylhexyl substituent as the hydrophobic unit and oligo(ethylene glycol) as the hydrophilic segment exhibited exceptional foamability. A series of statistical copolymers with various backbone structures, molecular weights, and comonomer ratios were synthesised via free radical copolymerisation to explore performance optimisation. Foam studies revealed that the (meth)acrylic backbone structure significantly affected foamability. Small-angle X-ray scattering (SAXS) was employed to characterise copolymer micelles in aqueous solution, revealing a strong correlation between comonomer composition, copolymer architecture, and foaming activity. Copolymers exhibiting superior foamability formed loosely packed micelles, which facilitates rapid surface adsorption. Synthesis of the analogous vinyl ether-based copolymers was also attempted for comparison with the best-performing acrylic statistical copolymers. Furthermore, eight tertiary amine-based dihydrophilic statistical copolymers were prepared to

investigate the influence of polyelectrolyte charge on chain flexibility. The conformations of both charged and uncharged chains were analysed using SAXS combined with the polymer reference interaction site model (PRISM) to evaluate the role of electrostatic interactions in modulating chain stiffness. The degree of protonation significantly influences the chain conformation and hence governs the aqueous solution behaviour.

In summary, this thesis provides new insights regarding the design of interfacially-active copolymer surfactants. In particular, tailoring the copolymer structure leads to optimal interfacial stabilisation efficiency.

List of Common Abbreviations

Abbreviation	Full Term
AIBN	Azobisisobutyronitrile
ATRP	Atom transfer radical polymerisation
ANOVA	Analysis of variance
CMC	Critical micelle concentration
CPDB	2-Cyano-2-propyl dithiobenzoate
CTA	Chain transfer agent
\bar{D}	Dispersity
DCM	Dichloromethane
DDMAT	2-(Dodecylthiocarbonothioylthio)-2-methylpropionic acid
DEER	Double electron-electron resonance
DLS	Dynamic light scattering
DMA	2-(Dimethylamino)ethyl methacrylate
DMF	Dimethylformamide
dn/dc	Refractive index increments
DoE	Design of Experiment
DP	Mean degree of polymerisation
dRI	Differential refractive index

DSC	Differential scanning calorimetry
EHA	2-Ethylhexyl acrylate
FRP	Free radical polymerisation
GPC	Gel permeation chromatography
GMA	Glycidyl methacrylate
HNC	Hyper-netted chain
HPC	High-performance computing
<i>i</i> OA	Isooctyl acrylate
LA	Lauryl acrylate
LRP	Living radical polymerisation
MAA	Methylacrylic acid
MALLS	Multi-angle laser light scattering
MALDI-TOF	Matrix-assisted laser desorption/ionisation time-of-flight
ML	Machine learning
M_n	Number-average molecular weight
M_p	Peak molecular weight
MPEGVE	Methoxy poly(ethylene glycol) vinyl ether
MS	Mass spectrometry
MSA	Mean spherical approximation
M_w	Weight-average molecular weight
$M_{w,abs}$	Absolute weight-average molecular weight
MWD	Molecular weight distribution
NMP	Nitroxide-mediated polymerisation
NMR	Nuclear magnetic resonance
NR	Neutron reflectivity
PAA	Polyacrylic acid
PALS	Phase-analysis light scattering

PDMA	Poly(2-dimethylamino)ethyl methacrylate
PEG	Poly(ethylene glycol)
PEGA	Poly(ethylene glycol)methyl ether acrylate
PEGMA	Poly(ethylene glycol)methyl ether methacrylate
PEO	Poly(ethylene oxide)
PETTC	4-Cyano-4-[(dodecylsulfanylthiocarbonyl)sulfanyl]pentanoic acid
PFAS	Perfluoroalkyl and polyfluoroalkyl substances
PMA	Poly(methyl acrylate)
PMMA	Poly(methyl methacrylate)
PMPC	Poly(2-methacryloyloxyethyl phosphorylcholine)
PMVE	Poly(methyl vinyl ether)
PPO	Poly(propylene oxide)
PQDMA	Poly[2-(methacryloyloxy)ethyl]trimethylammonium chloride
PRISM	Polymer reference interaction site model
PSS	Polystyrene sulfonate
PVE	Poly(vinyl ether)
RAFT	Reversible addition-fragmentation chain-transfer
RDRP	Reversible-deactivation radical polymerisation
R_{ee}	End-to-end distance
R_g	Radius of gyration
SAS	Small-angle scattering
SANS	Small-angle neutron scattering
SAXS	Small-angle X-ray scattering
SEC	Size exclusion chromatography
SDS	Sodium dodecyl sulfate

SLD	Scattering length density
SLS	Static light scattering
TEA	Triethylamine
TEM	Transmission electron microscopy
T_g	Glass transition temperature
TMHA	3,5,5-Trimethylhexyl acrylate
TMHMA	3,5,5-Trimethylhexyl methacrylate
TMHVE	3,5,5-Trimethylhexyl vinyl ether
WLC	Worm-like chain

Contents

1	Introduction	15
1.1	Background	15
1.2	Basic Concepts in Polymer Science	17
1.3	Polymerisation	21
1.3.1	Chain-Growth Polymerisation	21
1.3.1.1	Ionic Polymerisation	23
1.3.1.2	Free Radical Polymerisation (FRP)	26
1.3.1.3	Reversible Deactivation Radical Polymerisation (RDRP)	30
1.3.2	Chain-Growth Copolymerisation	39
1.4	Liquid Foam	45
1.4.1	Dispersion, Interface and Surface Tension	45
1.4.1.1	Dispersion	45
1.4.1.2	Interface	47
1.4.1.3	Surface Tension	48
1.4.2	Fundamentals of Liquid Foam	49
1.4.2.1	Foam Formation and Basic Structure	50
1.4.2.2	Foam Dynamics	52
1.5	Surfactants and Surfactancy	54
1.5.1	Amphiphilic Molecular Structure and Interfacial Behaviour	54
1.5.2	Classification of Surfactants by Hydrophilic Groups	56

1.5.3	Classification of Surfactants by Molecular Weight	58
1.5.4	Role of Surfactants in Foam Stabilisation	59
1.6	Aim and Objectives	62
1.7	References	64
2	Statistical Analysis based on Design of Experiments (DoE) and Analysis of Variance (ANOVA)	74
2.1	Introduction	75
2.2	Experimental	77
2.2.1	Materials and Dataset Sources	77
2.2.2	Design of Experiments	80
2.3	Results and Discussion	82
2.3.1	Pluronic Triblock Copolymer Surfactants	82
2.3.2	Methacrylic and Acrylic Statistical Copolymers Surfactants	83
2.4	Conclusions	86
2.5	References	87
3	Design Rules for Statistical Copolymer Surfactants for Foam-Forming Applications	89
3.1	Introduction	90
3.2	Experimental	93
3.2.1	Materials	93
3.2.2	Synthesis and Reaction Protocols	93
3.2.3	Analytical and Characterisation Methods	94
3.3	Results and Discussion	101
3.3.1	Synthesis and Characterisation	101
3.3.2	Foamability Analysis	106
3.3.3	Dynamic Surface Behaviour	108

3.3.4	Static Surface Behaviour and Foam Stability	112
3.3.5	SAXS Studies of Statistical Copolymer Surfactant Self-assembly in Aqueous Solution	114
3.3.6	How the Hydrophobe Affects the Foam?	129
3.3.7	How does the Nature of the Copolymer Backbone Affect the Foam? . .	131
3.4	Conclusions	134
3.5	Appendix	137
3.5.1	DMF GPC Data for P(TMHA- <i>stat</i> -PEGA) Statistical Copolymers . . .	137
3.5.2	Surface Tension, Foamability and Foam Stability Data for P(TMHA- <i>stat</i> -PEGA) Statistical Copolymers	138
3.5.3	SAXS Model Comparison	139
3.5.4	Estimation of Surface Coverage	140
3.5.5	Proposal for Approved Neutron Reflectivity Experiment	141
3.6	References	143
4	Applicability of the Kratky-Porod Worm-like Chain Model to Statistical Copoly- mers	149
4.1	Introduction	150
4.2	Experimental	155
4.2.1	Materials	155
4.2.2	Synthesis and Reaction Protocols	155
4.2.3	Characterisation Methods	157
4.3	Results and Discussion	161
4.3.1	Synthesis and Characterisation	161
4.3.2	Kinetics and Randomness Evaluation	162
4.3.3	pH-responsive Behaviour in Aqueous Solution	169
4.3.4	SAXS Analysis	172
4.3.5	Quaternisation of P(DMA- <i>stat</i> -PEGMA) and Characterisation	184

4.3.6	Interactions between Poly(ethylene glycol) and Salt	187
4.4	Conclusions	189
4.5	Appendix	191
4.5.1	Synthesis	191
4.5.2	NMR Kinetics	191
4.5.3	MALLS Measurements	193
4.5.4	SAXS Fitting Functions	194
4.5.5	Polydispersity Calculation	200
4.5.6	Additional SAXS Patterns and Fitting Results	201
4.6	References	203
5	Synthesis of Amphiphilic Statistical Copolymers with a Highly Flexible Backbone	212
5.1	Introduction	213
5.2	Experimental	215
5.2.1	Materials	215
5.2.2	Synthesis of Vinyl Ether Monomers	216
5.2.3	Copolymerisation of TMHVE with MPEGVE	217
5.2.4	Characterisation Methods	219
5.3	Results and Discussion	220
5.3.1	Preparation of 3,5,5-Trimethylhexyl Vinyl Ether (TMHVE) Monomer	220
5.3.2	Preparation of Methoxy Poly(ethylene glycol) Vinyl Ether (MPEGVE) Monomer	222
5.3.3	Free Radical Copolymerisation Synthesis of P(TMHE- <i>stat</i> -MPEGVE)	223
5.3.4	Cationic Homopolymerisation of PTMHVE	226
5.4	Conclusions	228
5.5	References	230

6	Conclusions and Future Work	232
6.1	References	238

Chapter 1

Introduction

1.1 Background

The foam performance of surfactants can be judged by evaluating foamability and long-term foam stability. However, conventional small molecule surfactants may have reached their physical and chemical limits in terms of structural optimisation.¹ For example, the limiting surface tension for the best-performing hydrocarbon-based surfactants is about $25 \text{ mN}\cdot\text{m}^{-1}$.²⁻⁴ To achieve lower surface tension, researchers have developed speciality surfactants with super-hydrophobic groups, such as perfluoro/polyfluoroalkyl compounds (PFAS) and silicone-based surfactants. The limiting surface tension of PFAS can be as low as $15 \text{ mN}\cdot\text{m}^{-1}$,² while that of silicone-based systems is around $20 \text{ mN}\cdot\text{m}^{-1}$.^{2,5} However, there are growing concerns regarding the environmental persistence and biosafety profiles for both perfluorinated and silicone-based surfactants, so their continued use over the longer term seems unlikely.⁶⁻¹⁰ For example, the bioaccumulation and potential toxicity of PFAS has prompted many countries to restrict their production and use.¹¹⁻¹³ Similarly, the potential pollution risks of silicone-based surfactants have also prompted stricter regulations.¹⁴ From the perspective of green chemistry and sustainable development, there is an urgent need to develop next-generation environmentally-friendly surfactants that offer sufficiently high performance to enable the replacement of existing perfluorinated and silicone-based products.

Given the well-documented limited structural tunability of small molecule surfactants,¹ polymeric surfactants provide a promising alternative. Recently, Jennings et al. reported that a class of acrylic-based amphiphilic statistical copolymers exhibited excellent interfacial activity, with a limiting surface tension just below 25 mN·m⁻¹.⁶ Moreover, such copolymers exhibited superior foamability for ethanol-rich ethanol-water mixtures. Notably, such performance could not be achieved using the corresponding diblock copolymers prepared using the same hydrophilic and hydrophobic comonomers. This indicates that the copolymer architecture plays a key role in determining surface activity.⁶

Nevertheless, there are rather few systematic studies of the quantitative relationship between chemical structure, comonomer composition, copolymer architecture, chain flexibility and the resulting interfacial behaviour of statistical copolymer surfactants. In this thesis, such parameters are evaluated with the aim of optimising both initial foamability and long-term foam stability.

1.2 Basic Concepts in Polymer Science

In 1920, the Chemistry Nobel Laureate Otto Wieland famously asserted that organic molecules could not exceed a molecular weight of $5,000 \text{ g}\cdot\text{mol}^{-1}$, which reflected prevailing scientific opinion at that time.¹⁵ However, Herman Staudinger challenged this paradigm by proposing the existence of polymers: long-chain molecules comprising individual repeat units linked together by covalent bonds. Despite huge initial scepticism, this hypothesis was finally accepted by the scientific community by around 1930, due to Herman Staudinger's and Wallace Carothers' pioneering contributions to the emerging field of polymer science.¹⁶ Over the past century, polymer science has achieved remarkable success, enabling the development of a diverse range of synthetic polymers that have revolutionised our daily lives.

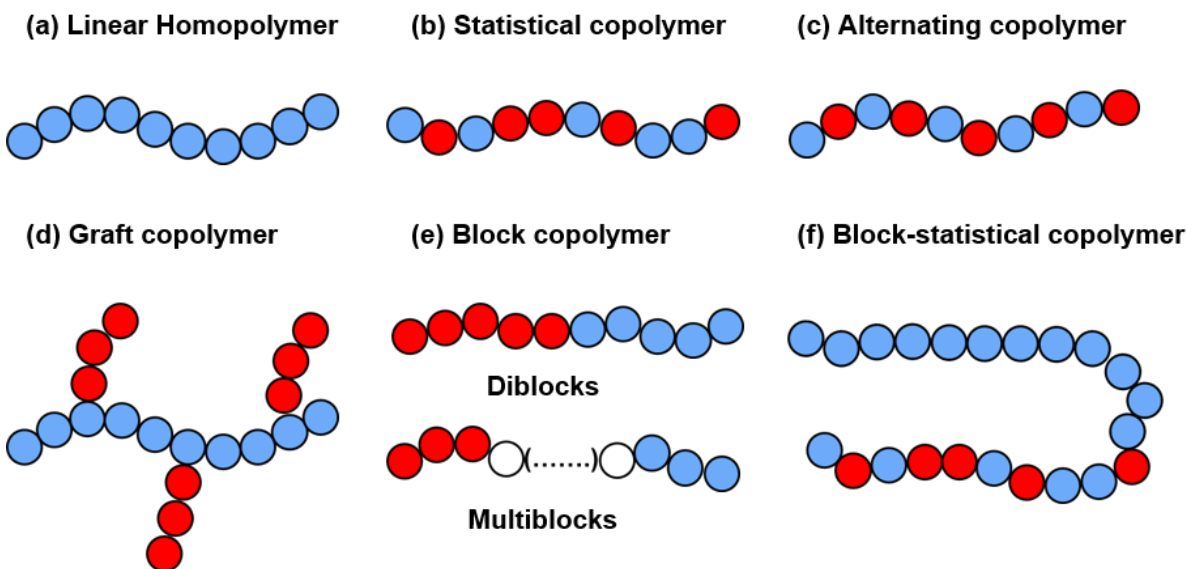


Figure 1.1: Examples of various (co)polymer architectures.

Polymer properties depend on the chemical structure of their repeat units and how these units are connected together to form the polymer backbone.¹⁷ A linear homopolymer consists of a single type of repeat unit (Figure 1.1a). Nevertheless, such polymers may exhibit a broad range of physical and chemical behaviour, depending on the type of repeat unit, the degree of polymerisation (DP) and dispersity (\mathcal{D}). In addition, the incorporation of two or more

comonomers enables the design of various copolymer architectures, depending on the spatial arrangement of the repeat units. In statistical copolymers, two comonomers are statistically distributed along the copolymer chains (Figure 1.1b). In contrast, alternating copolymers comprise a strictly regular ABABAB comonomer sequence (Figure 1.1c). Graft copolymers are formed by grafting side-chains to a linear backbone, resulting in branched architectures (Figure 1.1d). Moreover, modern synthetic polymer chemistry has enabled the controlled synthesis of many well-defined block copolymers (Figure 1.1e) and block-statistical copolymers (Figure 1.1f).¹⁸

Unlike small organic molecules such as toluene or ethylene, polymer molecules in the same sample do not exhibit an identical molecular weight. Instead, polymers exhibit a molecular weight distribution (MWD) because they typically comprise a wide range of chain lengths. To accurately describe the MWD, statistical methods are required.¹⁷ Two important parameters are the number-average molecular weight (M_n , Equation 1.1) and the weight-average molecular weight (M_w , Equation 1.2), which are mathematically defined moments on the MWD curve of a polymer:

$$M_n = \frac{\sum n_i M_i}{\sum n_i} \quad (1.1)$$

$$M_w = \frac{\sum n_i M_i^2}{\sum n_i M_i} = \frac{\sum w_i M_i}{\sum w_i} \quad (1.2)$$

where n_i is the number of chains with mass M_i , and w_i is the total mass of chains of mass M_i (where $w_i = n_i \cdot M_i$).

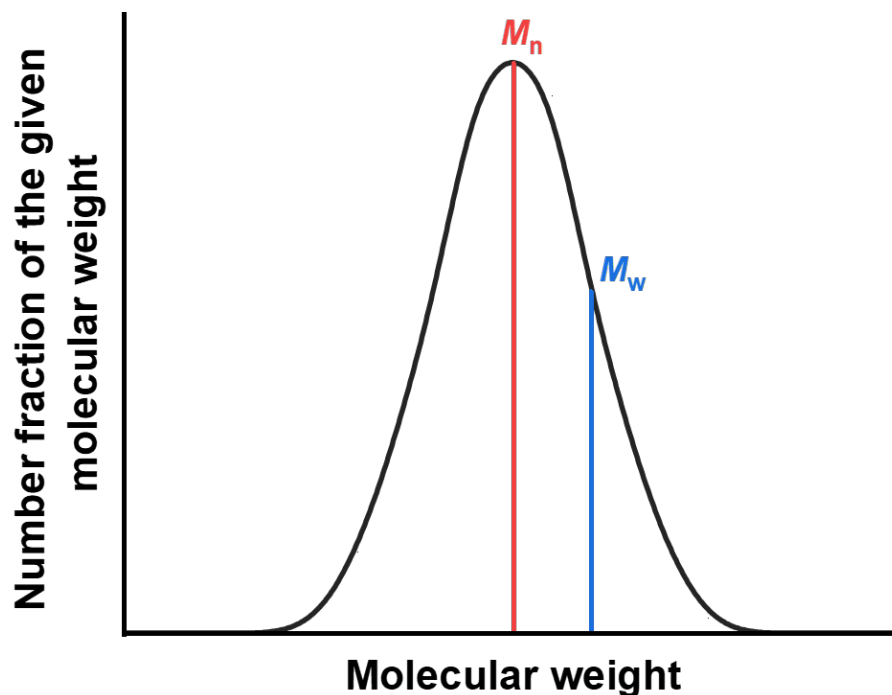


Figure 1.2: Schematic representation of a unimodal polymer molecular weight distribution, where M_n lies near the peak maximum and M_w is located at higher molecular weight.

The M_n represents a weighted average based on the number of polymer chains. Thus this parameter is relatively sensitive to the presence of lower molecular weight species within the distribution. In contrast, M_w is weighted by the mass of each chain and is therefore biased towards higher molecular weight species. Most synthetic polymers have relatively broad MWDs, so M_w is usually significantly greater than M_n (see Figure 1.2).

Dispersity is a crude measure of the width of the molecular weight distribution curve and is defined according to Equation (1.3):¹⁷

$$\mathcal{D} = \frac{M_w}{M_n} \quad (1.3)$$

If \mathcal{D} lies close to unity, then the MWD is relatively narrow and the polymer chains are relatively uniform in length (and mass). Conversely, a high \mathcal{D} value (e.g. above 2.0) indicates a broad MWD curve. In general, near-monodisperse polymers are considered to have a dispersity below 1.20. \mathcal{D} is strongly influenced by the polymerisation chemistry.^{19,20} Perfectly monodisperse

polymers cannot be prepared by conventional synthetic methods but are known in nature. For example, proteins typically exhibit a unique molecular weight owing to the precise control achieved during their biosynthesis.²¹

To assess the molecular weight and dispersity of polymers, size exclusion chromatography (SEC), also known as gel permeation chromatography (GPC), is widely employed. This technique typically requires calibration with polymer standards of known molecular weight to determine M_n , M_w and \bar{D} .²² When coupled with a static light scattering (SLS) detector, SEC can also provide an absolute M_w without the need for calibration.²³ In addition to SEC, other characterisation methods such as matrix-assisted laser desorption/ionisation time-of-flight mass spectrometry (MALDI-TOF MS),²⁴ nuclear magnetic resonance (NMR) spectroscopy, and intrinsic viscosity measurements²⁵ can be used to determine polymer molecular weight.

The glass transition temperature (T_g) marks the transition of a polymer from a glassy state to a rubbery state.¹⁷ Below the T_g , the local mobility of chain segments is restricted, and the polymer is brittle. Above the T_g , the chain segments acquire significant mobility, resulting in rubber-like elastic behaviour. In contrast to the melting point of a small molecule, which corresponds to a well-defined phase transition from solid to liquid, the T_g does not represent a true phase change. Rather, it denotes a gradual transition in a polymer's dynamic and mechanical behaviour.

For statistical copolymers, variations in T_g are closely associated with the weight fraction of each comonomer within the copolymer. These variations are commonly predicted using the Fox equation (1.4):²⁶

$$\frac{1}{T_g} = \frac{w_1}{T_{g,1}} + \frac{w_2}{T_{g,2}} \quad (1.4)$$

where T_g , $T_{g,1}$ and $T_{g,2}$ describe the glass transition temperatures (in K) of the overall copolymer and the two corresponding homopolymers, respectively and w_1 and w_2 are the respective comonomer weight fractions, respectively.

1.3 Polymerisation

Polymerisation is the chemical process by which multiple monomer units are covalently linked together to produce long-chain macromolecules. Most polymerisation mechanisms can be broadly classified as either step-growth or chain-growth processes.¹⁷ In step-growth polymerisation, polymer chains are formed through successive reactions between monomers, oligomers and polymers. In contrast, chain-growth polymerisation involves the generation of an active centre that propagates the polymer chain via the sequential addition of multiple monomer units. Chain-growth mechanisms can be further categorised into free radical, ionic, and reversible-deactivation radical polymerisation (RDRP) techniques, such as nitroxide-mediated polymerisation (NMP),²⁷ atom transfer radical polymerisation (ATRP)²⁸ and reversible addition-fragmentation chain transfer (RAFT)¹⁸ polymerisation. These methods differ significantly in terms of their degree of control over the molecular weight distribution, dispersity, copolymer architecture and chain-end functionality. Moreover, radical copolymerisation provides a powerful strategy for tuning copolymer composition and physical properties. A comprehensive understanding of the underlying polymerisation mechanism is therefore essential for the design of polymer materials, particularly amphiphilic copolymers.

1.3.1 Chain-Growth Polymerisation

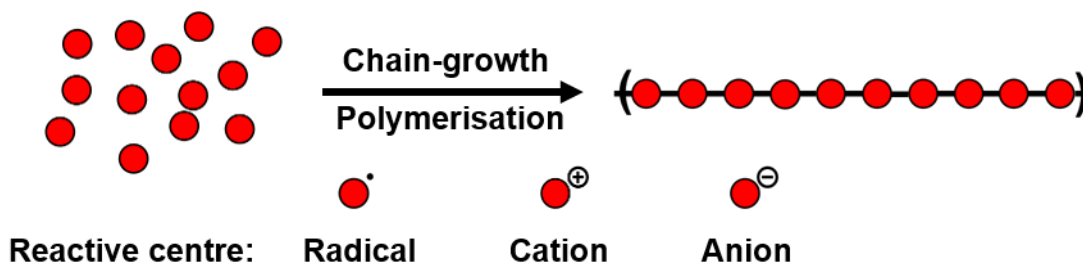


Figure 1.3: Schematic representation of chain-growth polymerisation. Each red circle denotes a monomer repeat unit. The active centre can be a radical, a cation, or an anion.

Chain-growth polymerisation is a type of reaction in which monomers are added sequentially to a growing polymer chain via an active centre, resulting in the formation of polymers (Figure 1.3). Polymer chains grow continuously once initiated. In conventional uncontrolled free radical polymerisation, high molecular weight chains are typically formed at an early stage and the molecular weight is relatively independent of the monomer conversion during the polymerisation, whereas in controlled chain-growth polymerisation, such as anionic and RDRP, the molecular weight increases linearly with conversion, reflecting its living nature (Figure 1.4). The general mechanism of chain-growth polymerisation involves four key steps: initiation, propagation, chain transfer, and termination. Based on the nature of the active centre, chain-growth processes can be classified into radical, cationic, anionic, or coordination polymerisation (Figure 1.3).¹⁷

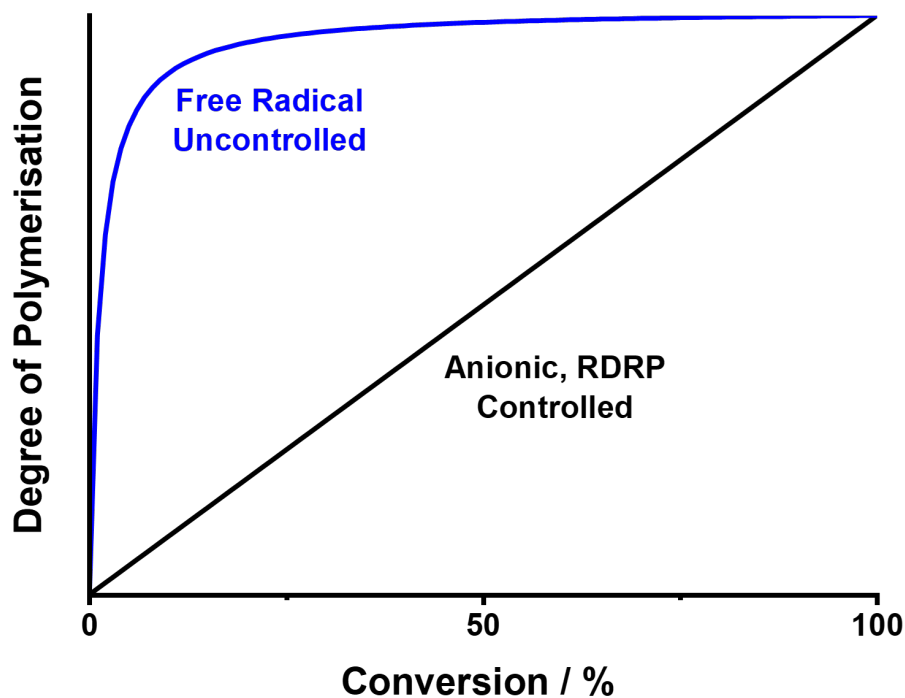


Figure 1.4: Schematic representation of the evolution of molecular weight as a function of monomer conversion for free radical, living anionic and RDRP.

A major achievement in chain-growth polymerisation is the development of living polymerisation, which has no intrinsic termination step.^{19,29} The active centres on the polymer chain-ends remain reactive throughout the reaction, which enables precise control over the target molecular

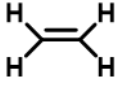
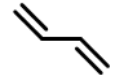
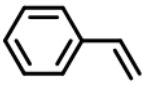
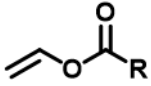
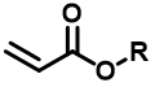
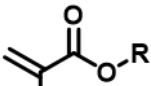
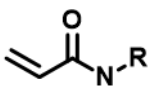
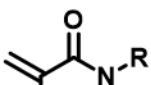
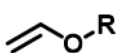
weight, \bar{D} and the copolymer architecture. Living polymerisation allows the construction of block copolymers through the sequential addition of two or more comonomers. Common examples include living anionic polymerisation, living cationic polymerisation, and living radical polymerisation (LRP). The term 'LRP' has been largely replaced by 'RDRP', as recommended by IUPAC in 2010.^{20,30} Nitroxide-mediated polymerisation,²⁷ atom transfer radical polymerisation,²⁸ and reversible addition-fragmentation chain transfer¹⁸ polymerisation all fall within the framework of RDRP.

1.3.1.1 Ionic Polymerisation

Ionic polymerisation is a form of chain-growth polymerisation in which initiation and propagation occur via either anionic or cationic active centres.¹⁷ Compared with free radical polymerisation, ionic polymerisations impose stricter requirements on both monomer structures and reaction conditions. Whereas radical polymerisation is compatible with a broad range of monomers, cationic polymerisation is typically restricted to monomers bearing electron-donating substituents such as isobutyl,³¹ phenyl³² or alkoxy groups.³³ In contrast, anionic polymerisation is effective only with monomers containing electron-withdrawing groups such as carbonyl,³⁴ vinyl³⁵ or phenyl groups.³⁶ This high degree of selectivity is primarily due to the weak stabilisation of the propagating ionic species, which are highly reactive and sensitive to protic impurities (e.g. water).¹⁷

Although ionic polymerisation has enabled the large-scale production of polystyrene, polydiene rubbers or other thermoplastic elastomers,³⁷ it has far fewer commercial applications than free radical polymerisation in the area of multifunctional polymer synthesis due to its sensitivity to impurities and limited monomer scope.¹⁷ However, it offers several important advantages. Most notably, the active centres remain reactive over relatively extended periods unless deliberately quenched. This enables the synthesis of polymers with narrow MWDs, particularly by anionic polymerisation.^{17,19,38} While cationic polymerisation generally affords less precise control over dispersity, it does provide useful access to vinyl monomers that are poorly suited to radical

Table 1.1: Summary of monomer suitability for radical, cationic and anionic polymerisation.¹⁷

Monomer	Chemical structure	Type of chain polymerisation		
		Radical	Cationic	Anionic
Ethylene		✓	X	✓
1,3-diene		✓	✓	✓
Styrene		✓	✓	✓
Vinyl ester		✓	X	X
Acrylate		✓	X	✓
Methacrylate		✓	X	✓
Acrylamide		✓	X	✓
Methacrylamide		✓	X	✓
Vinyl ether		X	✓	X

polymerisation, such as vinyl ethers.³³

Table 1.1 summarises the compatibility of various common monomers with three different polymerisation mechanisms. Free radical polymerisation exhibits broad applicability across a wide range of monomers, while ionic polymerisation is highly sensitive to the specific substituents on the monomer.

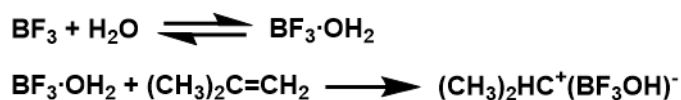
Only vinyl monomers bearing both electron-donating and electron-withdrawing groups such as 1,3-dienes and styrene are generally compatible with both cationic and anionic polymerisation. In contrast, monomers containing exclusively electron-withdrawing groups such as (meth)acrylates and (meth)acrylamides are typically suitable only for free radical or anionic

polymerisation.

An important case of cationic polymerisation is vinyl ethers.³⁹ The strong electron-donating effect of the oxygen atom significantly increases the electron density on the vinyl group, making these monomers typically unsuitable for either radical or anionic polymerisation.¹⁷ However, this same feature stabilises the carbocation intermediate that is formed during cationic polymerisation, thereby making vinyl ethers highly suitable for such formulations.

Cationic Polymerisation

During initiation, Lewis acids (e.g. BF_3 , AlCl_3)^{40,41} are usually used in conjunction with protic sources (such as water or alcohols) to generate the initiating carbocations that lead to polymerisation at relatively low temperature (Scheme 1.1):

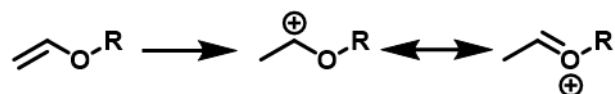


Scheme 1.1: Cationic initiation mechanism for isobutene when using a boron trifluoride-water initiator-coinitiator system.⁴⁰

During propagation, the active carbocation chain-ends attack the carbon-carbon double bonds of incoming monomers, generating new carbocation species and thereby extending the polymer chain. Cationic polymerisation is characterised by a rapid rate of reaction and extreme sensitivity to proton impurities such as water, alcohols, and amines, and therefore rigorously anhydrous conditions are required. To moderate this reactivity and suppress undesirable chain transfer side-reactions,⁴² cationic polymerisations are typically conducted at low temperatures (e.g. -78°C).⁴³ Termination can occur via the introduction of nucleophilic reagents.¹⁷ Owing to the extremely fast kinetics, cationic polymerisation is generally more difficult to control in terms of molecular weight and dispersity.^{17,42,44}

Vinyl ethers represent a class of monomers that effectively stabilise the corresponding carbocations. Their $\text{C}=\text{C}$ bond is electron-rich, while the alkoxy substituent serves as an electron-donating group; together, these features contribute to carbocation stabilisation. Upon elec-

trophilic attack by a cationic initiator, the resulting intermediate adopts a resonance-stabilised structure, as illustrated in Scheme 1.2.



Scheme 1.2: Resonance stabilisation of the carbocation intermediate during cationic polymerisation of a generic vinyl ether monomer.

Vinyl ethers are generally considered to be only amenable to cationic polymerisation. However, Sugihara and co-workers reported that free radical polymerisation of certain vinyl ethers bearing specific substituents is also feasible.⁴⁵ In particular, when the R group consists of a short hydrocarbon or PEG chain, the oxygen atoms within the ether group can engage in hydrogen bonding interactions with water that stabilise the resulting radical intermediate, see Figure 1.5.

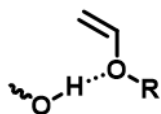
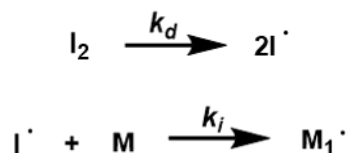
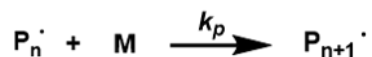
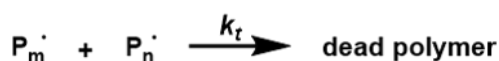
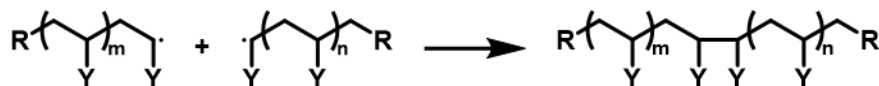
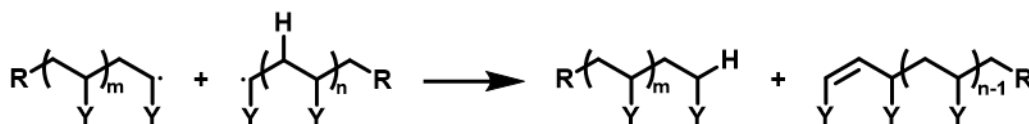


Figure 1.5: Hydrogen bonding-assisted stabilisation of the vinyl ether, as suggested by Sugihara and co-workers.⁴⁵

1.3.1.2 Free Radical Polymerisation (FRP)

Free radical polymerisation (FRP) is one of the most widely employed chain-growth polymerisation techniques and is applicable to a broad range of vinyl monomers, such as styrene,⁴⁶ acrylates,⁴⁷ and methyl methacrylate.⁴⁸ Owing to its operational simplicity and tolerance towards various functional groups and reaction conditions, FRP can be performed under relatively mild conditions without the need to rigorously eliminate water. However, oxygen can react with free radicals to form less reactive peroxy species,⁴⁹ thereby retarding or even inhibiting the polymerisation.⁵⁰ Hence, degassing the reaction mixture and performing the polymerisation under an inert atmosphere (e.g. nitrogen or argon) is typically required to eliminate oxygen. Free radical polymerisation generally proceeds via initiation, propagation and termination, as illustrated in Scheme 1.3.¹⁷

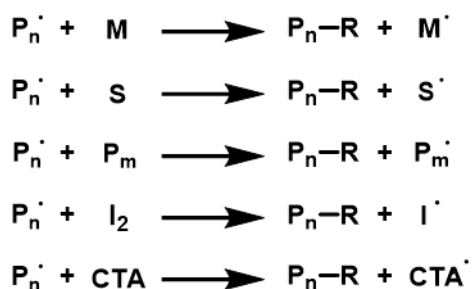
Initiation**Propagation****Termination****Combination****Disproportionation**

Scheme 1.3: General reaction scheme for a free radical polymerisation. The thermal decomposition of initiator is the slow rate-determining step. Once radicals are formed, they immediately react with monomer to form a monomer radical adduct, which then reacts with many more monomer units to produce a polymer radical. Termination of such polymer radicals can proceed by either combination or disproportionation. Here, k_d denotes the rate constant for initiator decomposition, k_i is the rate constant for initiation, k_p is the rate constant for propagation, and k_t is the overall rate constant for termination.¹⁷

Free radical polymerisation is initiated by the generation of free radicals via various mechanisms, including thermal decomposition, redox reactions, photochemical activation, ionising radiation, plasma, or electrochemical initiation.¹⁷ External initiators (I_2) are commonly employed to enhance initiation efficiency. Upon homolytic cleavage, the initiator produces free radicals (I^\bullet), which then react with a reactive monomer (M) to form a monomer-radical adduct (M_1^\bullet). Such radicals subsequently react with multiple monomer units to rapidly generate propagating polymer radicals (P^\bullet), see Scheme 1.3.

Termination marks the final stage of a free radical polymerisation. Termination typically occurs via two primary mechanisms: combination and/or disproportionation.¹⁷ In the case of combination, two polymer radicals react with each other to form a single polymer chain, effectively doubling the molecular weight. In the case of disproportionation, one radical chain end abstracts a hydrogen atom from another, resulting in the formation of one chain bearing a saturated chain-end and a terminal vinyl group at the end of the other chain, see Scheme 1.3.

In addition to the three principal stages of free radical polymerisation, chain transfer side-reactions also play a critical role in determining the molecular weight and dispersity of the resulting polymer. Chain transfer involves the transfer of a radical from a growing polymer radical to monomer, solvent,⁵¹ polymer,⁵² initiator, or an added chain transfer agent, thereby terminating the original chain and initiating growth from a new radical species, see Scheme 1.4. This prevents the original chain from reaching a higher molecular weight and creates a new chain, thus reducing the average chain length (or mean DP). On the other hand, chain transfer to polymer can lead to the formation of branched structures and is accompanied by an increase in M_w . However, chain transfer does not affect the overall rate of polymerisation, as the radical concentration in the reaction mixture remains constant before and after the chain transfer event.



Scheme 1.4: Chain transfer reaction to monomer (M), solvent (S), polymer (P_m), initiator (I_2) and chain transfer agent (CTA). R is either a hydrogen atom or a fragment derived from the chain transfer species, depending on the type of chain transfer reaction.¹⁷

The overall rate of polymerisation (R_p) is expressed by Equation (1.5):

$$R_p = k_p[M] \left(\frac{fk_d[I_2]}{k_t} \right)^{1/2} \quad (1.5)$$

where k_p is the rate constant for propagation, $[M]$ is the monomer concentration, f denotes the initiator efficiency, k_d is the rate constant for homolytic dissociation of the initiator, $[I_2]$ is the initiator concentration and k_t is the overall termination rate constant, including both combination and disproportionation. This expression is derived based on the steady-state approximation, in which the rate of initiation (R_i) is assumed to be equal to the rate of termination (R_t), as shown in Equation (1.6) - (1.7):

$$R_i = 2fk_d[I_2] = R_t = 2t[P_n\cdot]^2 \quad (1.6)$$

$$[P_n\cdot] = \left(\frac{fk_d[I_2]}{k_t} \right)^{1/2} \quad (1.7)$$

where $[P_n\cdot]$ denotes the polymer radical concentration. According to the steady-state approximation, $[P_n\cdot]$ is small and remains constant owing to the balance between the rates of radical generation and consumption. This approximation has been verified by electron spin resonance (ESR) spectroscopy studies.⁵³

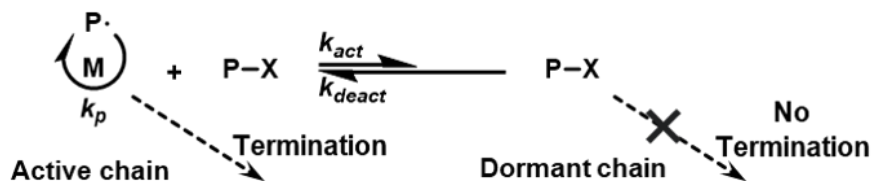
The kinetic chain length, D_k , is defined as the mean number of monomer units polymerised per radical centre, and is equal to the ratio of the rate of polymerisation to the rate of initiation, as expressed in Equation (1.8):

$$D_k = \frac{R_p}{R_i} = \frac{k_t[M]}{2(fk_dk_t[I_2])^{1/2}} \quad (1.8)$$

In the case of combination by termination, the DP is equal to $2D_k$, whereas for disproportionation termination, the DP is equal to D_k . Both termination pathways occur simultaneously, in most practical free-radical polymerisation systems, leading to average DP values between these two extremes and contributing to relatively broader MWDs ($1.5 < \bar{D} < 2.0$).¹⁷ According to Equation (1.8), the DP is directly proportional to the monomer concentration and inversely proportional to the square root of the initiator concentration. This relationship underpins a general principle in free radical polymerisation: higher $[M]/[I_2]^{1/2}$ yield polymers with higher molecular weights, while lower ratios result in lower molecular weights. Free radical polymerisation is

extensively employed for industrial polymer syntheses owing to its operational simplicity, broad monomer compatibility, and mild reaction conditions. However, its inherent lack of control over chain termination and chain transfer leads to even broader MWDs ($\bar{D} > 2.0$) and limited control over the copolymer architecture.^{17,51,52} For applications requiring more precise control over the target molecular weight, MWD and copolymer structure, living radical polymerisation techniques are often adopted to overcome the inherent limitations of conventional FRP.^{18,28,54}

1.3.1.3 Reversible Deactivation Radical Polymerisation (RDRP)



Scheme 1.5: General mechanism for RDRP. The propagating radical ($P\bullet$) is converted into the corresponding dormant species ($P-X$) through a reversible activation-deactivation process, thereby limiting irreversible termination and enabling controlled polymer growth.⁵⁵

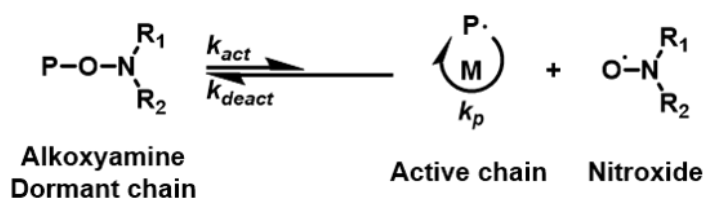
In conventional free radical polymerisation, the high reactivity of radical species leads to frequent chain termination and transfer events, resulting in broad molecular weight distributions and limited structural control. RDRP addresses these limitations by introducing a reversible activation-deactivation mechanism, in which growing chains alternate dynamically between active and dormant states. This significantly reduces termination events and confers control over polymer characteristics (Scheme 1.5).⁵⁵ RDRP preserves the operational simplicity and broad monomer scope of traditional free radical polymerisation, while affording greater synthetic precision. The development of RDRP has considerably expanded the design space of functional polymers. Compared to conventional FRP, RDRP can produce polymers with narrower molecular weight distributions and well-defined end-group functionalities, facilitating the synthesis of block copolymers, gradient copolymers, and polymer brushes. The three principal RDRP techniques are discussed in turn below.

Nitroxide-mediated Polymerisation (NMP)

Nitroxide-mediated polymerisation (NMP) is the earliest reported controlled radical polymerisation, being first proposed by Solomon et al.^{56,57} In their initial experiments, nitroxide radicals were found to effectively trap propagating radicals generated from vinyl monomers, forming stable alkoxyamine structures at relatively low temperatures. Subsequent studies revealed that increasing the temperature induced the reversible dissociation of these alkoxyamines, releasing active radicals capable of initiating polymerisation, thereby enabling the synthesis of low molecular weight acrylic polymers and oligomers.

Building on this new concept, Georges et al. reported the controlled polymerisation of styrene mediated by TEMPO (2,2,6,6-tetramethylpiperidiny-N-oxyl), which resulted in polystyrene with relatively low dispersity ($\bar{D} \approx 1.2 - 1.3$).⁵⁸

The NMP mechanism involves a reversible addition-dissociation equilibrium between propagating radicals and persistent nitroxide radicals to form 'dormant' alkoxyamine species (as illustrated in Scheme 1.6). This dynamic equilibrium establishes a balance between active and dormant chains, such that only a small fraction of propagating polymer radicals is present at any given time. As a result, polymer growth proceeds in a controlled fashion, minimising termination and enabling regulation of molecular weight and architecture.²⁷



Scheme 1.6: General NMP mechanism. The propagating radical ($P\cdot$) reversibly reacts with a nitroxide radical ($N-O\cdot$) to form a dormant alkoxyamine species ($P-O-NR_2$). This establishes a dynamic equilibrium between active and dormant chain-ends, thereby enabling controlled chain growth and suppressing irreversible termination.⁵⁹

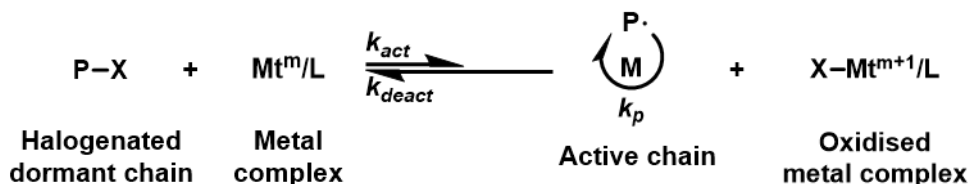
The stability of nitroxide radicals is a critical aspect of NMP. The dissociation energy of the C-O bond can be tuned by varying the steric and electronic properties of substituents on the nitrogen atom.⁶⁰ This changes the minimum temperature required to achieve reversible

dissociation and broadens the types of monomers that are amenable to NMP.^{61,62} NMP has been applied to the polymerisation of styrenes, acrylic acid, and acrylamides.^{63–65} However, the polymerisation of methacrylic monomers remains challenging, due to their propensity to undergo radical disproportionation side-reactions under typical NMP conditions.

Compared with other controlled polymerisation techniques, NMP offers the distinct advantage of a simplified formulation. It does not require metal catalysts; polymerisation can proceed using just monomer, an initiator, and a suitably designed alkoxyamine.²⁷ Moreover, NMP-synthesised polymers generally do not require complex post-polymerisation purification, making this technique particularly attractive for applications that demand metal-free environments or high-purity polymer products.

Atom Transfer Radical Polymerisation (ATRP)

Atom transfer radical polymerisation (ATRP) was independently reported in 1995 by Wang and Matyjaszewski⁶⁶ and Sawamoto et al.⁶⁷ The fundamental ATRP mechanism is based on the reversible transformation between active polymer radicals and dormant halogen-capped species (typically bromide or chloride), mediated by a transition metal catalyst, which is normally a copper complex. During initiation, a halogenated initiator (R-X) undergoes an atom transfer reaction with a low-valent copper complex (Cu(I)/L), thereby generating an active radical (R•) and a corresponding Cu(II)-X/L complex, see Scheme 1.7. The resulting radical initiates chain growth through successive addition of multiple monomer units.



Scheme 1.7: General ATRP mechanism. The dormant halogen-terminated species (R-X) undergoes reversible activation via atom transfer with a metal complex (Cu(I)/L), generating an active radical (P•) and an oxidised metal complex (Cu(II)X/L).²⁸

A dynamic equilibrium between activation and deactivation is established during ATRP,

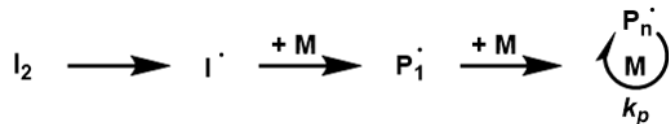
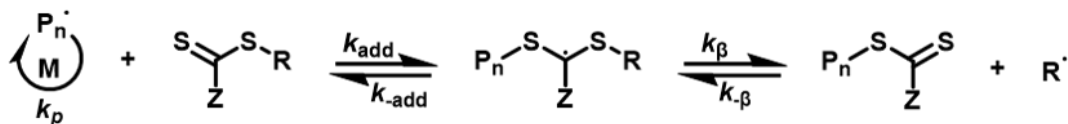
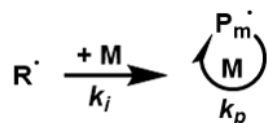
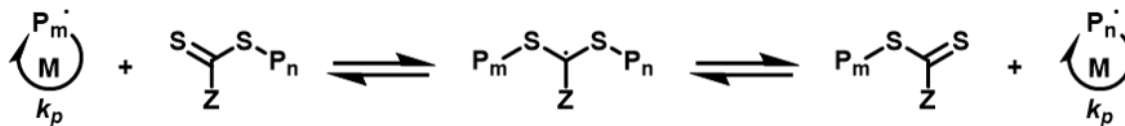
whereby the propagating polymer radicals are continuously and reversibly converted into dormant halogen-capped species. This equilibrium maintains a very low polymer radical concentration, effectively suppressing irreversible termination and conferring excellent control over polymer chain growth.²⁸

ATRP is suitable for the controlled polymerisation of a wide range of monomers, including styrenes, (meth)acrylates, (meth)acrylamides, and various functional vinyl monomers. Its advantages include mild reaction conditions and broad compatibility with both monomers and initiators.²⁸ However, residual metal catalysts are problematic for certain applications,⁶⁸ particularly in applications requiring high purity, such as electronics and biomaterials.^{69–72}

To address this issue, several refined ATRP formulations have been developed, including activators generated by electron transfer (AGET),^{73,74} activators regenerated by electron transfer (ARGET),^{75,76} and initiators for continuous activator regeneration (ICAR).⁷⁶ These variants significantly reduce the required metal catalyst loading, simplify purification, and extend ATRP applicability to aqueous media and other environmentally-friendly solvents.²⁸

Reversible Addition-Fragmentation Chain Transfer (RAFT) Polymerisation

Reversible addition-fragmentation chain transfer (RAFT) polymerisation was first reported in 1998 by Chiefari et al.⁷⁷ In this seminal study, RAFT was introduced as a novel controlled radical polymerisation technique with “excellent efficiency and broad versatility”. In essence, the addition of a small quantity of an organosulfur compound to a conventional free radical polymerisation conferred precise control, enabling the synthesis of polymers with exceptionally narrow MWDs (typically $\bar{D} < 1.20$) and well-defined copolymer architectures. Moreover, this approach proved to be applicable across a broad range of monomer types and reaction conditions. Since its invention, RAFT polymerisation has attracted considerable interest from both academic and industrial research groups and has evolved into one of the most widely adopted methods in the field of controlled radical polymerisation.¹⁸

Initiation and propagation**Reversible chain transfer and propagation****Re-initiation****Chain equilibrium and propagation****Termination**

Scheme 1.8: General mechanism for RAFT polymerisation.⁷⁸ The process begins with conventional radical initiation and propagation, followed by reversible addition of the propagating radical (P_n^\bullet) to a chain transfer agent (CTA), forming a stabilised intermediate. This intermediate undergoes β -scission to release a new radical (R^\bullet), which can reinitiate polymerisation and form a second propagating chain (P_m^\bullet).

The fundamental mechanism of RAFT polymerisation is based on a reversible addition-fragmentation chain transfer process involving RAFT chain transfer agents (RAFT-CTAs), typically dithiocarbamates or trithiocarbonates or dithiobenzoates.¹⁸ During initiation, a radical initiator undergoes thermal decomposition to generate primary radicals. These radicals initiate the polymerisation of monomer, producing active propagating radicals (P_1^\bullet and P_n^\bullet), consistent with the mechanism of conventional free radical polymerisation (Scheme 1.8).

Unlike in conventional FRP, the propagating radicals do not immediately react with monomers. Instead, they tend to undergo rapid reversible chain transfer with the thiocarbonylthio group of the RAFT agent to form a stabilised intermediate radical. This latter radical is stabilised by the Z group of the CTA and can undergo β -scission to release a new radical (R^\bullet). A dormant CTA-capped polymer adduct ($P_n^\bullet\text{-CTA}$) is formed at the same time. Alternatively, the intermediate radical may undergo fragmentation, regenerating the original propagating radical P_n^\bullet and releasing the CTA (Scheme 1.8).

Subsequently, the liberated R^\bullet must possess high re-initiation efficiency (i.e. $k_i > k_p$) to generate a new radical (P_m^\bullet). As a result, a dynamic equilibrium is established among active and dormant chains via a series of rapid, reversible addition-fragmentation events, enabling continuous transfer and exchange of the active radical centre between polymer chains. However, towards the end of the polymerisation (i.e. under monomer-starved conditions) the propagating radicals are more likely to undergo termination, thereby yielding 'dead' polymer chains.

The efficiency of the RAFT process depends on several critical kinetic parameters: the rate constant for addition (k_{add}) must be sufficiently high to ensure effective trapping of radicals; the intermediate must be short-lived, with a fast fragmentation rate ($k_\beta \geq k_{-\text{add}}$), and the R substituent must function as a good leaving group and form a suitable reinitiating radical to avoid undesirable side-reactions.

In contrast to ATRP, a defining characteristic of RAFT polymerisation is that the target DP is not governed by the initiator concentration, but rather by the [monomer]/[CTA] molar ratio, as shown in Equation (1.9):¹⁷

$$DP = \frac{f[M_0]}{[CTA]_0} \quad (1.9)$$

where f is the fractional monomer conversion and $[M_0]$ and $[CTA_0]$ are the initial concentrations of monomer and CTA, respectively. Consequently, a typical RAFT formulation employs a relatively low initiator concentration and maintains a relatively high [CTA]/[initiator] molar ratio, typically in the range of 5 to 10. This ensures that most of the free radicals are rapidly intercepted by the CTA and incorporated into the reversible addition-fragmentation process.

The choice of CTA plays a critical role in determining the level of control achieved during RAFT polymerisation. As illustrated in Figure 1.6, RAFT CTAs typically comprise trithiocarbonates, dithioesters, xanthates, or dithiocarbamates.¹⁸ The Z group primarily governs the stability of the intermediate radical species, whereas the R group controls the chain initiation efficiency. By varying the nature of the Z and R groups, it is possible to tailor the CTA to suit a wide range of vinyl monomers.

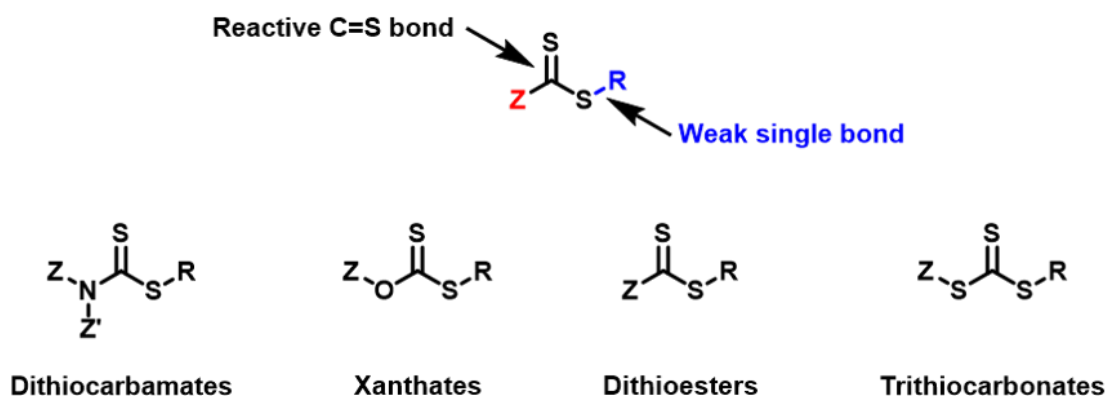


Figure 1.6: Representative chemical structures of the four main classes of RAFT CTAs: trithiocarbonates, dithioesters, xanthates, and dithiocarbamates. Each CTA contains a Z group, which determines the stability of the intermediate radical species, and an R group, which governs the re-initiation efficiency.

The Z group is directly bonded to the C=S bond in the RAFT CTA and plays a key role in regulating both the addition of propagating radicals and the fragmentation of the intermediate radical. Its electronic nature influences the reactivity of the thiocarbonyl group and the stability of the resulting intermediate radical. Electron-withdrawing or conjugated Z groups (aromatic rings) increase the electrophilic character of the C=S bond, facilitating radical addition and stabilising the intermediate, which leads to a controlled polymerisation. However, excessive stabilisation may retard the rate of fragmentation, causing either retardation or inhibition.⁷⁹ In contrast, electron-rich heteroatoms (e.g. alkoxy groups in xanthates or amino groups in dithiocarbamates) reduce radical addition reactivity but accelerate intermediate fragmentation, helping to maintain a dynamic equilibrium.¹⁸ Accordingly, highly active monomers (e.g. acrylates) benefit from electron-deficient Z groups, whereas low-activity monomers (e.g. vinyl

acetate) require less electrophilic Z groups to avoid excessive stabilisation of the intermediate radical species.⁷⁹

The R group governs the leaving ability and reinitiation efficiency of the CTA. Ideally, it should closely resemble the chemical structure of the desired monomer to promote efficient reinitiation. However, in the polymerisation of methacrylates, overly similar R groups may trigger the penultimate unit effect, reducing propagation efficiency.^{79,80} In such cases, either tertiary or sterically-hindered aromatic alkyl groups are preferred. Conversely, acrylic monomers are compatible with either primary or secondary alkyl R groups, providing good control over molecular weight and dispersity.⁷⁹

Vinyl monomers are generally classified as more activated monomers (MAMs) or less activated monomers (LAMs), which differ in reactivity and thus require suitable CTAs for well controlled RAFT polymerisation. MAMs contain a vinyl group conjugated with an electron-withdrawing group (e.g. carbonyl, aromatic, nitrile, or a second double bond), including (meth)acrylates, (meth)acrylamides, acrylonitriles, and styrenes. In contrast, LAMs possess an electron-rich double bond due to an adjacent electron-donating heteroatom, as seen in vinyl esters (e.g. vinyl acetate) and vinyl amides (e.g. N-vinylpyrrolidone).¹⁸

In recent years, numerous review articles have outlined guidelines for the selection of appropriate R and Z groups for RAFT polymerisation, with key recommendations summarised in Figure 1.7.¹⁸ Commonly used CTAs include 4-cyano-4-((2-phenylethanesulfonyl)-thiocarbonylsulfanyl)pentanoic acid (PETTC) and 2-cyano-2-propyl dithiobenzoate (CPDB), which are suitable for a wide range of methacrylic monomers such as hydroxyethyl methacrylate (HEMA),⁸¹ 2-(dimethylamino)ethyl methacrylate (DMA),⁸² methylacrylic acid (MAA),^{83,84} and glycidyl methacrylate (GMA).⁸⁵ In contrast, 2-(dodecylthiocarbonothioylthio)-2-methylpropionic acid (DDMAT) is widely applied to acrylate and acrylamide systems.^{6,86,87} Such RAFT agents provide excellent control over the target molecular weight and dispersity ($\bar{D} \leq 1.20$) and are broadly applicable for the synthesis of functional homopolymers, statistical copolymers and block copolymers.^{6,81–90}

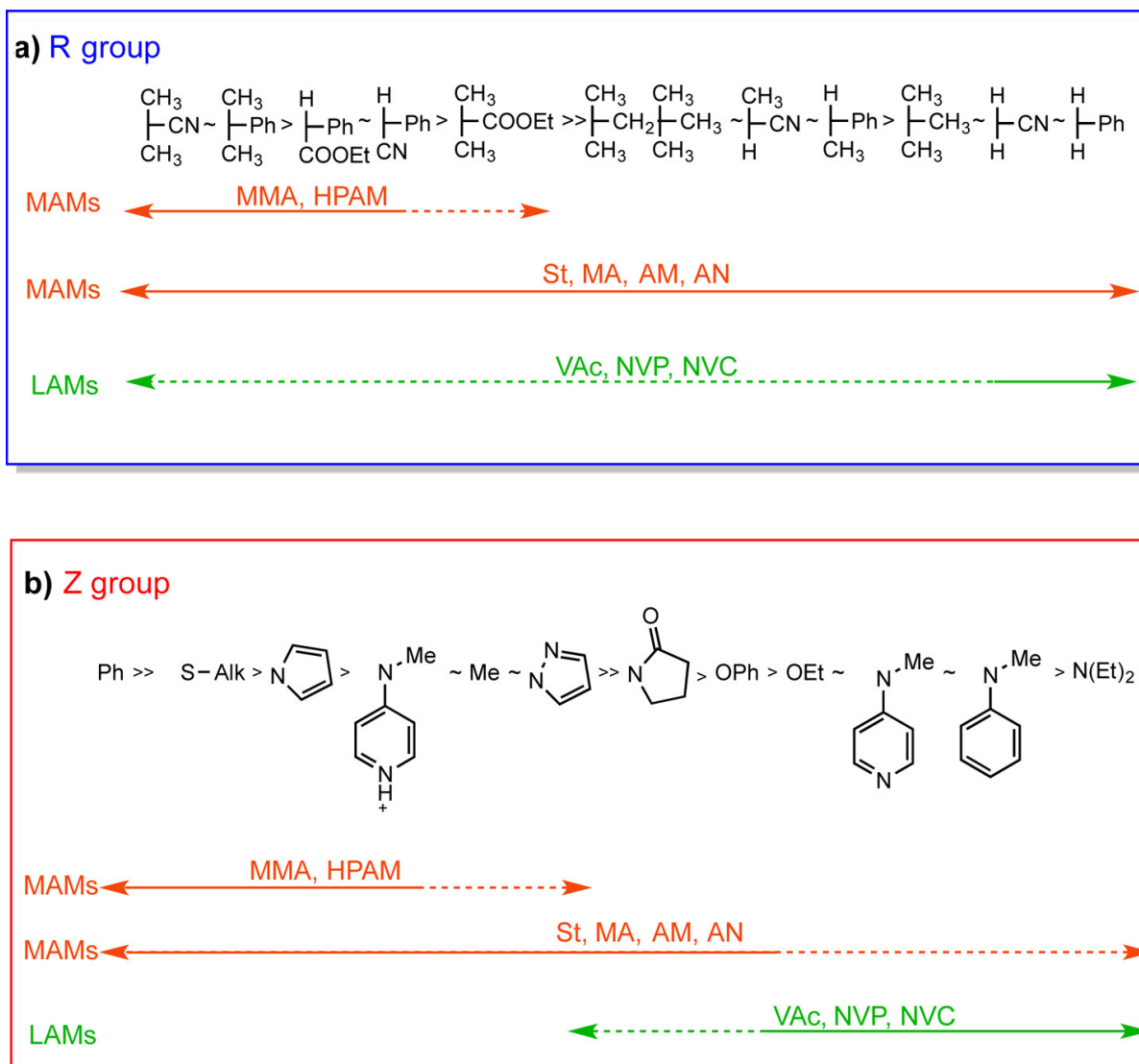


Figure 1.7: (a) Guidelines for selection of the RAFT agent R group for various vinyl monomers, transfer coefficients and fragmentation rates both decrease from left to right, a dashed line indicates poor control; (b) guidelines for selection of the RAFT agent Z group for various monomers, addition rates decrease and fragmentation rates increase from left to right, a dashed line indicates poor control. MMA = methyl methacrylate, HPAM = N-(2-hydroxypropyl)methacrylamide, St = styrene, MA = methyl acrylate, AM = acrylamide, AN = acrylonitrile, VAc = vinyl acetate, NVP = N-vinylpyrrolidone and NVC = N-vinylcarbazole (adapted from Ref. [18]).

Over the past two decades, RAFT polymerisation has emerged as one of the most versatile and efficient RDRP techniques.¹⁸ It is particularly advantageous for monomers that are challenging by other methods, including vinyl acetate, acidic monomers, and those bearing hydroxyl groups.^{81,83–85,91} RAFT chemistry enables precise control over molecular weight, dispersity, ar-

chitecture, and end-group functionality, while also offering excellent compatibility with a wide range of functional monomers and formulations (e.g. bulk, solution, dispersion, or emulsion polymerisation).

Despite its many advantages, RAFT polymerisation is not without its limitations. Potential side-reactions may arise with certain amine-based monomers,^{18,77,92} and some CTAs suffer from drawbacks such as colour, odour, or toxicity.^{93,94} However, these challenges can often be mitigated by optimising reaction conditions or employing end-group removal strategies. Compared to ATRP and NMP, RAFT polymerisation operates under conditions similar to those used for traditional FRP, which should aid its adoption by industrial companies.¹⁸ While the relatively high cost of CTAs was once a barrier to commercialisation, the expiration of key patents and the recent availability of more affordable CTAs have significantly enhanced the commercial viability of RAFT technology.

1.3.2 Chain-Growth Copolymerisation

Chain copolymerisation refers to the synthesis of copolymers via a chain-growth mechanism, wherein two or more distinct monomers are incorporated into the growing polymer chain during the polymerisation. While it shares the same fundamental mechanism as a homopolymerisation, the key distinction lies in the presence of two or more comonomers. These comonomers are incorporated into the copolymer backbone in an alternating, statistical, or block structure, giving rise to copolymers with diverse copolymer architectures. The general concept of chain copolymerisation is illustrated schematically in Figure 1.8.

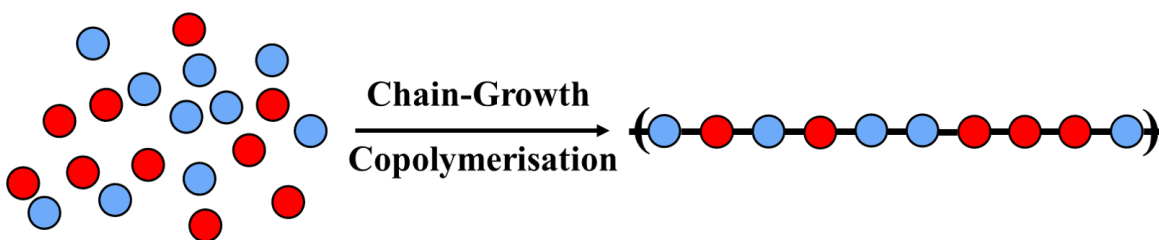
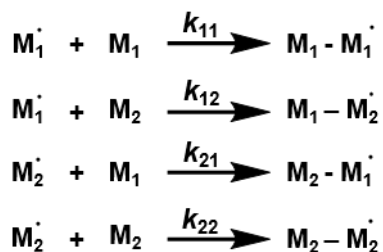


Figure 1.8: Schematic representation of chain copolymerisation when two comonomers are incorporated into a growing copolymer chain.

Copolymers can be broadly classified as statistical copolymers, alternating copolymers, block copolymers, or gradient copolymers (Figure 1.1). However, statistical copolymers are the most commonly encountered architecture in the context of chain-growth polymerisation. In this case, the comonomer units are arranged in a statistical sequence, and they are frequently employed to tailor properties such as glass transition temperature, solubility, and mechanical behaviour. Alternating copolymers feature a regular ABAB-type sequence, in which the two monomers alternate in a strict one-to-one fashion. Block copolymers consist of two or more distinct homopolymer blocks covalently linked together.^{17,95} These structures are typically accessed via RDRP techniques such as RAFT polymerisation or ATRP. The chemical incompatibility between the two blocks usually drives microphase separation, giving rise to ordered nanostructures via self-assembly in either the solid state or in solution.^{96,97} Gradient copolymers, by contrast, exhibit a gradual compositional change along the polymer backbone.¹⁷ This continuous variation in comonomer content can produce a smooth transition in materials properties.

The reaction kinetics of chain copolymerisation provide critical insight into the relative reactivity of different comonomers towards the growing chain-ends and serve as the theoretical foundation for understanding and controlling the copolymer composition, sequence distribution, and resulting physical properties. In a typical binary free radical copolymerisation involving two monomers (denoted M_1 and M_2), the propagation stage comprises four possible addition pathways, see Scheme 1.9:



Scheme 1.9: Four possible propagation pathways in the free radical copolymerisation of two comonomers (M_1 and M_2).¹⁷

where k_{ij} represents the rate constant for the addition of monomer M_j to the active centre with

chain end M_i^\bullet . Based on these rate constants, the reactivity ratio (r) is defined as the relative preference of the active chain-end for each of the two comonomers:

$$r_1 = \frac{k_{11}}{k_{12}}, \quad r_2 = \frac{k_{22}}{k_{21}} \quad (1.10)$$

This reactivity ratio reflects the selectivity of the propagating radical during polymerisation. For example, $r_1 > 1$ indicates that M_1^\bullet radical preferentially adds M_1 rather than M_2 ; such behaviour is described as a preference for self-propagation. Conversely, if $r_1 < 1$, this suggests a preference for cross-propagation with M_2 . Similarly, r_2 describes the relative tendency of M_2^\bullet to react with M_2 , as opposed to M_1 .¹⁷

Assuming steady-state conditions and equal reactivity for the radical centres regardless of their origin, the Mayo-Lewis equation can be derived.⁹⁸ This nonlinear relationship describes the instantaneous mole fraction of monomer M_1 incorporated into the copolymer F_1 as a function of the comonomer feed composition f_1 and the respective comonomer reactivity ratios:

$$F_1 = \frac{r_1 f_1^2 + f_1 f_2}{r_1 f_1^2 + 2f_1 f_2 + r_2 f_2^2} \quad (1.11)$$

where $f_1 = 1 - f_2$. This equation constitutes the fundamental expression in the kinetics of chain copolymerisation, allowing prediction of the instantaneous copolymer composition at any given comonomer feed ratio. Building on this framework, Wu developed a computational model incorporating the Mayo-Lewis equation and Monte Carlo simulations to predict the evolution of copolymer composition in response to varying comonomer feed ratios and reactivity ratios.⁹⁹ Comonomer reactivity ratios are typically determined at low conversion, where the relationship between copolymer composition and monomer feed ratio is considered most reliable.¹⁰⁰ Among the various methods available, the Kelen-Tüdös approach is widely adopted for copolymerisation kinetics owing to its strong fitting stability and broad applicability.^{101,102} This method is derived from a linear transformation of the Mayo-Lewis equation, in which two normalised variables, ξ and η , are introduced to scale the data obtained from the Fineman-Ross method:^{98,101–103}

$$X = \frac{f_1^2}{f_2}, \quad Y = \frac{F_1 - f_1}{f_2}, \quad \xi = \frac{X}{\alpha + X}, \quad \eta = \frac{Y}{\alpha + X} \quad (1.12)$$

where α is an arbitrary positive constant, typically defined as the square root of $X_{\min} \cdot X_{\max}$ in practice. The introduction of these normalised variables enhances the uniformity of data distribution within the coordinate system, effectively reducing deviations and fitting errors.^{17,101} As a result, this method is particularly well-suited for systems with limited sample sizes or unevenly distributed data.¹⁰⁰

By performing a linear regression of η versus ξ , the monomer reactivity ratios r_1 and r_2 can be extracted from the slope and intercept of the fitted line. These values can then be used to predict the copolymer composition and comonomer sequence distribution.^{101,102}

The theoretical basis of the Kelen-Tüdös method assumes low comonomer conversions, such that the original comonomer concentrations remain nearly constant. However, in certain applications, to improve data utilisation or better reflect realistic reaction conditions, refinements to this methodology have been proposed. A subsequent extended model incorporates corrections for the instantaneous comonomer concentrations, thereby extending its applicability to higher conversion ranges (e.g. 40 - 60%) and producing more accurate estimates for the comonomer reactivity ratios.^{100,102}

Different combinations of reactivity ratios result in varying comonomer distribution patterns along the copolymer backbone. When $r_1 r_2 = 1$, the active chain-end exhibits no significant selectivity between the two monomers, yielding a truly random copolymer. When $r_1 r_2 = 0$, cross-propagation is dominant, producing an alternating copolymer with a highly regular sequence. If both $r_1 > 1$ and $r_2 > 1$, then the propagating chain end preferentially adds the same type of comonomer repeatedly, hence favouring the formation of blocky or gradient segment distributions. However, this kinetic regime is relatively uncommon for most examples of free radical copolymerisation.¹⁷

Producing well-defined block copolymers typically requires either anionic polymerisation or reversible-deactivation radical polymerisation (RDRP) techniques.^{18,28,54} On the macroscopic

level, differing sequence distributions can profoundly influence the thermodynamic phase behaviour, mechanical properties, solubility, and self-assembly behaviour of the resulting copolymers.¹⁷

To tune the relative reactivity between comonomers in a copolymerisation, structural modification of the comonomer(s) is often undertaken. The chemical structure of the monomer plays a decisive role in determining reactivity ratios, which is mainly controlled by electronic, resonance and steric effects.¹⁷ Electron-withdrawing substituents tend to promote cross-propagation, whereas electron-donating groups favour homopropagation.¹⁷ Resonance effects such as the conjugation in styrene can stabilise the propagating radical and enhance monomer selectivity,¹⁰⁴ while sufficient steric hindrance may impede monomer addition altogether. These structural factors collectively influence the sequence distribution of comonomer repeat units within the copolymer chain. In addition to monomer structure, the choice of solvent, temperature,¹⁰⁵ and pressure¹⁰⁶ can also influence the copolymerisation behaviour. Though often regarded as a secondary consideration, the reaction medium can induce local deviations in comonomer composition via partitioning, diffusion, or preferential adsorption, particularly in heterogeneous systems such as emulsions or high-viscosity formulations.^{107,108} For example, *N*-vinylcarbazole may become selectively adsorbed, thereby altering the effective local monomer concentration near active centres.¹⁰⁷

The polarity of the solvent can affect comonomer reactivity by either modulating resonance stabilisation or promoting tautomeric shifts.¹⁷ Temperature generally has a moderate influence on reactivity ratios. For example, in the copolymerisation of styrene and methyl methacrylate (MMA), both r_1 and r_2 increase slightly with temperature, indicating lower selectivity and a tendency towards more statistical incorporation.¹⁰⁵ While pressure effects are typically negligible under ambient conditions, they become significant under high-pressure conditions, whereby a higher number of molecular collisions reduce selectivity and promote ideal random copolymerisation.¹⁰⁶

In practice, attaining the desired polymer sequence and material properties requires the holistic

consideration of monomer structure, reaction parameters, and medium-specific effects. Datasets compiled by Greenley on comonomer reactivity ratios provide an invaluable reference for the design of statistical copolymerisation systems.¹⁰⁵

1.4 Liquid Foam

Liquid foams are colloidal dispersions characterised by a large liquid-gas interface, in which the liquid serves as the continuous phase and the gas as the dispersed phase.^{109,110} Owing to the much higher surface area compared with conventional liquid-gas systems, liquid foams exhibit higher surface energy, which makes them thermodynamically unstable. This instability results from several spontaneous processes, including liquid drainage, bubble coalescence, and eventual collapse. Such foam behaviour reduces the interfacial area and consequently the surface energy.^{109,110}

Nevertheless, liquid foams are commonly found in both natural phenomena and industrial applications. The latter include materials processing, enhanced oil recovery, firefighting, food production and personal care products. Due to the inherent instability of foams, understanding and regulating foamability and foam stability remains a key challenge in colloid and interface science. Surfactants are generally applied to alter the physical and chemical properties of the liquid-gas interface, thereby affecting both the initial formation and persistence of long-term foam structures.^{109–111}

1.4.1 Dispersion, Interface and Surface Tension

To understand the thermodynamically unstable nature of liquid foams and the role of surfactants in altering surface behaviour, it is necessary to consider the fundamentals of dispersion, interface, and surface tension. These basic concepts contribute to the foundations of foam formation and stabilisation mechanisms.

1.4.1.1 Dispersion

A dispersion is a heterogeneous system in which one substance, referred to as the dispersed phase, is distributed within another, known as the continuous phase or dispersion medium. Depending on the size of the dispersed phase, dispersions are typically classified as molecular,

colloidal, or coarse. Molecular dispersions, consisting of solute molecules smaller than 1 nm, behave much like solutions and are thermodynamically stable. Coarse dispersions, with particle sizes exceeding 1 μm , are generally unstable and easily undergo rapid precipitation or phase separation, especially in the case of liquid-liquid or solid-liquid dispersions. Colloidal dispersions, whereby the particle size ranges from approximately 1 nm to 1 μm , represent an important intermediate regime.¹¹⁰ This domain has been described by Nobel Laureate Wilhelm Ostwald as “the world of neglected dimensions”, with its own distinctive physical properties and complex interfacial behaviour.¹¹⁰ Colloidal dispersions possess relatively high interfacial area and can exhibit unique surface behaviour. Such systems may exhibit physical properties (e.g. optical properties, diffusion behaviour, and thermodynamic stability) that differ significantly from those of bulk phases or molecular solutions.¹¹² Colloidal dispersions can be classified according to the physical states of the dispersed and continuous phases, as summarised in Table 1.2.

Table 1.2: Classification of various types of colloids.¹¹⁰

Disperse phase	Disperse medium	Nomenclature	Examples
Gas	Gas	N/A*	N/A*
Gas	Liquid	Foam	Fire extinguisher, whipped cream
Gas	Solid	Solid foam	Aerogel, sponge
Liquid	Gas	Liquid aerosol	Fog, mist, steam
Liquid	Liquid	Emulsion	Milk, latex, hand cream
Liquid	Solid	Gel	Jelly, agar
Solid	Gas	Solid aerosol	Smoke
Solid	Liquid	Suspension or sol	Paint, ink
Solid	Solid	Solid sol	Alloy, glass

*Gas-gas interfaces do not exist due to the rapid mixing of gas molecules.

Due to their intrinsic instability, the formulation and stabilisation of liquid foams requires a comprehensive understanding of interfacial forces, surface energy, and the role played by the surfactant. Consequently, surface science is often studied together with colloid science as a complementary discipline.¹¹⁰

1.4.1.2 Interface

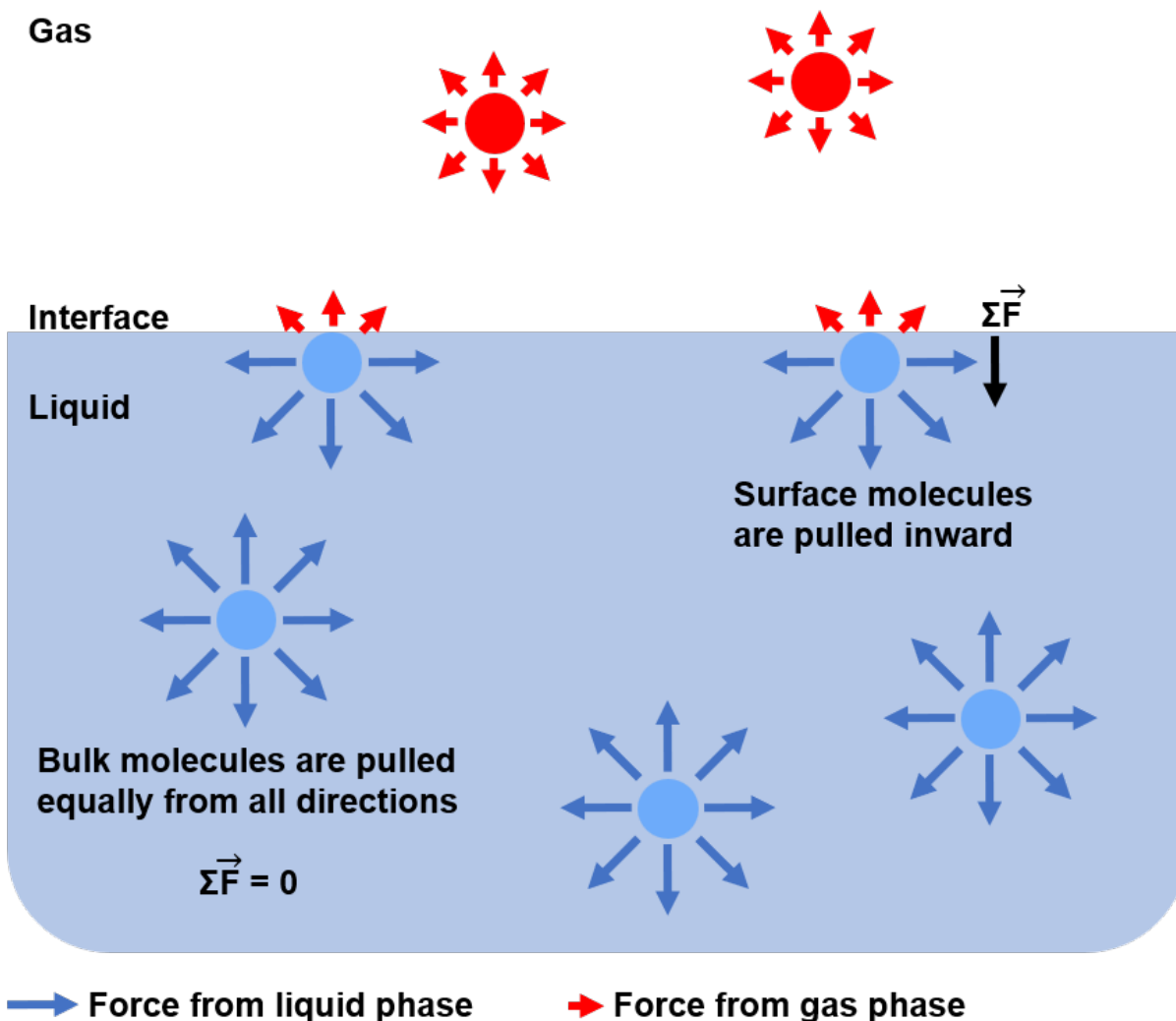


Figure 1.9: Intermolecular forces acting at the liquid-gas interface. $\Sigma \vec{F}$ is the vector sum of all forces acting on a given molecule. Molecules in the bulk phase are subjected to forces acting equally in all directions, hence $\Sigma \vec{F} = 0$. In contrast, molecules located at the surface experience either weaker or no interactions from the gas phase and are therefore pulled inward towards the liquid phase.

An interface, or surface, refers to the transitional region between two adjacent immiscible phases, where physical and chemical properties change from one phase to the other. Although often conceptualised as a two-dimensional boundary, a real interface possesses finite thickness, typically spanning one to several molecular layers. The molecular arrangements and interactions

vary markedly across this region.¹¹⁰

Interfaces strongly influence system properties despite their much smaller dimensions compared to the bulk phases. Depending on the nature of the adjoining phases, interfaces may be classified as solid-solid, solid-liquid, solid-gas, liquid-liquid, or liquid-gas.¹¹⁰ These categories can also be further grouped according to the physical states of the continuous and dispersed phases, as summarised in Table 1.2. Gas-gas interfaces cannot be formed because gas molecules mix rapidly via diffusion. However, the eight other possible interfaces are known.

The liquid-gas interface is characterised by asymmetric interactions.¹¹⁰ Molecules located in the bulk liquid are uniformly surrounded by neighbouring molecules, resulting in isotropic interactions that cancel out each other. Hence the vector sum of all forces ($\sum \vec{F}$) on such molecules is zero. In contrast, molecules located at the air-water interface are exposed to no neighbouring molecules on the gas side, leading to unbalanced forces and a net inward attraction force. As illustrated in Figure 1.9, gas-phase molecules are sparsely distributed and interact weakly, whereas liquid-phase molecules exhibit stronger interactions. The imbalance at the interface results in contraction by pulling surface molecule inward to the liquid phase, highlighting the fundamental role of surface forces in influencing interfacial behaviour.

1.4.1.3 Surface Tension

Surface tension originates from the asymmetry in intermolecular forces acting on molecules at an interface. Molecules at the boundary experience a net inward force from the denser phase, which causes the interface to contract and reduce its surface area.¹¹³ This phenomenon is exemplified by the formation of spherical droplets of water or mercury on solid surfaces, as shown in Figure 1.10, where the spherical shape corresponds to the minimum surface area for a given volume.

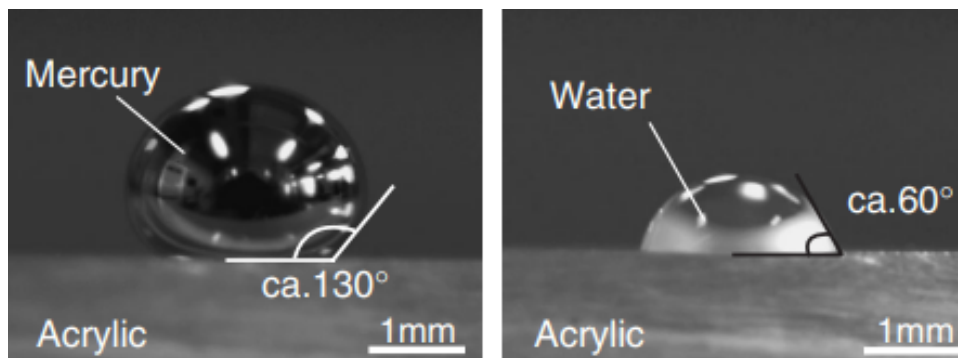


Figure 1.10: Mercury and water droplets on an acrylic substrate in air (adapted from Ref. [113]).

Surface tension (γ) quantifies the tendency of a liquid interface to contract and is defined by the force required to increase unit surface area. It is typically expressed in SI units of $\text{mN}\cdot\text{m}^{-1}$. Surface tension can be determined experimentally using static methods, such as the Du Noüy ring and Wilhelmy plate methods,¹¹⁴ which rely on measuring the force applied at the interface. Dynamic methods such as maximum bubble pressure tensiometry enable time-resolved measurements and are particularly useful for studying the kinetics of surfactant adsorption at interfaces.^{115,116}

1.4.2 Fundamentals of Liquid Foam

Based on the fundamental concepts of dispersion systems and surface tension, this section examines liquid foams, which is a representative example of gas-in-liquid dispersions with distinct structural and dynamic features.^{109,110} Liquid foams are found in a wide range of commercial products, including soaps, shaving creams, and beverages. They may arise from chemical reactions, mechanical agitation, or biological activity. In foam structures, gas is dispersed as discrete bubbles within a continuous liquid phase. Due to buoyancy, bubbles accumulate near the liquid surface and are separated by thin films. Depending on their stability, foams are classified as transient or persistent. For example, beer foam (e.g. Guinness) may persist for hours, whereas bubbles in carbonated drinks burst rapidly. Only gas-in-liquid systems that exhibit sufficient stability are generally considered to be true foams.¹⁰⁹ Foam formation is

not always desirable. In certain processes, such as wastewater treatment, excessive foaming can hinder gas exchange and reduce process efficiency.¹¹⁷ Consequently, both foam generation and suppression are active areas of research in colloid and interface science.

Foams are characterised by low density, large interfacial area, and high surface energy. However, foams are thermodynamically unstable due to mechanisms including drainage, coalescence, and gas diffusion.¹⁰⁹ Without stabilising agents such as surfactants, foam structures collapse rapidly. Unless otherwise specified, the term “foam” in this context refers to liquid foams. Solid foams, in which gas is dispersed within a solid matrix, differ fundamentally and are excluded from this discussion.

1.4.2.1 Foam Formation and Basic Structure

Mechanical methods are commonly employed to generate foam owing to their simplicity and effectiveness in incorporating gas into liquids. However, they are generally unsuitable for quantitative analysis, as the degree of gas-liquid mixing is difficult to control precisely.¹⁰⁹ Gas sparging through a porous nozzle offers a more reproducible and controllable technique, which is widely adopted in laboratory experiments. Standardised methods, such as the Bikerman and Ross-Miles tests, have been developed to assess foamability under well-defined gas-liquid mixing conditions.^{118,119}

Regardless of the formation method, gas bubbles introduced into a pure liquid typically rupture within seconds due to the high surface energy of the newly formed interface. The addition of surfactant is therefore essential to lower interfacial tension and stabilise the foam structure.^{109,110}

Foams are broadly classified as wet or dry, depending on their liquid content (Figure 1.11a, b). This distinction reflects not only their visual characteristics but also their mechanical behaviour and stability. Wet foams contain a high liquid fraction, with nearly spherical bubbles separated by relatively thick liquid films.¹²⁰ As drainage proceeds, the liquid content decreases, and the foam transitions into a dry state. Dry foams consist of polyhedral bubbles separated by thin, flat films and well-defined Plateau borders, as illustrated in Figure 1.11c, d.

A Plateau border is the liquid-filled, channel-like region where three or more foam films meet. Vertices are formed at the intersection of multiple Plateau borders. Geometrically, it adopts a curved triangular cross-section due to the balance of capillary forces at the junction. Under ideal conditions, the angles between films are approximately 120° in two-dimensional structures and 109.28° in three-dimensional foams.¹²¹ This curvature ensures continuity of internal pressure across adjacent films. Plateau borders form a connected network that facilitates liquid drainage and plays a critical role in foam instability.¹²²

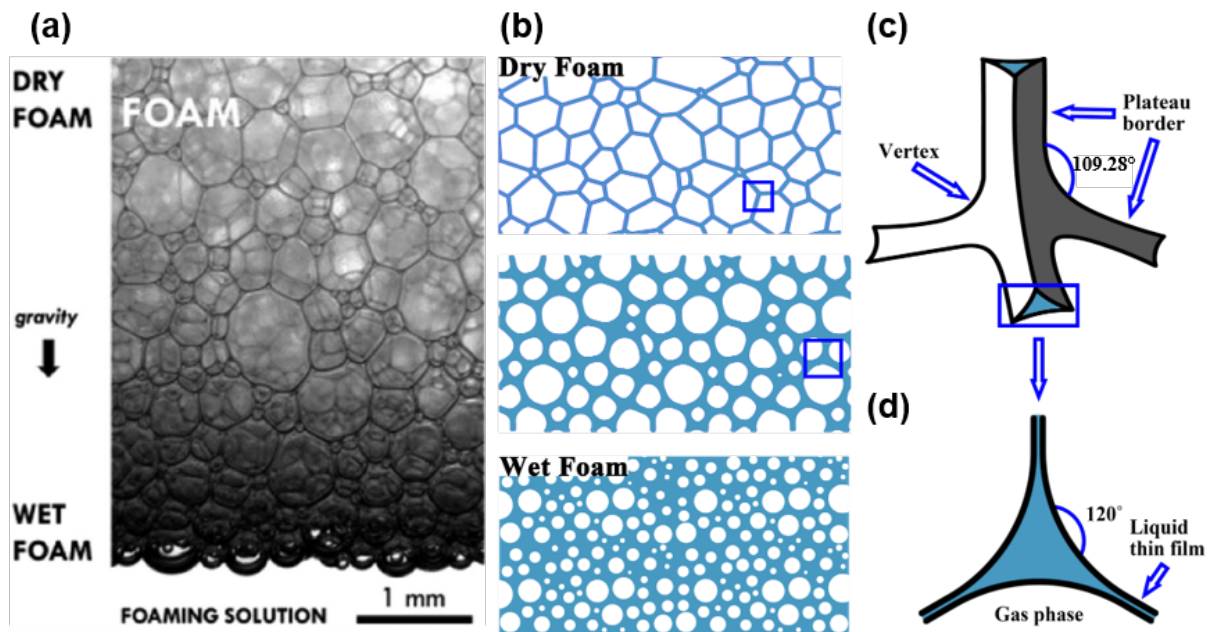


Figure 1.11: (a) Digital photograph illustrating foam drainage under gravity, which leads to a distribution of wet and dry foams. At the top, dry foams form polyhedral structures while wet foams are nearly spherical at the bottom (adapted from Ref. [120]). (b) Schematic diagram of the change of foam structure with increasing wetness. (c) 3D structures of the Plateau border. (d) Cross-section of the Plateau border.

The morphological distinction between wet and dry foams arises from interfacial energy considerations. In wet foams, spherical bubbles minimise surface area for a given volume. As liquid drains, film thickness decreases, inter-bubble forces increase, and the bubbles deform to maintain mechanical stability. If the films become too thin to sustain the pressure difference, either rupture and/or foam collapse may occur.¹⁰⁹

The relationship between foam structure and pressure differences across curved interfaces is

described by the Young-Laplace equation,¹²³ which relates the pressure difference Δp to the interfacial tension γ and the principal radii of curvature R_1 and R_2 :

$$\Delta p = \gamma \left(\frac{1}{R_1} + \frac{1}{R_2} \right) \quad (1.13)$$

In the case of ideal spherical bubbles, where $R_1 = R_2 = R$, Equation (1.13) can be simplified to:

$$\Delta p = \frac{2\gamma}{R} \quad (1.14)$$

For gas-liquid systems such as foams, the Young-Laplace relationship indicates that smaller bubbles exhibit higher internal pressure, which significantly influences foam stability and the evolution of bubble size distribution through gas diffusion.

1.4.2.2 Foam Dynamics

Foam structures are dynamic and evolve over time due to several destabilisation mechanisms governed by interfacial physics, fluid mechanics, and thermodynamics.¹²⁴ Understanding these processes is essential for the rational design and stabilisation of foams. The primary ageing mechanisms are liquid drainage, bubble coalescence, and gas diffusion.¹²⁴

Foam drainage refers to the gravitational flow of liquid through the foam film, mainly via Plateau borders and nodes between adjacent bubbles. As liquid drains, the films gradually thin, compromising mechanical stability and increasing the risk of rupture. Drainage occurs immediately after foam generation and the rate of drainage is retarded as the liquid fraction decreases. Factors influencing drainage include the viscosity of the continuous phase, bubble size, Plateau border geometry, and the presence of surfactants. Surfactants can retard drainage by forming viscoelastic interfacial films and increasing the effective viscosity within Plateau borders.

Coalescence occurs when the lamella formed between adjacent bubbles becomes sufficiently

thin and ruptures, leading to coalescence. This process is more prevalent in dry foams where films are already substantially thinned. The likelihood of coalescence depends on film thickness, capillary effect, interfacial elasticity, and the presence of surfactants or impurities. Surfactants can inhibit coalescence by the Gibbs-Marangoni effect, which redistributes liquid toward regions of local thinning and mitigates rupture.¹²⁵

Even in the absence of drainage and coalescence, foams remain unstable due to internal pressure differences between bubbles of differing size. According to Equation 1.13, smaller bubbles have higher internal pressure than large bubbles. This pressure gradient drives gas diffusion from smaller to larger bubbles through the liquid film, which is known as foam coarsening or Ostwald ripening.¹²⁶ Consequently, small bubbles shrink while large ones grow, which promotes destabilisation. The rate of coarsening is influenced by gas solubility, diffusivity, film thickness, and surfactant.¹²⁴

These three destabilising mechanisms—drainage, coalescence, and Ostwald ripening—act concurrently and interactively, making foam stabilisation particularly challenging. Effective control often requires the use of carefully designed surfactants or amphiphilic polymers.

1.5 Surfactants and Surfactancy

Surfactants are a class of amphiphilic molecules that play a critical role in both the formation and stabilisation of foams. Their unique molecular architecture enables them to adsorb at gas-liquid interfaces, reduce surface tension, and impart mechanical resilience to foam films.¹⁰⁹

1.5.1 Amphiphilic Molecular Structure and Interfacial Behaviour

Surfactants are amphiphilic compounds composed of hydrophilic and hydrophobic groups, which enable their adsorption at interfaces. This leads to a reduction in interfacial tension even at relatively low concentrations. This property contributes to their effectiveness in foam formation and stabilisation. Although the systematic study of surfactants began in the 20th century, amphiphilic molecules such as soaps have been used empirically for millennia.

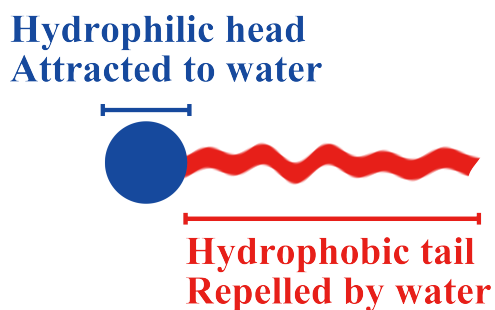


Figure 1.12: Schematic structure of a surfactant molecule comprising a hydrophilic head-group (blue) and a hydrophobic tail (red).

At the molecular level, a typical surfactant comprises a hydrophilic head-group and a hydrophobic tail, as illustrated in Figure 1.12. The hydrophilic head is typically either ionic or polar, facilitating surfactant solubility in aqueous media. Common examples include sulfate groups (e.g. sodium dodecyl sulfate), quaternary ammonium compounds (e.g. benzalkonium chloride), and zwitterionic groups such as betaines. Non-ionic surfactants, particularly those containing hydrophilic PEG chains, are also widely used. The hydrophilic character of PEG-based surfactants generally increases with PEG chain length.¹²⁷ The tail usually consists of a hydrocarbon chain containing 8-18 carbon atoms, with its hydrophobic character influenced by

both overall chain length and its degree of branching.¹²⁸ For certain applications, either perfluorinated or silicone-based surfactants are employed due to their exceptional surface activity.^{2,5} However, environmental and toxicity concerns have led to increasing regulatory restrictions on the use of such compounds.^{11–14}

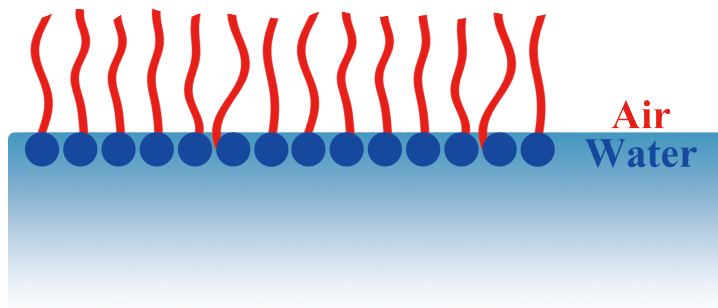


Figure 1.13: Schematic representation of surfactant adsorption at the air-water interface. Surfactant molecules align with their hydrophilic heads immersed within the lower aqueous phase and their hydrophobic tails oriented toward the upper air phase, thereby reducing interfacial tension by replacing the air-water interface with water-surfactant-air interfaces.¹¹⁰

When dissolved in water, the hydrophilic head of a surfactant interacts favourably with water, while its hydrophobic tail is repelled. To minimise this unfavourable interaction, surfactant molecules tend to migrate to the gas-liquid interface and orient themselves with the hydrophobic tails pointing towards the air phase and the hydrophilic heads immersed within the aqueous phase (Figure 1.13). Such adsorption displaces water molecules from the interface, thereby reducing the surface tension.

All surfactants exhibit a critical micelle concentration (CMC), which is defined as the concentration above which surfactant molecules begin to self-assemble into micelles rather than adsorb at interfaces (Figure 1.14a). Below the CMC, added surfactant molecules reduce surface tension through interfacial adsorption. Once the interface becomes saturated, addition of further surfactant molecules leads to the formation of micelles within the bulk solution. Although micelles play an important role in solubilisation and encapsulation, they no longer substantially influence surface tension. In addition to its relevance to interfacial behaviour, the CMC also affects bulk properties such as osmotic pressure, turbidity, and molar conductivity

(Figure 1.14b).¹¹⁰

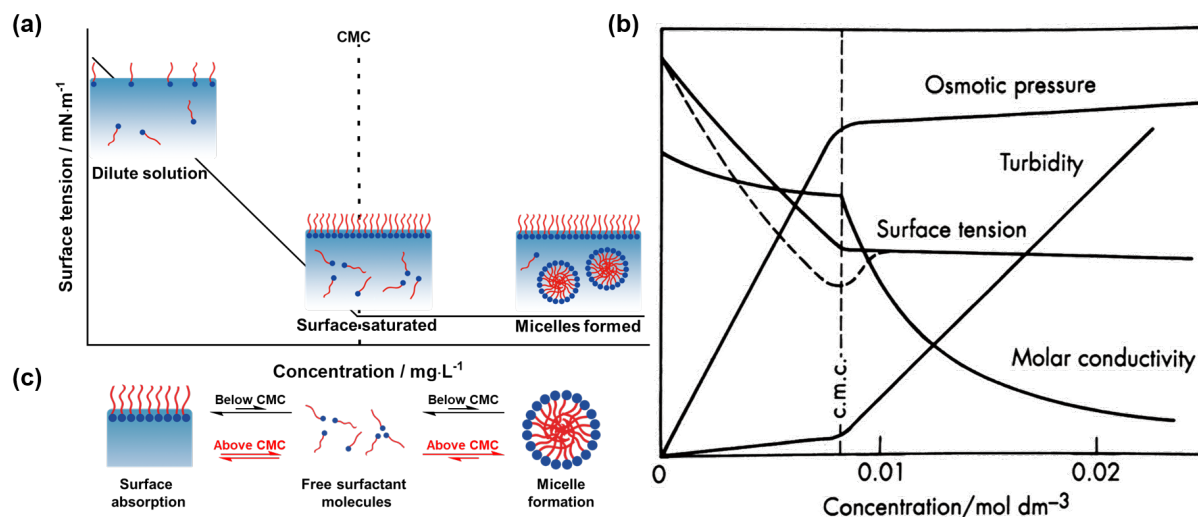


Figure 1.14: (a) Schematic illustration of surfactant behaviour as a function of concentration. At low concentration, surfactant adsorbs at the gas-liquid interface; upon reaching surface saturation, further surfactant addition exceeds the critical micelle concentration (CMC) and hence micelle formation occurs in the bulk and the surface tension no longer decreases. (b) Effect of surfactant concentration on various solution properties, e.g. surface tension, turbidity, molar conductivity, and osmotic pressure, reflecting the onset of micellisation (adapted from Ref. [110]). (c) Dynamic equilibrium of surfactant molecules below and above the CMC. Once the surface is saturated, excess surfactant molecules dynamically self-assemble into micelles in the bulk solution.

1.5.2 Classification of Surfactants by Hydrophilic Groups

Based on the nature of their hydrophilic head-group(s), surfactants are commonly classified as anionic, cationic, non-ionic, or zwitterionic (also referred to as amphoteric). This classification has a substantial impact on surfactant solubility, interfacial behaviour, compatibility with other components, and the range of potential applications. The selection of a suitable surfactant is typically guided by the required interfacial tension reduction, foam stability, chemical compatibility, and considerations of safety and/or regulatory compliance. Table 1.3 summarises the four main surfactant classes according to head-group type, together with representative example(s) in each case.

Table 1.3: Summary of the four main classes of surfactants plus representative examples.

Class	Head Group Type	Commercial examples
Anionic	Sulfate, sulfonate	Sodium dodecyl sulfate (SDS)
Cationic	Quaternary ammonium	Benzalkonium chloride
Non-ionic	Polyethylene glycol (PEG)	Tween 80, Triton X-100
Zwitterionic	Betaine, amino acids	Cocamidopropyl betaine

Anionic Surfactant

Anionic surfactants bear a negative charge on their hydrophilic head-group, typically derived from a sulfate, sulfonate, or carboxylate group. A widely used example is sodium dodecyl sulfate (SDS), which is well known for its strong surface activity and cost-effectiveness, particularly in detergent and foaming formulations.¹²⁹ However, anionic surfactants tend to exhibit inferior performance in hard water due to interactions with divalent cations, and they are generally incompatible with cationic compounds.¹³⁰

Cationic Surfactant

Cationic surfactants feature positively-charged head-groups such as quaternary ammonium ions or primary amine groups. Benzalkonium chloride is a typical example; its antimicrobial efficacy has led to its widespread use in disinfectants.¹³¹

Non-ionic Surfactant

Non-ionic surfactants lack any formal charge but possess polar hydrophilic groups such as short PEG chains. They are characterised by their insensitivity to changes in pH and ionic strength, thus offering superior formulation stability.¹³² Common examples include Tween 80, Triton X-100, and amphiphilic block copolymers such as Pluronics. More recently, hydroxyl-functional sugar surfactants have also gained considerable attention in the literature.¹³³

Zwitterionic Surfactant

Zwitterionic (or amphoteric) surfactants contain both cationic and anionic groups within the same molecule. Their net charge is often pH-dependent, leading to pH-responsive behaviour

under certain conditions.¹³⁴ A representative example is cocamidopropyl betaine, which is frequently used in personal care products for its excellent foamability, low skin irritation potential, and good environmental profile.¹³⁵

1.5.3 Classification of Surfactants by Molecular Weight

Surfactants can also be categorised into either small-molecule or polymeric types according to their molecular weight. Although both classes possess amphiphilic character and can reduce surface tension, they differ substantially in their interfacial behaviour, adsorption kinetics, and stabilisation mechanisms. Given their high molecular weight, polymeric surfactants exhibit much lower CMC compared with that of conventional small-molecule surfactants.¹³⁶

Small-molecule surfactants such as SDS (Figure 1.15a) diffuse fast and adsorb rapidly at interfaces. This makes them highly effective in dynamic systems that require prompt surface tension reduction.¹³⁷ However, their limited molecular size leads to the formation of weak interfacial films with low mechanical strength. As a result, small-molecule surfactants may fail to confer long-term foam stability.¹³⁸

In contrast, polymeric surfactants such as Pluronic[®] poly(ethylene oxide)-*block*-poly(propylene oxide)-*block*-poly(ethylene oxide) (PEO-PPO-PEO) triblock copolymers (Figure 1.15b) adsorb much more slowly owing to their relatively large size.¹³⁹ Once adsorbed, they form robust interfacial layers that enhance resistance to coalescence, film rupture, and liquid drainage.¹⁴⁰

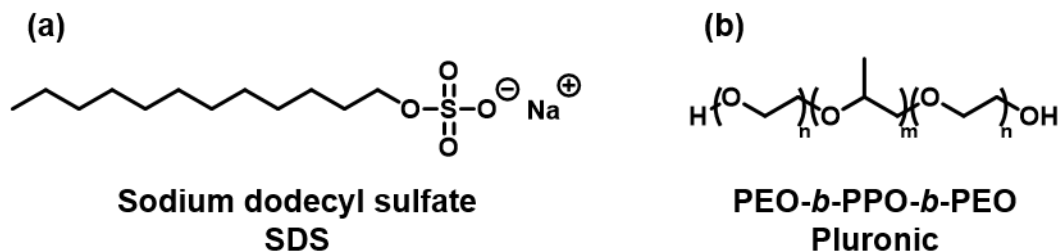


Figure 1.15: Chemical structure of (a) Sodium dodecyl sulfate (SDS), and (b) Pluronic PEO-PPO-PEO triblock copolymer.

In terms of self-assembly, small-molecule surfactants typically form micelles above their CMC.

Depending on their architecture and block composition, polymeric surfactants can form a wide range of aggregates including worm-like micelles and vesicles (Figure 1.16). These differences in self-assembly behaviour also influence their performance in stabilising foams, emulsions, and other dispersed systems.

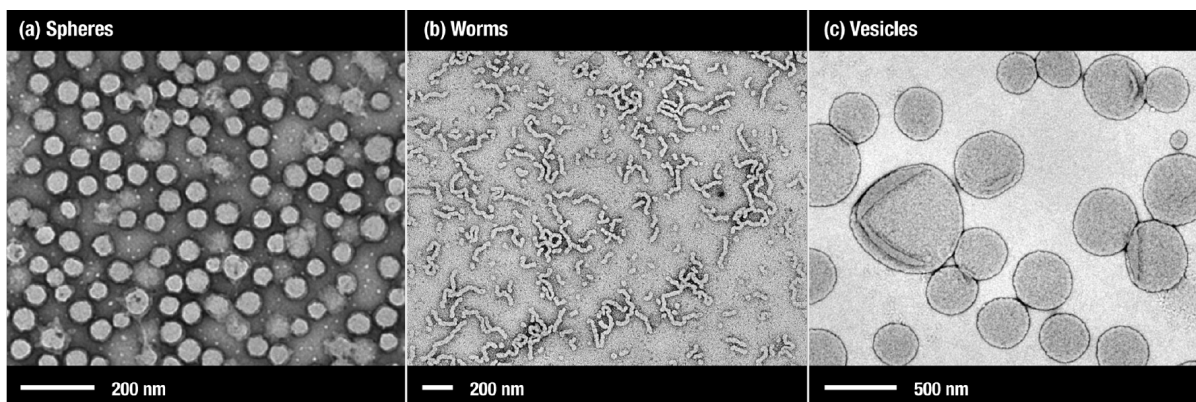


Figure 1.16: Representative transmission electron microscopy (TEM) images for block copolymer micelles exhibiting various morphologies in water: (a) [Poly(quaternised 2-(dimethylamino) ethyl methacrylate)-*stat*-glycerol monomethacrylate]-*block*-poly(2-hydroxypropyl methacrylate) [P(QDMA₁₁-*stat*-GMA₁₁₆)-*block*-PHPMA₉₀₀] spheres. (b) Poly(glycerol monomethacrylate)-poly(2-hydroxypropyl methacrylate) (PGMA₄₇-*block*-PHPMA₁₃₀) worms. (c) Poly(glycerol monomethacrylate)-*block*-poly(2-hydroxypropyl methacrylate) (PGMA₄₇-*block*-PHPMA₂₀₀) vesicle (adapted from Ref. [97]).

The choice between traditional small-molecule surfactants and polymeric surfactants depends on the specific requirements. For applications that require a rapid interfacial response, small-molecule surfactants are generally preferred. However, if long-term stability and durability are prioritised, then polymeric surfactants offer superior performance owing to their ability to form robust, viscoelastic interfacial layers. In some formulations, a combination of both types of surfactants may be employed to achieve synergistic effects, balancing dynamic responsiveness with good long-term stability.

1.5.4 Role of Surfactants in Foam Stabilisation

Foams are thermodynamically unstable due to their high surface area, which leads to elevated interfacial free energy. In the absence of stabilising agents, foams formed in pure liquids

typically collapse within time scales ranging from milliseconds to seconds. Foam stability is therefore a dynamic property, commonly characterised by foam lifetime and resistance to external disruption. So-called 'stable' foams may persist for hours or even days. The lifetime of a foam is primarily governed by (i) the rate of liquid drainage through the Plateau borders and (ii) the mechanical strength and thickness of the foam films.

Surfactants play a multifaceted role in foam stabilisation. By lowering surface tension, they reduce the energy barrier for interface formation, thereby facilitating foam generation. More critically, they suppress bubble coarsening and rupture. Surfactant molecules adsorbed at the gas-liquid interface reinforce the interfacial layer and hinder gas diffusion between adjacent bubbles, thus enhancing static foam stability. In addition, layers of adsorbed surfactant improve the mechanical integrity of foam films, thus increasing their resistance to deformation.

Foam rupture may compromise foam stability by locally stretching the foam film. This leads to a local reduction in the surfactant concentration, which creates a surface tension gradient (Figure 1.17a). Surfactant molecules are driven by this gradient backflow towards the depleted region, which is called the Gibbs-Marangoni effect.¹²⁵ This interfacial self-healing mechanism restores film uniformity and enhances resistance to rupture (Figure 1.17b). However, its effectiveness strongly depends on the surfactant concentration. At concentrations above the critical micelle concentration (CMC), any newly formed interface is rapidly saturated by individual surfactant molecules released from micelles, thus preventing the redistribution of pre-adsorbed molecules. As a result, the Marangoni-driven backflow is suppressed, which reduces the foam's self-repair capacity and explains the lower foamability that is often observed at high surfactant concentrations (Figure 1.17c).

Beyond interfacial phenomena, the rate of liquid drainage from foam films is directly related to the foam lifetime.¹⁴¹ As drainage proceeds, films become thinner and eventually rupture.¹⁰⁹ Increasing the bulk viscosity of the continuous phase is a common strategy to mitigate drainage. Studies have shown that the addition of non-surfactant thickeners—such as glycerol, liquid paraffin, or silicone oil—can significantly extend the foam lifetime, regardless of any surface

tension effect.^{142,143} High molecular weight amphiphilic polymers are particularly effective in this context, providing superior viscosity enhancement compared to small-molecule surfactants. This rheological contribution is a major advantage when using polymeric surfactants, which combine interfacial activity with viscosity modulation to improve foam stability.

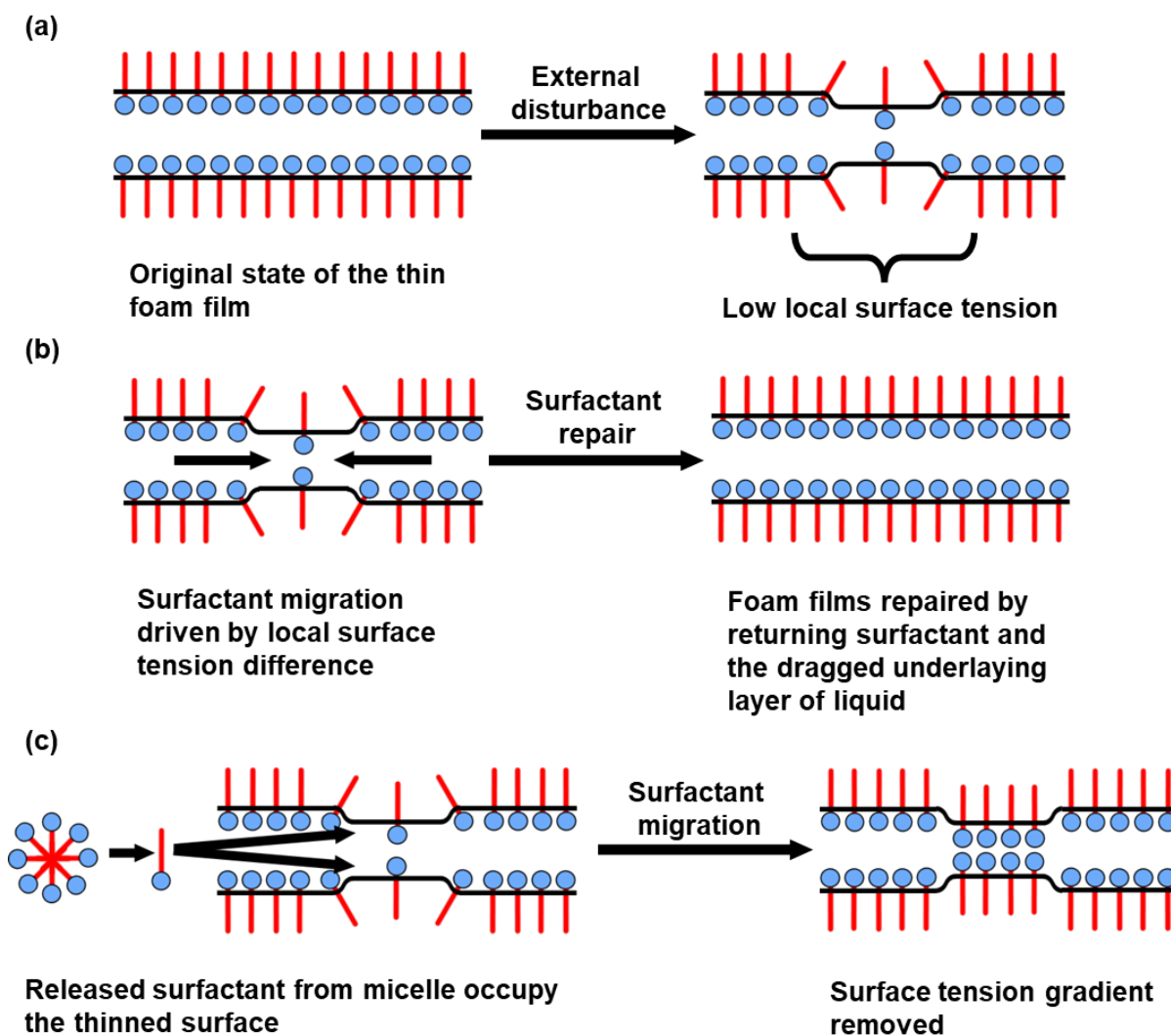


Figure 1.17: (a) External disturbance leads to stretching and thinning of the foam film. (b) The Gibbs-Marangoni effect induces surfactant migration, which can repair the extended foam film. (c) The extended foam film is stabilised by individual surfactant molecules released from micelles, thereby forming thinner films that are easier to rupture.

1.6 Aim and Objectives

This project aims to investigate the foamability and interfacial behaviour of synthetic polymeric surfactants in aqueous solutions, with particular emphasis on amphiphilic statistical copolymers. Building on fundamental principles of surfactant science and preliminary evidence from prior studies,^{6,136} the research explores the potential of these materials as next-generation, silicone-free surfactants for liquid foaming applications. A key challenge lies in the inherently slow interfacial adsorption of polymeric surfactants, arising from their macromolecular structure, which contrasts with the rapid kinetics required for dynamic foam formation. Moreover, effective foam stabilisation is not solely dependent on low equilibrium surface tension, but also on establishing sufficient surface tension gradients, film elasticity, and resistance to drainage, coarsening, and coalescence. There is a trade-off between foamability and foam stability. This work aims to uncover the fundamental mechanisms involved.

To address these complexities, the project systematically investigates how structural factors, such as hydrophobe/hydrophile ratio, molecular weight and chain flexibility, affect the foamability and interfacial properties of amphiphilic copolymers. Several open questions drive this research: how polymer composition modulates foamability; how to characterise chain flexibility precisely; and how to prepare statistical copolymers with more flexible backbones. In parallel, the solution behaviour of these copolymers is examined using small-angle X-ray scattering to establish the structure-property correlations.

In addition, considering that chain flexibility is a key parameter governing the performance of statistical copolymer surfactants, a protonatable statistical copolymer model system is designed and prepared to investigate this property. Within this system, the degree of protonation and the backbone charge density can be precisely controlled by adjusting the solution pH. As chain flexibility is strongly affected by electrostatic interactions, the model copolymer exhibit tunable chain flexibility. Systematic investigation of these model copolymers enables a deeper understanding of how chain flexibility regulates the physicochemical properties of statistical

copolymers. Moreover, an additional advantage of this model design is that these copolymers possess polyelectrolyte characteristics, thereby providing an ideal platform for further exploration of the structure-property relationships and solution behaviour of polyelectrolytes. Through this integrative approach, the project seeks to establish both practical design guidelines and fundamental insights into the behaviour of polymeric surfactants in dynamic foaming environments.

1.7 References

- (1) A. Czajka, G. Hazell and J. Eastoe, *Langmuir*, 2015, **31**, 8205–8217.
- (2) N. M. Kovalchuk, A. Trybala, V. Starov, O. Matar and N. Ivanova, *Advances in Colloid and Interface Science*, 2014, **210**, 65–71.
- (3) F. Hernáinz and A. Caro, *Colloids and Surfaces A: Physicochemical and Engineering Aspects*, 2002, **196**, 19–24.
- (4) W.-H. Wu, J.-L. Wang, Y.-Q. Zhou, Y. Sun, J. Duan and A. Zhang, *Chemical Papers*, 2023, **77**, 6763–6771.
- (5) R. Wagner, L. Richter, Y. Wu, J. Weißmüller, A. Kleewein and E. Hengge, *Applied Organometallic Chemistry*, 1998, **12**, 265–276.
- (6) J. Jennings, R. R. Webster-Aikman, N. Ward-O’Brien, A. Xie, D. L. Beattie, O. J. Deane, S. P. Armes and A. J. Ryan, *ACS Applied Materials & Interfaces*, 2022, **14**, 39548–39559.
- (7) L. C. Brown, K. M. Hinnant, G. C. Daniels, P. E. Sudol, S. R. Vaughan, N. K. Weise and B. C. Giordano, *Langmuir*, 2023, **39**, 8559–8567.
- (8) G. C. Daniels, K. M. Hinnant, L. C. Brown, N. K. Weise, M. C. Aukerman and B. C. Giordano, *Langmuir*, 2022, **38**, 4547–4554.
- (9) E. Panieri, K. Baralic, D. Djukic-Cosic, A. Buha Djordjevic and L. Saso, *Toxics*, 2022, **10**, 44.
- (10) B. Laubie, E. Bonnafous, V. Desjardin, P. Germain and E. Fleury, *Science of The Total Environment*, 2013, **454-455**, 199–205.
- (11) D. Savoca and A. Pace, *International Journal of Molecular Sciences*, 2021, **22**, 6276.
- (12) A. J. Lewis, X. Yun, D. E. Spooner, M. J. Kurz, E. R. McKenzie and C. M. Sales, *Science of The Total Environment*, 2022, **822**, 153561.

- (13) J. Li, J. Sun and P. Li, *Environment International*, 2022, **158**, 106891.
- (14) J. Chen, J. D. Fine and C. A. Mullin, *Science of The Total Environment*, 2018, **612**, 415–421.
- (15) R. Mülhaupt, *Angewandte Chemie International Edition*, 2004, **43**, 1054–1063.
- (16) W. H. Carothers, *Chemical Reviews*, 1931, **8**, 353–426.
- (17) G. Odian, *Principles of Polymerization*, Wiley, Hoboken, NJ, USA, 4th edn., 2004.
- (18) S. Perrier, *Macromolecules*, 2017, **50**, 7433–7447.
- (19) M. Szwarc, M. Levy and R. Milkovich, *Journal of the American Chemical Society*, 1956, **78**, 2656–2657.
- (20) G. Moad, *Polymer International*, 2023, **72**, 861–868.
- (21) J. Yang, I. Gitlin, V. M. Krishnamurthy, J. A. Vazquez, C. E. Costello and G. M. Whitesides, *Journal of the American Chemical Society*, 2003, **125**, 12392–12393.
- (22) J. C. Moore, *Journal of Polymer Science Part A: General Papers*, 1964, **2**, 835–843.
- (23) B. H. Zimm, *The Journal of Chemical Physics*, 1948, **16**, 1093–1099.
- (24) K. Tanaka, H. Waki, Y. Ido, S. Akita, Y. Yoshida, T. Yoshida and T. Matsuo, *Rapid Communications in Mass Spectrometry*, 1988, **2**, 151–153.
- (25) P. J. Flory, *Principles of polymer chemistry*, Cornell University Press, Ithaca, NY, USA, 1953.
- (26) T. G. Fox, *Bull. Am. Phys. Soc.*, 1956, **1**, 1236.
- (27) H. R. Lamontagne and B. H. Lessard, *ACS Applied Polymer Materials*, 2020, **2**, 5327–5344.
- (28) K. Matyjaszewski, *Macromolecules*, 2012, **45**, 4015–4039.
- (29) M. Sawamoto, *Progress in Polymer Science*, 1991, **16**, 111–172.

- (30) A. D. Jenkins, R. G. Jones and G. Moad, *Pure and Applied Chemistry*, 2009, **82**, 483–491.
- (31) O. Nuyken and M. Vierle, *Designed Monomers and Polymers*, 2005, **8**, 91–105.
- (32) M.-L. Yang, K. Li and H. D. H. Stöver, *Macromolecular Rapid Communications*, 1994, **15**, 425–432.
- (33) M. Sawamoto and T. Higashimura, *Makromolekulare Chemie. Macromolecular Symposia*, 1986, **3**, 83–97.
- (34) W. Busfield and J. Methven, *Polymer*, 1973, **14**, 137–144.
- (35) D. Baskaran and A. H. Müller, *Progress in Polymer Science*, 2007, **32**, 173–219.
- (36) W. Lee, H. Lee, J. Cha, T. Chang, K. J. Hanley and T. P. Lodge, *Macromolecules*, 2000, **33**, 5111–5115.
- (37) H. L. Hsieh, in *Applications of Anionic Polymerization Research*, ed. R. P. Quirk, 1998, ch. 2, pp. 28–33.
- (38) A. Hirao, R. Goseki and T. Ishizone, *Macromolecules*, 2014, **47**, 1883–1905.
- (39) S. Singha, S. Pan, S. S. Tallury, G. Nguyen, R. Tripathy and P. De, *ACS Polymers Au*, 2024, **4**, 189–207.
- (40) J. P. Kennedy and S. C. Feinberg, *Journal of Polymer Science: Polymer Chemistry Edition*, 1978, **16**, 2191–2197.
- (41) S. Zhu, Y. Lu, K. Wang and G. Luo, *RSC Adv.*, 2016, **6**, 97983–97989.
- (42) J. Puskás, G. Kaszás, J. P. Kennedy, T. Kelen and F. T. and, *Journal of Macromolecular Science: Part A - Chemistry*, 1982, **18**, 1229–1244.
- (43) J. P. Kennedy, S. Y. Huang and S. C. Feinberg, *Journal of Polymer Science: Polymer Chemistry Edition*, 1977, **15**, 2801–2819.
- (44) S. Aoshima and S. Kanaoka, *Chemical Reviews*, 2009, **109**, 5245–5287.

- (45) S. Sugihara, A. Yoshida, T.-a. Kono, T. Takayama and Y. Maeda, *Journal of the American Chemical Society*, 2019, **141**, 13954–13961.
- (46) L. I. Gabaston, R. A. Jackson and S. P. Armes, *Macromolecules*, 1998, **31**, 2883–2888.
- (47) N. Ballard and J. M. Asua, *Progress in Polymer Science*, 2018, **79**, 40–60.
- (48) T. Pirman, M. Ocepek and B. Likozar, *Industrial & Engineering Chemistry Research*, 2021, **60**, 9347–9367.
- (49) A. K. O'Brien and C. N. Bowman, *Macromolecules*, 2006, **39**, 2501–2506.
- (50) T. Lee, C. Guymon, E. S. Jönsson and C. Hoyle, *Polymer*, 2004, **45**, 6155–6162.
- (51) C. Magee, Y. Sugihara, P. B. Zetterlund and F. Aldabbagh, *Polym. Chem.*, 2014, **5**, 2259–2265.
- (52) N. M. Ahmad, F. Heatley and P. A. Lovell, *Macromolecules*, 1998, **31**, 2822–2827.
- (53) B. Yamada, D. G. Westmoreland, S. Kobatake and O. Konosu, *Progress in Polymer Science*, 1999, **24**, 565–630.
- (54) T. Otsu, T. Matsunaga, A. Kuriyama and M. Yoshioka, *European Polymer Journal*, 1989, **25**, 643–650.
- (55) A. Ghadban and L. Albertin, *Polymers*, 2013, **5**, 431–526.
- (56) C. Johnson, G. Moad, D. Solomon, T. Spurling and D. Vearing, *Australian Journal of Chemistry*, 1990, **43**, 1215–1230.
- (57) C. Johnson, G. Moad, D. Solomon and T. Spurling, *Australian Journal of Chemistry*, 1986, **39**, 1943–1950.
- (58) M. K. Georges, R. P. N. Veregin, P. M. Kazmaier and G. K. Hamer, *Macromolecules*, 1993, **26**, 2987–2988.
- (59) A. Bagheri, C. M. Fellows and C. Boyer, *Advanced Science*, 2021, **8**, 2003701.
- (60) E. Beaudoin, D. Bertin, D. Gigmes, S. R. A. Marque, D. Siri and P. Tordo, *European Journal of Organic Chemistry*, 2006, **2006**, 1755–1768.

- (61) R. B. G. and, *Polymer Reviews*, 2011, **51**, 104–137.
- (62) D. Benoit, V. Chaplinski, R. Braslau and C. J. Hawker, *Journal of the American Chemical Society*, 1999, **121**, 3904–3920.
- (63) M. K. Georges, R. P. N. Veregin, P. M. Kazmaier and G. K. Hamer, *Macromolecules*, 1993, **26**, 2987–2988.
- (64) C. Xu, T. Wu, C. M. Drain, J. D. Batteas and K. L. Beers, *Macromolecules*, 2005, **38**, 6–8.
- (65) G. Delaître, J. Rieger and B. Charleux, *Macromolecules*, 2011, **44**, 462–470.
- (66) J.-S. Wang and K. Matyjaszewski, *Journal of the American Chemical Society*, 1995, **117**, 5614–5615.
- (67) M. Kato, M. Kamigaito, M. Sawamoto and T. Higashimura, *Macromolecules*, 1995, **28**, 1721–1723.
- (68) M. F. Cunningham, *Progress in Polymer Science*, 2008, **33**, 365–398.
- (69) W. A. Braunecker, N. V. Tsarevsky, A. Gennaro and K. Matyjaszewski, *Macromolecules*, 2009, **42**, 6348–6360.
- (70) N. V. Tsarevsky and K. Matyjaszewski, *Journal of Polymer Science Part A: Polymer Chemistry*, 2006, **44**, 5098–5112.
- (71) N. Bortolamei, A. A. Isse, A. J. D. Magenau, A. Gennaro and K. Matyjaszewski, *Angewandte Chemie International Edition*, 2011, **50**, 11391–11394.
- (72) S. Averick, A. Simakova, S. Park, D. Konkolewicz, A. J. D. Magenau, R. A. Mehl and K. Matyjaszewski, *ACS Macro Letters*, 2012, **1**, 6–10.
- (73) J. Gromada and K. Matyjaszewski, *Macromolecules*, 2001, **34**, 7664–7671.
- (74) K. Min, W. Jakubowski and K. Matyjaszewski, *Macromolecular Rapid Communications*, 2006, **27**, 594–598.
- (75) H. Dong and K. Matyjaszewski, *Macromolecules*, 2008, **41**, 6868–6870.

- (76) L. Mueller, W. Jakubowski, W. Tang and K. Matyjaszewski, *Macromolecules*, 2007, **40**, 6464–6472.
- (77) J. Chiefari, Y. K. (Bill) Chong, F. Ercole, J. Krstina, J. Jeffery, T. P. T. Le, R. T. A. Mayadunne, G. F. Meijs, C. L. Moad, G. Moad, E. Rizzardo and S. H. Thang, *Macromolecules*, 1998, **31**, 5559–5562.
- (78) G. Moad and C. Barner-Kowollik, in *Handbook of RAFT Polymerization*, ed. C. Barner-Kowollik, John Wiley & Sons, Ltd, New York, USA, 2008, ch. 3, pp. 51–104.
- (79) D. J. Keddie, G. Moad, E. Rizzardo and S. H. Thang, *Macromolecules*, 2012, **45**, 5321–5342.
- (80) K. Ono and S. Teramachi, *Polym J*, 1995, **27**, 790–796.
- (81) C. György, J. S. Wagstaff, S. J. Hunter, E. U. Etim and S. P. Armes, *Macromolecules*, 2024, **57**, 6816–6827.
- (82) S. M. North and S. P. Armes, *Green Chem.*, 2021, **23**, 1248–1258.
- (83) A. A. Cockram, T. J. Neal, M. J. Derry, O. O. Mykhaylyk, N. S. J. Williams, M. W. Murray, S. N. Emmett and S. P. Armes, *Macromolecules*, 2017, **50**, 796–802.
- (84) E. J. Cornel, G. N. Smith, S. E. Rogers, J. E. Hallett, D. J. Gowney, T. Smith, P. S. O’Hora, S. van Meurs, O. O. Mykhaylyk and S. P. Armes, *Soft Matter*, 2020, **16**, 3657–3668.
- (85) D. H. H. Chan, S. J. Hunter, T. J. Neal, C. Lindsay, P. Taylor and S. P. Armes, *Soft Matter*, 2022, **18**, 6757–6770.
- (86) S. J. Hunter and S. P. Armes, *Journal of Colloid and Interface Science*, 2023, **634**, 906–920.
- (87) H. Buksa, T. J. Neal, S. Varlas, S. J. Hunter, O. M. Musa and S. P. Armes, *Macromolecules*, 2023, **56**, 4296–4306.

- (88) E. Girard, J.-D. Marty, B. Ameduri and M. Destarac, *ACS Macro Letters*, 2012, **1**, 270–274.
- (89) A. Guinaudeau, O. Coutelier, A. Sandeau, S. Mazières, H. D. Nguyen Thi, V. Le Drogo, D. J. Wilson and M. Destarac, *Macromolecules*, 2014, **47**, 41–50.
- (90) M. J. Derry, L. A. Fielding and S. P. Armes, *Progress in Polymer Science*, 2016, **52**, 1–18.
- (91) E. Girard, T. Tassaing, J.-D. Marty and M. Destarac, *Polym. Chem.*, 2011, **2**, 2222–2230.
- (92) A. Postma, T. P. Davis, R. A. Evans, G. Li, G. Moad and M. S. O’Shea, *Macromolecules*, 2006, **39**, 5293–5306.
- (93) L. Barner and S. Perrier, in *Handbook of RAFT Polymerization*, John Wiley & Sons, Ltd, New York, USA, 2008, ch. 12, pp. 455–482.
- (94) G. Moad, E. Rizzardo and S. H. Thang, *Polymer International*, 2011, **60**, 9–25.
- (95) H. Feng, X. Lu, W. Wang, N.-G. Kang and J. W. Mays, *Polymers*, 2017, **9**.
- (96) J. Massey, K. N. Power, I. Manners and M. A. Winnik, *Journal of the American Chemical Society*, 1998, **120**, 9533–9540.
- (97) S. L. Canning, G. N. Smith and S. P. Armes, *Macromolecules*, 2016, **49**, 1985–2001.
- (98) F. R. Mayo and F. M. Lewis, *Journal of the American Chemical Society*, 1944, **66**, 1594–1601.
- (99) V. Wu, Compositional Drift, <https://vince-wu.github.io/CompositionalDrift/>, (accessed June 2025).
- (100) D. Fournier, R. Hoogenboom, H. M. L. Thijs, R. M. Paulus and U. S. Schubert, *Macromolecules*, 2007, **40**, 915–920.
- (101) J. P. Kennedy, T. Kelen and F. Tüdös, *Journal of Polymer Science: Polymer Chemistry Edition*, 1975, **13**, 2277–2289.

- (102) T. Kelen, F. Tüdös, B. Turcsányi and J. P. Kennedy, *Journal of Polymer Science: Polymer Chemistry Edition*, 1977, **15**, 3047–3074.
- (103) M. Fineman and S. D. Ross, *Journal of Polymer Science*, 1950, **5**, 259–262.
- (104) C. Walling, *Free Radicals in Solution*, Wiley, New York, USA, 1957.
- (105) R. Z. Greenley, in *The Wiley Database of Polymer Properties*, Wiley, Hoboken, NJ, USA, 2003.
- (106) M. Buback and H. Dietzsch, *Macromolecular Chemistry and Physics*, 2001, **202**, 1173–1181.
- (107) A. Ledwith, G. Galli, E. Chiellini and R. Solaro, *React Kinet Catal Lett*, 1974, **1**, 487–492.
- (108) T. Kelen and F. Tüdös, *Polymer Bulletin*, 1979, **1**, 491–499.
- (109) R. J. Pugh, *Bubble and Foam Chemistry*, Cambridge University Press, Cambridge, UK, 2016.
- (110) D. J. Shaw, *Introduction to Colloid and Surface Chemistry*, Butterworth-Heinemann, Oxford, UK, 4th edn., 1992.
- (111) In *Foam and Foam Films*, ed. D. Exerowa and P. M. Kruglyakov, Elsevier, Amsterdam, Netherlands, 1998, ch. 3, pp. 88–344.
- (112) L. Qiu, N. Zhu, Y. Feng, E. E. Michaelides, G. Żyła, D. Jing, X. Zhang, P. M. Norris, C. N. Markides and O. Mahian, *Physics Reports*, 2020, **843**, 1–81.
- (113) T. Naoe, S. Hasegawa, A. Bucheeri and M. Futakawa, *Journal of Nuclear Science and Technology*, 2008, **45**, 1233–1236.
- (114) P. L. du Noüy, *Journal of General Physiology*, 1925, **7**, 625–631.
- (115) X. Y. Hua and M. J. Rosen, *Journal of Colloid and Interface Science*, 1991, **141**, 180–190.

- (116) X. Y. Hua and M. J. Rosen, *Journal of Colloid and Interface Science*, 1988, **124**, 652–659.
- (117) M. C. Collivignarelli, M. Baldi, A. Abbà, F. M. Caccamo, M. Carnevale Miino, E. C. Rada and V. Torretta, *Applied Sciences*, 2020, **10**.
- (118) J. J. Bikerman, in *Foams*, Springer, Heidelberg, Germany, 1973, ch. 3, pp. 65–97.
- (119) J. Ross and G. D. Miles, *Oil & Soap*, 1941, **18**, 899–102.
- (120) W. Drenckhan and S. Hutzler, *Advances in Colloid and Interface Science*, 2015, **224**, 1–16.
- (121) D. Liu, H. Lin, X. Cheng, L. Sun, L. Guo and C. Hong, *Coasts*, 2025, **5**.
- (122) P. Grassia, S. Ubal, M. D. Giavedoni, D. Vitasari and P. J. Martin, *Chemical Engineering Science*, 2016, **143**, 139–165.
- (123) H. Liu and G. Cao, *Scientific reports*, 2016, **6**, 23936.
- (124) N. Moradpour, J. Yang and P. A. Tsai, *Current Opinion in Colloid & Interface Science*, 2024, **74**, 101845.
- (125) R. Pugh, *Advances in Colloid and Interface Science*, 1996, **64**, 67–142.
- (126) Z. Zhang, Z. Wang, S. He, C. Wang, M. Jin and Y. Yin, *Chem. Sci.*, 2015, **6**, 5197–5203.
- (127) J. K. Ogunjobi, T. J. Farmer, J. H. Clark and C. R. McElroy, *ACS Sustainable Chemistry & Engineering*, 2023, **11**, 1857–1866.
- (128) B. Kronberg, K. Holmberg and B. Lindman, *Surface Chemistry of Surfactants and Polymers*, John Wiley & Sons, Ltd, New York, USA, 2014.
- (129) J. Wang, A. V. Nguyen and S. Farrokhpay, *Colloids and Surfaces A: Physicochemical and Engineering Aspects*, 2016, **495**, 110–117.
- (130) R. Petkova, S. Tcholakova and N. Denkov, *Langmuir*, 2012, **28**, 4996–5009.
- (131) B. M. P. Pereira and I. Tagkopoulos, *Applied and Environmental Microbiology*, 2019, **85**, e00377–19.

- (132) B. Petkova, S. Tcholakova, M. Chenkova, K. Golemanov, N. Denkov, D. Thorley and S. Stoyanov, *Advances in Colloid and Interface Science*, 2020, **276**, 102084.
- (133) K. Neimert-Andersson, S. Sauer, O. Panknin, T. Borg, E. Söderlind and P. Somfai, *The Journal of Organic Chemistry*, 2006, **71**, 3623–3626.
- (134) H. Wu, X. Chen, R. Tan, Y. Luo, Y. Hu, Y. Li, J. Hou and W. Kang, *Fuel*, 2022, **312**, 122921.
- (135) V. T. Kelleppan, C. S. Butler, A. P. Williams, M. L. P. Vidallon, L. W. Giles, J. P. King, A. V. Sokolova, L. de Campo, G. R. Pearson, R. F. Tabor and K. L. Tuck, *Colloids and Surfaces A: Physicochemical and Engineering Aspects*, 2023, **656**, 130435.
- (136) P. Raffa, D. A. Z. Wever, F. Picchioni and A. A. Broekhuis, *Chemical Reviews*, 2015, **115**, 8504–8563.
- (137) D. Kawale, A. van Nimwegen, L. Portela, M. van Dijk and R. Henkes, *Colloids and Surfaces A: Physicochemical and Engineering Aspects*, 2015, **481**, 328–336.
- (138) N. Jiang, X. Yu, Y. Sheng, R. Zong, C. Li and S. Lu, *Chemical Engineering Science*, 2020, **216**, 115474.
- (139) A. Hädicke and A. Blume, *Journal of Colloid and Interface Science*, 2013, **407**, 327–338.
- (140) T. Tadros, A. Vandamme, B. Levecke, K. Booten and C. Stevens, *Advances in Colloid and Interface Science*, 2004, **108-109**, 207–226.
- (141) J. S. Lioumbas, E. Georgiou, M. Kostoglou and T. D. Karapantsios, *Colloids and Surfaces A: Physicochemical and Engineering Aspects*, 2015, **487**, 92–103.
- (142) M. Safouane, A. Saint-Jalmes, V. Bergeron and D. Langevin, *The European Physical Journal E*, 2006, **19**, 195–202.
- (143) X. Dong, D. Sun, H. Zhang, C. Cao, J. Xu and X. Jiang, *Colloid and Polymer Science*, 2010, **288**, 1271–1280.

Chapter 2

Statistical Analysis based on Design of Experiments (DoE) and Analysis of Variance (ANOVA)

2.1 Introduction

The development of novel materials is important for various industrial sectors such as energy, chemical engineering, personal care, and biomedical devices. Innovative materials contribute to higher efficiency, improved safety, and greater sustainability. Despite these significant benefits, new materials development faces notable challenges, including high costs, long timelines and inherent uncertainty. Traditional material development is highly resource-intensive, requiring extensive experimentation, iterative testing and refinement. Fundamental research into material properties is expensive and time-consuming, often taking many years or even decades before commercialisation.¹ Furthermore, unpredictable research outcomes add complexity to the development cycle. Overcoming these issues requires innovative strategies, such as computational materials science, high-throughput experimentation, and close collaboration between academia, industry, and government.²

Emerging technologies are transforming the landscape of materials development. Advancements in automation, high-performance computing (HPC),^{3,4} and machine learning (ML)^{3,5} can significantly enhance efficiency while reducing costs. Automated laboratories manned by robotic and equipped with high-throughput screening, accelerate experimentation by simultaneously conducting multiple tests, minimizing human error, and ensuring reproducible data.^{4,6} HPC is instrumental in modelling materials at the atomic and molecular level, predicting critical properties prior to any synthesis, and thereby reducing the need for trial-and-error experiments. By rapidly performing complex calculations, HPC enables identification of promising lead materials. ML optimises this process by analysing large datasets from experiments and simulations, detecting patterns, predicting outcomes, and recommending optimal experimental conditions. These predictive capabilities streamline research by minimising development time and resource expenditure. The combination of automation, computational power and data-driven insights creates a more efficient and cost-effective framework for discovering next-generation materials that meet the evolving demands of various industries.

The Design of Experiments (DoE) methodology plays a vital role in supporting machine learning-driven materials development by systematically planning experiments to explore relationships between multiple variables.⁷ DoE enhances experimental efficiency by identifying optimal conditions and minimizing resource wastage. Traditional experimental methods often test one variable at a time, leading to excessive trials and higher costs. In contrast, DoE simultaneously explores multiple factor combinations, reducing redundant testing and optimizing resource allocation. Structured approaches, such as factorial designs or response surface methodology, identify key variables and their interactions, ensuring informative and efficient experimentation.⁷ Understanding these interactions refines experimental conditions, improving accuracy and reliability.

Integrating DoE with ML and automation further enhances efficiency. It ensures optimal sample usage, which is particularly beneficial for relatively ill-defined, polydisperse copolymers prepared by free radical polymerisation. In the development of polymeric surfactants, many parameters such as molecular weight, dispersity, hydrophilic/hydrophobic balance, comonomer ratios, backbone structure, and comonomer distribution must be considered. In addition, various physical properties such as foamability, foam stability, equilibrated surface tension and dynamic surface tension should be considered.⁸ Single factor-response experiments may not identify complex interactions amongst all these variables. DoE overcomes this limitation by systematically analysing multiple parameters to provide a better understanding of copolymer performance.

By leveraging automation, computational tools, and strategic experimental design, materials research becomes more precise, cost-effective, and adaptable. These advancements accelerate materials discovery and optimization, ensuring faster innovation cycles that meet industrial and technological demands. In this Chapter, DoE and relevant analytical methods will be applied to analyse copolymer surfactant datasets for liquid foam-forming applications. The datasets are obtained from either the literature or our own laboratory.^{8,9} The resulting physical insights were expected to guide the direction of future experiments.

2.2 Experimental

2.2.1 Materials and Dataset Sources

Two distinct datasets were used in this chapter. The first dataset was derived from a previous publication on Pluronic-based block copolymers by Alexandridis et al. (Table 2.1).⁹ This system was briefly discussed in the Introduction (see Figure 1.16). This dataset was selected for DoE analysis to examine the feasibility of this approach for a well-known copolymer surfactant.

The second dataset comprises experimental data collected under laboratory conditions from our previous studies (Table 2.2).⁸ Relevant copolymer structures are shown in Figure 2.1.

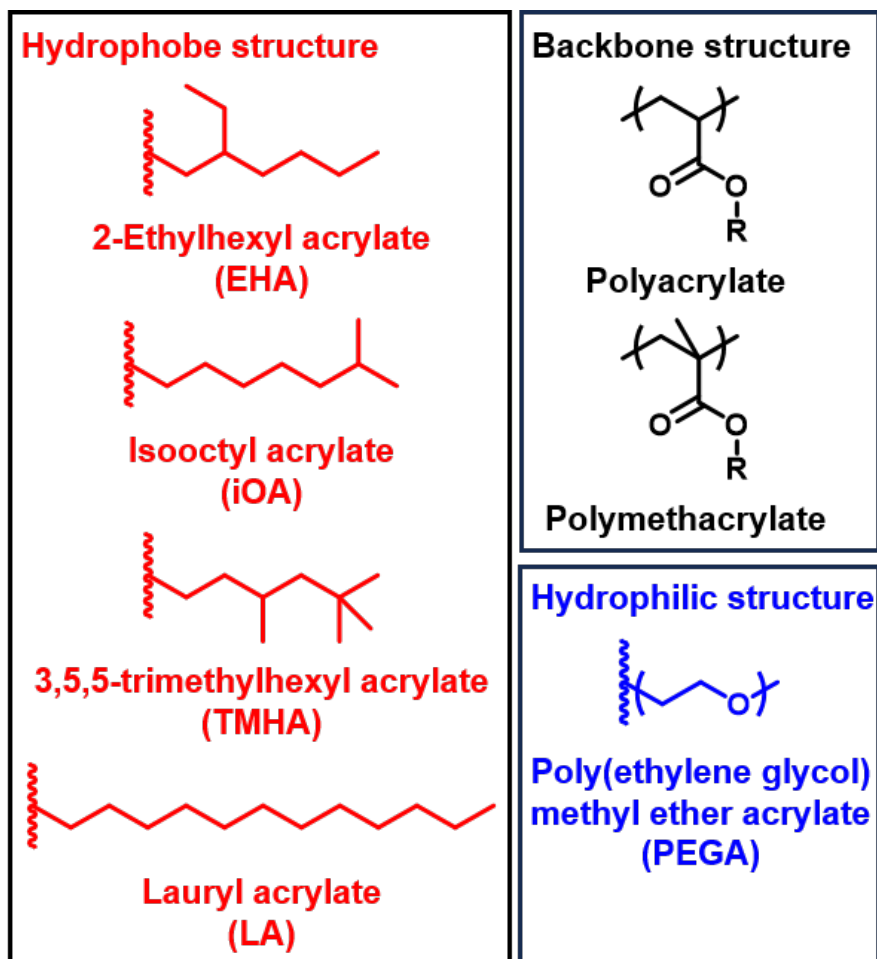


Figure 2.1: Chemical structures of lab synthesised copolymers.⁸

Table 2.1: Properties of Pluronic PEO-PPO-PEO triblock copolymers (data taken from Ref. [9]).

Copolymer ID^a	Molecular weight / g mol⁻¹	PEO / wt%	Viscosity / cps	Surface tension / mN m⁻¹	Foam height^b / mm
L35	1,900	50	375	49	25
F38	4,700	80	260	52	35
L42	1,630	20	280	46	0
L43	1,850	30	310	47	0
L44	2,200	40	440	45	25
L62	2,500	20	450	43	25
L63	2,650	30	490	43	30
L64	2,900	40	850	43	40
P65	3,400	50	180	46	70
F68	8,400	80	1,000	50	35
L72	2,750	20	510	39	15
P75	4,150	50	250	43	100
F77	6,000	70	480	47	100
P84	4,200	40	280	42	90
P85	4,600	50	310	42	70
F87	7,700	70	700	44	80
F88	11,400	80	2,300	48	80
F98	13,000	80	2,700	43	40
P103	4,950	30	285	34	40
P104	5,900	40	390	33	50
P105	6,500	50	750	39	40
F108	14,600	80	2800	41	40
L122	5,000	20	1,750	33	20
P123	5,750	30	350	34	45

^a L, P and F denote liquid, paste, or flake, respectively. The first one or two numbers (e.g. '6' in 'F68' or '12' in 'P123') indicate the molecular weight of the PPO block, while the last number represents the weight fraction of the PEO block (e.g. the '3' in 'P123' denotes 30%).

^b Copolymer dissolved at 0.1 wt% in water; foam tested by Ross-Miles method at 50 °C.

Table 2.2: Summary of the properties of copolymer surfactants (data taken from Ref. [8]).

Copolymer ID ^a	M_w / g mol ⁻¹	PEGMA / wt%	Backbone	Copolymer architecture	Foamability		
					61 ^b	57 ^b	53 ^b
PEGLA40	14,300	60	acrylate	statistical	N/A	N/A	N/A
PEGLA50	11,600	50	acrylate	statistical	N/A	N/A	0.30
PEGLA60	12,200	40	acrylate	statistical	N/A	N/A	N/A
PEGEH40	11,100	60	acrylate	statistical	N/A	N/A	0.52
PEGEH50	9,300	50	acrylate	statistical	N/A	0.32	0.67
PEGEH60	9,700	40	acrylate	statistical	N/A	0.32	0.52
PEGT40	11,500	60	acrylate	statistical	0.85	1.11	1.35
PEGT50	12,600	50	acrylate	statistical	1.02	1.27	1.35
PEGT60	13,200	40	acrylate	statistical	0.93	1.11	1.20
b-PEGT40	11,900	60	acrylate	diblock	N/A	N/A	N/A
b-PEGT50	12,200	50	acrylate	diblock	N/A	N/A	N/A
b-PEGT60	12,800	40	acrylate	diblock	N/A	N/A	0.60
PEGiO40	11,000	60	acrylate	statistical	N/A	N/A	0.67
PEGiO50	10,700	50	acrylate	statistical	N/A	0.72	0.90
PEGiO60	11,300	40	acrylate	statistical	N/A	0.48	0.82
MPEGT40	57,900	60	methacrylate	statistical	N/A	N/A	0.30
MPEGT50	29,600	50	methacrylate	statistical	N/A	N/A	0.67
MPEGT60	54,800	40	methacrylate	statistical	N/A	N/A	0.30
R-PEGT40	8,200	60	acrylate	statistical	0.51	0.95	1.27
R1-PEGT50	12,400	50	acrylate	statistical	0.76	0.87	1.20
R2-PEGT50	8,400	50	acrylate	statistical	1.02	1.11	1.35
R3-PEGT50	3,900	50	acrylate	statistical	0.85	1.11	1.27
R-PEGT60	8,900	40	acrylate	statistical	1.02	1.03	1.20

^a PEG, LA, EH, T, iO denote PEGA, LA, EHA, iOA, respectively, as shown in Figure 2.1
The last two numbers indicate the weight fraction of PEGMA presents in the copolymer.
"R" denotes the RAFT synthesised statistical copolymers.

^b Ethanol content in wt%.

2.2.2 Design of Experiments

DoE data analysis was performed using JMP Pro software (JMP Statistical Discovery LLC, USA). DoE works by systematically planning a structured set of experimental conditions to investigate how multiple factors and their interactions influence a response. The process begins by defining the objective, selecting key factors and their levels, and choosing an appropriate design such as full factorial, fractional factorial, or response surface methods. By running experiments according to this structured plan and analysing the results using statistical tools like ANOVA, DoE efficiently identifies the most influential factors, quantifies interactions, and determines the optimal conditions, allowing researchers to extract maximum insight with minimal experimental effort.⁷

Table 2.3: Summary of parameters for DoE analysis of the Pluronic triblock copolymers.

Response	Factor	Factor role	Levels
Foam height / mm	M_n / g·mol ⁻¹	Continuous	1,630 - 14,600
Surface tension / mN·m ⁻¹	PEO / wt%	Discrete numeric	20, 30, 40, 50, 70, 80

Given their relatively simple chemical structure, a full factorial design was applied to the series of Pluronic triblock copolymers. Two key factors describe such a Pluronic copolymer: its overall molecular weight and its weight% of poly(ethylene oxide) (PEO wt%). Foam height was selected as the response for this study. Molecular weight was treated as a continuous variable and PEO weight fraction was examined at six discrete levels, ranging from 20% to 80% (Table 2.3). These two factors are sufficient to precisely describe each Pluronic copolymer. The full factorial design allows all possible combinations of these factors to be explored with minimal computer resources. Furthermore, separate studies were conducted to explore the correlation between foam height and either viscosity or surface tension. This single-factor analysis indicates how each factor independently affected the foam height, complementing the results obtained from the full factorial design.

For the (meth)acrylic copolymer surfactants, a broader set of factors was required owing to

Table 2.4: Summary of parameters for DoE analysis of a range of statistical / block (meth)acrylic copolymers.

Response	Factor	Factor role	Levels
Foamability	Hydrophobe	Categorical	LA, EHA, iOA, TMH(M)A
	Hydrophobe / wt%	Discrete numeric	40, 50, 60
	M_n / g·mol ⁻¹	Continuous	3,900 - 58,000
	Backbone	Categorical	Acrylate, methacrylate
	Architecture	Categorical	Statistical, block
	Ethanol / wt%	Discrete numeric	53, 57, 61

their more diverse chemical structures. For efficient data analysis, both full factorial and fractional factorial design were applied to avoid uneven variance distribution. In this case, although various factors are included to describe the copolymer properties, the precise chemical structure of the hydrophobic groups is not described in detail. Instead, such groups are classified as a singleparameter, which simplifies the analysis. However, this approach neglects the known influence of the degree of branching of the hydrocarbon component on surface activity (Table 2.4).⁸ Furthermore, several other factors were considered, including hydrophobe weight fraction, number-average molecular weight, backbone composition and polymer architecture. Moreover, since the initial foaming experiments were focused on copolymer surfactants in ethanol-water mixtures, the alcohol content of the solvent was also included as a factor.⁸ This approach allows comprehensive investigation of the correlation between copolymer composition and copolymer surface activity. Data were analysed using the Analysis of Variance (ANOVA) model for various experimental conditions.⁷ ANOVA is a statistical method used to determine whether the mean values of a response variable differ significantly across multiple groups or experimental conditions. It works by partitioning the total variability in the data into components attributable to the factors being studied and to random error, allowing researchers to test whether the variation between groups is larger than would be expected by chance. By comparing these variance components through an F-test, ANOVA reveals whether one or more factors have a statistically significant effect on the response, making it a fundamental tool for analysing designed experiments and comparing multiple treatments simultaneously.⁷

2.3 Results and Discussion

2.3.1 Pluronic Triblock Copolymer Surfactants

ANOVA analysis was performed to evaluate the influence of PEO wt%, molecular weight and their interactions on the response variables. The results are summarized in Table 2.5, where all factors and interaction terms were assessed using *Logworth* and *p*-values. Both parameters describe whether a factor significantly contributes to the model when describing the response variables. A smaller *p*-value indicates greater statistical significance. *Logworth* is a transformation of the *p*-value as calculated using Equation 2.1

$$\text{Logworth} = -\log_{10}(p) \quad (2.1)$$

This transformation is performed to aid graphical representation. Mathematically, a higher logworth value corresponds to a smaller *p*-value. Normally, a logworth value greater than 2 indicates the existence of statistical significance at the 0.01 level.

Table 2.5: Summary of parameters for DoE analysis of a range of statistical / block (meth)acrylic copolymers.

Source	<i>Logworth</i>	<i>p</i> -value
PEO wt%	9.390	0
Molecular weight	8.471	0
PEO wt% * Molecular weight	3.772	0.0002
PEO wt% * PEO wt%	1.775	0.0168
Molecular weight * Molecular weight	1.154	0.0701

The analysis indicates that PEO wt% is the most important factor affecting the response, with a logworth of 9.390 and a corresponding *p*-value close to zero. Similarly, the copolymer molecular weight is also of high significance, with a log worth of 8.471 and a *p*-value close to zero. This suggests that both parameters should be considered simultaneously when seeking to optimise foaming performance (i.e. foam height). Furthermore, the interaction between these

two factors is statistically significant, as evidenced by a *Logworth* of 3.772. This suggests that these two factors are not simply additive. The quadratic interaction of the two factors with themselves has a much smaller impact compared to the primary factors.

Clearly, both PEO wt% and copolymer molecular weight are key parameters that determine surface activity. Moreover, their interaction appears to be synergistic. In principle, focusing on these primary factors and their interaction could reveal effective optimisation strategies for this series of Pluronic copolymers. In summary, DoE design and ANOVA analysis can provide a deeper understanding of the interfacial behaviour of a library of non-ionic copolymer surfactants. This data analysis method can be used to evaluate the relative importance of individual factors or their interactions, thus aiding the rapid identification of key factors for performance optimisation.

2.3.2 Methacrylic and Acrylic Statistical Copolymers Surfactants

The full factorial analysis of a series of (meth)acrylic copolymers identified copolymer architecture (i.e. statistical vs. diblock) as the most important factor influencing foamability in the molecular weight range investigated (10,000 - 15,000 g·mol⁻¹).¹⁰ High molecular weight block copolymers cannot efficiently occupy the air-water interface, leading to relatively poor foaming performance.^{11,12}

After excluding the influence of copolymer architecture and conducting a fractional factorial analysis, the chemical nature of the statistical copolymer backbone and pendant hydrophobic groups were identified as important parameters according to their *Logworth* values (Table 2.6). In particular, the type of hydrophobic group effectively governs surfactant performance, with a logworth value of 23.513 and a *p*-value of zero. According to Czajka et al.,¹³ hydrophobic groups with a higher degree of branching are more strongly adsorbed at the air-water interface. ANOVA analysis predicted that the most branched TMHA hydrophobe has the best foaming ability, followed by iOA. The less branched EHA and LA lead to lower foamability, as predicted by JMP in Figure 2.2.

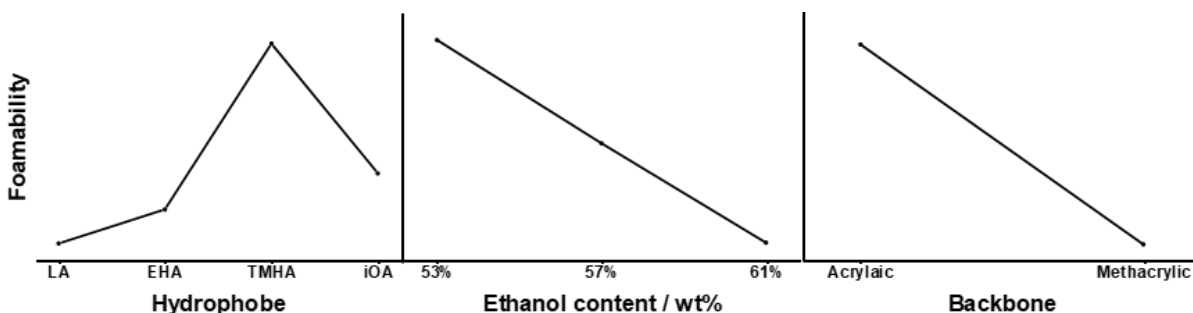


Figure 2.2: Fractional factorial analysis results obtained for a series of (meth)acrylic statistical copolymer surfactants.

Table 2.6: Summary of parameters for DoE analysis of a range of statistical / block (meth)acrylic copolymers.

Source	Logworth	p-value
Hydrophobe	25.513	0.0000
Backbone	19.983	0.0000
Ethanol wt%	11.703	0.0000
Hydrophobe wt%	0.475	0.3353

The backbone composition is the second most influential factor, with a logworth of 19.983. This highlights the importance of copolymer chain mobility, which affects the time scale on which the copolymer chains can adopt their preferred conformation during their adsorption at the air-water interface.⁸ Although statistically significant with a logworth of 11.703, the solvent environment controls the interaction between copolymer components, potentially masking the intrinsic effect of the copolymer molecular weight.¹⁴ The presence of ethanol introduces variability, so eliminating this factor should provide a clearer data interpretation of the various structural contributions. Moreover, preliminary industrial feedback indicated limited interest in developing hydrocarbon-based surfactants for ethanol/water systems. Therefore, the effect of varying the solvent composition will not be explored in future experiments. The hydrophobe weight% appears to have minimal impact, as reflected by its relatively low logworth value of 0.475. However, this may well reflect the relatively narrow range of variance for this parameter. For a second set of fractional factorial analyses that excluded the effect of hydrophobic structure and copolymer architecture, it was found that molecular weight and hydrophobe content had no

statistical significance on foamability (Table 2.7). This differs from the analysis of the Pluronic copolymer series. This is because the statistical significance of the chemical nature of the copolymer backbone and hydrophobic groups is much greater than the influence of molecular weight and hydrophobe content. Moreover, it is also possible that there is some interference from the ethanol content. Furthermore, the relatively narrow range of copolymer hydrophobe content has a negative impact on analysis.

Table 2.7: Summary of parameters for DoE analysis of a range of statistical/block (meth)acrylic copolymers.

Source	<i>Logworth</i>	<i>p-value</i>
Ethanol wt%	7.093	0.0000
Backbone	5.688	0.0000
Molecular weight	0.534	0.2925
Hydrophobe wt%	0.355	0.4413

2.4 Conclusions

The feasibility and effectiveness of DoE analysis have been verified in this Chapter. By applying ANOVA analysis, the key factors have been identified for a series of Pluronic triblock copolymers and a series of (meth)acrylic copolymers. For the former system, the PEO wt% and molecular weight are critical parameters for the optimisation of foamability. For the more complex (meth)acrylic copolymer system, the copolymer architecture was identified as the most significant factor affecting foamability. Specifically, statistical copolymers substantially outperform block copolymers owing to their ability to efficiently adsorb at the air-water interface. The chemical composition of the copolymer backbone emerged as the second most critical factor because this directly influences chain flexibility, which affects foam formation (as judged by the initial foam height). The hydrophobic structure plays a dominant role, with branched hydrophobic groups leading to superior surface activity. Regrettably, the effect of copolymer molecular weight and hydrophobe content could not be properly captured. This may be due to their relatively low statistical significance or the insufficient range explored in the current study. In conclusion, the combination of DoE with ANOVA provides a promising framework for optimising the foam-forming performance of copolymer surfactants. Based on these initial findings, the copolymer backbone could be replaced with more flexible alternatives such as poly(vinyl ethers), which may contribute to even higher chain mobility than that exhibited by acrylic copolymers. Additionally, more hydrophobic comonomers with higher degrees of branching should be explored to further enhance surface activity and foamability. Further optimisation of copolymer molecular weight and hydrophobe content should also be considered. These parameters will be systematically investigated in later chapters using conventional experimental approaches to address the limitations of the DoE analysis presented in this chapter and advancing the understanding and development of next-generation non-ionic statistical copolymer surfactants.

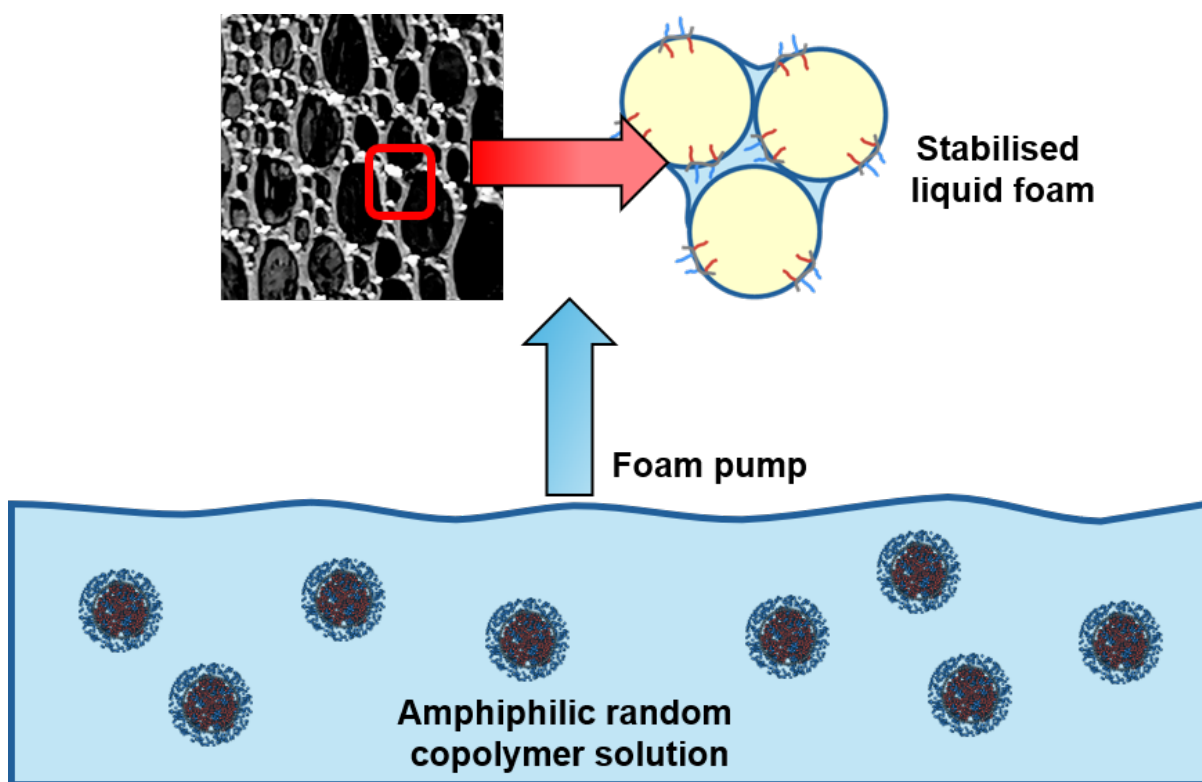
2.5 References

- (1) B. Cao, L. A. Adutwum, A. O. Oliynyk, E. J. Luber, B. C. Olsen, A. Mar and J. M. Buriak, *ACS Nano*, 2018, **12**, 7434–7444.
- (2) X. Jiang, D. Xue, Y. Bai, W. Y. Wang, J. Liu, M. Yang and Y. Su, *Review of Materials Research*, 2025, **1**, 100010.
- (3) J.-P. Correa-Baena, K. Hippalgaonkar, J. van Duren, S. Jaffer, V. R. Chandrasekhar, V. Stevanovic, C. Wadia, S. Guha and T. Buonassisi, *Joule*, 2018, **2**, 1410–1420.
- (4) E. O. Pyzer-Knapp, J. W. Pitera, P. W. Staar, S. Takeda, T. Laino, D. P. Sanders, J. Sexton, J. R. Smith and A. Curioni, *npj Computational Materials*, 2022, **8**, 84.
- (5) C. Lv, X. Zhou, L. Zhong, C. Yan, M. Srinivasan, Z. W. Seh, C. Liu, H. Pan, S. Li, Y. Wen and Q. Yan, *Advanced Materials*, 2022, **34**, 2101474.
- (6) S. T. Knox, K. E. Wu, N. Islam, R. O’Connell, P. M. Pittaway, K. E. Chingono, J. Oyekan, G. Panoutsos, T. W. Chamberlain, R. A. Bourne and N. J. Warren, *Polym. Chem.*, 2025, **16**, 1355–1364.
- (7) D. Montgomery, *Design and Analysis of Experiments*, John Wiley & Sons, Ltd, New York, USA, 8th edn., 2012.
- (8) J. Jennings, R. R. Webster-Aikman, N. Ward-O’Brien, A. Xie, D. L. Beattie, O. J. Deane, S. P. Armes and A. J. Ryan, *ACS Applied Materials & Interfaces*, 2022, **14**, 39548–39559.
- (9) P. Alexandridis and T. A. Hatton, *Colloids and Surfaces A: Physicochemical and Engineering Aspects*, 1995, **96**, 1–46.
- (10) M. Mu, F. A. Leermakers, J. Chen, M. Holmes and R. Ettelaie, *Journal of Colloid and Interface Science*, 2023, **644**, 333–345.
- (11) H. Matsuoka, H. Chen and K. Matsumoto, *Soft Matter*, 2012, **8**, 9140–9146.

-
- (12) A. Ghosh, S.-i. Yusa, H. Matsuoka and Y. Saruwatari, *Langmuir*, 2014, **30**, 3319–3328.
 - (13) A. Czajka, G. Hazell and J. Eastoe, *Langmuir*, 2015, **31**, 8205–8217.
 - (14) C. J. Thompson and A. J. Ryan, in *Neutrons, X-rays, and Light*, ed. P. Lindner and J. Oberdisse, Elsevier, Amsterdam, Netherlands, 2nd edn., 2025, ch. 11, pp. 285–310.

Chapter 3

Design Rules for Statistical Copolymer Surfactants for Foam-Forming Applications



3.1 Introduction

Foam-forming formulations are important components of modern industrial and personal care products.^{1,2} Surfactants stabilise liquid foams in laundry and pharmaceutical formulations, fire extinguishing foams, hand sanitisers, etc.^{3–6} Surfactants adsorb at the liquid-air interface to reduce the interfacial energy and hence stabilise liquid foams.⁷ Conventional surfactants are usually composed of hydrocarbon-based amphiphilic small molecules, comprising a polar hydrophilic, "head" and a non-polar, hydrophobic "tail". Their amphiphilic nature leads to self-assembly in aqueous solutions.^{7,8} However, the structural optimisation of conventional hydrocarbon surfactants has probably reached its limit.⁹ Their surface activity can be improved by increasing the degree of methylation of the hydrocarbon chain-end or by introducing multiple hydrophobic tails.^{9,10} Up to three methyl groups can be incorporated in the former case, while in the latter case the synthesis of multi-tail surfactants is technically challenging, which limits their commercial value.¹⁰ Typically, surfactants with perfluorocarbon ($15 - 20 \text{ mN}\cdot\text{m}^{-1}$)¹¹ or silicone ($20 - 30 \text{ mN}\cdot\text{m}^{-1}$)^{11,12} tails exhibit significantly lower limiting surface tensions than those with hydrocarbon ($24 - 38 \text{ mN}\cdot\text{m}^{-1}$)^{11,13,14} tails and are often used in specialty applications such as fire extinguishing foam that require superhydrophobic properties.⁵ However, environmental concerns regarding the persistence of perfluorocarbon chemicals and the hydrolytic instability of silicone alternatives have inspired renewed interest in further optimising the performance of hydrocarbon surfactants.^{15–19}

Polymeric surfactants offer distinct advantages over small molecule surfactants, including very low critical micelle concentration (CMC) and enhanced interfacial stability.²⁰ Like small-molecule surfactants, polymeric surfactants tend to undergo interfacial adsorption and bulk solution self-assembly in aqueous solution. But owing to their long-chain structure, the solution behaviour of polymers is different. For small molecules, surface adsorption is preferred at low concentration, typically below the CMC. Once the interface is fully occupied, small molecules tend to self-assemble in aqueous solution to form micelles. This is an alternative mechanism

to reduce their interfacial energy, driven by the entropy of water and hydrophobic effect.^{21,22} For statistical polymeric surfactants, the copolymer chains undergo a change in conformation such that the hydrophobic comonomer units are mainly located within the micelle cores and the hydrophilic comonomer units are mainly located with the micelle corona. However, owing to the inherent structural constraints of statistical copolymers, the hydrophobic comonomers cannot freely migrate along the chain. As a result, the extent of microphase separation is lower than that achieved by amphiphilic diblock copolymers, and the corresponding micelle aggregation numbers are accordingly reduced.^{23,24} Moreover, interfacial adsorption and solution self-assembly often coexist in dynamic equilibrium for polymeric surfactants; both processes incur a loss of configurational entropy, which complicates accurate CMC determination using conventional techniques such as surface tensiometry.²⁵

Polymers provide a flexible platform for combining hydrophilic and hydrophobic components into a single molecule. The basic design rules for small molecule surfactants also apply to polymeric surfactants, but polymers offer additional structural parameters that can be optimised, such as backbone flexibility, architecture, hydrophobic/hydrophilic monomer ratio, molecular weight, etc. Amphiphilic block copolymers are commonly used polymeric surfactants. For example, Pluronic[®] are composed of hydrophilic poly(ethylene oxide) (PEO) and weakly hydrophobic poly(propylene oxide) (PPO) blocks and have been widely used for many industrial applications.^{26,27} Recent advances have highlighted the untapped potential of statistical copolymers, whereby hydrophobic and hydrophilic monomers are statistically distributed along the backbone.^{15,16} Such copolymers can be optimised to achieve performance comparable to that of fluorocarbon surfactants in certain applications. Unlike block copolymers, statistical copolymers exhibit unique interfacial behaviour. Block copolymers tend to form multimolecular micelles that must overcome the energy penalties of dissociation and solubilisation to undergo interfacial adsorption, while statistical copolymers can self-assemble as unimolecular micelles.^{23,28} These relatively small structures can diffuse rapidly to the interface, where they undergo conformational unfolding, exposing the hydrophobic moieties to the gas phase while

the hydrophilic segments remain solvated within the aqueous phase.²⁹ This mechanism mimics the behaviour of natural proteins such as hydrophobins, which can stabilise foams through reversible intermolecular structural transitions.^{30,31} Free radical copolymerisation facilitates the synthesis of amphiphilic statistical copolymers. This method has the advantages of simple operation, mild reaction conditions, and adaptability to a wide range of functional comonomers.³² Hydrophilic and hydrophobic monomers can be copolymerised in a statistical manner, thereby flexibly regulating both the copolymer composition and the resulting physical properties. By selecting appropriate comonomer combinations and polymerisation conditions, amphiphilic copolymers with specific solubility, interfacial activity, and self-assembly ability can be prepared. Hydrophilic and hydrophobic monomers are generally difficult to copolymerise via conventional ionic polymerisation due to the sensitivity of ionic species to protic impurities (e.g. water).^{33,34} Such reactions invariably require multiple steps and stringent reaction conditions, which are often justified in terms of producing narrow dispersity block copolymers. Free radical copolymerisation remains the optimal choice for the synthesis of amphiphilic polymers, especially if some degree of polydispersity can be tolerated.

Recent progress suggests that the potential for statistical copolymer surfactants has not been fully explored.¹⁵ In particular, statistical copolymers prepared by free radical copolymerisation of 3,5,5-trimethylhexyl acrylate (TMHA) and poly(ethylene glycol)methyl ether acrylate (PEGA) exhibit superior surface activity in water/alcohol mixtures than their block copolymer analogues.¹⁵ Compared with conventional silicone-based surfactants, statistical copolymers are more environmentally benign, offering considerable potential as a next-generation hydrocarbon-based foaming agent for low surface tension liquids.^{15,16} Accordingly, we have undertaken an in-depth exploration of the performance-structure relationship of statistical copolymers, especially with regard to the effects of copolymer composition, molecular weight and chain stiffness on foam performance.

3.2 Experimental

3.2.1 Materials

Poly(ethylene glycol) methyl ether acrylate (PEGA, avg. $M_n = 480$), poly(ethylene glycol) methyl ether methacrylate (PEGMA, avg. $M_n = 300$), 3,5,5-trimethylhexyl acrylate (TMHA, technical grade) were purchased from Sigma-Aldrich (UK) and filtered over basic aluminium oxide (Al_2O_3) prior to use. 3,5,5-Trimethylhexyl methacrylate (TMHMA, ABCR) and lauryl acrylate (LA, > 98%, TCI Chemicals) were used as received. Ethanol ($\geq 99.8\%$) was purchased from Sigma-Aldrich (UK) and used as received. Azobisisobutyronitrile (AIBN) was purchased from Molekula (UK) and used as received. Jeffamine M-1000 and M-2005 were kindly donated by Huntsman Corporation via their UK distributor (Alfa Chemical). MilliQ water was obtained from an Elga Elgastat Option 3A Water Purifier system.

3.2.2 Synthesis and Reaction Protocols

Synthesis of P(TMHA-*stat*-PEGA) Statistical Copolymer by Free Radical Copolymerisation in Ethanol

The following example is representative of the statistical copolymerisations performed to produce the amphiphilic statistical copolymers reported in Table 3.1. AIBN (0.0050 g, 0.03 mmol, 0.1% w/w) was weighed into a 28 ml glass vial, followed by PEGA (4.0000 g, 8.33 mmol) and TMHA (1.0000 g, 5.05 mmol) to make up a mixture with a [TMHA]/[PEGA] mass ratio of 0.25 (i.e. 20:80). Ethanol (20.0000 g) was added to this comonomer mixture to make up a 20% w/w solution. The solution was vortex-mixed for 30 s to produce a homogeneous mixture and then sealed using a rubber septum after addition of a magnetic stir bar. The solution was degassed with the aid of an ice bath using a stream of nitrogen gas for 30 min and then immersed in an oil bath set at 70 °C with continuous stirring under nitrogen for 24 h. The copolymerisation was quenched by exposing the reaction mixture to air while cooling to room temperature. The crude

copolymer was dried under vacuum at 70 °C overnight. The overall comonomer conversion and copolymer composition were determined by ^1H NMR spectroscopy with CDCl_3 . Molecular weight and dispersity data were obtained by DMF GPC analysis.

Synthesis of β -Aminoester Small Molecular Analogues by Aza-Michael Addition

The following example is representative of the reactions undertaken to produce the amphiphilic small molecular analogues for the statistical copolymer surfactant. Jeffamine M-1000 (1.6423 g, 1.64 mmol) and TMHA (0.3577 g, 1.81 mmol) were weighed into a 7 ml glass vial, followed by ethanol (2.0000 g) to make up a 50% w/w solution with a [TMHA]/[Jeffamine] molar ratio of 1.1. The solution was vortex-mixed for 30 s to produce a homogenous mixture. The vial was placed in an oil bath set at 50 °C and stirred magnetically for 48 h. Most of the solvent was removed from the reaction mixture via rotary evaporation at 40 °C and the remaining product was dried in a vacuum oven at 40 °C overnight to remove residual ethanol. The overall conversion and composition were determined by ^1H NMR spectroscopy with CDCl_3 .

3.2.3 Analytical and Characterisation Methods

^1H NMR Spectroscopy

Spectra were recorded in CDCl_3 at 25 °C using 400 MHz Bruker Avance-400 spectrometer with 64 scans being averaged per spectrum. The equation used for calculating copolymer compositions is as follows:

$$x = \frac{A_1/n_1}{A_2/n_2} \quad (3.1)$$

where x is the comonomer mole fraction, A_1 and A_2 are the integrated NMR signals for a given comonomer and n_1 and n_2 are the numbers of the corresponding protons. The equation used for calculating comonomer conversion is as follows:

$$\text{Conversion} = \frac{[M]_{\text{initial}} - [M]_{\text{remaining}}}{[M]_{\text{initial}}} \quad (3.2)$$

where $[M]_{\text{initial}}$ is the initial mole of monomers, $[M]_{\text{remaining}}$ is the remaining mole of monomers after the reaction. These two quantities were determined by comparing the integrated ^1H NMR signal area of the acrylate vinyl protons (5.5-6.5 ppm) before and after polymerisation, normalised against an internal reference peak. In this work, the methyl signal at PEG side chain end (3.2 ppm) was selected as the internal reference.

Gel Permeation Chromatography (GPC)

Molecular weight data were obtained using an Agilent 1260 Infinity GPC system, which included a pump, degasser, and two PL-gel 5 μm Mixed-C columns connected in series, equipped with both UV and refractive index detectors. HPLC-grade DMF containing 0.02% w/w LiBr was used as the eluent, the column/detector temperature was set to 60 °C, and the flow rate was 1.0 mL $\cdot\text{min}^{-1}$. Near-monodisperse poly(methyl methacrylate) standards ranging from 370 to 2,520,000 g $\cdot\text{mol}^{-1}$ were employed for calibration, with data analysed using Agilent Technologies GPC/SEC software.

Maximum Bubble Pressure Dynamic Surface Tensiometry

Purified copolymer (0.0050 g) was weighed into a 7 mL glass vial and dissolved in deionised water (5.00 mL). This aqueous solution was placed on a roller mill at 40 rpm for 24 h to ensure full dissolution. The solution was then diluted to 100 mL to produce a final copolymer concentration of 0.50 g $\cdot\text{dm}^{-3}$. This solution was used for dynamic surface tensiometry, Du Noüy ring surface tensiometry and foamability studies, in that order.

The dynamic surface tension of aqueous copolymer solutions was determined using a Krüss BP100 bubble pressure tensiometer equipped with a SH2031 hydrophobically coated glass capillary (Krüss GmbH, Hamburg, Germany). The capillary tip inner diameter was calibrated by measuring the surface tension of deionised water at 25 °C (72.01 mN $\cdot\text{m}^{-1}$).³⁵ The dynamic surface tension was measured for different surface ages in the range of 10 to 10,000 ms with ten measurements being averaged per time point. The temperature was maintained at 25 °C using a thermostatted water bath. Each copolymer solution (~ 70 mL) was allowed to equilibrate at this

temperature for at least 1 h prior to measurements. The surface tension was calculated from the internal bubble pressure using (3.3):³⁶

$$\gamma_t = \frac{r(p_{\max} - p_0)}{2} \quad (3.3)$$

where γ_t is the surface tension value at t time, r is the inner radius of the capillary and p_{\max} is the maximum bubble pressure value obtained when the bubble radius is equal to the capillary radius, $p_0 = \rho g \Delta h$, where p_0 is the hydrostatic pressure resulting from the weight of a liquid column acting on an area, ρ is the liquid density, g is the standard gravity and Δh is the height of the liquid column.

The static surface tension is estimated by fitting dynamic surface tension vs. surface age data by using the modified Rosen-Hua equation:³⁷

$$\gamma = \frac{\gamma_0 - \gamma_\infty}{1 + \left(\frac{t}{t_0}\right)^p} + \gamma_\infty \quad (3.4)$$

where γ_0 is the static surface tension of the liquid ($\gamma_t = 72.01 \text{ mN}\cdot\text{m}^{-1}$ for deionised water at 25°C).³⁵ γ_∞ is the predicted equilibrium surface tension of the solution, t is the surface age, t_0 represents the time interval before the surface tension starts to rapidly decrease and p is the gradient of the reduction in surface tension.

Du Noüy Ring Surface Tensiometry

The quasi-static surface tension was obtained using an automatic Lauda TD3 tensiometer equipped with a 90:10 platinum/iridium ring (diameter = 0.955 cm, LAUDA Scientific GmbH, Lauda-Königshofen, Germany). The ring was washed with ethanol and flame-heated with a butane/propane blow torch before each measurement. Static surface tensions were measured at least ten times until a standard deviation of less than $0.1 \text{ mN}\cdot\text{m}^{-1}$ was achieved, and the mean value and its corresponding standard deviation were recorded. Each copolymer solution ($\sim 40 \text{ ml}$) was equilibrated at 25°C prior to any measurements using a temperature controller unit.

The result was automatically corrected using the Zuidema and Waters³⁸ method and surface tension was calculated from the maximum force, F_{\max} , according to (3.5):³⁹

$$\gamma = \frac{F_{\max}}{L \cos \theta} \quad (3.5)$$

where γ is the quasi-static surface tension, L is the wetted length, which is the sum of the inner and outer circumference, $\cos \theta = 1$ due to the platinum-iridium alloy exhibits a sufficiently high surface free energy to form a zero-degree contact angle.⁴⁰

Foamability and Foam stability Assay using a Bespoke Foam Pump

A commercially available foam soap dispenser was used to produce foam (see Figure 3.1 and 3.2). The foaming aqueous solution and air were mixed and pumped out through a narrow mesh in the foaming pump to generate air bubbles. Each dispensation mixes approximately 0.6 ml of liquid with 20 ml of air. The foam pump lever was depressed in a reproducible manner using a motor-driven cam. The rotation frequency of cam was set to 27.14 Hz by the control panel, which corresponds to about 0.6 s per depression-recovery cycle.



Figure 3.1: Digital photograph of the foam-forming apparatus used in this study. This equipment was designed and built by Ward-O'Brien et al.⁴¹

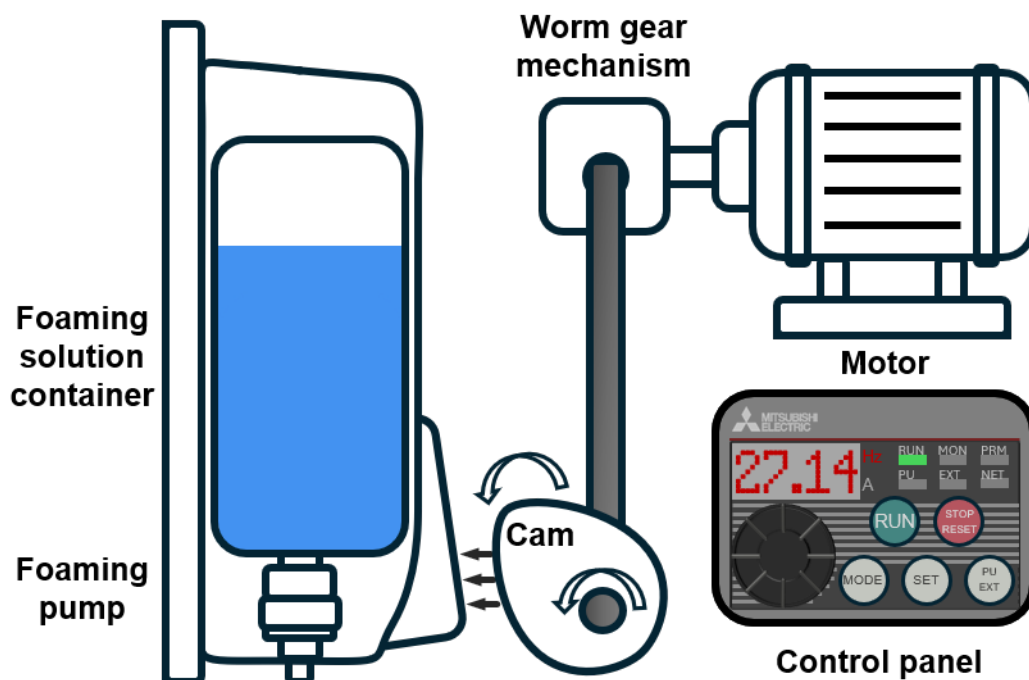


Figure 3.2: Schematic diagram of the foam forming apparatus. The motor controls the speed through the inverter (Mitsubishi Electric VFD) and drives the cam to rotate by a worm gear mechanism, which rotates the rod through an angle of 90° . The movement of the cam either squeezes or releases the foam dispenser pump to control the outflow of foam. This system enables reproducible foam production.

A custom foam cell was used to evaluate the foam (Figure 3.3). This cell comprised a glass hollow half cylinder and an embedded prism. The cylinder was cut longitudinally from top to bottom to form an open section, in which the prism was glued to the cylinder section using a chemical-resistant resin. This device was used to measure the foam/liquid volume. The prism was placed close to the side of the cylinder, which significantly improves image interpretation. This setup facilitated the observation of the single-layer foam formed along the side wall, appearing as a thin two-dimensional sheet of bubbles. Foam forms a wetting layer on the prism surface allowing direct imaging of a representative monolayer of foam and overcomes the imaging problems associated with a multilayer structure. The volume-height relationship of the foam cell was calibrated using a standard measuring cylinder. The maximum foam volume for this cell is approximately 200 ml.

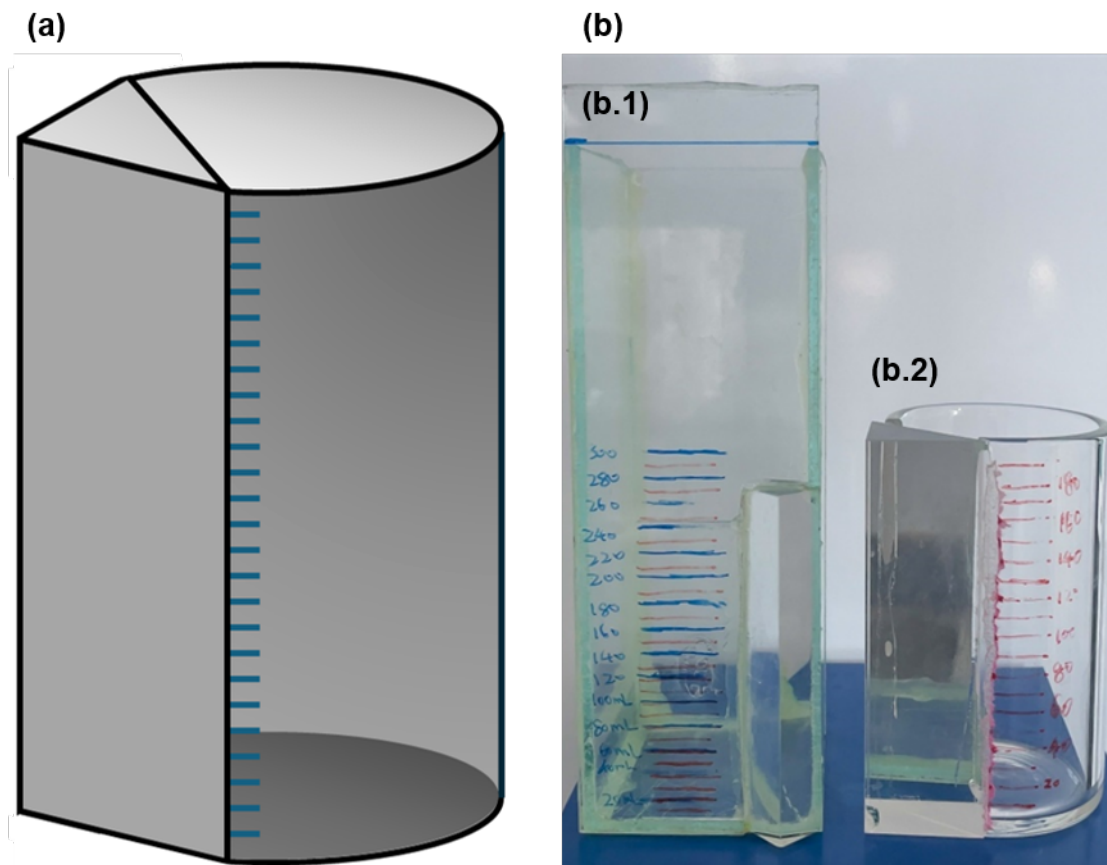


Figure 3.3: (a) Schematic diagram of the foam cell. The volume-height relationship of the foam cell is pre-calibrated using a standard measuring cylinder. (b) Digital photographs of the foam cell. (b.1) is the phototype constructed using four pieces of polycarbonate glass. (b.2) is the upgraded glass version that offers superior chemical resistance (the half-cylinder body was built by Jackson Scientific Glass Limited, Mansfield, UK).

The foam soap dispenser was washed sequentially with deionised water (50 ml), ethanol (50 ml) and deionised water (50 ml) prior to each measurement. Foamability and foam stability values were averaged over three measurements. Each copolymer solution was equilibrated at 25°C prior to measurement using a temperature control unit. The aqueous copolymer solution (30 ml) was gently transferred to the foam soap dispenser by pouring along the inner wall of the dispenser to prevent air entrainment and foam formation. 10 ml of the solution was transferred to the foam cell to serve as the stock solution, which ensured reproducibility and maintained uniform physicochemical properties throughout the experiments. The foam cell was placed below the dispenser. After starting the cam and pressing it fifty times, record the initial liquid

volume ($V_{l,0}$) and total volume ($V_{t,0}$) were recorded and timing commenced. The foam half-life was recorded, which is the time required for the foam volume to be reduced by half ($t_{V,1/2}$).

Foamability (F_a) was calculated using Equation (3.6) to enable comparison across experiments, where the initial foam volume ($V_{f,0}$) was determined as $V_{f,0} = V_{t,0} - V_{l,0}$, where $V_{t,0} = 40$ ml (30 ml + 10 ml) in this measurement. The foamability is the ratio of the initial foam volume $V_{f,0}$ to the effective foaming volume ($V_{t,0} - V_{l,0}$) of the surfactant solution:

$$F_a = \frac{V_{f,0}}{V_{t,0} - V_{l,0}} \quad (3.6)$$

The foam stability F_s was calculated from the foam half-life and initial foam volume using:

$$F_s = \frac{t_{V,1/2}}{\frac{V_{f,0}}{2}} \quad (3.7)$$

Small-Angle X-Ray Scattering (SAXS)

SAXS measurements were performed at the ESRF (ID02 beamline, Grenoble, France) using a monochromatic synchrotron X-ray beam ($\lambda = 0.0995$ nm) and a 2D Eiger2 4M SAXS detector (Dectris, Switzerland).⁴² Samples were analysed using a sealed flow-through borosilicate glass capillary of ~ 2 mm diameter (Capillary Tube Supplies Ltd, Cornwall, UK). Patterns were recorded at a camera length of 2.0 m, which correspond to a scattering vector q range of 0.004 \AA^{-1} to 0.4 \AA^{-1} , where $q = (4\pi \sin \theta)/\lambda$ corresponds to the modulus of the scattering vector and θ is half of the scattering angle. X-ray scattering data were reduced (integration, normalisation, and background subtraction) using standard routines available at the ID02 beamline. Solvent backgrounds and capillary shape factors were subtracted and calibrated using SAXSutilities2 software (version 1.255). Further fitting and modelling were performed using SASView software (version 6.0.0)⁴³ and Igor Pro software (version 8.04) with Irena package (release 2.71).⁴⁴ Copolymers were dissolved in deionised water at 1.0% w/w concentration. Deionised water was also used for absolute intensity calibration of all SAXS patterns.

3.3 Results and Discussion

3.3.1 Synthesis and Characterisation

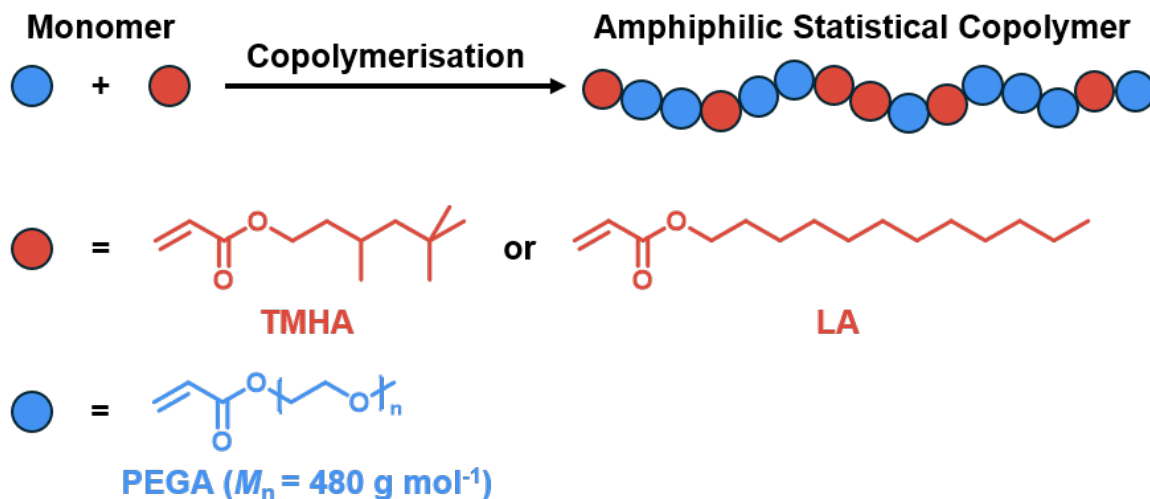


Figure 3.4: Synthesis of amphiphilic statistical copolymers via free radical copolymerisation of hydrophilic PEGA with either a linear (LA) or branched (TMHA) hydrophobic comonomer.

Conventional free radical polymerisation is particularly suitable for the statistical copolymer synthesis of various functional (meth)acrylic monomers. Given their wide commercial availability and low cost, such monomers are well suited to high-throughput synthesis to construct a diverse library of amphiphilic copolymer surfactants. Previous studies have shown that a statistical copolymer prepared by copolymerisation of 3,5,5-trimethylhexyl acrylate (TMHA) and polyethylene glycol methyl ether acrylate (PEGA) exhibits optimal foaming activity.¹⁵ Bearing in mind the known performance limits of hydrocarbon surfactants, the highly branched 3,5,5-trimethylhexyl structure is considered to be one of the most promising for foam stabilisation, and its corresponding acrylate and methacrylate monomers are both commercially available and amenable to free radical copolymerisation.^{9,45,46} Hence a series of statistical copolymers based on TMH(M)A and PEG(M)A were prepared with different comonomer compositions and molecular weights to systematically investigate the effect of these parameters on foam sta-

bilisation. In addition, amphiphilic copolymers bearing linear hydrophobic components were also prepared via statistical copolymerisation of LA and PEGA (Figure 3.4). Small molecule analogues were also synthesised as reference materials. Copolymer synthesis overcomes the technical challenge of introducing multiple hydrophobic units into small molecule surfactants.¹⁰ A series of P(TMHA-*stat*-PEGA480) statistical copolymers was synthesised via free radical copolymerisation in which the TMHA content and molecular weight were systematically varied (see Table 3.1). Five different hydrophilic PEGA weight fractions (75% - 95%, corresponding to PEGA/TMHA molar ratios of 7.84, 3.71, 2.34, 1.56 and 1.31, respectively) were used in turn to achieve a series of [hydrophile]/[hydrophobe] ([HL]/[HB]) molar ratios. Five different initiator concentrations (0.5% - 10% w/w) were used to adjust the copolymer molecular weight. According to the ANOVA analysis from Chapter 2, these two parameters were expected to affect the foamability. The dried copolymer was an oily transparent colourless liquid.

Table 3.1: Summary of experimental data obtained for P(TMHA-*stat*-PEGA) copolymers. Mean copolymer compositions were determined from ^1H NMR analysis. Apparent molecular weight and dispersity were determined from DMF GPC analysis.

Hydrophobe (HB)	Hydrophile (HL)	Copolymer ID ^a	Composition [HL]/[HB] ^b		DMF GPC	
			Target	Actual	M_n	\bar{D}
TMHA	PEGA	PT75E	1.24	1.30	9,400	1.92
		PT80A		1.65	21,600	2.68
		PT80B		1.65	17,500	2.44
		PT80C	1.65	1.76	16,100	2.54
		PT80D		1.65	9,500	2.05
		PT80E		1.55	9,400	2.02
		PT85A		2.34	20,300	2.55
		PT85B		2.53	17,600	2.35
		PT85C	2.34	2.34	16,400	2.55
		PT85D		2.17	9,800	2.00
		PT85E		2.01	8,900	2.08
		PT90A		3.71	21,800	2.46
		PT90B		3.71	17,500	2.25
		PT90C	3.71	3.34	17,000	2.62
		PT90D		3.71	9,900	1.98
		PT90E		4.73	9,400	1.79
		PT95A		7.84	21,900	2.34
		PT95B		7.84	19,300	2.27
		PT95C	7.84	7.84	17,600	2.46
		PT95D		6.46	10,800	1.91
		P100E	N/A	N/A	9,500	1.77
LA	PEGA	PL85C	2.83	3.07	9,500	1.82
TMHMA	PEGMA	MPT85E	4.00	3.71	12,100	2.42

^a PT for P(TMHA-*stat*-PEGA) copolymer, 75 - 100 for PEGA monomer feed weight fraction, 75 represents the comonomer mixture comprising 75% w/w of PEGA monomer, P100 represents a homopolymer of PEGA monomer; A - E for the initiator concentration (A for 0.1% w/w initiator, B for 0.5% w/w initiator, C for 2% w/w initiator, D for 5% w/w initiator, E for 10% w/w initiator, respectively).

^b Molar ratio.

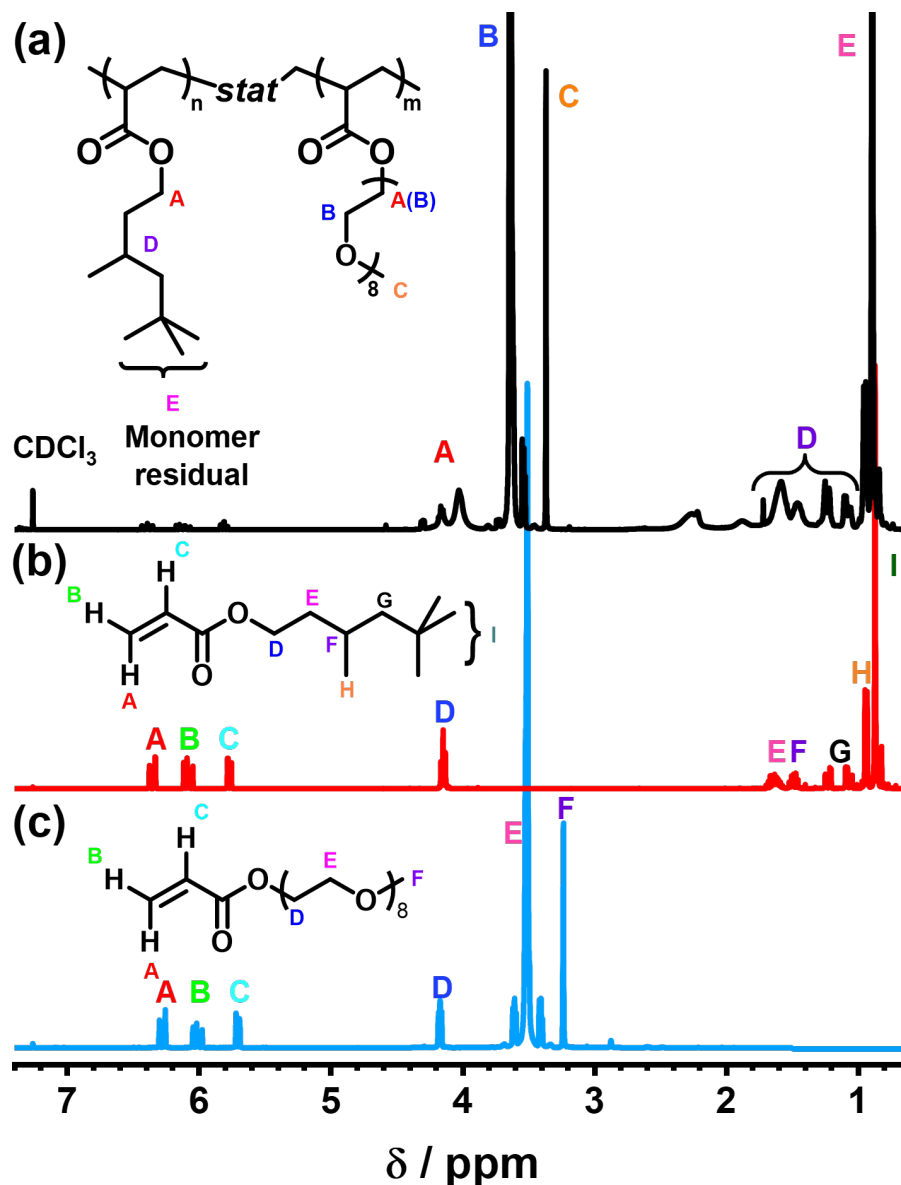


Figure 3.5: ^1H NMR spectrum (CDCl_3) recorded for (a) P(TMHA-*stat*-PEGA) statistical copolymer; (b) hydrophobic TMHA monomer; (c) hydrophilic PEGA monomer with partial peak assignments.

The copolymer structure was determined by ^1H NMR spectroscopy (see Figure 3.5). Characteristic signals corresponding to the expected chemical environments were observed. Signal A at relatively high chemical shift (3.90–4.20 ppm) was assigned to the oxymethylene protons adjacent to the ester groups. The strong signal B at 3.60 ppm was assigned to the oligo(ethylene glycol) side chain, while signal C at 3.40 ppm corresponds to the terminal methoxy group on the PEG unit. Signal D at 1.00–1.80 ppm was assigned to methylene and methine protons in

the acrylic backbone. The singlet peak at 0.90 ppm (signal E) was assigned to the trimethyl end-group of the TMHA comonomer units. The copolymer composition was estimated by comparing the integrals of the trimethyl and methyl chain ends of the TMHA and PEGA comonomers, respectively. An ^1H NMR spectrum recorded for the dried copolymer indicated that it had a similar composition to that of the comonomer feed ratio.

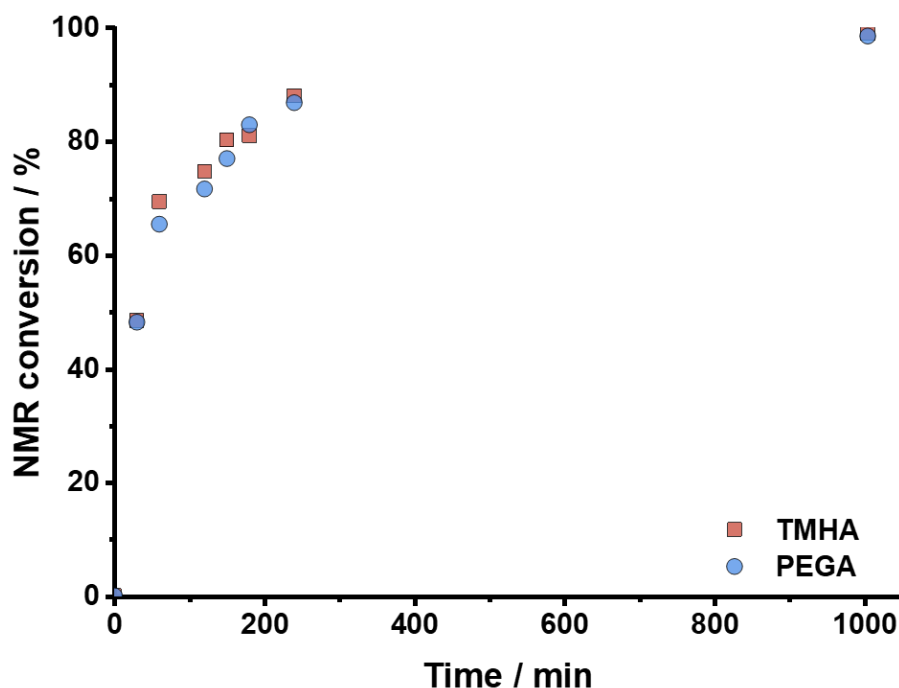


Figure 3.6: Comonomer conversion vs. time determined by ^1H NMR.

However, the mean copolymer composition does not provide any information about the comonomer distribution along the copolymer chain. This aspect was examined by kinetic studies conducted via ^1H NMR spectroscopy. The instantaneous conversion of each comonomer was very similar throughout the reaction. Therefore, a near-random distribution of the two comonomer repeat units along the copolymer chain can be assumed.

The molecular weight data are expressed relative to the PMMA calibration standards, which incurs a systematic error (see Appendix 3.5.1 for GPC data).⁴⁷ An increase in relative molecular weight was observed when a higher mass fraction of PEGA was used, which is mainly attributed to the higher molecular weight of this monomer. Higher initiator concentrations led to lower

molecular weights, which is consistent with the general principles of free radical polymerisation.³² For low molecular weight copolymers, the \bar{D} values lie between 1.5 and 2.0, indicating that termination involves both recombination and disproportionation.³² Higher \bar{D} values were observed for some copolymers, indicating that chain transfer to polymer is a prevalent side reaction.⁴⁸

3.3.2 Foamability Analysis

In addition to the foam pump method described above, various other foaming methods such as sparging, vortex, pouring and stirring/shaking are available.⁷ The pouring method is unsuitable for copolymer surfactants because the volume of foam produced was insufficient for analysis. Although the foam produced by the spraying method is easy to quantify, the foamability measured by this method is only weakly correlated with surface tension, making it difficult to analyse the relationship between foamability and other properties.⁴¹ Furthermore, previous studies have demonstrated that the foam volume generated by the foam pump method can be correlated ($R^2 > 0.75$) with the dynamic surface tension of the corresponding surfactant solutions.⁴¹ Therefore, the foam pump method was selected to measure the foam volume.

Figure 3.7 summarises the foaming performance data obtained for a series of acrylic copolymers at a copolymer concentration of $0.50 \text{ g}\cdot\text{dm}^{-3}$. All of the original data are detailed in the Appendix 3.5.2. Figure 3.7a shows the relationship between number-average molecular weight and foamability for copolymers of varying PEGA content. Regardless of the copolymer composition, the foamability of low molecular weight copolymers is always better than that of the corresponding higher molecular weight copolymers.

Figure 3.7b shows the effect of varying the PEGA content for four different molecular weight ranges. Increasing the hydrophobic content from zero to 15% w/w generally improves foamability for the higher molecular weight copolymer series, while higher hydrophobic contents reduce the foam volume. The 85% w/w PEGA copolymer exhibits optimal foaming ability regardless of the copolymer molecular weight. For low molecular weight copolymers, higher

PEGA contents produce larger foam volumes. Interestingly, the low molecular weight PPEGA (P100E) homopolymer and the copolymer containing the highest hydrophobic content (PT75E) also exhibited useful foamability. These observations are discussed in more detail below.

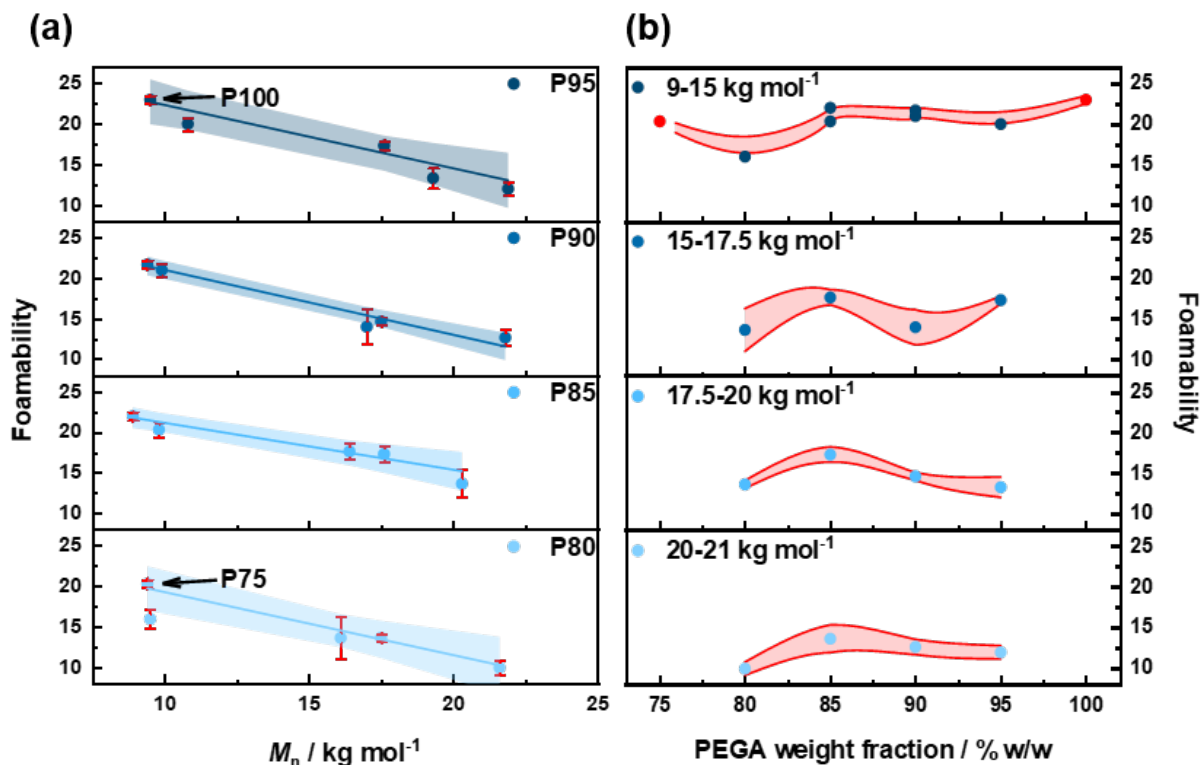


Figure 3.7: Foamability of a series of acrylic statistical copolymer surfactants dissolved in deionised water at a copolymer concentration of $0.50 \text{ g}\cdot\text{dm}^{-3}$. (a) The effect of varying the copolymer molecular weight on foamability is shown for four types of surfactants according to their PEGA content. The fitted curve is shown by the solid linear line, and the 95% confidence band is indicated by the shade area. (b) PEGA content was used to distinguish between surfactants according to their PEGA weight fraction for four ranges of copolymer molecular weight. The error margin is indicated by the red shade area.

In addition, the foamability of small molecule structural analogues (as shown in Figure 3.8) was also briefly studied. The mass fraction of the hydrophilic and hydrophobic components of this small molecule is comparable to that of the PT85 series copolymers. However, foam pump experimental data show that small molecules can only produce aqueous foams equivalent to the volume of the foaming solution ($\sim 40 \text{ mL}$). Moreover, this foam is relatively unstable and almost completely disappears within tens of seconds. This suggests that polymeric molecular

structure significantly affects interfacial activity. Compared with copolymers, small molecules lack the synergism conferred by long chains and hence cannot form a stable adsorption layer at the liquid-air interface, resulting in a significant reduction in their foamability.

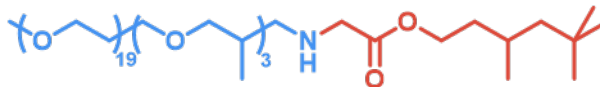


Figure 3.8: Chemical structures of small molecule analogues with similar hydrophilic/hydrophobic structures.

3.3.3 Dynamic Surface Behaviour

The migration and interfacial adsorption behaviour of surfactants play a crucial role in foam formation and foam stabilisation.⁷ Driven by the interfacial energy difference, surfactant molecules in solution rapidly migrate and adsorb to the newly formed liquid-air interface when an air bubble is generated. The adsorbed surfactant molecules form a thin film on the surface and reduce the surface tension. The rate of this process determines the initial foamability and the size distribution of the air bubbles.⁴⁹

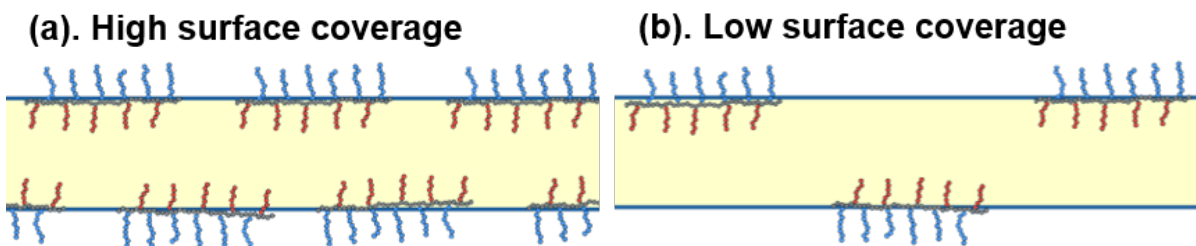


Figure 3.9: Schematic illustration of surfactant adsorption at the air-water interface during foam formation. (a) Fast-migrating surfactants rapidly adsorb to the newly formed interface, leading to dense interfacial coverage and enhanced foam stability. (b) Slow-migrating surfactants result in sparse coverage, insufficient surface adsorption, and poor foam stability.

As illustrated in Figure 3.9, faster-migrating surfactants can quickly adsorb at the interface, reduce its surface energy, facilitate foam formation and reduce bubble coalescence.⁵⁰ Conversely, slowly migrating surfactants may lead to the formation of an unsaturated surface, causing rapid bubble coalescence and foam collapse.⁵¹

Dynamic surface tension shows the rate at which the copolymer surfactant diffuses from the micelles to the air/water interface.⁵² This occurs on a relatively short time scale (milliseconds) for small molecule surfactant.⁷ Compared with the equilibrium surface tension, dynamic surface tension measures the change in surface tension over time under non-equilibrium conditions, and can characterise the diffusion and adsorption dynamics of surfactants.^{7,52}

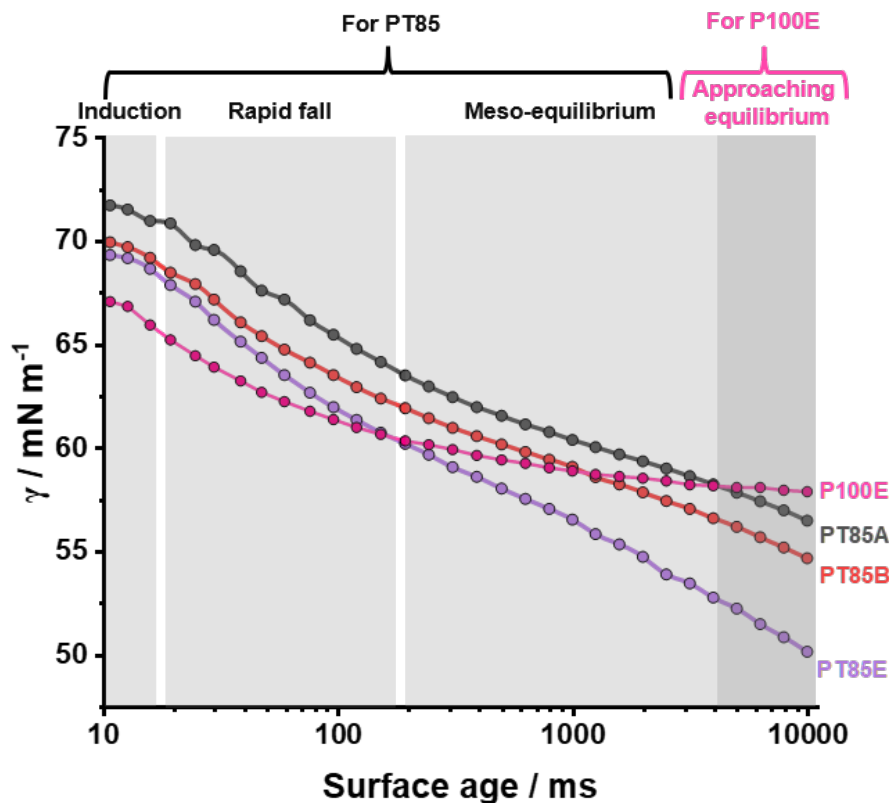


Figure 3.10: Evolution of dynamic surface tension over time recorded for $0.50 \text{ g} \cdot \text{dm}^{-3}$ aqueous solutions of three P(TMHA-*stat*-PEGA) statistical copolymer surfactants of varying molecular weight and a P100E homopolymer.

Bubble pressure tensiometry is an effective method to characterise dynamic surface tension. By measuring the change in surface tension at different bubble lifetimes, the diffusion rate and adsorption kinetics of surfactants can be characterised.⁵³ Figure 3.10 shows a representative dynamic surface tension diagram showing the surface tension changes of three surfactants with different molecular weights, at different bubble lifetimes. The X-axis represents the bubble life (surface age), which is the time allowed for the surfactant to migrate to the surface, while

the Y-axis represents the instantaneous surface tension corresponding to surface age. The three curves (grey, red and purple) represent three surfactants introduced above with different molecular weights, PT85A (black, 20,300 g·mol⁻¹), PT85B (red, 17,600 g·mol⁻¹) and PT85E (purple, 8,900 g·mol⁻¹). The pink curve represents the weakly surface active homopolymer of PPEGA.

The surface tension clearly decreases over time, indicating that the polymer gradually migrates to the interface. However, there is a significant molecular weight effect. The surface tension of PT85E, which has the lowest molecular weight, decreases fastest and reaches a limiting surface tension of less than 60 mN·m⁻¹ within one second, indicating significantly faster diffusion to the air-water interface compared to the other two copolymers. Given its relatively high molecular weight, a longer time is required for PT85A to reach the same limiting surface tension, while PT85B exhibits intermediate behaviour. The PPEGA homopolymer exhibits the fastest surface tension reduction within 200 ms, achieving optimal surface activity at low surface age. The maximum bubble pressure method shows that surface tension continues to decrease steadily even after 10,000 ms (10 seconds) for the amphiphilic statistical copolymers.^{54,55} This indicates that the interfacial adsorption of such amphiphilic copolymers is a very slow process. A typical dynamic surface induction zone can be observed at around 10 ms. For lower molecular weight copolymers, the rapid reduction in the dynamic surface tension appears at a lower surface age region, indicating greater dynamic surface activity. The rapid drop zone for all three surfactants occurs within 300 ms. Only the meso-equilibrium region can be observed for these copolymers (see Figure 3.10). Since the equilibrium surface age of the polymer surfactant is much higher than the measurement range for the maximum bubble pressure method, the equilibrium region cannot be identified by this method.⁷ The exception is the weakly surface-active P100E homopolymer, which reaches its equilibrium state within a few seconds.

The correlation between dynamic surface tension and foamability has been verified for several foaming methods.⁵⁶ Bubble pressure tensiometry provides the best fit to the foamability produced by the foam pump method at a specific surface age.⁴¹ However, its accuracy may be

limited by the type of surfactant. A series of plots of surface tension differences at specific surface ages versus foamability were constructed and fitted. The quality of the fit was used to evaluate the correlation between surface tension difference at surface age ($\Delta\gamma_t$) and foamability.

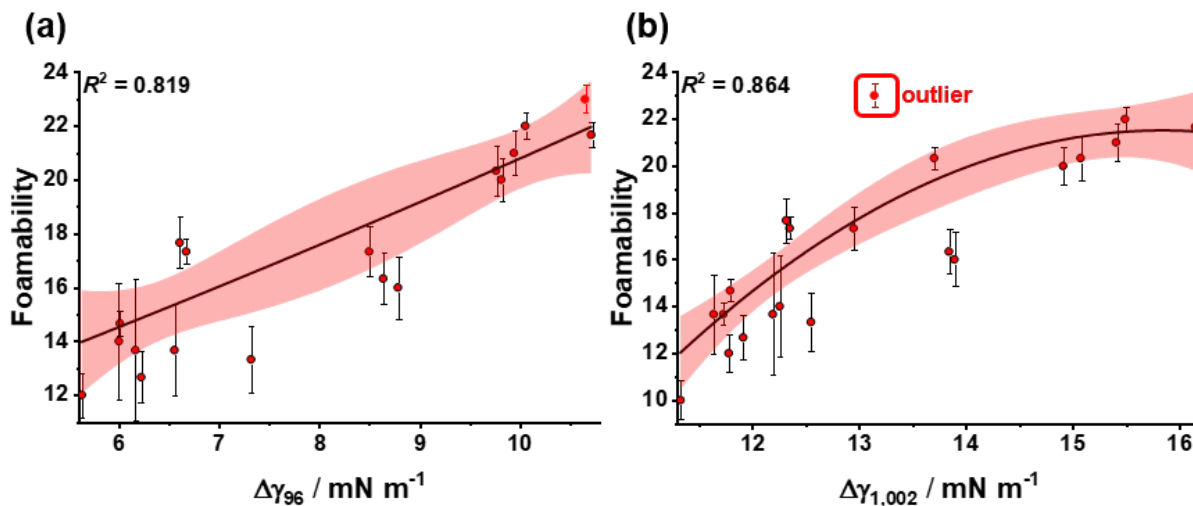


Figure 3.11: Foamability vs. reduction in dynamic surface tension. (a) After 100 ms; (b) After 1,000 ms (N. B. The P100E data point (see red point) is an outlier and accordingly excluded from the data fit). The black curve shows a polynomial fitting to the data with a degree of fit of 2. The red shading represents the 95% confidence band.

As shown in Figure 3.11, the X-axis represents the reduction in dynamic surface tension within 100 ms ($\Delta\gamma_{96} = \gamma_0 - \gamma_{96}$) for Figure 3.11a and 1,000 ms ($\Delta\gamma_{1,002} = \gamma_0 - \gamma_{1,002}$) for Figure 3.11b, respectively. The Y-axis represents the foamability. Overall, the larger the difference in dynamic surface tension, the stronger the foamability, which suggests that rapidly diffusing copolymer chains promote foam formation. Most of the data points fall within the red confidence band, giving an acceptable fitting quality. However, as the surface age increases, the weakly surface-active PPEGA homopolymer gradually deviates from the fit. As shown in Figure 3.10, the reduction in dynamic surface tension for this sample becomes slower after 100 ms and approaches its equilibrium value, indicating lower surface adsorption. Even at longer mixing times, PPEGA did not further adsorb at the air-water interface after 100 ms, resulting in poor correlation with surface age.

3.3.4 Static Surface Behaviour and Foam Stability

The foam stability (F_s) is assessed by dividing the foam half-life ($t_{V,1/2}$) by half of the initial foam volume ($V_{f,0}/2$), see Equation (3.7). This approach compares foam decay rates for foams with differing initial foam heights.

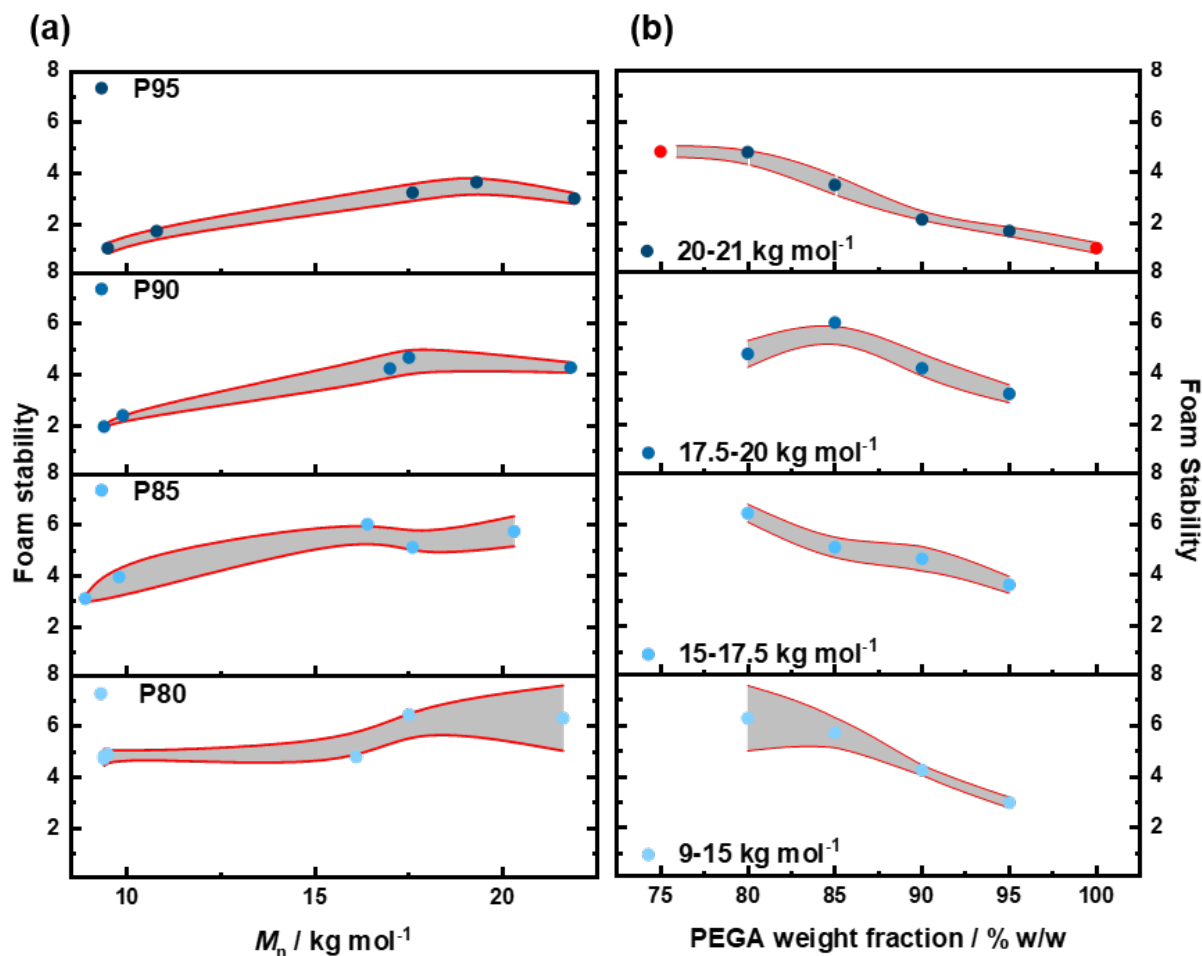


Figure 3.12: Foam stability observed for 0.50 g·dm⁻³ aqueous solutions of a series of acrylic statistical copolymer surfactants: (a) Effect of number-average molecular weight; (b) Effect of PEGA480 weight fraction. The error margin is indicated by red shading.

As shown in Figure 3.12, the foam stability of foams prepared using 0.50 g·dm⁻³ aqueous solutions of a series of P(TMHA-*stat*-PEGA) statistical copolymers is plotted against molecular weight and PEGA weight fraction, respectively. Clearly, more stable foams are produced when using higher molecular weight copolymers. This is attributed to the stronger adsorption at

the air-water interface, thereby forming a more elastic interfacial film that is more resistant to rupture under stress.⁵⁷ Moreover, the foam stability is typically reduced when increasing the PEGA weight fraction. Conversely, increasing the hydrophobic character of such copolymers enhances their adsorption at the air-water interface, thereby improving the stability of the interfacial film and the liquid foam.

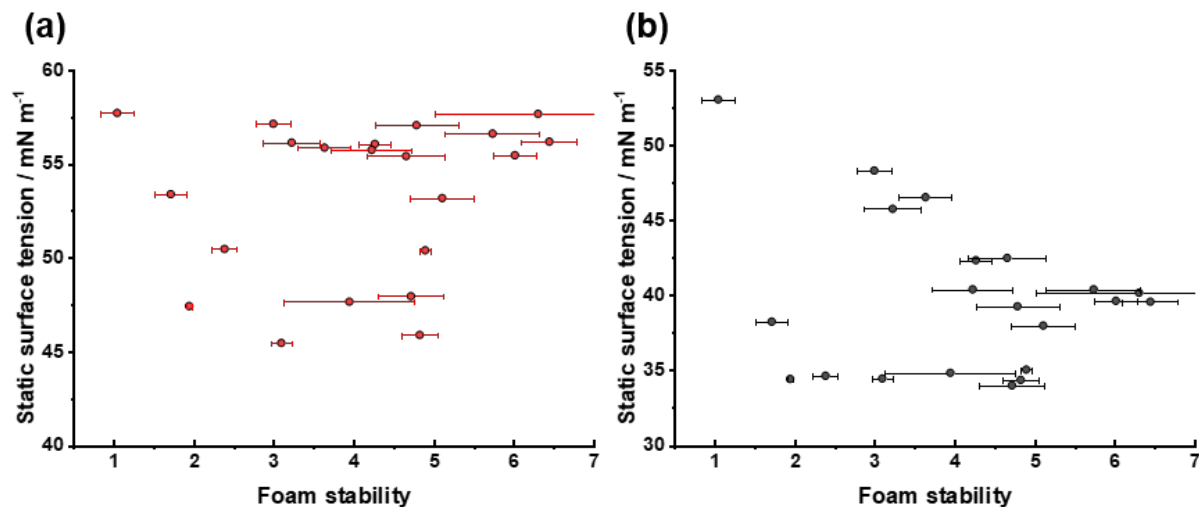


Figure 3.13: Relationship between static surface tension and foam stability achieved from various statistical copolymer surfactant solutions at 0.50 g·dm⁻³. (a) data derived from the maximum bubble pressure method, (b) data obtained using the Du Noüy ring method.

The static surface tension reflects the equilibrium adsorption of copolymer surfactants at the interface. It is therefore often considered as an indicator of potential foam stability. A lower static surface tension suggests a higher ability of the surfactant to reduce interfacial energy and may enhance interfacial film elasticity and stability.⁷ However, this relationship is not universal; certain defoamers can also lower surface tension while promoting foam collapse.⁵⁸

The static surface tension can be measured directly using the Du Noüy ring method or indirectly from dynamic surface tension versus surface age data fitted using the Rosen-Hua equation.³⁷ However, no obvious correlation between static surface tension and foam stability was observed in Figure 3.13. In addition, the two methods produce significantly different data sets. For the same copolymer surfactant, the static surface tension calculated from fitting dynamic data is always higher than the experimental value determined under equilibrium conditions. One

explanation for this difference is that the ideal adsorption model assumed for the Rosen-Hua equation does not consider conformational transitions of copolymer chains adsorbed at the interface, which usually results in higher values.³⁷ Moreover, the Du Noüy ring method only provides the quasi-static surface tension, rather than the 'real' equilibrium surface tension.⁵⁹ The lowest surface tension was around $35 \text{ mN}\cdot\text{m}^{-1}$, which is close to that for a conventional small molecule hydrocarbon-based surfactant.⁶⁰ Despite the static surface tension being widely measured in surfactant research, no useful relationship could be obtained between this parameter and the foam stability.

In summary, it is difficult to optimise foamability and foam stability simultaneously, as these parameters are opposed: shorter copolymer chains diffuse quickly but lead to weaker interfaces while longer chains diffuse more slowly but produce stronger interfaces. Strong foamability requires rapid mass transport of the copolymer to the air-water interface to reduce the surface tension. However, high foam stability requires longer chains to form an elastic interfacial film to minimise liquid drainage. There is a certain trade-off between the two: lower molecular weight copolymer chains form thinner interfaces and hence reduce foam stability, whereas the stronger interfacial films formed by higher molecular weight copolymer chains take longer to form, which can limit initial foam formation. To gain a deeper understanding of the relationship between foamability, foam stability and copolymer structure, the copolymer micelles formed in aqueous solution were analysed by SAXS in the following section.

3.3.5 SAXS Studies of Statistical Copolymer Surfactant Self-assembly in Aqueous Solution

SAXS data for dilute aqueous copolymer solutions were recorded at the ID02 station of the ESRF.⁴² Figure 3.14 shows the SAXS scattering intensity $I(q)$ versus the scattering vector q for 1.0% w/w aqueous solutions of four low molecular weight copolymers and one homopolymer P100E, for which the PEGA content ranges from 75% w/w to 100% w/w.

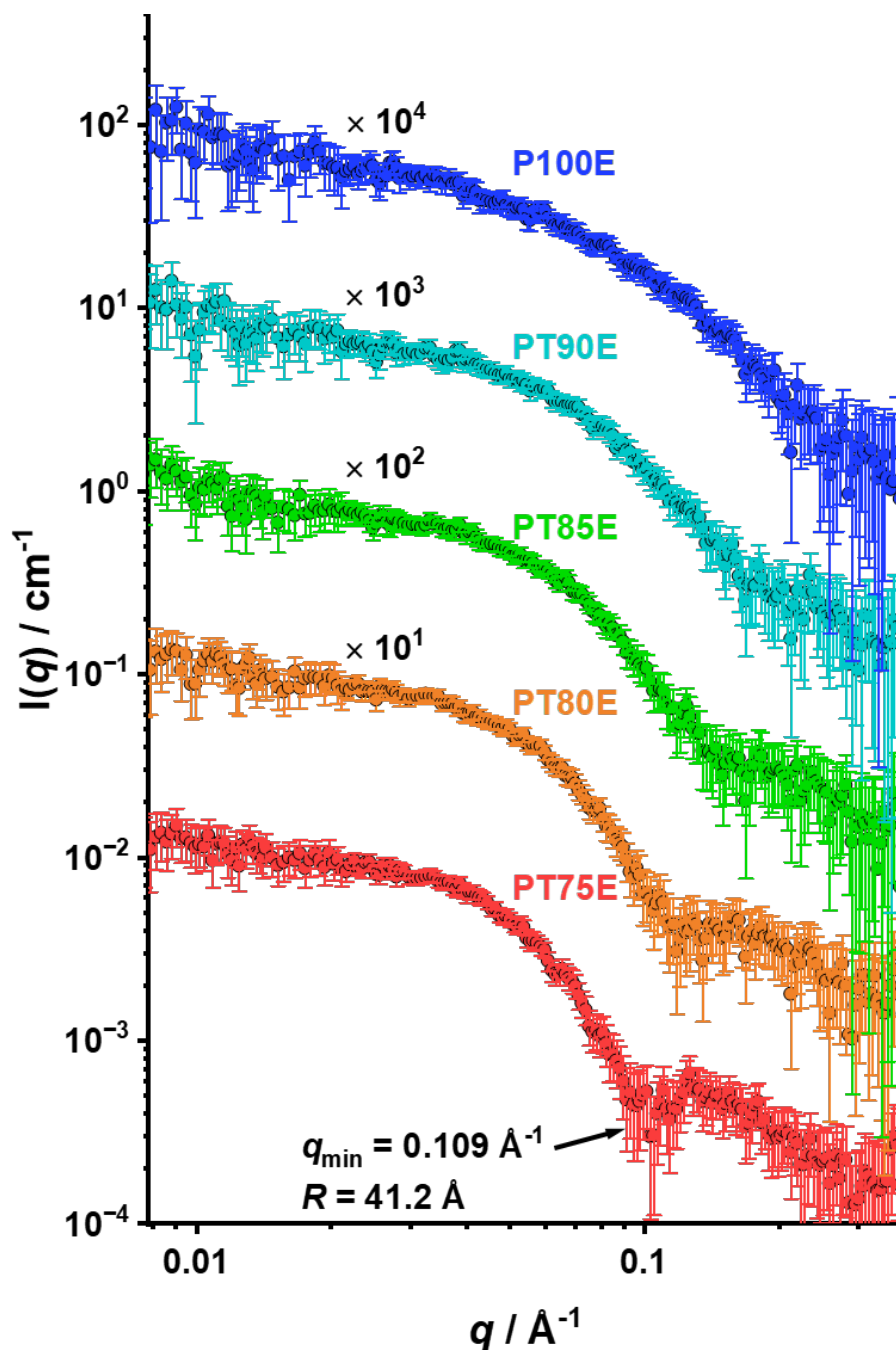


Figure 3.14: SAXS patterns recorded for 1.0% w/w aqueous solutions of four statistical copolymer surfactants and one homopolymer. These copolymers have similar molecular weights (9 kDa) but different copolymer compositions. The upper four patterns were shifted up using multiplication factors (as indicated) to aid comparison.

As the PEGA content of the copolymer is increased, the intensity minima of the form factor at $q \sim 0.1 \text{ \AA}^{-1}$ gradually weaken and eventually disappear. This indicates a change in the

particle cross-sectional dimensions as the position and visibility of these minima are governed by the cross-section form factor. Each SAXS pattern has a Guinier regime (i.e., $I(q) \sim q^0$) at low q regime ($q \ll 0.01 \text{ \AA}^{-1}$). This provides information regarding the size of the polymer aggregates. Upturns were observed at lower q for the more hydrophilic PT85E, PT90E copolymers and P100E homopolymers, which suggests the presence of larger particles, aggregates or particle interactions. For the copolymer with the lowest PEGA content (PT75E), an intensity minimum was observed. The form factor of a sphere has a first minimum of $qR \approx 4.49$ (where R is the particle radius),⁶¹ the particle radius corresponding to the position of this minimum ($q_{\min} = 0.109 \text{ \AA}^{-1}$) and is approximately 41.2 \AA .

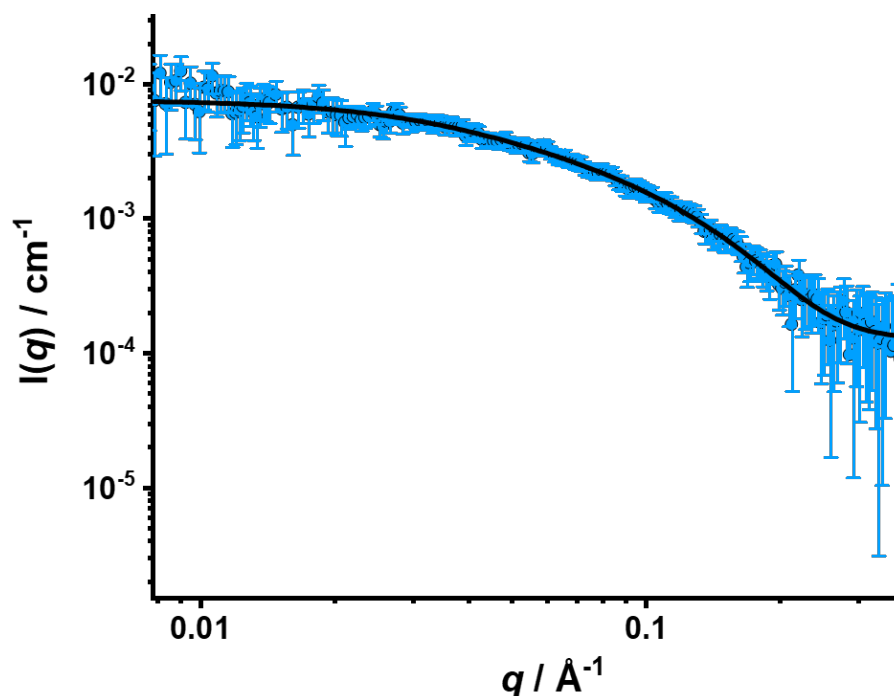


Figure 3.15: SAXS pattern recorded for the PPEGA homopolymer (P100E) fitted using rod model.^{62,63}

Since P100E is a homopolymer, its solution behaviour differs from that of the copolymers discussed in this chapter and therefore requires separate analysis. As shown in Figure 3.15, the SAXS profile of P100E in dilute aqueous solution does not exhibit pronounced features, making it difficult to directly identify its aggregation state in water. Based on its molecular weight and the chemical structure of the PEGA monomer, the homopolymer backbone contains

approximately 20 repeat units, while the PEG side chain consists of about 9 repeat units. Owing to this relatively low degree of polymerisation, neither the backbone nor the side chains are expected to adopt a typical random-coil conformation. Therefore, it is more likely that this polymer forms single-molecule, rod-like micellar structures in aqueous solution.

Guided by this hypothesis, the experimental data were fitted using a rod model.^{62,63} The fitting results indicate a rod length (L_{rod}) of 59.0 Å and a cross-sectional radius (r_x) of 12.8 Å. Using these geometrical parameters, the radius of gyration of the rod was calculated by the following equation:⁶¹

$$R_g^2 = \frac{L_{\text{rod}}^2}{12} + \frac{r_x^2}{2} \quad (3.8)$$

R_g was calculated as 19.3 Å, which is consistent with the expected dimensions of a rod-like chain.

Table 3.2: The rod-like structure was fitted by combining a rod model to determine the mean rod length, cross-section radius and the deduced radius of gyration. χ^2 is a measure of the fitting quality.

Homopolymer	$L_{\text{rod}} / \text{Å}$	$r_x / \text{Å}$	$R_g / \text{Å}$	χ^2
P100E	59.0	12.8	19.3	0.204

For the copolymer with the highest hydrophobic comonomer content (PT75E), the molar ratio of hydrophilic to hydrophobic comonomers is close to 1:1 and these two comonomers are almost randomly distributed along the copolymer chains. According to the literature, similar amphiphilic statistical copolymers can form pseudo-spherical structures in aqueous solution.^{23,28} However, unlike block copolymers, microphase separation may be restricted by the copolymer backbone.⁶⁴ Thus, micelles comprising well-defined hydrophobic cores and hydrophilic shells may not be formed.⁶⁵ To characterise the self-assembled structures formed by such an amphiphilic statistical copolymer in aqueous solution, the well-known homogeneous sphere model was initially used to fit these SAXS patterns.⁶⁶

Homogeneous Sphere Model

The scattering function of a homogeneous sphere was calculated using the following equation:

$$I(q) = \Phi \cdot \Delta\rho^2 \cdot V_{\text{sphere}} \cdot F_{\text{sphere}}^2(q, r) + \text{background} \quad (3.9)$$

where Φ is the volume fraction of the sample, and V_{sphere} is the volume of individual spherical particles, which is given by:

$$V_{\text{sphere}} = \frac{4\pi r^3}{3} \quad (3.10)$$

where r is the radius of the sphere. $\Delta\rho$ is the scattering length density (SLD) contrast between the solvent and the copolymer and $F_{\text{sphere}}(q, r)$ is the form factor amplitude of a sphere. $F_{\text{sphere}}(q, r)$ is given by Equation 3.11:⁶⁷

$$F_{\text{sphere}}(q, r) = \frac{3 \sin(qr) - qr \cdot \cos(qr)}{(qr)^3} \quad (3.11)$$

$\Delta\rho$ is given by $\Delta\rho = \xi_{\text{pol}} - \xi_{\text{sol}}$, where ξ_{pol} and ξ_{sol} are the scattering length densities of the copolymer and solvent, respectively. ξ_{sol} corresponds to the SLD of water, which is calculated as $\xi_{\text{H}_2\text{O}} = 9.42 \times 10^{10} \text{ cm}^{-2}$ (with $\rho_{\text{H}_2\text{O}} = 0.998 \text{ g} \cdot \text{cm}^{-3}$).^{43,68} ξ_{pol} corresponds to the average SLD of the copolymer and is calculated using the following equation:

$$\xi_{\text{pol}} = \xi_{\text{P1}} v_1 + \xi_{\text{P2}} v_2 \quad (3.12)$$

where v_X represents the volume fraction of the two comonomers in the copolymer, ξ_{PX} represents the SLD of the two corresponding homopolymers, and X represents the monomer. V_{co} is calculated from the sum of the volume of two comonomers $V_{\text{co}} = V_{\text{X1}} + V_{\text{X2}}$, hence the volume fraction value can be calculated using Equation 3.13:

$$v_X = \frac{V_X}{V_{\text{co}}} \quad (3.13)$$

The volume of each comonomer in the copolymer is calculated by Equation 3.14:

$$V_X = \frac{M_X}{N_A \cdot \rho_X} \quad (3.14)$$

where M_X is the molecular weight of the corresponding comonomer, given by $M_X = M_n \cdot m_X$, where M_n is the number-average molecular weight obtained from DMF GPC and m_X is the mass fraction determined by ^1H NMR spectroscopy. The mass densities of the two homopolymers were determined by solution densitometry as $\rho_{\text{TMHA}} = 0.90 \text{ g} \cdot \text{cm}^{-3}$ and $\rho_{\text{PEGA}} = 1.16 \text{ g} \cdot \text{cm}^{-3}$, respectively.

The mean aggregation number N_{agg} was calculated from the following equation:

$$N_{\text{agg}} = \frac{4\pi r^3}{3V_{\text{co}}} \quad (3.15)$$

assuming that there are no solvent molecules within the micelle cores.

Table 3.3: Summary of essential SAXS fitting parameters for a series of 1.0% w/w aqueous solutions of four statistical copolymers, based on the homogeneous sphere model. The mean sphere radius (R), standard deviation of the radius (σ_R), and mean aggregation number (N_{agg}) were calculated from the data fits. χ^2 is a measure of the fitting quality.

Copolymer ID	$R / \text{\AA}$	$\sigma_R / \text{\AA}$	N_{agg}	χ^2
PT75E	41.2	0.3	20.3	3.012
PT80E	35.8	0.3	13.4	1.822
PT85E	31.0	0.2	9.3	2.778
PT90E	26.8	0.2	5.7	4.165

According to the above simple spherical model, the mean sphere radius of PT75E dispersion is calculated to be $41.2 \pm 0.3 \text{ \AA}$, which is consistent with the radius estimated from the first intensity minimum. The results are summarised in Table 3.3. The aggregation number is approximately 20. The model provides a satisfactory fit to the data in the low q range. However, as shown in Figure 3.16, it does not properly describe the scattering curve for $q > 0.1 \text{ \AA}^{-1}$. This suggests that the copolymer particles are not homogeneous spheres, instead, there appear to be differing

SLD regions within the particles.⁶⁵

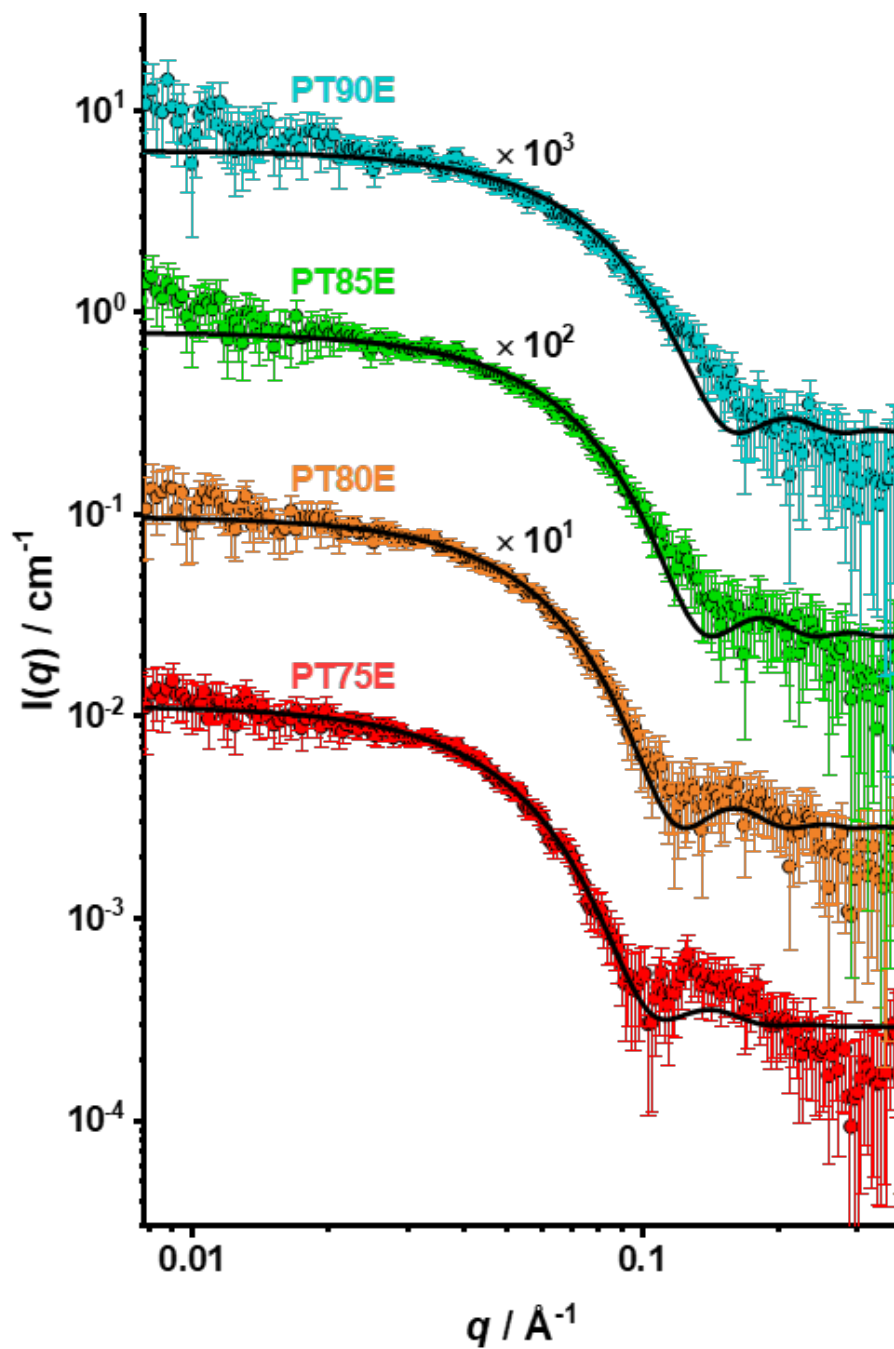


Figure 3.16: SAXS patterns fitted using the homogeneous sphere model. Some patterns were shifted up using multiplication factor (as indicated) for better clarity.

'Blob' Model

The spherical micelle model is widely used in the literature to analyse the structure of block copolymer micelles.^{66,69} This model can well describe the SLD contrast distribution between different regions (e.g. core and corona) located within the micelles. However, for the amphiphilic statistical copolymers discussed in this chapter, the structural characteristics of their micelles in aqueous solution differ significantly from those of block copolymers. Since microphase separation of the hydrophobic TMHA and hydrophilic PEGA units is restricted because they are both located on the same copolymer backbone, so cannot fully occupy the interior or exterior of the nanoparticles. This results in the formation of localised hydrophobic domains.⁶⁴ Unlike the strong microphase separation observed for block copolymers, this produces significant SLD fluctuations that account for the discrepancy between the SAXS patterns and the scattering model in the high q region. This is because the spherical micelle model cannot accurately describe such inhomogeneities. Instead, the so-called 'blob' model has been used for data analysis. This approach explicitly considers SLD fluctuations within the micelles, making it more suitable for their characterisation.²³

A numerical expression of the 'blob' model was initially derived from spherical micelle model by Pedersen et al. to interpret neutron scattering from the solvated cores of spherical micelles.^{65,69} Neal et al. then modified the relevant expression to describe polymer micelles formed by amphiphilic statistical copolymer.^{23,28}

The form factor of the "blob" model is described by the sum of a blob-blob correlation term and a blob self-correlation term $F_{\text{blob}}(q, r)$, as expressed in Equation 3.16:⁶⁵

$$F_{\text{blob}}(q, r) = \frac{N_{\text{agg}}^2(r) \beta_s^2 [n_{\text{blob}}(n_{\text{blob}} - 1) \psi^2(qR_{\text{g,blob}}) F_{\text{sphere}}^2(q, r) + n_{\text{blob}} P_{\text{Debye}}(qR_{\text{g,blob}})]}{n_{\text{blob}}^2} \quad (3.16)$$

where β_s is the scattering contrast between the copolymer and the solvent. The value of β_s is

calculated from the scattering volume and the SLD difference as $\beta_s = V_{co}(\xi_s - \xi_{sol})$, where V_{co} is the scattering volume of copolymer; ξ_s and ξ_{sol} are scattering length densities of the copolymer and background solvent, respectively. $R_{g,lob}$ is the radius of gyration of the blob, which is assumed to behave as a Gaussian chain. Assuming that multiple independent 'blobs' are uniformly distributed within the copolymer micelle, the number of blobs can be estimated as:

$$n_{blob} = \frac{A_1 V_{co}}{V_{blob}} \quad (3.17)$$

where A_1 is a fitting parameter, and V_{blob} is the volume of a single blob, which is calculated using:

$$V_{blob} = \frac{4\pi R_{g,lob}^3}{3} \quad (3.18)$$

$P_{Debye}(qR_{g,lob})$ (Equation 3.19) and $\psi(qR_{g,lob})$ (Equation 3.20) are the form factor for a Gaussian chain and the form factor amplitude of a Gaussian chain, respectively.^{70,71}

$$P_{Debye}(qR_{g,lob}) = \frac{2(e^{-u} + u - 1)}{u^2} \quad (3.19)$$

$$\psi(qR_{g,lob}) = \frac{1 - e^{-u}}{u} \quad (3.20)$$

where $u = q^2 R_{g,lob}^2$, and $R_{g,lob}$ is the ensemble-average radius of gyration of the Gaussian chains.

N_{agg} is calculated by reducing the solvent volume:

$$N_{agg}(r) = \frac{(1 - x_{sol}) \cdot \frac{4}{3}\pi r^3}{V_{co}} \quad (3.21)$$

where r is the radius of the copolymer object, V_{co} is the calculated volume of the copolymer, and x_{sol} is the solvent fraction within the micelles. Since the amount of solvent contained

within the micelle cores was not determined, this parameter was fixed at zero, i.e. the micelles were assumed to contain no internal solvent. Although this may lead to an overestimation of the aggregation number for more hydrophilic copolymers, the overall decreasing trend in aggregation number remains evident.

The 'blob' model provides satisfactory fits to some of the SAXS patterns. However, owing to the poor signal-to-noise ratio in the high q region, it is difficult to determine the 'blob' parameters more precisely. Moreover, these parameters are sensitive to the copolymer composition.

A lower hydrophobic content appears to be a necessary condition for the formation of 'blobs' within the micelle cores. According to previous studies, the blob size may be as small as 4.0 Å for methacrylic acid repeat units.²³ In the present study, the R_g of the blobs formed by PEG side chains is estimated to be 6.5 Å.

It is therefore proposed that these blobs do not significantly influence the scattering intensity at high q , allowing the scattering signal of SLD fluctuations to be approximated by a single fitting parameter. Thus the 'blob' model is expressed as:²⁸

$$I(q) = AF_{blob}(q, r) + B \quad (3.22)$$

where A is a scaling factor for the scattering intensity, B is a fitting parameter that is produced by the scattering length density fluctuations across the micelle.

Table 3.4: Summary of SAXS fitting parameters obtained for 1.0% w/w aqueous solutions of a series of statistical copolymers using the simplified 'blob' model. Mean micelle size (R) and mean aggregation number (N_{agg}) were fitted using this model. χ^2 is a measure of the fitting quality.

Copolymer ID	$R / \text{\AA}$	N_{agg}	χ^2
PT75E	41.2	16.9	0.894
PT80E	36.0	11.3	0.573
PT85E	31.4	7.9	0.554
PT90E	27.2	4.9	0.626

The fitting results are summarised in Table 3.4. As shown in Figure 3.17, satisfactory fits to the

experimental SAXS pattern were obtained, indicating the minor scattering contribution from the 'blob'.

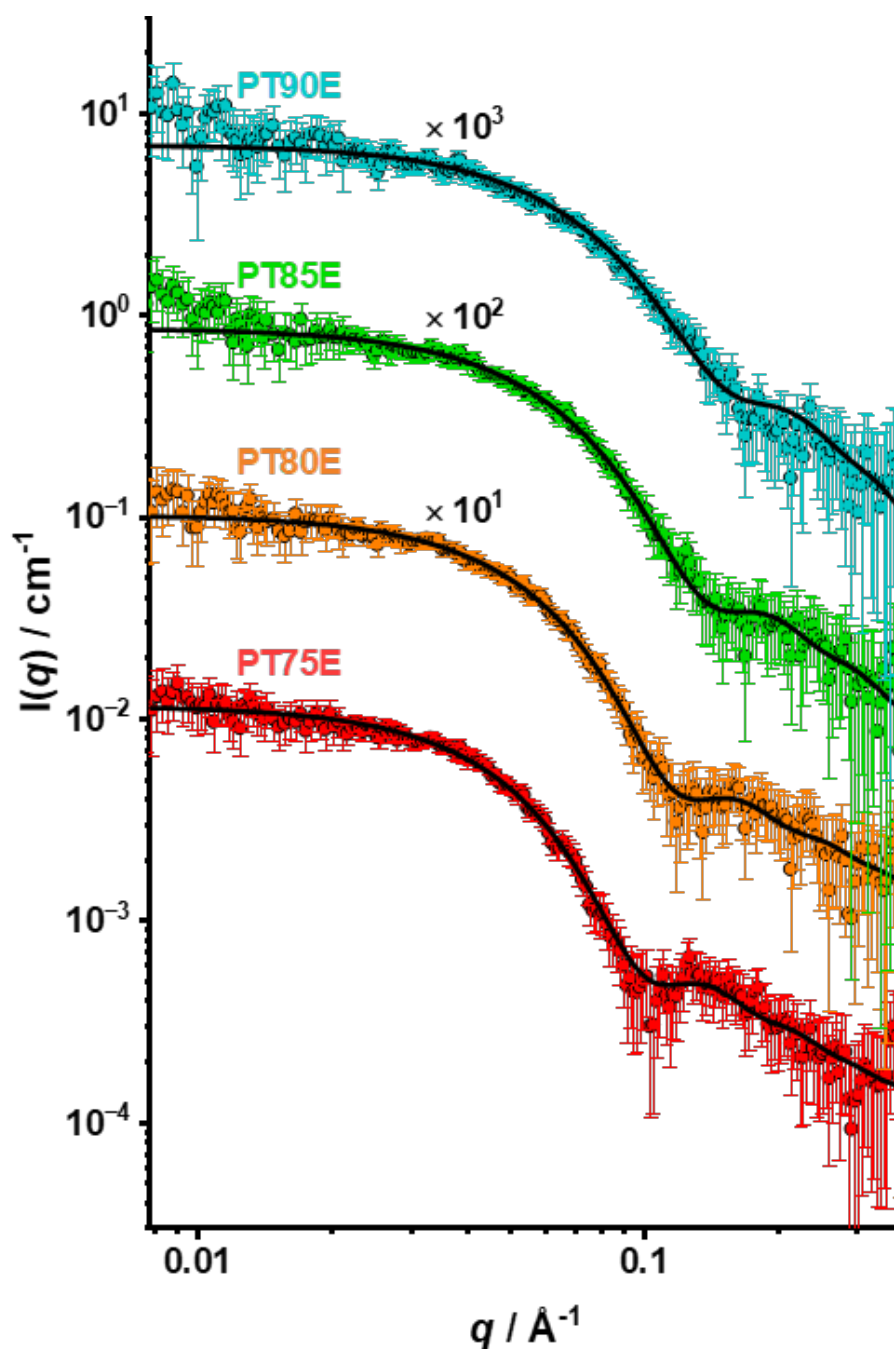


Figure 3.17: SAXS patterns fitted using the 'blob' model. The upper four patterns are shifted up using multiplication factors (as indicated) for clarity.

Model Comparison

The spherical model simply assumes that each micelle has a uniform SLD, which provides a satisfactory fit in the low q regime. However, it cannot adequately describe the solvated outer layer of the micelle. In contrast, the 'blob' model assumes that not all the hydrophilic PEG side chains are located at the outer surface. Some PEG chains may remain buried within the micelle core owing to conformational constraints and hence form 'blobs', which is a more realistic representation of the self-assembly behaviour of relatively hydrophilic statistical copolymers.⁶⁵ Although this model is the most sophisticated, its reliability is somewhat limited owing to poor signal-to-noise in the high q regime.

Comparing the fitting results for the two models reported in Tables 3.3 and 3.4, the 'blob' model provides better fit to the experimental SAXS patterns recorded for a range of copolymer compositions. However, uncertainties regarding the true volume fraction of copolymer particles combined with poor signal-to-noise ratio in the high q regime mean that the 'blob' model is prone to overfitting, thus producing numerically reasonable but physically unrealistic structural parameters. Therefore a simplified 'blob' model will be used to estimate the size and aggregation number of statistical copolymer micelles and the influence of such parameters on the dynamic surface tension will be examined.²⁸

The fitting parameters obtained using the simplified 'blob' model are summarised in Table 3.5. In contrast to previous work, in which a series of ethanol/water mixtures were used, unimolecular micelles were only observed for highly hydrophilic copolymers (PT95A-C) and homopolymer (P100E).¹⁵ Ethanol, as a good solvent for TMHA, can reduce the lyophobicity of TMHA and thus significantly reduce the aggregation number. However, water was the only solvent in this study. For the highly hydrophobic TMHA units, a fully aqueous phase system inevitably leads to an increase in the aggregation number due to an enhanced hydrophobic effect.

Table 3.5: Summary of dynamic surface tension and SAXS structural parameters obtained for 1.0% w/w aqueous solutions of a series of statistical copolymers.

Copolymer ID ^a	$\Delta\gamma_{1,002} / \text{mN}\cdot\text{m}^{-1}$	$R / \text{\AA}$	$\sigma_R / \text{\AA}$	N_{agg}
PT75E	13.71	41.2	4.1	16.9
PT80A	11.33	39.5	2.6	6.5
PT80B	11.73	36.2	0.2	6.2
PT80C	12.19	37.5	3.3	7.4
PT80D	13.85	35.5	3.3	10.7
PT80E	13.90	36.0	3.5	11.3
PT85A	11.64	37.2	2.7	5.8
PT85B	12.95	35.0	2.4	5.5
PT85C	12.32	34.5	3.1	5.7
PT85D	15.08	31.3	3.0	7.1
PT85E	15.50	31.4	3.3	7.9
PT90A	11.92	35.8	2.7	4.8
PT90B	11.79	33.6	2.4	4.9
PT90C	12.26	32.7	2.8	4.7
PT90D	15.42	27.4	3.2	4.7
PT90E	16.16	27.2	2.9	4.9
PT95A	11.78	62.2	22.7	1.0
PT95B	12.55	60.2	19.0	1.0
PT95C	12.35	50.2	19.4	1.0
PT95D	14.92	24.5	2.8	3.1

^a PT for P(TMHA-*stat*-PEGA) copolymer, 75 - 95 for PEGA monomer feed weight fraction, 75 represents the comonomer mixture comprising 75% w/w of PEGA monomer; A - E for the initiator concentration (A for 0.1% w/w initiator, B for 0.5% w/w initiator, C for 2% w/w initiator, D for 5% w/w initiator, E for 10% w/w initiator, respectively).

Copolymer Structure-Property Correlations

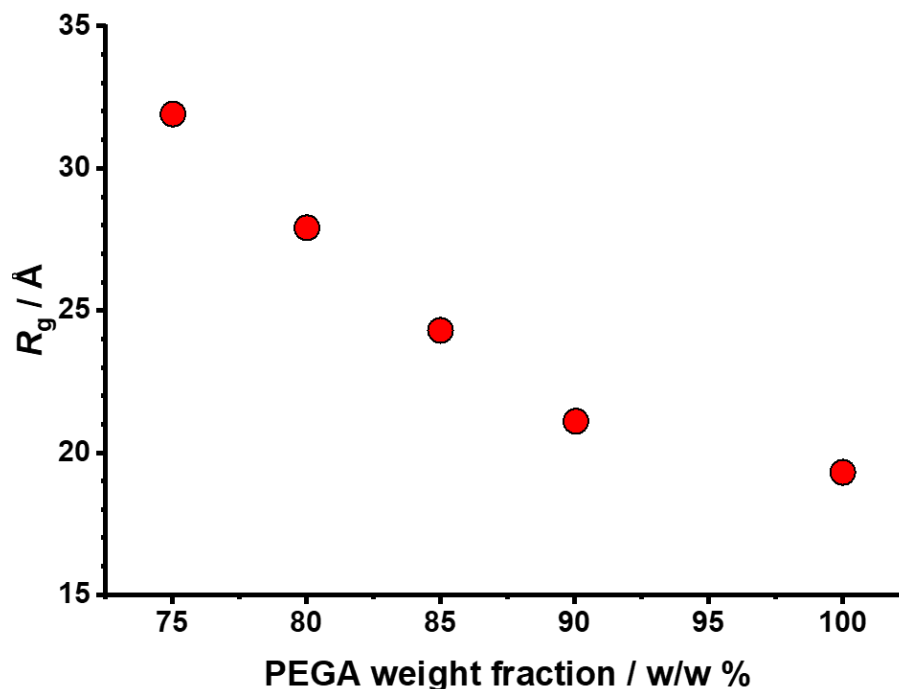


Figure 3.18: Copolymer/homopolymer particle R_g vs. monomer weight fraction.

For a given copolymer molecular weight range, larger micelles and higher aggregation numbers are obtained as the proportion of hydrophobic comonomer is increased, see Table 3.5. This is not conducive to the rapid reduction of surface tension. To produce a stable foam, the ideal surface-active species should be molecularly dispersed and hence able to diffuse rapidly to the evolving air-water interface, followed by interfacial adsorption and (perhaps) a conformational transition. However, micellar dissociation carries a high energy penalty. Higher degrees of aggregation typically implies more stable hydrophobic micelle cores, which increases the energy barrier for the transport of individual copolymer molecules from the solution to the air-water interface.²⁵ For copolymers of similar molecular weight, higher aggregation numbers usually correspond to a smaller difference in dynamic surface tension, which also explains why large micelles with high aggregation numbers exhibit poor foamability. In contrast, copolymers with lower hydrophobic character form relatively loose micelles, see Figure 3.18.

This reduces the energy penalty required for the extraction of individual copolymer chains from such micelles, which ultimately leads to a larger difference in surface tension. Moreover, PEGA homopolymers lack a sufficiently strong hydrophobic component to drive well-defined self-assembly; instead, owing to their limited solubility in water, they typically exist as swollen, poorly defined aggregates rather than true random coils. Such behaviour demonstrates that a suitable hydrophilic/hydrophobic balance is an important consideration for the self-assembly and foamability of statistical copolymers.

Higher copolymer molecular weight only leads to a minor increase in micelle size but a reduction in mean aggregation number, thereby maintaining the overall micelle size. The copolymer composition dominates the micelle size.²³ However, large micelles with low aggregation numbers do not necessarily ensure a lower dynamic surface tension. Polymer chains of higher molecular weight are more likely to be entangled.⁷² This results in a higher energy penalty for micelle disassembly. In addition, the diffusion of individual copolymer chains in solution depends on their molecular weight. Thus longer chains are unfavourable for foam generation since this requires rapid diffusion to the interface to lower the surface tension.

The micelle size depends mainly on the copolymer composition and can be predicted using various structural models.^{23,28,73,74} Moreover, the colloidal stability of statistical copolymer micelles does not require 100% surface coverage of the underlying hydrophobic micelle cores. If the hydrophilic PEG side-chains can attain a certain critical coverage at the micelle surface, then sufficient stability can be conferred by steric repulsion and solvation. Therefore, as the proportion of PEGA comonomer in the statistical copolymer increases, more PEG side-chains can migrate to the surface, resulting in a reduction in the micelle size and aggregation number. This hypothesis has been recently confirmed in the literature.^{23,28}

The surface coverage of the statistical copolymers synthesised in the current study was estimated to exceed 60% (see Appendix 3.5.4). PEG side-chains that do not migrate to the micelle surface may form localised hydrophilic regions (or 'blobs') within the hydrophobic cores, thereby producing local fluctuations in the SLD. In general, charged surface layers confer stronger

micelle stabilisation than the neutral PEG side-chains. This explains the relatively high surface coverage observed for the P(TMHA-*stat*-PEGA) system: the neutral PEGA comonomer repeat units are not mutually repulsive, so they can be packed more efficiently within the micelle corona.

3.3.6 How the Hydrophobe Affects the Foam?

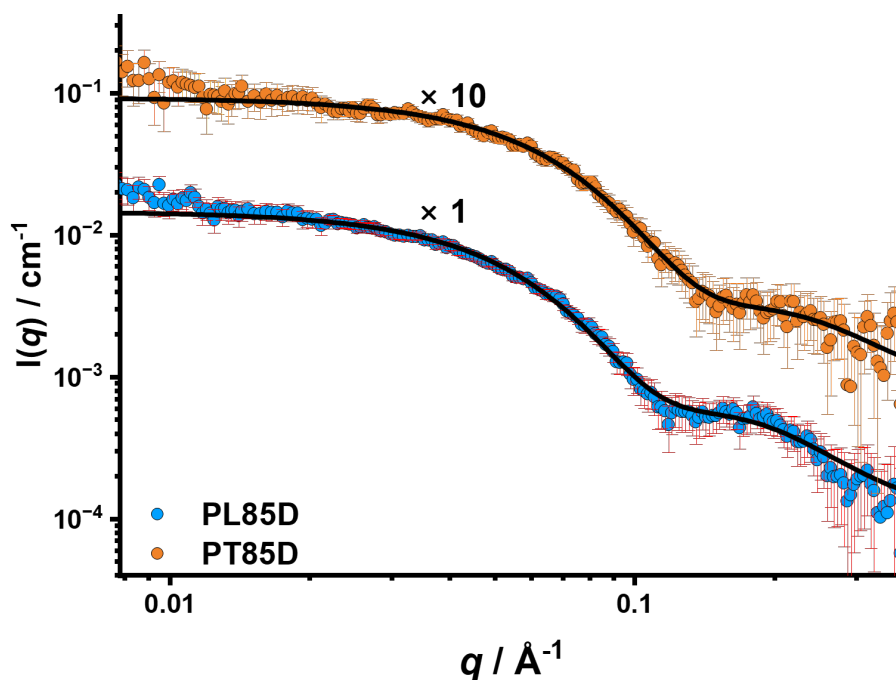


Figure 3.19: SAXS patterns recorded for PT85D and PL85D fitted using the simplified 'blob' model.

It is instructive to compare the behaviour of these amphiphilic statistical copolymers with that of equivalent copolymers in which the TMHA is replaced by LA. For example, an intensity minimum is observed in the corresponding SAXS pattern recorded for PL85D. Clearly, incorporating the more strongly hydrophobic LA comonomer leads to the formation of well-defined micelles compared to those formed by PT85D. In addition, an upturn is observed at low q , which suggests that the PL85D micelles may also form relatively large secondary structures. In contrast, the first minimum in the SAXS curve obtained for the PT85D micelles is less prominent,

indicating that this copolymer forms less compact structures in aqueous solution. However, this reduced clarity of the minimum may also partially arise from the broader copolymer dispersity, which leads to a wider distribution of micelle sizes and thus smears out the form factor features.

Table 3.6: Summary of molecular weight, foam property, dynamic surface tension and SAXS structural parameters obtained for 1.0% w/w aqueous solutions of PT85D and PL85C statistical copolymers.

Copolymer ID	M_n / $\text{g}\cdot\text{mol}^{-1}$	F_a	F_s	$\Delta\gamma_{1,002}$ / $\text{mN}\cdot\text{m}^{-1}$	R / \AA	σ_R / \AA	N_{agg}
PT85D	9,800	20.3	3.9	15.08	31.3	3.0	7.1
PL85C	9,500	13.8	3.2	12.68	36.4	2.3	13.5

The structural properties and foam performance of these two copolymers are summarised in Table 3.6. Although PT85D and PL85C have similar molecular weights, their foamability F_a and foam stability F_s , differ significantly. For PL85C, $F_a = 13.8$ and $F_s = 3.2$, whereas the corresponding values for PT85D are 20.3 and 3.9. This suggests that more hydrophobic LA monomers do not necessarily confer superior foamability and foam stability. In particular, the interfacial adsorption of the linear LA comonomer repeat units is less effective than that of the highly branched TMHA. In addition, PL85C has a higher aggregation number ($N_{\text{agg}} = 13.5$) and a larger radius of gyration $R_g = 36.4 \text{ \AA}$, indicating that the stronger hydrophobic character of the LA comonomer drives the formation of more well-defined micelles. However, this structure is not conducive to either rapid micelle dissociation or the surface adsorption. This is because more strongly hydrophobic micelle cores have a higher energy barrier towards dissociation, thereby reducing the transport of copolymer chains to the air-water interface. Indeed, the surface tension reduction, $\Delta\gamma$, of $12.68 \text{ mN}\cdot\text{m}^{-1}$ conferred by PL85C is significantly lower than that of PT85D ($15.08 \text{ mN}\cdot\text{m}^{-1}$), indicating weaker surface activity for the former copolymer. Although the LA monomer has a longer and ostensibly more hydrophobic side-chain, its linear structure limits the rearrangement and adsorption behaviour of the copolymer chains at the air-liquid interface, resulting in inferior foam performance and a lower reduction in the dynamic surface tension.⁹

3.3.7 How does the Nature of the Copolymer Backbone Affect the Foam?

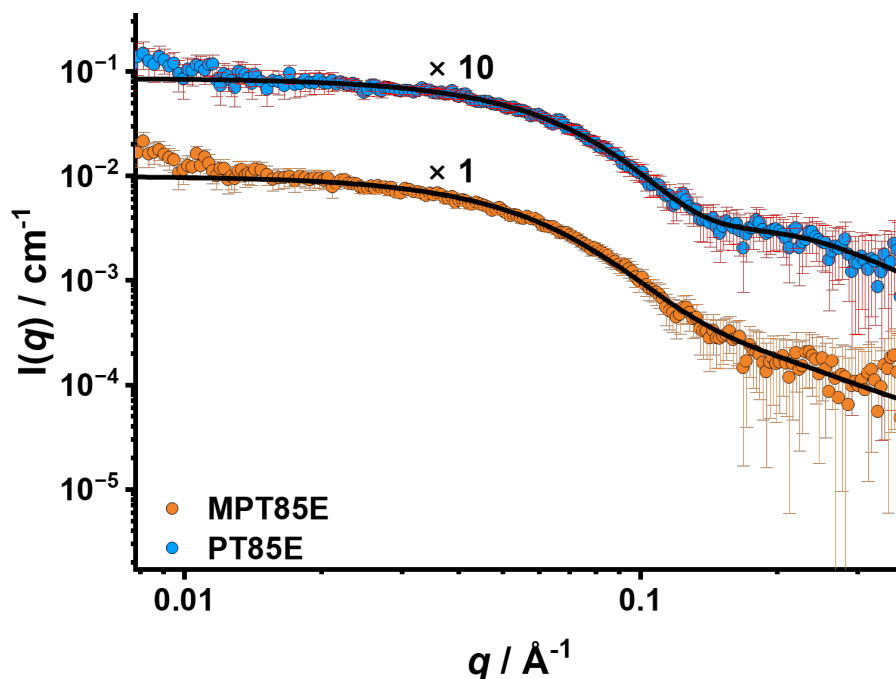


Figure 3.20: SAXS patterns recorded for MPT85E and PT85E fitted using the simplified 'blob' model.

As mentioned in Chapter 2, chain mobility (or backbone flexibility) plays an important role in determining the foaming properties and surface activity of copolymers, especially when individual copolymer chains undergo conformational transitions at interfaces. To explore this effect, a series of methacrylic copolymers with lower chain mobility were also synthesised. However, the SAXS patterns recorded in dilute aqueous solution did not show any significant differences between acrylic and methacrylic copolymer backbones. Thus the micelle structures formed by self-assembly in water are more or less indistinguishable. Each SAXS pattern could be satisfactorily fitted using the spherical micelle model and the corresponding micelle diameters and mean aggregation numbers are very similar. However, these two copolymers exhibited significant differences in their interfacial activity. More specifically, the foaming ability of MPT85E was significantly reduced, even though its $\Delta\gamma_{1,002}$ was only slightly lower than that of PT85E. This suggests that MPT85E can adsorb rapidly at the interface but its less

mobile chains restrict further rearrangement at the evolving interface, ultimately leading to inferior foam stability. Although chain mobility does not significantly change the self-assembly behaviour of the copolymer in aqueous solution, its effect on foam stability after interfacial adsorption is significant, especially when the interface must respond quickly to changes in surface tension.

Table 3.7: Summary of molecular weight, foam property, dynamic surface tension and SAXS structural parameters obtained for 1.0% w/w aqueous solutions of PT85D and PL85C statistical copolymers.

Copolymer ID	M_n / $\text{g}\cdot\text{mol}^{-1}$	F_a	$\Delta\gamma_{1,002}$ / $\text{mN}\cdot\text{m}^{-1}$	R / \AA	σ_R / \AA	N_{agg}
PT85E	9,800	22.0	15.08	31.4	3.3	7.9
MPT85E	12,100	13.0	14.41	31.6	13.2	10.6

Glass transition temperature serves as a useful proxy for polymer chain flexibility.⁷⁵ According to DSC measurements, no distinct glass transition was observed for either copolymer (Figure 3.21). This is due to the relatively long PEG side chains, which obscure the mobility changes in the main chain. As the polymer exists as a single-phase mixture in the bulk, the measured glass transition reflects that of the mixture rather than that of the individual components.

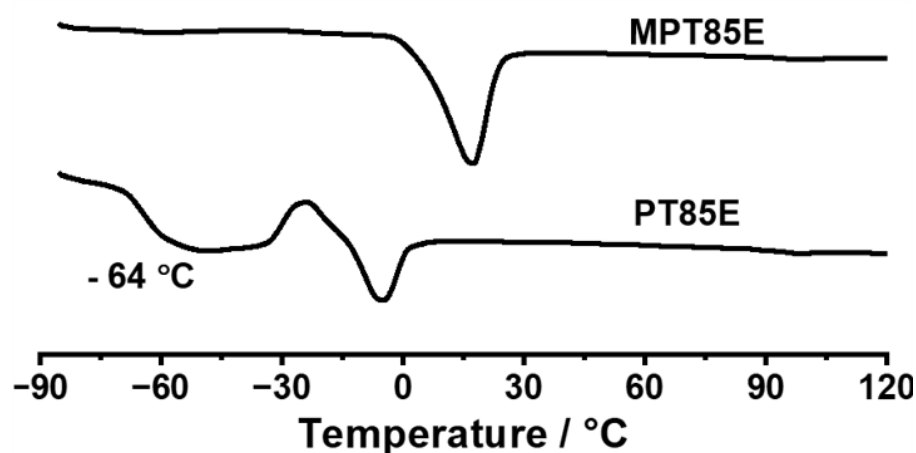


Figure 3.21: DSC measurements were performed on two amphiphilic statistical copolymers, P(TMHA-stat-PEGA) (PT85E) and P(TMHEMA-stat-PEGMA) (MPT85E), each with a [HB]/[HL] ratio of 1.0. The curves shown correspond to the heating trace from the second heating-cooling cycle.

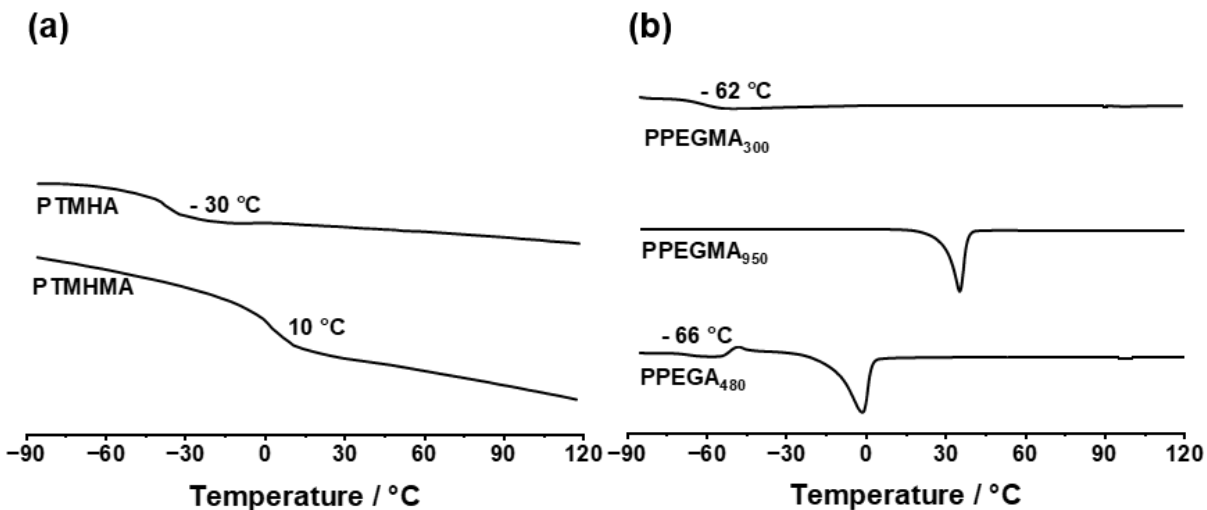


Figure 3.22: DSC measurements for (a) Two hydrophobic homopolymers (PTMHA and PTMHMA); (b) Three hydrophilic homopolymers (PPEGMA₃₀₀, PPEGMA₉₅₀ and PPEGA₄₈₀). The curves shown correspond to the heating trace from the second heating-cooling cycle.

As shown in Figure 3.22, the T_g values of the two hydrophobic homopolymer and three PEG-based (meth)acrylic homopolymers were measured as: $T_{g, \text{TMHA}} = -30^\circ\text{C}$, $T_{g, \text{TMHMA}} = 10^\circ\text{C}$, $T_{g, \text{PPEGMA300}} = -62^\circ\text{C}$ and $T_{g, \text{PPEGA480}} = -66^\circ\text{C}$, respectively. The glass transition was not observed for PPEGMA₉₅₀ homopolymer. PTMHMA has a higher T_g and hence exhibits lower chain mobility. However the DSC measurements of the acrylic copolymers show a T_g nearly identical to that of the homopolymers, which is inconsistent with expectations. Furthermore, the observed T_g deviates significantly from the prediction given by the Fox equation,⁷⁶ suggesting that DSC alone is insufficient to characterise the thermal behaviour of copolymers with long PEG side chains. In the next chapter, the worm-like chain model will be used and its variants to evaluate chain flexibility for another series of model copolymers to understand how this important parameter influences physical properties.

3.4 Conclusions

Structure-property relationships for amphiphilic statistical copolymer surfactants in aqueous solution have been systematically investigated. More specifically, the effect of varying the copolymer composition and molecular weight on initial foamability and long-term foam stability were examined. Low molecular weight copolymers generally exhibit superior foamability owing to their faster diffusion and interfacial adsorption, while high molecular weight copolymers appear to form stronger interfacial films, leading to more stable foams. This hypothesis will be tested in a set of neutron reflectivity measurement after this thesis was submitted. These opposing effects highlight the intrinsic trade-off between foam generation and foam lifetime when designing such next-generation copolymer surfactants.

Dynamic surface tension measurements provided useful insights with regard to the kinetics of interfacial adsorption, with a strong correlation being observed between the rate of surface tension reduction and foamability. SAXS analysis revealed that these amphiphilic copolymers self-assemble in aqueous solution to form micelles, with the morphology and mean aggregation number depending on the copolymer composition.²³ Statistical copolymers containing a higher proportion of hydrophobic comonomer tend to form well-defined spherical micelles, whereas more hydrophilic copolymers formed relatively ill-defined aggregates or even unimolecular micelles.²³ The latter can be described conceptually as an interconnected network of nano-objects, in which the local density fluctuations arise from heterogeneous distributions of solvophobic units along the chain and are stabilised by the surrounding PEG segments.²³ It should be emphasised that, unlike systems with high hydrophobic content, the relatively hydrophilic statistical copolymers do not form a distinct hydrophobic core or discrete hydrophobic 'blobs'. Importantly, increasing the hydrophobic content of such amphiphilic copolymers not only produced more compact micelles but also increased the aggregation number and the energetic barrier required for micelle dissociation, thus leading to slower mass transport of the copolymer to the air-water interface and reducing foamability.

Comparison of LA- and TMHA-based copolymers confirmed that the chemical structure of the hydrophobic comonomer significantly influenced self-assembly and interfacial behaviour. Although LA confers greater hydrophobic character owing to its longer C12 chain, its linear structure results in slightly denser micelles and hence weaker foam performance compared to the branched TMHA-based copolymers.¹⁰ In addition, using the analogous methacrylic copolymers had minimal impact on micelle morphology but significantly affected foam performance compared to all-acrylic copolymers. This highlights the importance of chain mobility in enabling rapid optimisation of the interfacial layer structure.¹⁵

Following our disappointing static surface tension experiments, we submitted a neutron reflectivity (NR) beamtime proposal to ISIS (Didcot, UK), which was subsequently approved. NR can be used to measure the thickness of the film formed by the copolymer chains adsorbed at the air-water interface.⁷⁷ In principle, this technique also enables further exploration of the precise relationship between the surface adsorption and foam stability. Our NR experiment was originally scheduled for September 2024 but was postponed to February 2025 and then further postponed to July 2025. As of the time of submission of this manuscript, the experiments had not yet been performed. In view of this problem, these NR experiments unfortunately cannot form part of this thesis. Nevertheless, we expect that future NR studies will provide the foundation for understanding the interfacial adsorption behaviour of such copolymers and its impact on foam properties. Our successful NR proposal is included in the Appendix 3.5.5.

In addition, regarding to the low signal-to-noise ratio at high- q region observed for statistical copolymers, either a longer acquisition time or shorter camera length could be employed to improve the data quality at specific q range, thereby providing sufficient resolution for the complicated 'blob' model. Moreover, the copolymer did not form the anticipated unimolecular micelles in pure aqueous solution, which is attributed to the limited compatibility between the copolymer and water. To identify the solvent conditions under which unimolecular micelles may form, it is therefore proposed that a series of ethanol/water mixtures with systematically varied compositions be examined. The critical solvent composition was determined experi-

mentally using the PSC model, as it directly depends on the specific balance of polymer-solvent interactions in this system.⁷⁸

In summary, optimal foam performance involves a delicate balance between hydrophobicity, chain length, and flexibility. These findings provide useful design principles for the development of next-generation copolymer surfactants for the generation and stabilisation of aqueous foams.

3.5 Appendix

3.5.1 DMF GPC Data for P(TMHA-*stat*-PEGA) Statistical Copolymers

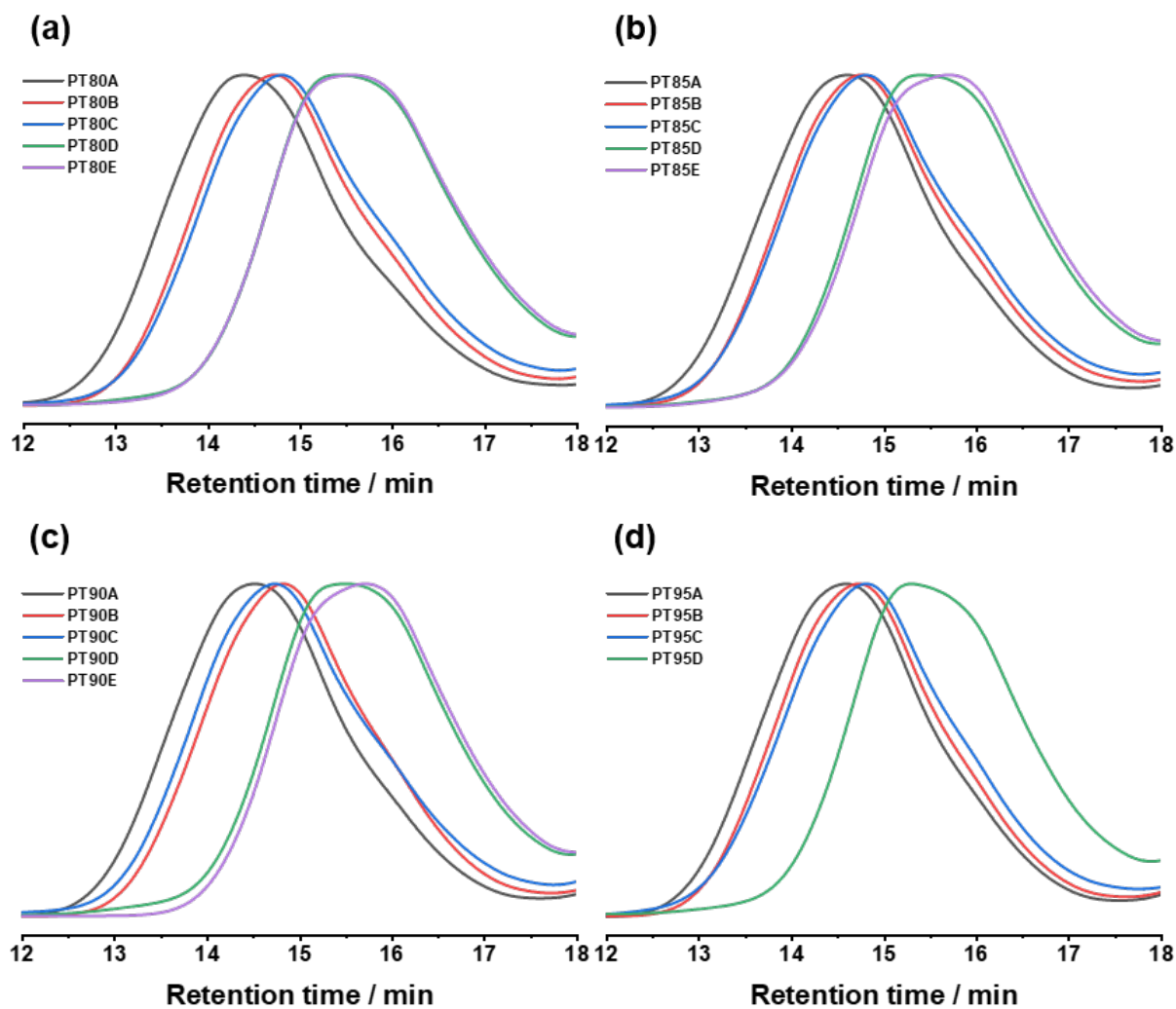


Figure 3.23: DMF GPC curves recorded for the PT series copolymers: (a) PT80; (b) PT85; (c) PT90; (d) PT95.

3.5.2 Surface Tension, Foamability and Foam Stability Data for P(TMHA-*stat*-PEGA) Statistical Copolymers

Table 3.8: Summary of surface tension and foam data obtained for P(TMHA-*stat*-PEGA) copolymers and P100E homopolymer.

Copolymer ID	$\Delta\gamma_{1,002}^a$ / mN·m ⁻¹	γ_{fitted}^b	γ_{ring}^c	F_a	F_s
PT75E	13.71	45.88	34.36	20.33 ± 0.47	4.82 ± 0.22
PT80A	11.33	57.67	40.16	10.00 ± 0.82	6.30 ± 1.28
PT80B	11.73	56.18	39.56	13.67 ± 0.47	6.44 ± 0.35
PT80C	12.19	57.07	39.26	13.67 ± 2.62	4.78 ± 0.52
PT80D	13.85	50.39	35.04	16.33 ± 0.94	4.89 ± 0.07
PT80E	13.90	47.95	33.99	16.00 ± 1.15	4.71 ± 0.40
PT85A	11.64	56.61	40.39	13.67 ± 1.70	5.73 ± 0.59
PT85B	12.95	53.18	37.97	17.33 ± 0.94	5.10 ± 0.40
PT85C	12.32	55.46	39.62	17.67 ± 0.94	6.01 ± 0.27
PT85D	15.08	47.65	34.83	20.33 ± 0.94	3.94 ± 0.82
PT85E	15.50	45.45	34.44	22.00 ± 0.00	3.09 ± 0.13
PT90A	11.92	56.06	42.33	12.67 ± 0.94	4.26 ± 0.20
PT90B	11.79	55.41	42.49	14.67 ± 0.47	4.65 ± 0.48
PT90C	12.26	55.74	40.39	14.00 ± 2.16	4.22 ± 0.50
PT90D	15.42	50.46	34.63	21.00 ± 0.82	2.38 ± 0.16
PT90E	16.16	47.42	34.42	21.67 ± 0.47	1.94 ± 0.04
PT95A	11.78	57.14	48.31	12.00 ± 0.82	2.99 ± 0.21
PT95B	12.55	55.87	46.53	13.33 ± 1.25	3.63 ± 0.33
PT95C	12.35	56.14	45.76	17.33 ± 0.47	3.22 ± 0.35
PT95D	14.92	53.39	38.23	20.00 ± 0.82	1.71 ± 0.20
P100E	13.15	57.72	53.05	23.00 ± 0.00	1.04 ± 0.21

^a $\Delta\gamma_{1,002}$ is the decrease in dynamic surface tension relative to the initial surface tension at 1,002 ms.

^b γ_{fitted} is the fitted equilibrium surface tension from maximum bubble pressure method.

^c γ_{ring} is the measured surface tension from the Du Noüy ring method.

3.5.3 SAXS Model Comparison

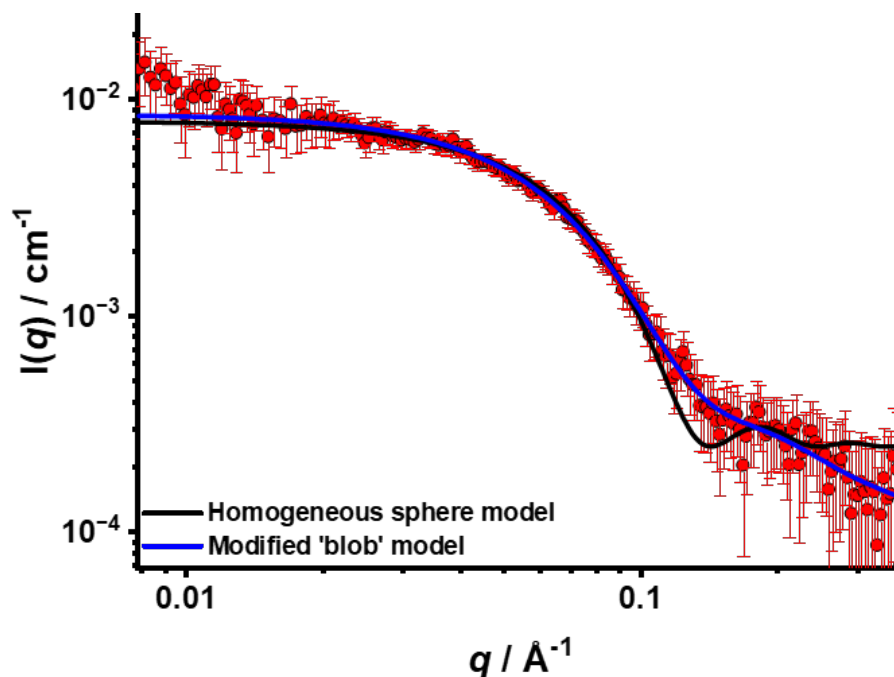


Figure 3.24: SAXS patterns recorded for 1.0% w/w aqueous solution for PT85E statistical copolymer. The red data set obtained for the copolymer was fitted using three models: (a) Homogenous sphere model (black line) and (b) Modified 'blob' model (blue line).

Model fits to the SAXS pattern obtained for the PT85E copolymer in a 1.0% w/w dilute aqueous solution using two different models (Equation (3.9) and (3.22)) are presented in Figure 3.24. The simple sphere model provides a substantially poorer fit to the data than the modified 'blob' model. The deviation observed in the high q region indicates that the simple sphere model fails to capture the structural features of the PT85E copolymer in aqueous solution. It is reasonable to simplify the blob contribution to a constant term during data fitting without significantly affecting the overall quality of the fit. This simplification not only improves the stability of the fitting, but also reduces its complexity, providing a feasible strategy for subsequent model optimisation.²³

3.5.4 Estimation of Surface Coverage

The chemical composition of the micelles is related to the composition of the copolymer, thereby the mole fraction of the PEGA in the micelles ($\phi_{\text{PEGA,micelle}}$) is defined by the following equation:²³

$$\phi_{\text{PEGA,micelle}} = \phi_{\text{PEGA,copolymer}} = \frac{N_{\text{PEGA}}}{N_{\text{PEGA}} + N_{\text{TMHA}}} \quad (3.23)$$

where N_{PEGA} and N_{TMHA} are the mean numbers of PEGA and TMHA comonomers per copolymer chain, respectively. These two numbers can be either determined from ^1H NMR or estimated from a related model as described in (3.24) and (3.25):

$$N_{\text{agg}}N_{\text{PEGA}} = \frac{4\pi R_{\text{micelle}}^2 SC}{CS_{\text{PEGA}}} \quad (3.24)$$

$$N_{\text{agg}}N_{\text{TMHA}} = \frac{\frac{4}{3}\pi R_{\text{micelle}}^3 - N_{\text{agg}}N_{\text{PEGA}}V_{\text{PEGA}}}{V_{\text{TMHA}}} \quad (3.25)$$

where $V_{\text{TMHA}} = 365 \text{ \AA}^3$ and $V_{\text{PEGA}} = 886 \text{ \AA}^3$ calculated from (3.14). CS_{PEGA} is the approximate cross-sectional area of a individual PEGA repeat unit, which is calculated by $CS_{\text{PEGA}} = V_{\text{PEGA}}^{2/3} = 92.2 \text{ \AA}^2$. SC is the surface coverage fraction defined by the ratio of hydrophobic 'core' surface covered by PEGA chains. By applying the experimental data to Equation (3.23) - (3.25), SC was estimated to be higher than 60%.

3.5.5 Proposal for Approved Neutron Reflectivity Experiment

Understanding the surface adsorption of random copolymer foaming surfactant at equilibrium

Andi Xie, Rachel C. Kilbride, Anthony J. Ryan and Steven P. Armes

1. Background and scientific context: This proposal is part of a PhD project awarded to A. Xie with funding from EPSRC and the University of Sheffield scholarship. It's an extension of a previously published work: *Hydrocarbon-Based Statistical Copolymers Outperform Block Copolymers for Stabilization of Ethanol–Water Foams*, *ACS Appl. Mater. Interfaces* 2022, 14, 34, 39548–39559.¹

The most intuitive feeling that consumers have for cleaning and personal care products is their foamability. Surfactant is a class of amphiphilic molecule that can reduce the surface tension of liquids, which are beneficial for producing foam. In addition, the surface adsorption of foaming surfactant can further stabilize the foam, producing long-life foam that meets customers' sensory expectations. However, traditional high-performance surfactant, particularly those based on carbon-fluorine or siloxane, presents a conflict between performance, environment and biocompatibility. Pluronics are a successful fluorine and siloxane free polymeric surfactant, which have been commercialized for decades (Figure 1b). Although this class of block copolymers of hydrophilic poly(ethylene oxide) (PEO) and hydrophobic polypropylene oxide (PPO) has notable surface activity, the foam performance is limited due to the poor hydrophobic nature of PPO, making it less suitable for applications requiring massive foam. Silicone-based surfactant remains necessary additives for personal care formulations. To address these issues, researchers have increasingly focused on structural optimization of hydrocarbon-based surfactants to achieve better performance. As research progresses, especially the recent development of living radical polymerization techniques such as reversible addition–fragmentation chain-transfer polymerization (RAFT), the precise control of polymer architecture is feasible. In addition, a larger available library of hydrophobic monomers provides more combinations for polymeric surfactant formulations.

Preliminary research in Sheffield compared the surfactant activities of amphiphilic random and block copolymers from multiple monomer pairs (Figure 1a and 1c). The random copolymer of branched hydrophobic structure (3,5,5-trimethylhexyl acrylate, TMHA) and hydrophilic poly(ethylene glycol)methyl ether acrylate demonstrates superior surface and foaming activities than their block analogues and Pluronic F127, despite the similar molecular weight and PEG weight fraction.

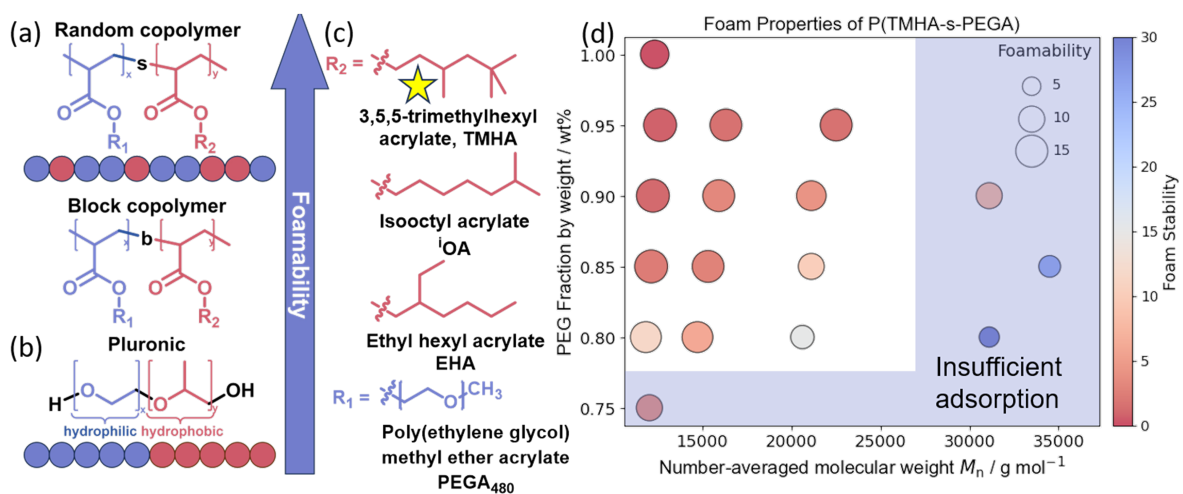


Figure 1: Architectures of (a) amphiphilic random and block copolymer, (b) Pluronic surfactant, (c) chemical structure of hydrophobic and hydrophilic parts of amphiphilic copolymers. Random copolymer of TMHA and PEGA has the best foamability among all shown combination. (d) Foam properties of random copolymers of TMHA and PEGA: low M_n samples have better foamability; high M_n samples produce less but more stable foam.

analogues and Pluronic F127, despite the similar molecular weight and PEG weight fraction. Further investigation on the best foaming monomer pair reveals that a shorter chain allows better foaming. Better foam stability requires more adsorption anchor points, which need either longer chain lengths or more hydrophobic units. However, more rigid hydrophobic units significantly restrict chain flexibility and inhibits free chain

motion, resulting in insufficient adsorption. Longer chains not only provide more adsorption anchor points but also require more time to extend and expose the hydrophobe to the surface, resulting in a slower adsorption rate, hence producing less foam (Figure 1d). A correlation is observed between dynamic surface tension and foamability (Figure 2a). The surface tension decrease rate within 1 s linearly associated to the foamability (Figure 2b). Data points that deviate from the confidence interval are considered to be affected by foam stability. Although the dynamic surface tension can predict the foamability, the equilibrated interface behaviour and structure which affects the foam stability remains unclear. Conventional equilibrium surface tension measurement methods, such as the Du Nouy Ring method, can't measure the surface tension of random polymer surfactants at equilibrium. The mechanical movement of the ring on the liquid surface would desorb surfactant molecules. Any mechanical perturbation is detrimental to polymers with slow surface adsorption. To address this, this proposal comprehensively investigates the equilibrated interfacial structure of random copolymer surfactants using neutron reflectometry (NR). By combining the study of equilibrium and dynamic behaviour, we hope to establish the correlation between equilibrated adsorption strength, dynamic adsorption rate and foaming, to indicate the design rule of random copolymer surfactant.

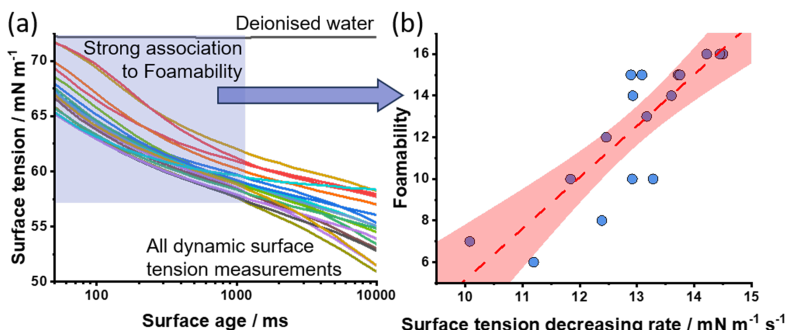


Figure 2: (a) Dynamic surface tension graph of all samples compared with deionised water. (b) Surface tension decreasing rate within 1,000 ms is strongly associated with foamability of random copolymers. Foam stability is not taken into account here.

2. Proposed Experiment: Static NR measurements will be performed on INTER reflectometer. Standard method will be applied.² We will use the 7-position sample trough on the active anti-vibration table, and the corresponding number of samples will be prepared at a time. The first measurement will start after at least 60 mins upon loading the samples to allow full adsorption to the surface. Between each set of measurement, the trough will be cleaned by H₂O – EtOH – H₂O, and then dried with a heat gun. 24 samples, including 6 different PEGA weight fractions, 4 different molecular weights and 2 polymer backbones will be dissolved with the same concentration in two solvent contrasts (H₂O, D₂O) respectively. Such sample distribution allows statistically significant data.

3. Justification of beamtime request: The high penetration and non-destructive nature of neutrons make NR an ideal technique for this study, especially the static non-mechanical contact measurement allows the copolymer to fully adsorb to the surface. Neutron scattering length densities of all random copolymer samples have been estimated from the measured mass density. The random copolymers with 80 - 85 wt% PEGA are considered to have a weak contrast with H₂O. To obtain sufficient neutron contrast for all samples and restrict the phase space for fitting, both H₂O and D₂O will be used as the solvent. 60 mins standing time will be allocated before each set of measurement (48 measurements is divided into 7 sets). 30 and 60 mins acquisition time will be allocated for D₂O and H₂O solutions respectively. The actual beamtime will be $0.5 \times 24 + 1 \times 24 + 1 \times 7 = 43$ hours. Therefore, it is expected that 48 hrs will be required, including the preparation time for the experiment and samples

4. Reference: 1) J. Jennings, A. Xie et al. *ACS Appl. Mater. Interface.*, 2022, 14, 24, 39548. 2) E. M. Lee, J. Penfold et al. *J. Phys. Chem.*, 1989, 93, 381

3.6 References

- (1) N. Moradpour, J. Yang and P. A. Tsai, *Current Opinion in Colloid & Interface Science*, 2024, **74**, 101845.
- (2) G. S. Luengo, O. Aubrun and F. Restagno, *Current Opinion in Colloid & Interface Science*, 2025, **77**, 101906.
- (3) A. P. Golin, D. Choi and A. Ghahary, *American Journal of Infection Control*, 2020, **48**, 1062–1067.
- (4) V. P. Torchilin, *Journal of Controlled Release*, 2001, **73**, 137–172.
- (5) X. Yu, N. Jiang, X. Miao, F. Li, J. Wang, R. Zong and S. Lu, *Process Safety and Environmental Protection*, 2020, **133**, 201–215.
- (6) M. H. Amaral, J. das Neves, Â. Z. Oliveira and M. F. Bahia, *Journal of Surfactants and Detergents*, 2008, **11**, 275–278.
- (7) R. J. Pugh, *Bubble and Foam Chemistry*, Cambridge University Press, Cambridge, UK, 2016.
- (8) P. W. Atkins, J. D. Paula and J. Keeler, *Atkins' physical chemistry*, Oxford University Press, Oxford, UK, 2023.
- (9) A. Czajka, G. Hazell and J. Eastoe, *Langmuir*, 2015, **31**, 8205–8217.
- (10) A. Mohamed, M. Sagisaka, F. Guittard, S. Cummings, A. Paul, S. E. Rogers, R. K. Heenan, R. Dyer and J. Eastoe, *Langmuir*, 2011, **27**, 10562–10569.
- (11) N. M. Kovalchuk, A. Trybala, V. Starov, O. Matar and N. Ivanova, *Advances in Colloid and Interface Science*, 2014, **210**, 65–71.
- (12) R. Wagner, L. Richter, Y. Wu, J. Weißmüller, A. Kleewein and E. Hengge, *Applied Organometallic Chemistry*, 1998, **12**, 265–276.

- (13) W.-H. Wu, J.-L. Wang, Y.-Q. Zhou, Y. Sun, J. Duan and A. Zhang, *Chemical Papers*, 2023, **77**, 6763–6771.
- (14) F. Hernáinz and A. Caro, *Colloids and Surfaces A: Physicochemical and Engineering Aspects*, 2002, **196**, 19–24.
- (15) J. Jennings, R. R. Webster-Aikman, N. Ward-O'Brien, A. Xie, D. L. Beattie, O. J. Deane, S. P. Armes and A. J. Ryan, *ACS Applied Materials & Interfaces*, 2022, **14**, 39548–39559.
- (16) L. C. Brown, K. M. Hinnant, G. C. Daniels, P. E. Sudol, S. R. Vaughan, N. K. Weise and B. C. Giordano, *Langmuir*, 2023, **39**, 8559–8567.
- (17) G. C. Daniels, K. M. Hinnant, L. C. Brown, N. K. Weise, M. C. Aukerman and B. C. Giordano, *Langmuir*, 2022, **38**, 4547–4554.
- (18) E. Panieri, K. Baralic, D. Djukic-Cosic, A. Buha Djordjevic and L. Saso, *Toxics*, 2022, **10**, 44.
- (19) B. Laubie, E. Bonnafous, V. Desjardin, P. Germain and E. Fleury, *Science of The Total Environment*, 2013, **454-455**, 199–205.
- (20) A. Laschewsky, in *Polysoaps/Stabilizers/Nitrogen-15 NMR*, Springer, Heidelberg, Germany, 1995, ch. 1, pp. 1–86.
- (21) P. Shi, H. Zhang, L. Lin, C. Song, Q. Chen and Z. Li, *RSC Advances*, 2019, **9**, 3224–3231.
- (22) E. F. Marques and B. F. B. Silva, in *Encyclopedia of Colloid and Interface Science*, ed. T. Tadros, Springer, Heidelberg, Germany, 2013, pp. 1202–1241.
- (23) T. J. Neal, D. L. Beattie, S. J. Byard, G. N. Smith, M. W. Murray, N. S. J. Williams, S. N. Emmett, S. P. Armes, S. G. Spain and O. O. Mykhaylyk, *Macromolecules*, 2018, **51**, 1474–1487.

- (24) A. Hashidzume, A. Kawaguchi, A. Tagawa, K. Hyoda and T. Sato, *Macromolecules*, 2006, **39**, 1135–1143.
- (25) Y. E. Omari, M. Yousfi, J. Duchet-Rumeau and A. Maazouz, *Polymers*, 2022, **14**, 2844.
- (26) M. S. H. Akash and K. Rehman, *Journal of Controlled Release*, 2015, 120–138.
- (27) P. Alexandridis and T. A. Hatton, *Colloids and Surfaces A: Physicochemical and Engineering Aspects*, 1995, **96**, 1–46.
- (28) T. J. Neal, A. J. Parnell, S. M. King, D. L. Beattie, M. W. Murray, N. S. J. Williams, S. N. Emmett, S. P. Armes, S. G. Spain and O. O. Mykhaylyk, *Macromolecules*, 2021, **54**, 1425–1440.
- (29) G. B. Brandani, S. J. Vance, M. Schor, A. Cooper, M. W. Kennedy, B. O. Smith, C. E. MacPhee and D. L. Cheung, *Physical Chemistry Chemical Physics*, 2017, **19**, 8584–8594.
- (30) A. Cooper, S. J. Vance, B. O. Smith and M. W. Kennedy, *Colloids and Surfaces A: Physicochemical and Engineering Aspects*, 2017, **534**, 120–129.
- (31) C. D. Mackenzie, B. O. Smith, A. Meister, A. Blume, X. Zhao, J. R. Lu, M. W. Kennedy and A. Cooper, *Biophysical Journal*, 2009, **96**, 4984–4992.
- (32) G. Odian, *Principles of Polymerization*, Wiley, Hoboken, NJ, USA, 4th edn., 2004.
- (33) M. Morton and L. J. Fetters, *Rubber Chemistry and Technology*, 1975, **48**, 359–409.
- (34) B. Wakefield, *The Chemistry of Organolithium Compounds*, Pergamon Press, Oxford, UK, 1974.
- (35) G. Vazquez, E. Alvarez and J. M. Navaza, *Journal of Chemical & Engineering Data*, 1995, **40**, 611–614.
- (36) C. Johnson and J. Lane, *Journal of Colloid and Interface Science*, 1974, **47**, 117–121.
- (37) X. Y. Hua and M. J. Rosen, *Journal of Colloid and Interface Science*, 1991, **141**, 180–190.

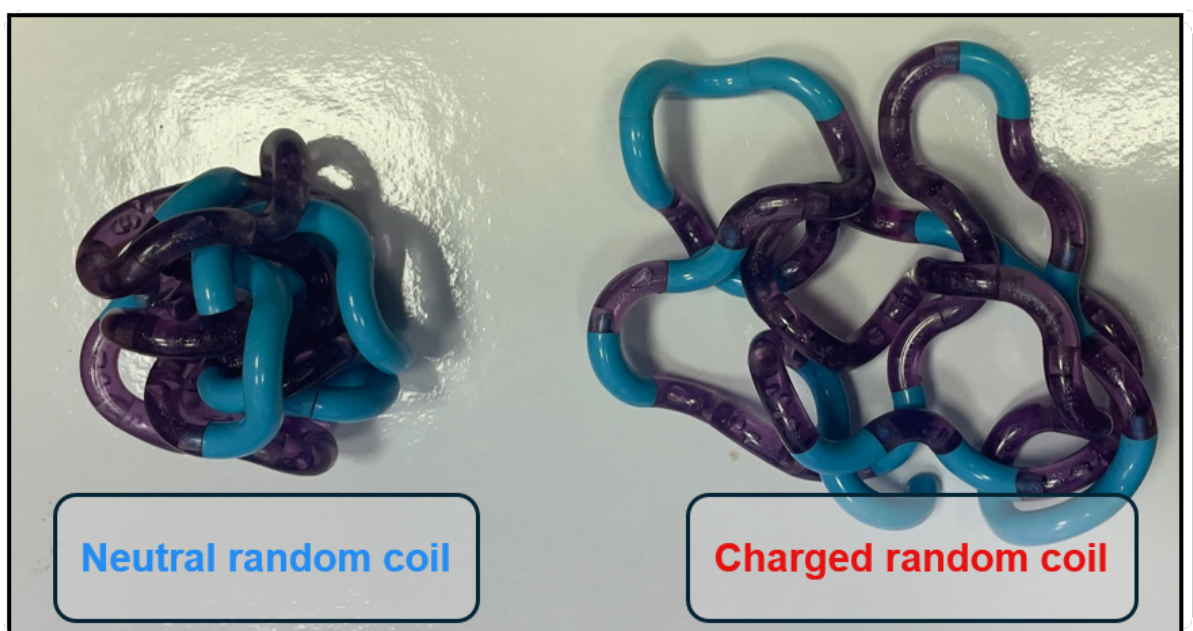
- (38) H. Zuidema and G. Waters, *Industrial & Engineering Chemistry Analytical Edition*, 1941, **13**, 312–313.
- (39) P. L. du Noüy, *Journal of General Physiology*, 1925, **7**, 625–631.
- (40) K. W. Bewig and W. A. Zisman, *The Journal of Physical Chemistry*, 1965, **69**, 4238–4242.
- (41) N. Ward-O’Brien, PhD thesis, University of Sheffield, 2021.
- (42) T. Narayanan, M. Sztucki, T. Zinn, J. Kieffer, A. Homs-Puron, J. Gorini, P. Van Vaerenbergh and P. Boesecke, *Journal of Applied Crystallography*, 2022, **55**, 98–111.
- (43) SASView, <https://www.sasview.org/>, (accessed May 2025).
- (44) J. Ilavsky and P. R. Jemian, *Journal of Applied Crystallography*, 2009, **42**, 347–353.
- (45) S. Alexander, G. N. Smith, C. James, S. E. Rogers, F. Guittard, M. Sagisaka and J. Eastoe, *Langmuir*, 2014, **30**, 3413–3421.
- (46) M. Sagisaka, T. Narumi, M. Niwase, S. Narita, A. Ohata, C. James, A. Yoshizawa, E. T. de Givenchy, F. Guittard, S. Alexander and J. Eastoe, *Langmuir*, 2014, **30**, 6057–6063.
- (47) D. Papp, G. Carlström, T. Nylander, M. Sandahl and C. Turner, *Analytical Chemistry*, 2024, **96**, 10612–10619.
- (48) N. M. Ahmad, F. Heatley and P. A. Lovell, *Macromolecules*, 1998, **31**, 2822–2827.
- (49) D. Kawale, A. van Nimwegen, L. Portela, M. van Dijk and R. Henkes, *Colloids and Surfaces A: Physicochemical and Engineering Aspects*, 2015, **481**, 328–336.
- (50) K. Golemanov, N. D. Denkov, S. Tcholakova, M. Vethamuthu and A. Lips, *Langmuir*, 2008, **24**, 9956–9961.
- (51) J. M. Rodríguez Patino, C. Carrera Sánchez and M. R. Rodríguez Niño, *Advances in Colloid and Interface Science*, 2008, **140**, 95–113.
- (52) R. Miller, E. Aksenenko and V. Fainerman, *Advances in Colloid and Interface Science*, 2017, **247**, 115–129.

- (53) V. Fainerman and R. Miller, *Advances in Colloid and Interface Science*, 2004, **108-109**, 287–301.
- (54) J. Kloubek, *Colloid and Polymer Science*, 1975, **253**, 754–759.
- (55) X. Y. Hua and M. J. Rosen, *Journal of Colloid and Interface Science*, 1988, **124**, 652–659.
- (56) D. Kawale, A. van Nimwegen, L. Portela, M. van Dijk and R. Henkes, *Colloids and Surfaces A: Physicochemical and Engineering Aspects*, 2015, **481**, 328–336.
- (57) D. Georgieva, A. Cagna and D. Langevin, *Soft Matter*, 2009, **5**, 2063–2071.
- (58) N. Politova-Brinkova, M. Hristova, V. Georgiev, S. Tcholakova, N. Denkov, M. Grandl and F. Achenbach, *Colloids and Surfaces A: Physicochemical and Engineering Aspects*, 2021, **610**, 125747.
- (59) K. Ullmann, L. Poggemann, H. Nirschl and G. Leneweit, *Colloid and Polymer Science*, 2020, **298**, 407–417.
- (60) C. Frese, S. Ruppert, M. Sugár, H. Schmidt-Lewerkühne, K. Wittern, V. Fainerman, R. Eggers and R. Miller, *Journal of Colloid and Interface Science*, 2003, **267**, 475–482.
- (61) O. O. Mykhaylyk, in *Neutrons, X-rays, and Light*, ed. P. Lindner and J. Oberdisse, Elsevier, Amsterdam, Netherlands, 2nd edn., 2025, ch. 2, pp. 19–59.
- (62) J. S. Pedersen, *Advances in Colloid and Interface Science*, 1997, **70**, 171–210.
- (63) G. Fournet, *Bull. Soc. Fr. Mineral. Cristallogr.*, 1951, **74**, 39–113.
- (64) G. Hattori, M. Takenaka, M. Sawamoto and T. Terashima, *Journal of the American Chemical Society*, 2018, **140**, 8376–8379.
- (65) J. S. Pedersen, I. W. Hamley, C. Y. Ryu and T. P. Lodge, *Macromolecules*, 2000, **33**, 542–550.
- (66) A. Guinier and G. Fournet, *Small-angle Scattering of X-rays*, Wiley, Hoboken, NJ, USA, 1955.

- (67) J. W. Strutt, *Proc. R. Soc. Lond.*, 1910, **84**, 25–46.
- (68) M. Tanaka, G. Girard, R. Davis, A. Peuto and N. Bignell, *Metrologia*, 2001, **38**, 301.
- (69) J. S. Pedersen and M. C. Gerstenberg, *Macromolecules*, 1996, **29**, 1363–1365.
- (70) P. Debye, *The Journal of Physical and Colloid Chemistry*, 1947, **51**, 18–32.
- (71) B. Hammouda, *Journal of Polymer Science Part B: Polymer Physics*, 1992, **30**, 1387–1390.
- (72) P.-G. de Gennes, *Scaling concepts in polymer physics*, Cornell University Press, Ithaca, NY, USA, 1979.
- (73) T. Kawata, A. Hashidzume and T. Sato, *Macromolecules*, 2007, **40**, 1174–1180.
- (74) Y. Morishima, S. Nomura, T. Ikeda, M. Seki and M. Kamachi, *Macromolecules*, 1995, **28**, 2874–2881.
- (75) V. P. Privalko and Y. S. L. and, *Journal of Macromolecular Science, Part B*, 1974, **9**, 551–564.
- (76) T. G. Fox, *Bull. Am. Phys. Soc.*, 1956, **1**, 1236.
- (77) S. W. An, T. J. Su, R. K. Thomas, F. L. Baines, N. C. Billingham, S. P. Armes and J. Penfold, *The Journal of Physical Chemistry B*, 1998, **102**, 387–393.
- (78) T. J. Neal, R. E. Stone, C. György, S. B. Tzokov, S. G. Spain and O. O. Mykhaylyk, *Macromolecular Rapid Communications*, 2025, **46**, 2400898.

Chapter 4

Applicability of the Kratky-Porod Worm-like Chain Model to Statistical Copolymers



4.1 Introduction

Polyelectrolytes are polymers containing charged groups along their backbones. Most linear polyelectrolytes are soluble in aqueous media. These materials have been considered significant in various fields, including water treatment,^{1,2} drug delivery,^{3,4} colloidal stabilisation,^{5,6} battery electrolytes,^{7,8} and biological processes.^{9,10} Despite their broad applications, the understanding of polyelectrolyte behaviour remains incomplete. The presence of charged groups confers physicochemical properties that differ from those of neutral polymers.^{11,12} As a result, the characterisation of aqueous polyelectrolyte solutions remains one of the most challenging subjects in soft matter and biological systems.

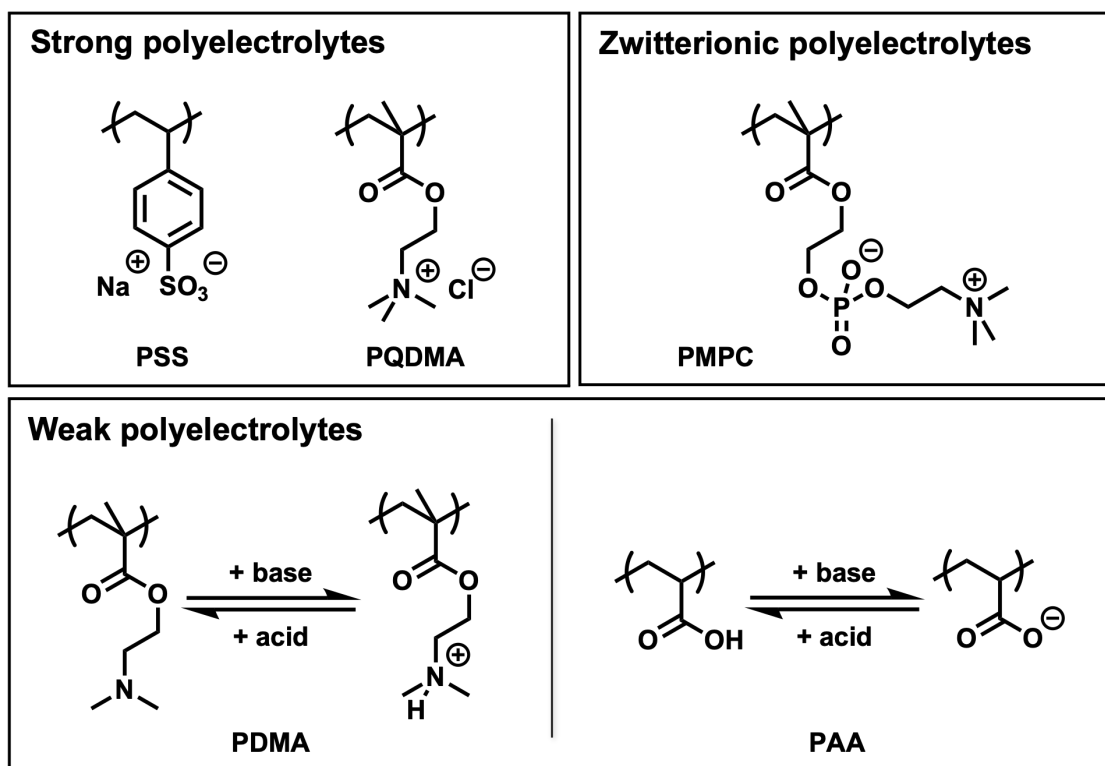


Figure 4.1: Representative chemical structures of polyelectrolytes exhibiting distinct charge regulation mechanisms, including strong polyelectrolytes (anionic PSS and cationic PQDMA), zwitterionic polyelectrolyte (PMPC), and weak polyelectrolytes (PDMA and PAA).

Polyelectrolytes can be classified as either strong or weak, depending on the protonation or ionisation characteristics of their charged groups (Figure 4.1).^{11,13} Strong polyelectrolytes possess

ionic groups that remain charged over a wide pH range.^{11,14} For example, sodium polystyrene sulfonate (PSS) contains sulfonate groups that are permanently negatively charged, independent of pH. Similarly, poly([2-(methacryloyloxy)ethyl] trimethylammonium chloride) (PQDMA) is classified as a strong cationic polyelectrolyte bearing quaternary ammonium groups that retain positive charges across all pH levels. Poly(2-methacryloyloxyethyl phosphorylcholine) (PMPC) is zwitterionic, containing both quaternary ammonium and phosphate groups within the same repeat unit. Although it belongs to the class of polyelectrolyte, the opposite charges result in an overall neutral state.^{15,16} In contrast, weak polyelectrolytes exhibit pH-dependent charge densities due to the reversible protonation or ionisation of their functional groups.^{11,13} Poly(2-(dimethylamino)ethyl methacrylate) (PDMA) is protonated at its tertiary amine groups under acidic conditions. Polyacrylic acid (PAA) acquires negative charges at high pH as a result of the ionisation of the carboxylic acid groups.

The conformation of polyelectrolyte chains is determined by various complex interactions, including electrostatic interactions,¹⁴ hydrogen bonding,¹⁷ polymer-solvent interactions,¹⁸ excluded volume effects,^{19–21} and covalent chain connectivity.²² These interactions have substantial influence on the flexibility of polyelectrolyte chains, thereby affecting their physical and biochemical properties. In general, charged polyelectrolyte backbones are observed to be less flexible than their neutral analogues due to intra-chain electrostatic repulsion, which leads to expanded chain conformations in dilute solution.^{14,23} Electrostatic interactions are typically dominant, and the strength of such interactions may be modulated by adjusting salt concentration and pH. For example, the addition of salt is known to screen long-range electrostatic repulsion, which results in chain contraction and decreased stiffness.^{24,25} In addition, pH affects the charge density of weak polyelectrolytes, thereby affecting their chain conformation.²⁶

Understanding the structural characteristics of polyelectrolytes, particularly the relationship between chain conformations, charge distribution, and ionic strength, remains a complex challenge. Extensive investigations have been carried out over several decades using experimental methods,^{27,28} theoretical models,^{29,30} and computer simulations.^{31,32} Small-angle scattering

(SAS) techniques (neutron, X-ray and light) are commonly employed to study polymer chain conformation.^{33–35} However, the relatively low X-ray scattering contrast of synthetic polyelectrolytes limits the image resolution obtained from SAXS experiments.³⁶ Moreover, preparation of near-monodisperse polyelectrolytes that are suitable for SAS experiments remains non-trivial. Consequently, theoretical modelling has become an essential tool for investigating polyelectrolyte behaviour in solution.

The worm-like chain (WLC) model, also referred to as the Kratky-Porod model, is widely used to describe the behaviour of semi-flexible polymers.³⁷ This model includes two primary parameters: the contour length L and the Kuhn length b . The contour length defines the fully extended length of the polymer chain, whereas the Kuhn length represents the distance over which the tangent vectors remain directionally correlated, reflecting chain stiffness. The WLC form factor $P(q)$ can be fitted to SAS data to extract values for L , b , and the cross-sectional radius r . This model has been successfully applied to synthetic semi-flexible polymers, including liquid crystalline and conjugated systems.^{38–40} It has been shown to predict chain conformation and its response to stimuli, which is helpful in clarifying the relationship between molecular structure and properties. Weakly charged polymers are expected to exhibit semi-flexible behaviour due to electrostatically induced chain stiffening. Therefore, the WLC model is considered suitable for describing polyelectrolytes. For example, Murnen et al. investigated the conformations of synthetic polypeptide chains with various ionisable repeat units using small-angle neutron scattering (SANS), and showed that the persistence length decreased progressively with increasing salt concentration.⁴¹

When applying the WLC model to polyelectrolytes, it is necessary to minimise strong interactions between chain segments, such as hydrophobic interactions or strong electrostatic repulsions. Such interactions can result in deviations between experimental data and theoretical predictions based on the WLC model. In addition, intermolecular electrostatic interactions may introduce a structure factor contribution into SAS pattern, thereby complicating data analysis. Two important structural parameters that are not directly covered by the WLC model,

namely the radius of gyration (R_g) and the end-to-end distance (R_{ee}).^{42,43} The former can be obtained experimentally by SAS, while the latter requires theoretical derivation or computer simulation.⁴⁴ Recent studies have achieved notable progress in measuring R_{ee} using double electron-electron resonance (DEER) spectroscopy. These two parameters are essential for a comprehensive description of polymer chain conformation and solution behaviour.⁴⁵

In WLC model, when the Kuhn length exceeds the contour length, semi-flexible chains adopt rigid rod-like conformations. In this case, the end-to-end distance is approximately equal to the copolymer contour length. This behaviour is typically observed for semi-flexible polymers with relatively low molecular weights. For longer chains, more flexible coil conformations are adopted with an intrinsic chain stiffness, resulting in the following Equation (4.1) that links R_{ee} and L using l_p :⁴⁶

$$R_{ee}^2 = 2Ll_p \left[1 - \frac{l_p}{L} \left(1 - e^{-L/l_p} \right) \right] \quad (4.1)$$

where the square end-to-end distance R_{ee}^2 is equivalent to $6R_g^2$ for a Gaussian copolymer coil when the chain length tends to infinity. Note that this expression neglects excluded volume effects. Although the physical properties of synthetic ionisable water-soluble copolymers have been extensively examined in aqueous solution, the influence of charge on chain conformation remains poorly understood. Furthermore, the combined use of scattering techniques, structural analysis, and theoretical modelling to systematically investigate such systems has remained limited. Pedersen et al. performed a series of Monte Carlo simulations to explore the properties of worm-like chains, thereby providing a theoretical framework.^{20,47–49}

In the present work, the effects of protonation, polymer concentration, salt concentration and comonomer composition on the conformation of cationic amphiphilic copolymers in aqueous solution were systematically investigated. A series of methacrylic statistical copolymers was synthesised via RAFT polymerisation to yield well-defined architectures spanning a controlled range of comonomer ratios with narrow MWDs. SAXS measurements were performed in dilute aqueous solution to assess how electrostatic repulsion modulates chain expansion at

varying degrees of protonation. Uncharged copolymer coils were analysed using worm-like chain (WLC) models to extract chain flexibility parameters, whereas data for charged chains were interpreted using structure factor analyses based on mean spherical approximation (MSA) or the polymer reference interaction site model (PRISM).^{50–52} To assess the generality of these observations, an additional set of polydisperse analogues was synthesised via free radical polymerisation (FRP).

For the controlled protonation series, the copolymer composition and degree of polymerisation were held constant, ensuring that all observed conformational changes arose primarily from variations in charge density induced by pH or salt concentration. The resulting modulation of intrachain electrostatic repulsion enabled reversible tuning of chain stiffness. This well-defined design provides an ideal platform for elucidating the mechanisms underlying flexibility changes in statistical copolymers and for assessing the suitability of the WLC framework for determining chain flexibility parameters such as the Kuhn length, b . In contrast to DSC, which measures global thermal transitions such as the glass transition temperature (T_g), T_g only reflects chain flexibility at a macroscopic level.^{53,54} It does not offer the spatial resolution needed to distinguish whether changes arise from the backbone or the side chains. As a result, T_g is sometimes unreliable indicator of molecular level flexibility in statistical copolymers. By comparison, the Kuhn length extracted from WLC analysis offers a direct, molecular scale descriptor of chain stiffness. On the basis of experimentally confirming that the WLC model is applicable to statistical copolymers, this study then investigates how the Kuhn length can be used to characterise chain flexibility in such systems. These measurements allow a more detailed understanding of copolymer conformational behaviour in aqueous solution and thereby inform the rational design of statistical copolymer surfactants. Furthermore, the intrinsic polyelectrolyte character of this model copolymer enables parallel evaluation of the applicability of the WLC model to polyelectrolyte systems.

4.2 Experimental

4.2.1 Materials

2-(Dimethylamino)ethyl methacrylate (DMA, 98%) and poly(ethylene glycol) methyl ether methacrylate (PEGMA, avg. $M_n = 300 \text{ g}\cdot\text{mol}^{-1}$) were purchased from Sigma-Aldrich (Gillingham, UK) and filtered through basic aluminium oxide (Al_2O_3) to remove the inhibitor prior to use. Azobisisobutyronitrile (AIBN) was purchased from Molekula (UK) and used as received. 2-Cyano-2-propyl benzodithioate (CPDB, 97%), iodomethane (99%), *n*-hexane ($\geq 99\%$), diethyl ether ($\geq 99.8\%$) hydrochloric acid solution (0.1 M), sodium hydroxide solution (0.1 M), potassium chloride, sodium nitrate and sodium azide were purchased from Sigma-Aldrich (UK) and used as received. Ethanol ($\geq 99.8\%$) and sodium hydrogen carbonate were purchased from Fisher Scientific (Loughborough, UK) and used as received. HPLC-grade dimethylformamide (DMF) and technical grade triethylamine (TEA) were purchased from VWR Chemicals (Lutterworth, UK). Deionised water was obtained using an Elga PURELAB Option water purification system.

4.2.2 Synthesis and Reaction Protocols

The quantities of reagents used in the synthesis of the copolymers are summarised in Appendix 4.5.1.

Synthesis of P(DMA-*stat*-PEGMA) Statistical Copolymer by RAFT Copolymerisation in Ethanol

The following procedure is representative. Stock solutions of AIBN, CPDB, PEGMA and DMA were first prepared at accurately known concentrations. The required volumes of each stock solution were then transferred into a 28 mL glass vial using micropipettes to obtain

copolymer feeds with [DMA]/[PEGMA] molar ratios of 0.11 (1:9), 0.25 (2:8), 0.43 (3:7) and 0.67 (4:6), respectively, while targeting an overall copolymer DP of 250. The precise masses of the corresponding reagents for each formulation are provided in Appendix 4.5.1. Ethanol was added to the mixture to make up a 20% w/w solution. The solution was vortex-mixed for 30 s to produce a homogeneous mixture and then sealed using a rubber septum after the addition of a magnetic stir bar. The solution was degassed with the aid of an ice bath using a stream of nitrogen gas for 30 min and then immersed in an oil bath set at 70 °C with continuous stirring under nitrogen for 3 h. The copolymerisation was quenched by exposing the reaction mixture to air while cooling to 20 °C. The crude copolymer was purified by precipitation from ethanol into excess cold *n*-hexane three times to remove any unreacted comonomer and residual initiator before being dried under vacuum at 40 °C overnight. The overall comonomer conversion and composition were determined by ¹H NMR spectroscopy. Molecular weight data were obtained by DMF GPC and online MALLS analysis in aqueous solution.

Synthesis of P(DMA-*stat*-PEGMA) Statistical Copolymer by Free Radical Copolymerisation in Ethanol

The following example is representative. AIBN initiator (13.6 mg, 0.0828 mmol) was weighed into a 250 mL round-bottom flask, followed by PEGMA (12.0000 g, 40.0 mmol) and DMA (1.5721 g, 10.0 mmol) to give a [DMA]/[PEGMA] molar ratio of 0.25 (i.e. 1:4). Ethanol (136.0 g) was added to the mixture to make up a 10% w/w solution. After the adding a magnetic stir bar, the solution was sealed using a rubber septum. The solution was degassed in an ice bath using a stream of nitrogen gas for 1 h and then immersed in an oil bath set at 70 °C and stirred continuously under nitrogen for 24 h. The crude copolymer was dried at 40 °C under vacuum overnight. The overall comonomer conversion and composition were determined by ¹H NMR spectroscopy. Molecular weight data were obtained by DMF GPC and online MALLS analysis in aqueous solution.

Quaternisation of P(DMA-*stat*-PEGMA) Statistical Copolymer

P(DMA-*stat*-PEGMA) statistical copolymer (0.5000 g) was weighed into a 14 mL glass vial, followed by methanol (2.0 g) to make up a 20% w/w solution. Iodomethane (24 μ L) was then added to this copolymer solution, which was stirred at 50 °C in air for 24 h. The product was washed twice with diethyl ether and then dried under vacuum overnight at 40 °C.

4.2.3 Characterisation Methods

Acid-Base Titration

Acid-base titration was performed manually using an M114-SC pH probe supplied by Malvern Instruments (Malvern, UK). A 5.0 mL aliquot of 1.0% w/v aqueous copolymer solution was placed in a 14 mL glass vial and stirred with a magnetic stir bar. A standard solution of 0.1 M HCl or NaOH was added dropwise in 20 μ L increments to the solution. The total volume of added solution and the corresponding solution pH were recorded over the range from the initial pH to pH 2 and pH 11, respectively.

^1H NMR spectroscopy

^1H NMR spectra were recorded in CDCl_3 at 25 °C using Bruker Avance 400 MHz spectrometer with 64 scans averaged per spectrum.

Gel Permeation Chromatography (GPC) with DMF Eluent

Molecular weight data were obtained using an Agilent 1260 Infinity GPC system, which included a pump, degasser, and two PL-gel 5 μ m Mixed-C columns connected in series, equipped with both UV and refractive index detectors. HPLC-grade DMF containing 0.02% w/w LiBr was used as the eluent. The column and detector temperatures were set to 60 °C, and the flow rate was 1.0 mL \cdot min $^{-1}$. Near-monodisperse poly(methyl methacrylate) standards ranging from 370 to 2,520,000 g \cdot mol $^{-1}$ were employed for calibration, with data analysed using Agilent Technologies GPC/SEC software.

Gel Permeation Chromatography - Multi-Angle Laser Light Scattering (GPC-MALLS) with Aqueous Eluent

A DAWN HELEOS II multi-angle laser light scattering instrument (Wyatt Technology Corp., USA) was used to determine absolute weight-average molecular weights ($M_{w,abs}$) and radii of gyration (R_g). The system featured a 130 mW linearly polarised gallium arsenide laser ($\lambda = 658$ nm) and 18 detectors positioned at fixed angles from 22.5° to 147° . The instrument was operated in online mode and connected in series to an Agilent 1260 Infinity GPC system, which included a pump, a degasser, two PL-Aquagel Mixed-H columns, and an Optilab T-rEX differential refractometer (Wyatt Technology Corp., USA) serving as a concentration detector. The eluent was an aqueous solution containing 0.10 M NaNO_3 , 0.02 M TEA, and 0.05 M NaHCO_3 at pH 10. The column and detector temperatures were maintained at 35°C , with a flow rate of $0.5\text{ mL}\cdot\text{min}^{-1}$. MALLS normalisation coefficients and the delay volume between the light scattering and refractive index detectors were determined using a near-monodisperse poly(ethylene glycol) standard ($M_p = 6,000\text{ g}\cdot\text{mol}^{-1}$) dissolved in the same aqueous eluent. Polymer samples were dissolved in this eluent at a relatively high concentration ($\sim 10\text{ g}\cdot\text{dm}^{-3}$) and injected using an autosampler. Data were analysed using Astra 7 (Wyatt Technology Corp., USA) software according to the Zimm formalism (4.2):⁵⁵

$$\frac{K^*c}{R_\theta} = \frac{1}{M_w P_\theta} + 2A_2c \quad (4.2)$$

where K^* is the specific optical constant for the instrument, wavelength, copolymer sample and solvent; c is the copolymer concentration; R_θ is the Rayleigh ratio corresponding to the ratio of scattered light intensity to the incident light; A_2 is the second virial coefficient (which is negligible when $c \rightarrow 0$ in dilute solution); and P_θ is the form factor.

Differential Refractive Index (dRI)

Refractive index increments (dn/dc) for various copolymers dissolved in the aqueous GPC eluent were determined using an Optilab T-rEX differential refractometer (Wyatt Technology

Corp., USA) operated in batch mode. A series of dilute copolymer solutions with concentrations ranging from 0.5 to 5.0 g·dm⁻³ were injected sequentially, starting from the lowest concentration, using a syringe pump at the same flow rate employed in the online mode experiments. The dn/dc values were obtained from the slope of a linear calibration plot of refractive index versus copolymer concentration. These dn/dc data were subsequently used to calculate copolymer concentrations in the online mode measurements.

Small-Angle X-Ray Scattering (SAXS)

SAXS patterns were recorded using a Xeuss 2.0 laboratory SAXS instrument (Xenocs, Grenoble, France) and at an international synchrotron facility (I22 station, Diamond Light Source, Oxfordshire).⁵⁶ The former instrument was equipped with an Excillum liquid gallium MetalJet X-Ray source ($\lambda = 1.34 \text{ \AA}$) (Krista, Sweden) and a 2D Pilatus 1M pixel detector from Dectris (Baden-Daettwil, Switzerland). Samples were analysed using a sealed flow-through borosilicate glass capillary of approximately 2 mm diameter from Capillary Tube Supplies Ltd (Cornwall, UK). Patterns were recorded at a camera length of 1.2 m, which corresponds to a scattering vector range of 0.01 - 0.30 \AA^{-1} . The resulting 2D X-Ray scattering patterns collected from Xeuss 2.0 were masked and reduced to 1D curves using XSACT software provided by Xenocs. For the synchrotron experiments performed at Diamond, background subtraction and data re-binning were performed using SAXSutilities2 software (version 1.255). Further fitting and modelling were carried out using either SASView (version 6.0.0)⁵⁷ or WLSQSAXS Least Squares Nonlinear Fit SuperSAXS Programs (Version May 2019) developed by Pedersen and Oliveira.⁵⁸ Deionised water was used for the absolute intensity calibration of all SAXS patterns.

Dynamic Light Scattering (DLS)

Measurements were conducted using a Malvern Zetasizer NanoZS instrument fitted with a 4 mW He-Ne laser ($\lambda = 633 \text{ nm}$) and an avalanche photodiode detector. The instrument was set to automatically determine both the measurement duration and optical attenuation. Each copolymer was diluted to 1.0% w/w using deionised water and subsequently passed through

a 0.20 μm filter. An aqueous solution of 0.1 M HCl was added to the solution to adjust the solution pH and thereby control the degree of protonation of the pendent tertiary amine groups on the copolymer chains. Backscattered light was detected at 173° and all measurements were conducted at 25°C using a 10 mm path length quartz cuvette. Zetasizer software (Version 7.11, Malvern Instruments Ltd.) was used to calculate the hydrodynamic diameter (D_h) using the Stokes-Einstein equation, which assumes perfectly monodisperse, non-interacting spherical particles.⁵⁹

Phase-Analysis Light scattering (PALS)

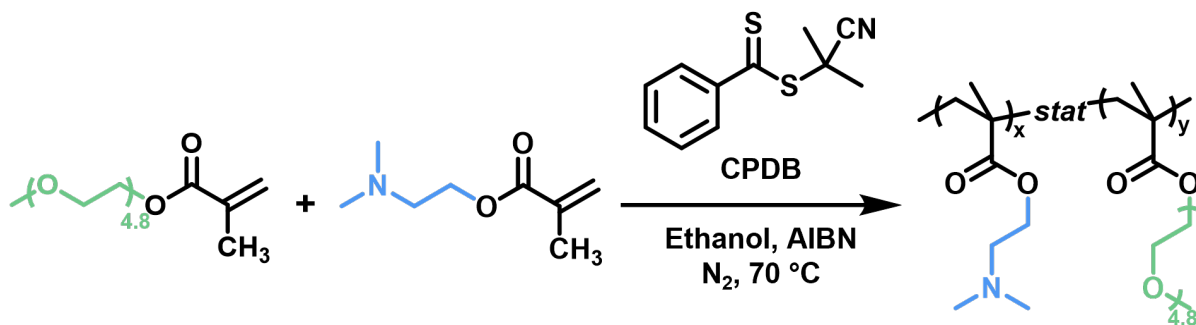
Electrophoretic mobilities were determined by PALS measurements using a Malvern ZetaSizer Nano ZS with a universal dip cell electrode at 25°C . Measurements were performed at a copolymer concentration of 1.0% w/w concentration and five runs comprising between 50 and 200 measurements each, depending on the scattered light intensity. Data were analysed using Zetasizer software (Version 7.11, Malvern Instruments Ltd.)

Transmission Electron Microscopy (TEM)

Aqueous dispersions of statistical copolymer nanoparticles were diluted to 1.0% by weight. Copper-palladium TEM grids were surface-coated with a thin carbon film before being plasma glow-discharged for 30 seconds to produce a hydrophilic surface. An 11 μL droplet of a dilute aqueous nanoparticle dispersion was deposited onto the surface of each TEM grid for 3 minutes before blotting with filter paper to remove excess liquid. An 11 μL droplet of a 0.75% w/v aqueous uranyl formate solution was then applied as a negative stain for 25 s prior to careful blotting and drying using a vacuum hose. Imaging was performed at 80 kV using a FEI Tecnai G2 spirit instrument equipped with a Gatan 1k CCD camera.

4.3 Results and Discussion

4.3.1 Synthesis and Characterisation



Scheme 4.1: Synthesis of P(DMA-*stat*-PEGMA) statistical copolymers by RAFT copolymerisation in ethanol, using CPDB as the RAFT agent and AIBN as the initiator to produce a series of water-soluble copolymers with tuneable degrees of protonation.

A series of P(DMA-*stat*-PEGMA) copolymers with different comonomer compositions and molecular weights were synthesised in ethanol by RAFT copolymerisation (Scheme 4.1). CPDB was used as the chain transfer agent and AIBN was used as the initiator. The [CPDB]/[AIBN] molar ratio was maintained at 4.0 in all copolymerisations to achieve efficient chain transfer.⁶⁰ RAFT polymerisation enabled the synthesis of copolymers with narrow molecular weight distributions and precisely controlled target molecular weights.^{60–62} The resulting copolymers were purified by precipitation into *n*-hexane to remove unreacted comonomers and were dried under vacuum at 40 °C. The residual comonomer content was less than 0.5% in all cases as determined by ¹H NMR spectroscopy. The final copolymers were viscous pink liquids, with the colour resulting from the dithiobenzoate chain-ends. GPC analysis (DMF eluent) indicated relatively narrow molecular weight distributions, with copolymer dispersities ranging from 1.26 to 1.35. All copolymers had absolute weight-average molecular weights ($M_{w,abs}$) between 20 and 45 kDa, as determined using a MALLS coupled with a differential refractometer (Table 4.1).

Table 4.1: Summary of comonomer conversions, compositions, and molecular weights for two series of P(DMA-*stat*-PEGMA) statistical copolymers.

Sample ID	¹ H NMR ^a			DMF GPC ^b		Aqueous MALLS ^c	
	DMA / mol%	Conversion	DP	M_w / g·mol ⁻¹	\bar{D}	$M_{w,abs}$ / g·mol ⁻¹	dn/dc / mL·g ⁻¹
PD9010:150	10	63%	158	37,300	1.35	44,000	0.1235
PD8020:150	21	57%	143	34,100	1.35	41,300	0.1266
PD7030:150	29	59%	148	34,300	1.34	37,800	0.1294
PD6040:150	38	61%	153	31,800	1.33	36,900	0.1330
PD9010:75	11	60%	75	21,500	1.27	24,300	N/A
PD8020:75	20	61%	76	20,000	1.26	22,600	
PD7030:75	30	64%	80	19,500	1.27	21,400	
PD6040:75	42	62%	78	18,800	1.27	19,600	

^a Copolymer composition, conversion and DP were determined by ¹H NMR spectroscopy in CDCl₃.

^b Weight-average molecular weights (M_w) and dispersities (\bar{D}) obtained by GPC analysis in DMF containing 0.02% w/w LiBr.

^c Absolute weight-average molecular weights ($M_{w,abs}$) and refractive index increment (dn/dc) values determined by MALLS and dRI analysis using aqueous eluent (pH 10) comprising 0.10 M NaNO₃, 0.02 M TEA, 0.05 M NaHCO₃, and 0.02% w/w NaN₃.

4.3.2 Kinetics and Randomness Evaluation

The distribution of comonomers strongly affects the structure and properties of copolymers.⁵³ Statistical control during copolymerisation allows the preparation of random copolymers, although perfectly random sequences are uncommon. In practice, sequences enriched in one comonomer often tend to arise. The reactivity ratios of the comonomers can be used to predict deviations in the copolymer composition from the initial monomer feed ratio.

DMA and PEGMA comonomers were added at molar feed ratios of 10:90, 20:80, 30:70 and 40:60 (Table 4.1.) ¹H NMR analysis of the final copolymers suggested that the DMA content approximated the feed ratio. However, the mean copolymer composition does not reveal the comonomer distribution along the copolymer chains. This was assessed by monitoring the individual monomer conversion kinetics during RAFT copolymerisation using ¹H NMR spectroscopy (see Figure 4.2).

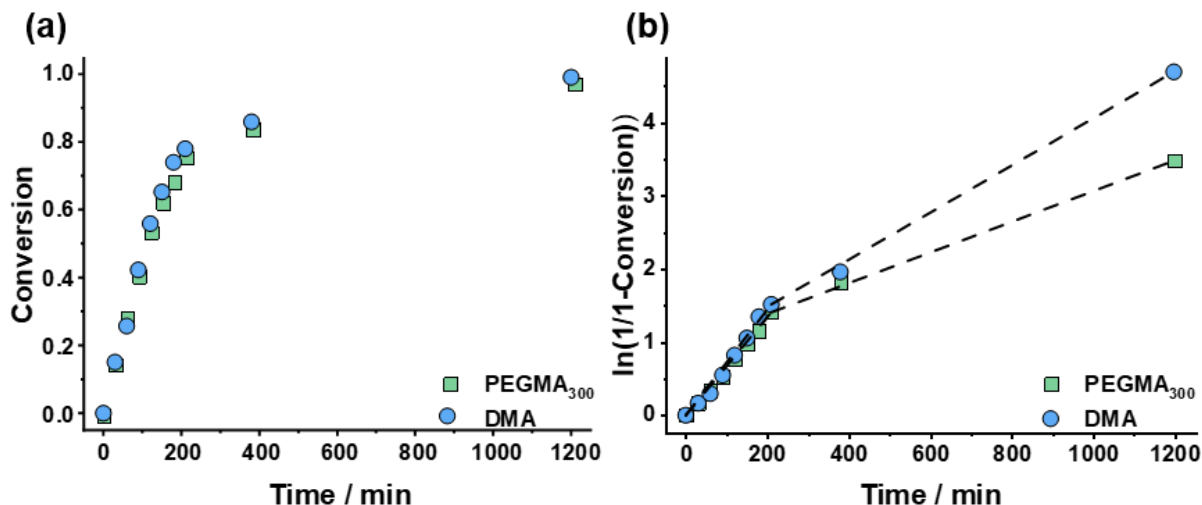


Figure 4.2: (a) Comonomer conversion as a function of time for the RAFT copolymerisation of DMA with PEGMA (target DP = 250; target DMA content = 20 mol%) conducted at 70 °C, as determined by ^1H NMR spectroscopy. (b) Pseudo-first order kinetic plots.

In the kinetics experiment, the comonomer feed ratio was $[\text{DMA}]:[\text{PEGMA}] = 0.25$ (*i.e.* 1:4). The reaction mixture was periodically sampled to monitor the copolymerisation kinetics using ^1H NMR spectroscopy and DMF GPC. The resulting comonomer conversion versus time plot indicated similar conversion profiles for both comonomers, with the instantaneous DMA conversion being slightly higher than that of PEGMA (see Figure 4.2a). Comparable initial polymerisation rates were observed: $k_{\text{obs, DMA}} = 0.0076 \text{ s}^{-1}$ and $k_{\text{obs, PEGMA}} = 0.0067 \text{ s}^{-1}$. After 200 min, both rates decreased to $k_{\text{obs, DMA}} = 0.0033 \text{ s}^{-1}$ and $k_{\text{obs, PEGMA}} = 0.0021 \text{ s}^{-1}$ (see Figure 4.2b). These data indicate that under the applied conditions, DMA was consumed faster than PEGMA, consistent with previous reports.^{63,64}

Targeting higher comonomer conversions resulted in broader molecular weight distributions and increased dispersities, as determined by DMF GPC analysis (Figure 4.3). In the GPC trace of the product obtained after 20 h of reaction, the molecular weight of the peak (M_p) corresponding to the shoulder ($22,700 \text{ g}\cdot\text{mol}^{-1}$) was slightly less than twice that of the main peak ($40,500 \text{ g}\cdot\text{mol}^{-1}$). This observation was attributed to premature termination via combination and chain transfer to polymer.⁶⁵ Relatively low dispersities were maintained by limiting reaction times to a maximum of 4 h. Low dispersities were desirable for precise measurement of the R_g by SAXS.

Hence, all RAFT copolymerisations were quenched after 4 h to obtain relatively well-defined copolymers (Table 4.1).

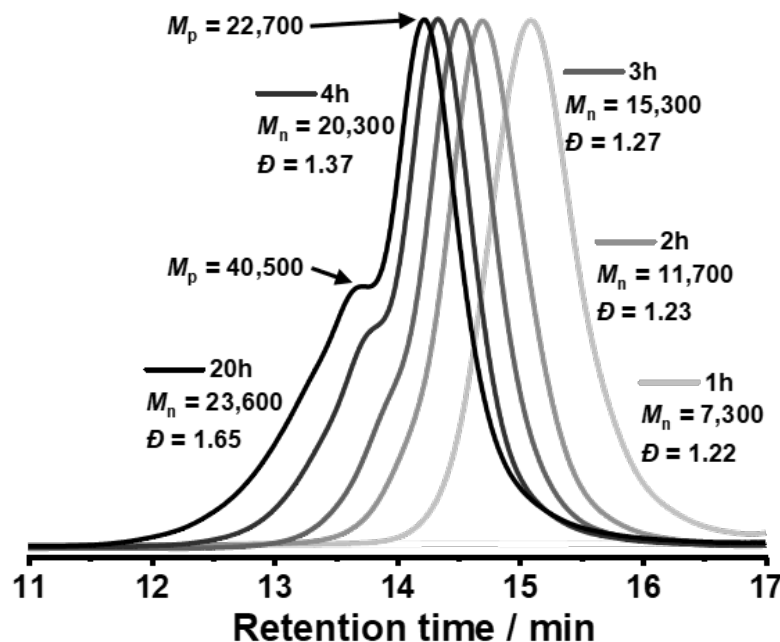


Figure 4.3: DMF GPC traces obtained during the RAFT copolymerisation of DMA with PEGMA, showing the evolution of M_n and \bar{D} overtime (target DP = 250; target DMA content = 20 mol%) conducted at 70 °C.

The comonomer reactivity ratios for DMA and PEGMA ($r_{1,\text{DMA}}$ and $r_{2,\text{PEGMA}}$) were determined. Several methods have been developed for such analyses, including linear methods (Fineman-Ross and Kelen-Tüdös)^{66,67} and a non-linear method (Mayo-Lewis and Meyer-Lowry).^{68,69} These methods are typically based on copolymer composition data at relatively low comonomer conversions (i.e. below 25%). However, the extended Kelen-Tüdös method allows determination of reactivity ratios at overall conversions of up to 85%.^{63,70} Figure 4.4 presents the plot generated using the extended Kelen-Tüdös method. A linear dependence of η on ξ was observed, with a correlation coefficient (R^2) of 0.9913, where η and ξ are dimensionless normalisation parameters defined within the method (see Table 4.2). Reactivity ratios were obtained by linear regression: $r_{1,\text{DMA}} = 0.88$ and $r_{2,\text{PEGMA}} = 0.83$. Given that $r_{1,\text{DMA}} > r_{2,\text{PEGMA}}$, slightly preferential incorporation of DMA is expected at the early stages of polymerisation. However,

this mild preference is gradually offset at higher comonomer conversions due to the faster consumption of DMA in the reaction mixture. This minor reactivity difference is insufficient to promote block formation, and the resulting P(DMA-*stat*-PEGMA) copolymers are consistent with a near random distribution.

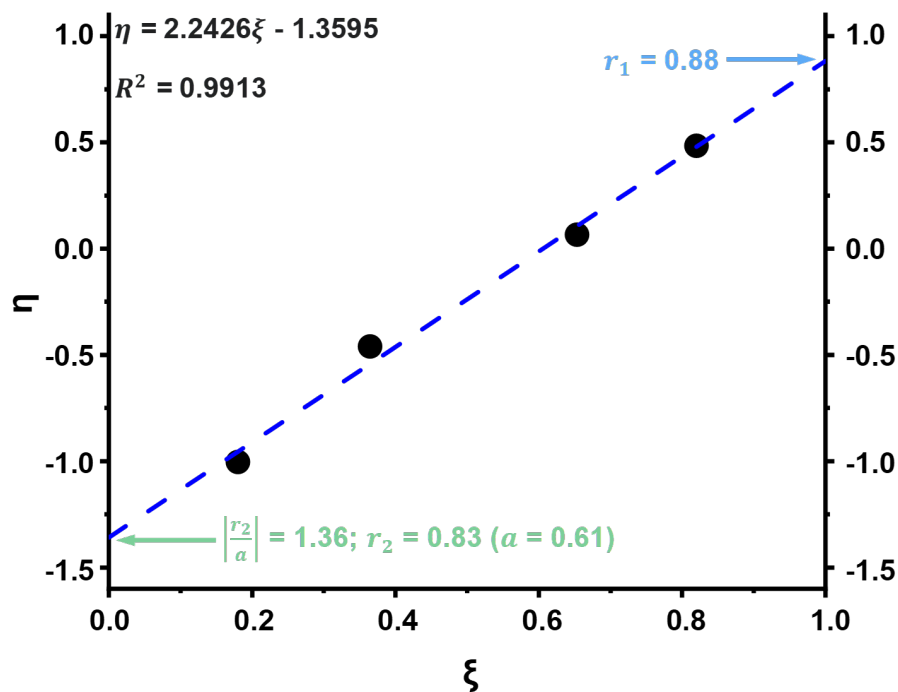


Figure 4.4: Corresponding comonomer reactivity ratio plot ($\alpha = 0.61$), calculated using the Kelen-Tüdös method. α is the normalisation factor as calculated in Table 4.2 The reactivity ratios were $r_{1,\text{DMA}} = 0.88$ and $r_{2,\text{PEGMA}} = 0.83$, indicating comparable reactivity between the two comonomers.

In the reactivity ratio calculation using the extended Kelen-Tüdös method, it is assumed that the reactivity of a growing chain in RAFT copolymerisation depends on the growing chain end only.⁷⁰ The monomer consumption rates of two comonomers are therefore given by:

$$\text{Monomer 1: } -\frac{d[M_1]}{dt} = k_{11}[M_1][M_1] + k_{21}[M_2][M_1] \quad (4.3)$$

$$\text{Monomer 2: } -\frac{d[M_2]}{dt} = k_{22}[M_2][M_2] + k_{12}[M_1][M_2] \quad (4.4)$$

where $[M_a]$ is the concentration of the monomer and k_{ab} is the propagation rate constant of

monomer 'b' being polymerised onto the growing polymer chain with 'a' as the active chain end.

When the instantaneous reaction rates $\frac{d[M_1]}{dt}$ and $\frac{d[M_2]}{dt}$ approach zero, the reaction ratio is given by:

$$\frac{d[M_1]}{d[M_2]} = \frac{[M_1]}{[M_2]} \times \frac{r_1[M_1] + [M_2]}{[M_1] + r_2[M_2]} \quad (4.5)$$

where $r_1 = \frac{k_{11}}{k_{12}}$ and $r_2 = \frac{k_{22}}{k_{21}}$, respectively.

When $r_1 > 1$, monomer M_1 preferentially reacts with itself. When $r_1 < 1$, M_1 exhibits a greater tendency to react with M_2 . If $r_1 \times r_2 = 1$, the resulting copolymer is expected to exhibit an ideally random distribution of comonomer units.

To simplify Equation (4.5), let $x = \frac{[M_1]}{[M_2]}$ (monomer feed ratio), $y = \frac{d[M_1]}{d[M_2]}$ (copolymer composition), and $z = \frac{r_1[M_1] + [M_2]}{[M_1] + r_2[M_2]}$. Thus, Equation (4.5) may be rewritten as $y = x \times z$.

Considering the differences in monomer consumption rates and the changes in their initial and instantaneous concentrations, a correlation between z and monomer conversion can be established:

$$z = \frac{r_1[M_1] + [M_2]}{[M_1] + r_2[M_2]} = \frac{\log(1 - \zeta_1)}{\log(1 - \zeta_2)} \quad (4.6)$$

where ζ_1 and ζ_2 represent the molar conversion of M_1 and M_2 , respectively.

The differential Equation (4.5) can be linearised using the Kelen-Tüdös method:⁷⁰

$$\eta = \left(r_1 + \frac{r_2}{\alpha}\right) \xi - \frac{r_2}{\alpha} \quad (4.7)$$

where $\eta = \frac{G}{\alpha + F}$ and $\xi = \frac{F}{\alpha + F}$.

In the above Equation (4.7), F and G are concentration-related parameters:

$$F = \frac{\left(\frac{[M_1]}{[M_2]}\right)^2}{\frac{d[M_1]}{d[M_2]}} = \frac{x^2}{y} = \frac{y}{z^2} \quad (4.8)$$

$$G = \frac{\frac{[M_1]}{[M_2]}}{\frac{d[M_1]}{d[M_2]}} \left(\frac{d[M_1]}{d[M_2]} - 1 \right) = \frac{y - 1}{z} \quad (4.9)$$

Parameter α , which is used to normalise all the experimental data from 0 to 1, is calculated by:

$$\alpha = F_{\max} \cdot F_{\min} \quad (4.10)$$

where the two F values correspond to the highest and lowest values calculated from the above expression. An example calculation based on experimental data obtained during the synthesis of four representative P(DMA-*stat*-PEGMA) copolymers is summarised on the following page (Table 4.2):

Table 4.2: Summary of data and calculated parameters used to construct the η versus ξ correlation for determining comonomer reactivity ratios via the extended Kelen-Tüdös method.^{70 a}

DMA mol% in		Monomer conversion	x	y	ζ_1	ζ_2	z	\bar{x}^b	F	G	ξ	η
Monomer	Copolymer											
47.0%	47.3%	20.8%	1.1299	1.1130	0.2062	0.2094	0.9831	1.1321	1.1516	0.1149	0.6532	0.0652
27.3%	27.9%	24.9%	2.6667	2.5843	0.2472	0.2551	0.9643	2.6801	2.7794	1.6430	0.8197	0.4846
70.7%	67.5%	8.8%	0.4141	0.4819	0.0978	0.0840	1.1726	0.4110	0.3505	-0.4418	0.3644	-0.4594
86.7%	85.7%	37.4%	0.1533	0.1667	0.4019	0.3697	1.1134	0.1497	0.1344	-0.7484	0.1803	-1.0037

^a In this case, the normalisation factor α was calculated as $\alpha = \sqrt{F_{\max} \times F_{\min}} = \sqrt{2.7794 \times 0.1344} = 0.6113$.

^b \bar{x} is $\frac{y}{z}$.

4.3.3 pH-responsive Behaviour in Aqueous Solution

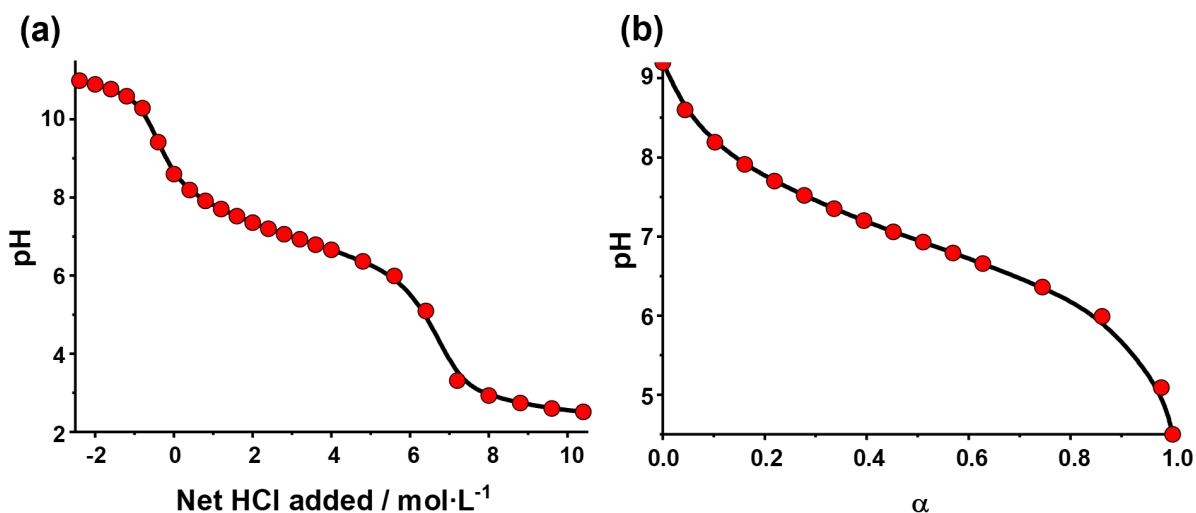


Figure 4.5: (a) Acid-base titration curve recorded for a 1.0% w/v aqueous solution of the PD8020:150 statistical copolymer. (b) Same titration data plotted against the mean degree of protonation, α .

The pH-responsive behaviour of these copolymers and their corresponding chain conformations were systematically investigated as a function of solution pH using acid titration, DLS, and zeta potential measurements. Acid titrations were conducted on aqueous copolymer solutions prepared using deionised water to examine the correlation between net acid addition, mean degree of protonation and solution pH. As described previously, the copolymer was dissolved in deionised water at 1.0% w/v, and the resulting solution was divided into two portions. These were titrated to pH 2 and pH 11 using 0.1 M HCl and KOH, respectively. Figure 4.5a presents the titration curves, where the x-axis represents the net amount of added HCl (negative values correspond to added KOH). A discernible buffer region was observed, indicating that the copolymer behaves as a weak base and is partially protonated within a specific pH range. At pH 9, the copolymer was fully deprotonated. Due to the presence of hydrophilic PEG units, these neutral chains remained water-soluble. At pH 4.5, the DMA repeat units were fully protonated. Figure 4.5b displays the same titration curve as in Figure 4.5a, with the x-axis replaced by the mean degree of protonation (α) of the DMA units. The pK_a of the copolymer was determined

to be between 6.9 and 7.0, which is slightly lower than that of PDMA homopolymer ($pK_a = 7.6$).⁷¹

DLS and TEM are commonly used techniques for the characterisation of nanoparticles. The former provides the hydrodynamic diameter (D_h) under the assumption that particles behave as perfectly non-interacting spheres.⁵⁹ TEM provides direct imaging but often suffers from limited statistical relevance and may not reflect the overall particle size distribution.⁷² Scattering techniques can be employed to investigate the nanoscale structure of polyelectrolyte chains. The resolution limit of MALLS (a.k.a. SLS), is normally considered to be 10 nm,⁷³ whereas the shorter wavelengths used in SAXS allow for the characterisation of smaller particles. Accordingly, copolymers were characterised using DLS, TEM, SAXS, and MALLS.

It is well established that weak polyelectrolytes tend to adopt more extended conformations in solution than their neutral forms, due to electrostatic repulsion between charged segments.^{14,23} Based on this principle, we predicted that increasing the degree of protonation would lead to an expansion of the model copolymer coils.

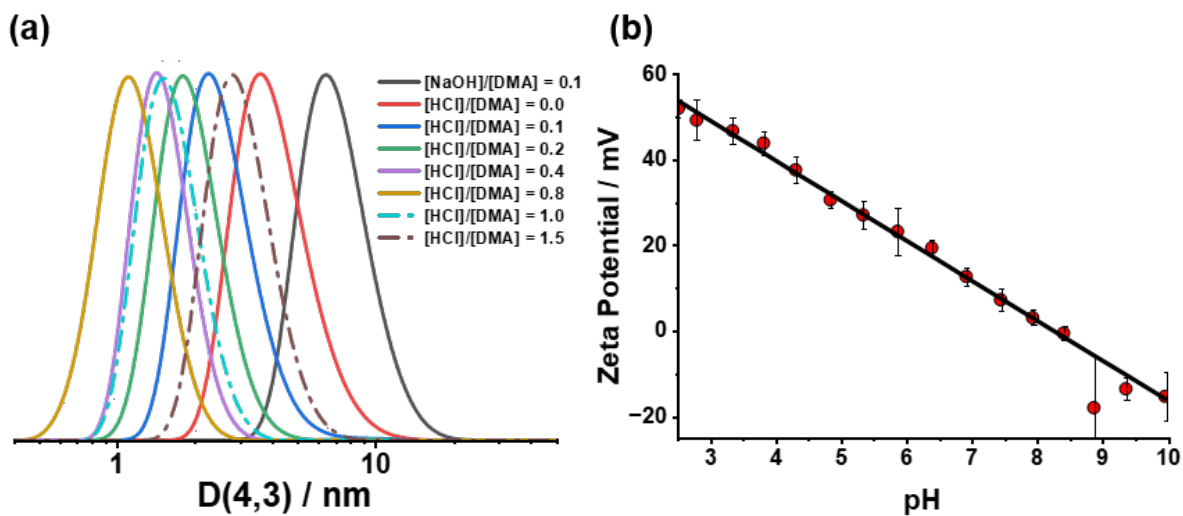


Figure 4.6: (a) Particle size distributions obtained by DLS at various acid addition conditions and (b) zeta potential as a function of pH for the PD8020:150 copolymer in aqueous solution (0.5% w/w).

Contrary to this expectation, DLS results showed a decrease in D_h with increasing acid concentration. Upon full protonation of the DMA units, further acid addition led to a slight increase

in size (Figure 4.6a). To investigate this unexpected trend, zeta potential data were examined. At approximately pH 8, the zeta potential approached zero (Figure 4.6b), indicating that the copolymers were nearly neutral under these conditions, which corresponded to the maximum D_h . This observation implies that neutral chains may form loose aggregates, which is a phenomenon well known for hydrophilic or amphiphilic copolymers in aqueous solutions.⁷⁴ As protonation progressed, increasing electrostatic repulsion likely disrupted these aggregates, resulting in smaller, fully solvated individual chains.⁷⁵ Although intrachain repulsion contributes to conformational expansion, the associated change in size was relatively minor compared to the reduction caused by aggregate dissociation. Therefore, the observed decrease in D_h is more plausibly attributed to the disassembly of neutral aggregates rather than coil expansion.

It should also be noted that DLS has inherent limitations in resolution and relies on simplified models, which limit its accuracy to non-spherical particles.⁷⁶ In addition, the motion of charged particles in solution is highly sensitive to ionic strength, which further complicates the measurements.⁷⁷ Consequently interpreting the solution behaviour of weak polyelectrolytes based solely on DLS data can be misleading. Complementary techniques, including zeta-potential, TEM and SAXS are essential for more reliable analysis.

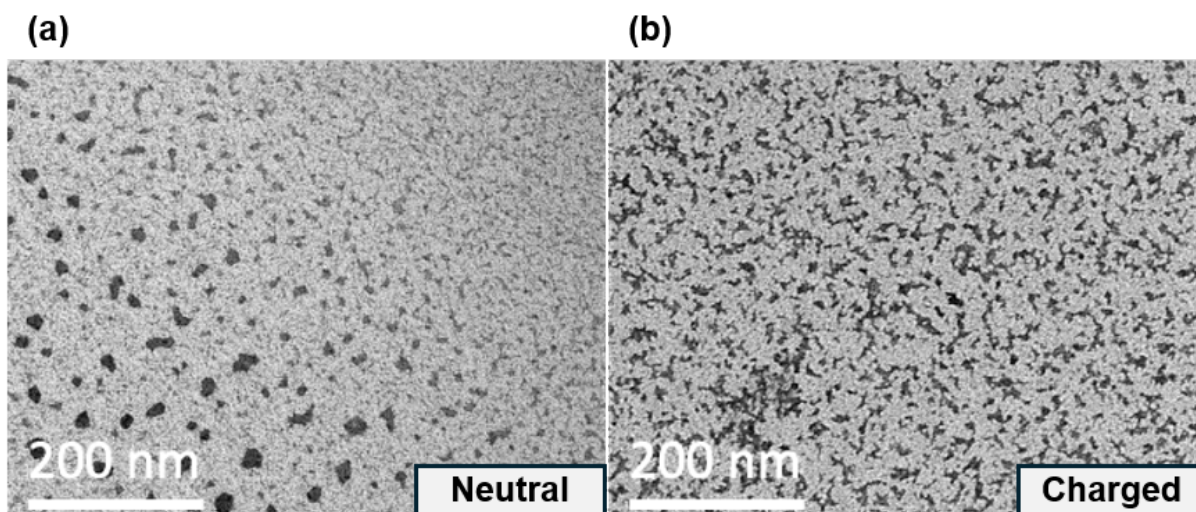


Figure 4.7: TEM images recorded for dilute aqueous solutions of (a) neutral and (b) protonated PD8020:150 copolymer chains.

TEM images revealed a clear morphological difference between neutral and protonated PD8020:150 copolymer chains. Under neutral conditions, larger and less defined dried aggregates were observed (Figure 4.7a), whereas the protonated copolymers formed smaller worm-like structures, potentially corresponding to individual chains or small agglomerates (Figure 4.7b). To further investigate the chain conformation, SAXS analysis was subsequently conducted in the following section.

4.3.4 SAXS Analysis

SAXS experiments were performed on dilute aqueous copolymer solutions to obtain a deeper understanding of the effect of varying the solution pH. The impact of cationic charge on chain extensibility and flexibility was assessed by comparing the scattering patterns recorded at various copolymer concentrations, salt concentrations and solution pH. Structural parameters were extracted using the worm-like chain-polymer reference interaction site model (WLC-PRISM).^{78,79}

The copolymer was first dissolved in deionised water at a relatively high concentration of 5.0% w/w. A 0.1 M HCl solution was then added to protonate the DMA units, resulting in positively charged copolymer chains. The [DMA]/[HCl] molar ratio was varied from 0.1 to 2.0. The correlation between acid addition and the degree of protonation was examined by acid titration, as discussed in the previous section. The resulting solution was diluted with deionised water to prepare copolymer solutions at concentrations ranging from 1.5% to 0.1% w/w. For salt-containing samples, aqueous solutions of HCl and KCl were prepared at volume ratios of 2:1 and 1:1 to obtain solutions with two distinct [HCl]/[KCl] molar ratios. These solutions were added to the copolymer to both protonate the DMA units and introduce background salt. The presence of salt was expected to screen electrostatic interactions.⁸⁰ This preparation protocol was used for all SAXS samples.

Table 4.3: Summary of sample environments used in all SAXS experiments.

Sample ID	Concentration / w/w %	Acid addition [HCl]/[DMA]	Salt addition [KCl]/[DMA]
PD8020:150	1.0	0.00	0.0
		0.25	
		0.50	
		0.75	
		1.00	
		2.00	
PD8020:150	1.0	1.00	0.0
			1.0
			2.0
PD8020:150	1.5	1.00	0.0
	1.2		
	1.0		
	0.8		
	0.6		
	0.4		
	0.2		
PD6040:150	1.0	0.20	0.0
		0.40	
		0.50	
		0.60	
		0.80	
		1.00	

Model Selection

As shown in Figure 4.8, the SAXS patterns recorded for 1.0% w/w aqueous solutions of PD8020:150 in either acidic medium ($[\text{HCl}]/[\text{DMA}] = 1.0$) or deionised water exhibit significant differences. The pattern obtained for the neutral copolymer in water is consistent with that expected for semi-flexible random coils in dilute solution. In the Guinier regime, the R_g was approximately 51 Å, as estimated from a Gaussian flexible chain model.⁸¹ For polymer chains lacking a well-defined surface, the scattering intensity $I(q)$ follows a power-law decay in the intermediate q region (also referred to as the scaling region), where $I(q) \sim q^{-p}$.⁴² The fitted power-law exponent of $p = 2.2$ is characteristic of a self-avoiding chain in a slightly poor, near-theta solvent, indicating a contracted coil conformation.^{82–84}

Under acidic conditions ($[\text{HCl}]/[\text{DMA}] = 1.0$), the SAXS pattern shows a strong structure

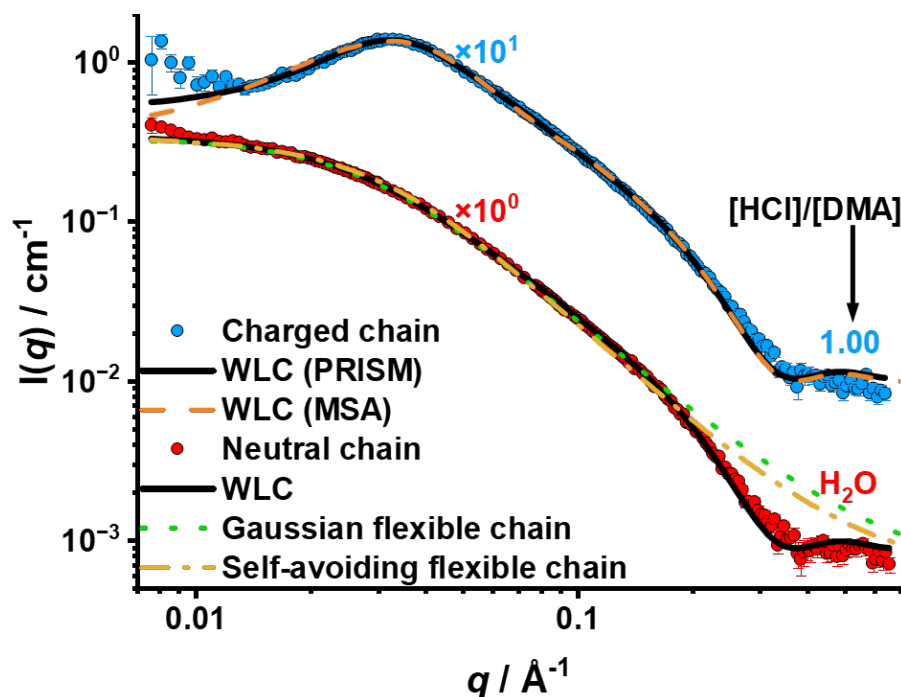


Figure 4.8: Synchrotron SAXS patterns recorded for 1.0% w/w aqueous solutions of PD8020:150 in its neutral (red symbols) and charged (blue symbols) states. The red data set obtained for the neutral copolymer was fitted using three models: Gaussian chain model (dashed orange line), self-avoiding flexible chain model (dotted green line), and a WLC model (solid black line). While all three models describe the low q region reasonably well, which take a finite cross section into account, provides a satisfactory fit across the entire q range. The charged copolymer (blue symbols) was fitted using the WLC model combined with structure factor corrections derived from PRISM theory (black line) and the MSA repulsive structure factor (orange dashed line), with both accounting quite well for interchain electrostatic interactions.

factor peak at low q , indicating significant interchain interactions.⁴² As a result, the particle size cannot be simply estimated using the Guinier approximation, which makes the analysis more complicated. Accordingly, various scattering models were applied to fit the SAXS pattern. These were (i) Gaussian flexible chains, (ii) self-avoiding flexible chains, (iii) wormlike chain (WLC), (iv) WLC with repulsive structure factor in MSA, and (v) WLC with a structure factor PRISM expression. (Appendix 4.5.4)

For neutral copolymer coils, models (i), (ii) and (iii) each provided satisfactory fits to the SAXS data in the low- q region. The Gaussian chain model, neglects both local stiffness and electrostatic interactions.⁸¹ Although the inclusion of excluded volume effects improves the fit,⁸⁵

it still fails to account for the finite cross section size of the chains. This limitation explains the poor agreement observed in the high- q regime ($0.2 < q < 0.4 \text{ \AA}^{-1}$), which is influenced by the finite cylindrical cross-section of the chains. Due to the methacrylic backbone, these copolymers possess restricted flexibility and exhibit rod-like character at short length scales. Therefore, the chains are more accurately described as flexible cylinders, and their scattering profiles are best fitted using the WLC model that allows inclusion of the finite cross section, Equation (4.17).^{37,47} This approach yielded a satisfactory fit to the SAXS pattern for the neutral copolymer. The contour length of the PD8020:150 copolymer in deionised water was fitted as 378 \AA , which is consistent with the mean degree of polymerisation ($DP = 143$) determined by ^1H NMR spectroscopy, assuming a projection length of 2.5 \AA per repeat unit. The fitted r was 10.2 \AA , and the b was estimated as 35.1 \AA . The absolute dispersity \mathcal{D}_{abs} was calculated using the M_n from NMR and the weight-average molecular weight M_w from MALLS, giving $\mathcal{D}_{\text{abs}} = 1.1$ (see Appendix 4.5.5). For comparison, GPC analysis in DMF gave a higher value of $\mathcal{D} = 1.3$. The former value was used in model fitting via the Schulz-Zimm distribution, as described in Equation (4.34).^{55,86,87}

For semi-flexible polymers with comparable contour length to Kuhn length ratios, the R_g was calculated as 51.1 \AA using Equation (4.1). While the WLC model provides an overall satisfactory fit to the SAXS pattern, it does not account for the low- q upturn. Casse et al. suggested that most hydrophilic copolymers exist as isolated chains in dilute solution, although a small fraction may form weak aggregates due to slight differences in hydrophilicity.⁷⁴ On this basis, the increase in scattering intensity observed in the low- q region is likely attributable to a minor population of copolymer aggregates.

For charged copolymer chains, a appropriate structure factor must be introduced to account for the electrostatic interactions. Commonly used approaches for modelling such charged particles include the Hyper-Netted Chain (HNC),^{88,89} Rogers-Young closure (RY),⁹⁰ mean spherical approximation (MSA)⁵² and polymer reference interaction site model (PRISM).^{50,78,79} However, HNC and RY only provide numerical solutions, and their physical meaning has not

been rigorously verified. The MSA model is widely used for the analysis of charged particles. Nevertheless, this model has various theoretical limitations: it neglects the connectivity of polymer segments, and fails to capture the spatial inhomogeneity of the charge distribution, assuming that the particles are rigid spheres of uniform diameter. Thus, although MSA may be an appropriate simplified model for preliminary evaluation, it is not well-suited for the analysis of (semi-)flexible coils or non-spherical particles.⁵² In contrast, the PRISM model can systematically describe the topology, flexibility, and charge-regulated structural response of copolymer chains by combining the inter-chain and intra-chain structural correlations, making it particularly suitable for analysing charged random coils.⁹¹

As shown in Figure 4.8, the quality of the data fit provided by the MSA model is similar to that obtained with the PRISM model but the physical meaning of its parameters is far less reliable. In summary, PRISM provides a more physically realistic scattering model for analysing polyelectrolyte conformations in the current study. The contour length and cross-sectional cylinder radius were determined from the data fit for the uncharged copolymer. The contour length only depends on the mean degree of polymerisation and hence should remain constant regardless of the solution pH or salt concentration. The cross-sectional cylinder radius is related to the R_g of the PEG side-group. To fit copolymer chains with differing degrees of protonation, it is assumed that PEG is not affected by HCl or by the development of charge on the DMA repeat units. The rationale for this assumption is discussed in Section 4.3.6. If this assumption is valid, then the cylinder radius must be independent of the degree of protonation of the copolymer chains. To fit the charged copolymer chains, dimensional parameters (contour length, cylinder radius and Kuhn length for neutral copolymer) obtained for the neutral copolymer chains were used as initial input parameters to fit the structure factor parameters related to the PRISM model, and subsequently fit the parameters related to chain flexibility. For a [HCl]/[DMA] molar ratio of 1.0, the Kuhn length b was 39.4 Å and the three PRISM related parameters were $\nu = 7$ Å, $\sigma = 44$ Å and $R_c = 51$ Å, respectively. The formal definitions of these parameters can be found in Appendix 4.5.4.

Degree of Protonation and Salt Screening

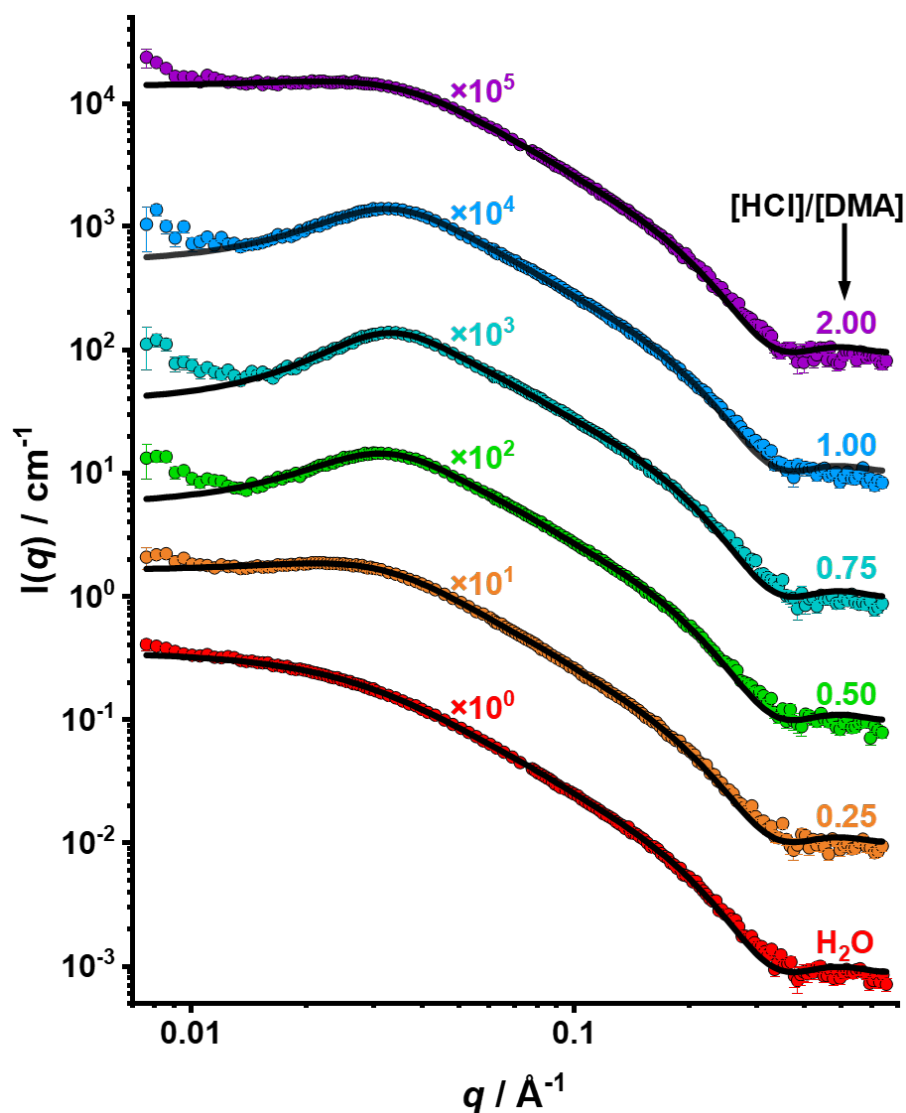


Figure 4.9: Synchrotron SAXS patterns recorded for 1.0% w/w aqueous solutions of PD8020:150 at various $[\text{HCl}]/[\text{DMA}]$ molar ratios. All scattering data were fitted using the WLC-PRISM model. For clarity, some curves are vertically shifted by arbitrary factors.

After identifying the appropriate scattering model and fitting strategy, the SAXS data obtained for PD8020:150 at varying degrees of protonation were fitted to examine changes in the conformation adopted by this copolymer in its neutral form, fully protonated state, and charge-screened condition. Analysis of the variations in the Kuhn length and charge-related parameters revealed the relationship between the mean degree of protonation and the chain flexibility. The SAXS

patterns and corresponding fitting curves are shown in Figure 4.9 and the corresponding fitting data are summarised in Table 4.4.

As shown in Figure 4.9, the SAXS patterns recorded for the copolymer at various pH differ significantly. No obvious structure factor was observed for copolymer solutions in either deionised water or in the presence of excess acid, indicating that electrostatic interactions are either weak or negligible under such conditions. In deionised water, the near-neutral copolymer chains experience minimal electrostatic repulsion, resulting in a relatively compact conformation. In contrast, in acid solutions containing excess HCl, electrostatic repulsion between fully protonated DMA repeat units is effectively screened by excess HCl owing to the relatively high ionic strength. This attenuates the otherwise strong interaction, thereby producing a relatively compact chain conformation. In addition, the neutral copolymer was fitted by assuming that there was no electrostatic interaction between chains, i.e. interaction-related parameter, ν , was fixed to zero.

An additional layer of condensed counterions may surround the copolymer chains in the presence of excess acid.⁹² The interaction is difficult to be fully captured by the WLC-PRISM model, resulting in a relatively large fitting error. It is also worth noting that weak protonation of the DMA repeat units in deionised water leads to its b being slightly larger than that of the screened copolymer. Between the two boundary conditions mentioned above, the expected polyelectrolyte behaviour was observed as the solution pH was gradually adjusted from neutral to acidic. The effective Kuhn length of the copolymer chains increased with higher degrees of protonation due to the resulting intra-chain electrostatic repulsion leads to significantly stiffer chains.^{93,94}

Furthermore, three key parameters were extracted from fitting the structure factor: the strength of direct interactions between charges at different spatial scales, ν , interaction fuzziness σ and effective interaction distance R_c , as shown in Table 4.4. The ν term gradually increases at higher degrees of protonation, suggesting that electrostatic repulsion plays a major role for the change in copolymer conformation. Although a 1:1 [HCl]/[DMA] ratio matches the stoichiometry for

full protonation, DMA is nearly fully charged at slightly lower ratios. Additional HCl acts as background salt and increases ionic strength. Furthermore, no consistent trend was observed for the fuzziness and the effective interaction distance. This suggests that such parameters are not only affected by the copolymer charge density, but also by changes in the copolymer chain conformation, counterion condensation, and inhomogeneities in the copolymer composition.

Table 4.4: Summary of SAXS fitting results obtained for 1.0% w/w aqueous solutions of PD8020:150 with varying [HCl]/[DMA] molar ratios. All scattering data were fitted using the WLC-PRISM model. The copolymer contour length and cross-sectional cylinder radius were fixed at 378 Å and 10.2 Å, respectively. The copolymer dispersity was fixed at 1.1. The b was fitted from WLC form factor. The R_g was calculated using Equation (4.1) rather than fitted. v , σ and R_c were fitted from the structure factor.

[HCl]/[DMA]	Form factor		Structure factor		
	$b / \text{Å}$	$R_g / \text{Å}$	v	$\sigma / \text{Å}$	$R_c / \text{Å}$
H ₂ O	35.1 ± 0.4	53.3	N/A	N/A	N/A
0.25	33.2 ± 0.7	52.1	1.2 ± 0.0	30.0 ± 2.7	79.8 ± 3.2
0.50	37.9 ± 0.7	54.9	6.1 ± 0.3	46.7 ± 6.5	45.9 ± 33.0
0.75	42.3 ± 0.9	57.2	10.1 ± 0.6	43.9 ± 3.1	64.3 ± 7.5
1.00	39.4 ± 0.8	55.7	7.0 ± 0.3	44.3 ± 4.9	50.6 ± 19.8
2.00	34.2 ± 0.7	52.8	1.6 ± 0.1	26.5 ± 2.8	54.5 ± 5.6

A similar set of experiments was carried out on PD6040:150, which is a copolymer of comparable molecular weight with a higher DMA content. Comparable SAXS patterns and corresponding fitting results were obtained for this copolymer (see Appendix 4.5.6).

The above WLC-PRISM analysis assumes that the cross-sectional cylinder radius of the flexible copolymer chains remains consistent during protonation of its DMA repeat units. At around neutral pH, this scattering model provides a satisfactory fit to the experimental SAXS patterns. However, the SAXS patterns gradually deviate from the data fits in the high q range on addition of HCl. This is presumably related to the condensed counterions associated with the increasingly cationic chains, which increase the effective cylinder cross-sectional area and change the mean electron density, thereby affecting the X-ray contrast. This additional structural feature was not introduced to avoid over-parameterisation. A quantitative description of this additional layer of

condensed counterions requires a more complex electric field-density coupling model.^{95,96} In addition, contrast matching techniques using SANS with appropriate H₂O/D₂O mixtures could provide further physical insights.⁹⁷ However, such additional scattering experiments are beyond the scope of the current study. Instead, the interaction between the PEG side chains and cations was assessed to verify the consistency of the cylinder cross-sectional area (see Section 4.3.6). Contraction of copolymer chains in the presence of excess HCl was observed. To investigate the effect of ionic strength on copolymer conformation and electrostatic interactions, SAXS experiments were performed at [KCl]/[HCl] molar ratios of 0.0, 1.0 and 2.0 while maintaining a constant [HCl]/[DMA] molar ratio and copolymer concentration to ensure the same mean degree of protonation. This strategy allows the effect of charge screening to be studied.

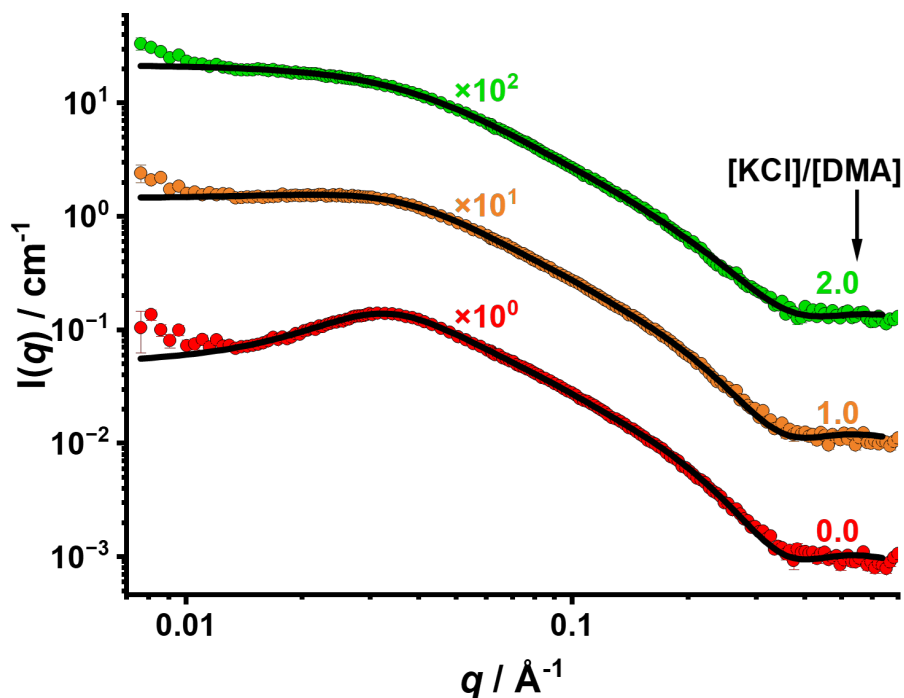


Figure 4.10: Synchrotron SAXS patterns recorded for 1.0% w/w aqueous solutions of PD8020:150 at varying salt concentrations and a fixed [HCl]/[DMA] molar ratio = 1.0. All scattering data were fitted using the WLC-PRISM model. Salt concentrations are expressed in terms of the [KCl]/[HCl] molar ratio, as indicated for each curve. For clarity, some curves are vertically shifted by arbitrary factors.

Table 4.5: Summary of SAXS fitting results obtained for a 1.0% w/w aqueous solution of PD8020:150 at varying salt concentrations and a fixed [HCl]/[DMA] molar ratio = 1.0. All scattering data were fitted using the WLC-PRISM model. The copolymer contour length was fixed at 378 Å. The copolymer dispersity was fixed at 1.1. The b and r was fitted from the WLC form factor. ν , σ and R_c were fitted from the structure factor.

[KCl]/[DMA]	Form factor		Structure factor		
	$b / \text{\AA}$	$r / \text{\AA}$	ν	$\sigma / \text{\AA}$	$R_c / \text{\AA}$
0.0	30.9 ± 1.2	9.5	6.1 ± 0.3	44.4 ± 3.3	55.1 ± 10.9
1.0	28.3 ± 0.5	9.5	1.3 ± 0.3	N/A	N/A
2.0	19.9 ± 1.5	8.7	0.2 ± 6.1	N/A	N/A

As shown in Figure 4.10, the structure factor gradually disappears at higher salt concentrations. The reduction in the Kuhn length suggests a transition from a charge-dominated extended state to a more compact copolymer conformation. The cylinder cross-sectional radius was treated as a variable in the data fits to capture any changes caused by the anticipated layer of condensed counterions. However, the complex charge interactions limited the fitting accuracy. Nevertheless, the Kuhn length and the structure factor parameter ν both decreased with increasing salt concentration, which was consistent with charge screening. These observations confirm that the ionic strength effectively modulates interchain interactions (Table 4.5).

Concentration Effect

The copolymer concentration significantly affects the inter-chain and intra-chain interactions, especially during the transition from dilute to semi-dilute regimes. This boundary is defined by the critical overlap concentration, c^* , above which the copolymer chains begin to interpenetrate and interact with each other.⁹⁸ The value of c^* is given by:^{46,99}

$$c^* = \frac{M_w}{N_A R_g^3} \quad (4.11)$$

where M_w is the weight-average molecular weight, N_A is Avogadro's constant and R_g is the radius of gyration.

However, the applicability of this approach for the analysis of polyelectrolytes in aqueous

solution is controversial: increasing the copolymer charge density introduces long-range electrostatic repulsion, so cationic chains may exhibit inter-chain interactions at copolymer concentrations much lower than c^* although the chains are not overlapping.¹⁰⁰

In this study, SAXS measurements were performed at seven copolymer concentrations (0.2, 0.4, 0.6, 0.8, 1.0, 1.2 and 1.5% w/w) at a fixed degree of protonation. The copolymer concentration was treated as the only variable to evaluate its effect on the chain configuration. As shown in Figure 4.11a, the overall scattering intensity and the structure factor decreased both at lower copolymer concentration. In particular, the weak structure factor was still observed even at 0.2% w/w, indicating electrostatic repulsion between neighbouring copolymer chains.

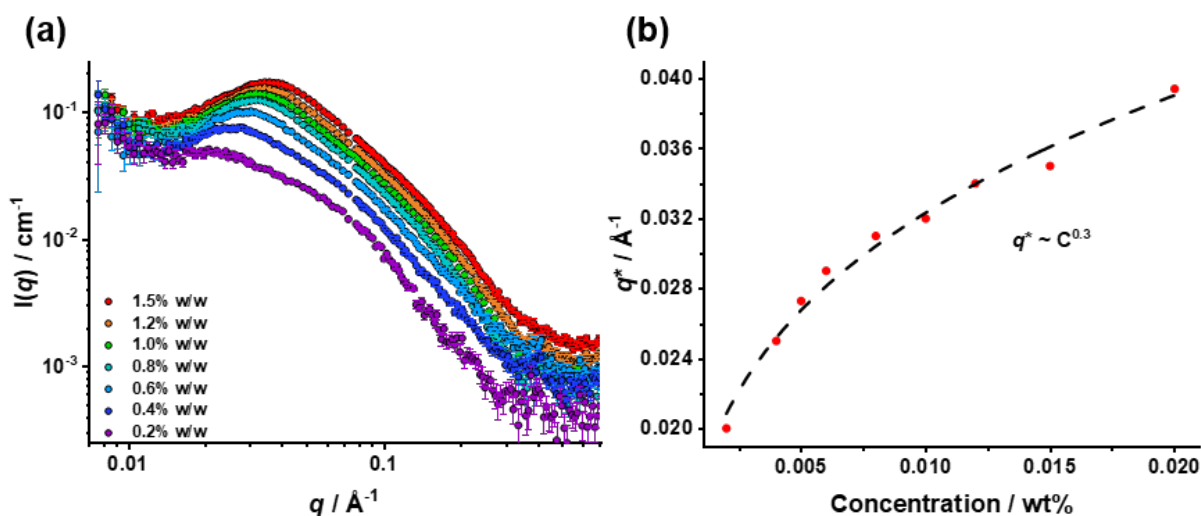


Figure 4.11: (a) Synchrotron SAXS patterns recorded for aqueous solutions of PD8020:150 at various copolymer concentrations and a fixed $[\text{HCl}]/[\text{DMA}]$ molar ratio = 1.0. Copolymer concentrations are indicated in the Figure. Curves are presented without vertical shifting to illustrate the effect of copolymer concentration and the corresponding shift in the structure factor. (b) Copolymer concentration dependence of the structure factor peak position q^* . The dashed line represents a power law fit to the data, indicating that q^* scales with concentration as $c^{0.3}$.

Inspecting Figure 4.11b, the structure factor peak position q^* is clearly dependent on the copolymer concentration. A plot of q^* versus copolymer concentration, c , reveals a power-law relationship with an exponent close to 0.3, as expected for a polyelectrolyte in dilute aqueous solution below c^* ,^{23,100} in contrast to above c^* , where the scaling changes to $c^{0.5}$.¹⁰¹ Despite the

presence of a structure factor, this suggests that the copolymer chains do not overlap or form entanglements so any change in conformation is primarily governed by long-range electrostatic repulsion.

To assess the effect of copolymer concentration on chain conformation and inter-chain interactions, SAXS patterns were fitted using the WLC-PRISM model at a fixed degree of protonation for the DMA repeat units. At lower copolymer concentration, the copolymer chains expanded, as judged by the increase in Kuhn length, which indicates enhanced chain stiffness. This is attributed to greater separation between isolated copolymer chains, rather than any variation in their charge density. Given the relatively low X-ray scattering contrast between the copolymer and water, the corresponding data fits should be interpreted with caution. A summary of the fitting results is presented in Table 4.6. As the structure factor exhibits limited sensitivity to changes in R_c in dilute solution, this number was fixed for diluted solutions during fitting to minimise unnecessary variables.

Table 4.6: Summary of SAXS fitting results obtained for aqueous solutions of PD8020:150 at a fixed [HCl]/[DMA] molar ratio = 1.0 and variable copolymer concentrations. All scattering data were fitted using the WLC-PRISM model. The contour length was fixed to 378 Å. The copolymer dispersity was taken to be 1.1. The b and r were fitted from the WLC form factor. The ν , σ and R_c were calculated from the structure factor.

Conc. / % w/w	Form factor		Structure factor		
	$b / \text{\AA}$	$r / \text{\AA}$	ν	$\sigma / \text{\AA}$	$R_c / \text{\AA}$
1.5	23.4 ± 1.2	8.6	5.5 ± 0.3	38.3 ± 2.2	54.5 ± 6.7
1.2	25.3 ± 1.2	8.9	5.9 ± 0.3	41.8 ± 2.4	59.2 ± 6.7
1.0	29.1 ± 1.2	9.4	5.8 ± 0.3	43.4 ± 3.3	60.2 ± 9.4
0.8	30.0 ± 1.5	9.7	5.8 ± 0.2	52.4 ± 0.7	10.0 (fixed)
0.6	19.9 ± 0.9	9.0	5.4 ± 0.5	65.8 ± 1.9	10.0 (fixed)
0.4	15.7 ± 0.5	9.4	3.2 ± 0.5	75.8 ± 3.4	10.0 (fixed)
0.2	27.3 ± 9.5	12.5	1.1 ± 0.4	12.8 ± 6.2	10.0 (fixed)

4.3.5 Quaternisation of P(DMA-*stat*-PEGMA) and Characterisation

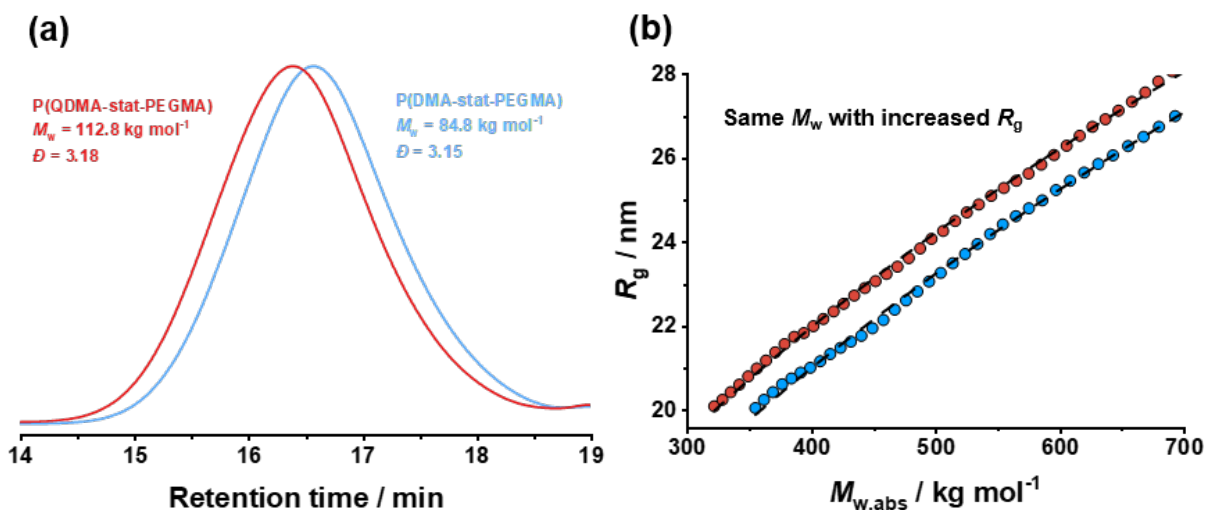


Figure 4.12: (a) Molecular weight distributions recorded for the precursor FRP copolymer and its quaternized analogue. (b) M_w vs. R_g plot obtained for the neutral precursor FRP copolymer and its cationic quaternised analogue in aqueous solution using the GPC-MALLS instrument.

To investigate polyelectrolyte behaviour over a broader molecular weight range, a polydisperse statistical copolymer denoted P(DMA_{0.2}-*stat*-PEGMA_{0.8}), was synthesised via free radical copolymerisation. This copolymer exhibited a relatively broad molecular weight distribution, ranging from a few thousand to several million $\text{g}\cdot\text{mol}^{-1}$. The pendent tertiary amine units were subsequently quaternised to form quaternary ammonium groups (P(QDMA_{0.2}-*stat*-PEGMA_{0.8})), thereby imparting a permanent cationic charge independent of solution pH. Both P(DMA_{0.2}-*stat*-PEGMA_{0.8}) and P(QDMA_{0.2}-*stat*-PEGMA_{0.8}) were analysed by aqueous GPC-MALLS. An aqueous eluent was selected because, unlike the P(DMA_{0.2}-*stat*-PEGMA_{0.8}) precursor, the quaternised copolymer was found to be insoluble in DMF.

Figure 4.12a presents the aqueous GPC curves for each copolymer. The M_w and \bar{D} for the free radical polymerised copolymer were $84.8 \text{ kg}\cdot\text{mol}^{-1}$ and 3.15, respectively. Quaternisation of the precursor resulted in an increase in M_w , while the dispersity remained essentially unchanged. It should be noted that this M_w value is relative, as calibration was performed using poly(methyl methacrylate) standards. A MALLS detector was coupled to the aqueous GPC instrument, and

a RI detector was employed to determine the copolymer concentration based on the known differential refractive index increment (dn/dc) for each sample.

The dn/dc values were measured for four higher molecular weight copolymers using an eluent at pH 10 (Figure 4.13a). The dn/dc value was found to increase with increasing DMA content. Although PDMA is not water-soluble at pH 10, extrapolation yielded a dn/dc of $0.172 \text{ mL}\cdot\text{g}^{-1}$ for this homopolymer under such conditions, which is comparable with values previously reported in acidic aqueous solution (Figure 4.13b).¹⁰²

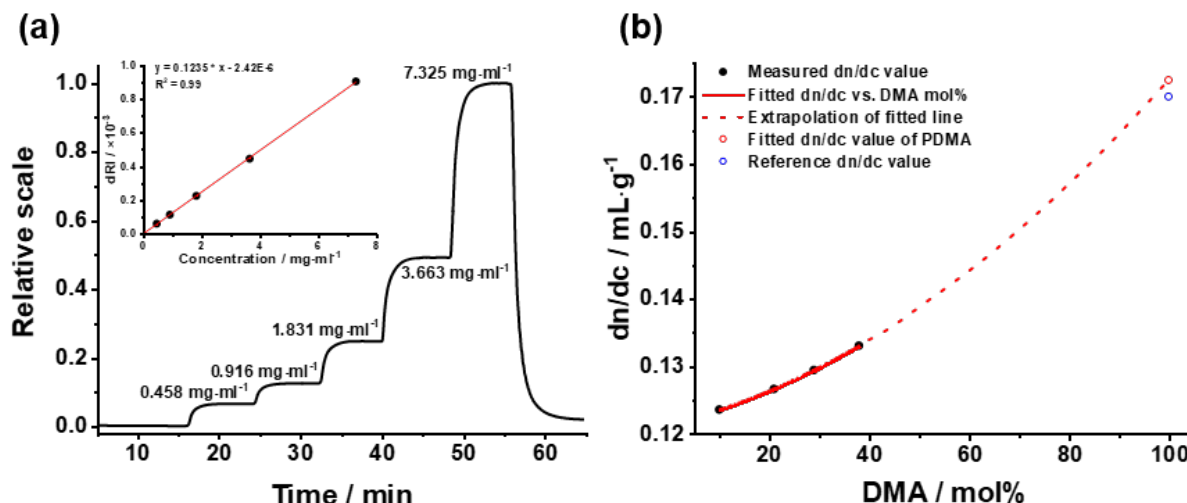


Figure 4.13: (a) Representative differential refractive index data for a PD9010:150 statistical copolymer dissolved in pH 10 GPC buffer. The signal response is shown for copolymer concentrations ranging from 0.458 to $7.325 \text{ g}\cdot\text{dm}^{-3}$. The signal intensity increases stepwise with copolymer concentration, attaining a plateau value at each target concentration. The inset shows a linear plot of dRI vs. copolymer concentration. The slope indicates a dn/dc value of $0.1235 \text{ mL}\cdot\text{g}^{-1}$ for PD9010:150 copolymer. (b) Relationship between dn/dc and the DMA content of such copolymers. The extrapolated dn/dc value for PDMA homopolymer is consistent with literature data.¹⁰²

GPC column can effectively separate the copolymer chains, with longer chains eluting prior to shorter chains. Hence the MALLS detector can simultaneously and continuously detect the M_w and R_g . Given the relatively long wavelength of visible light and the poor sensitivity of MALLS for the analysis of dilute copolymer solutions ($< 0.001 \text{ g}\cdot\text{dm}^{-3}$), R_g values below 20 nm are considered to be unreliable. Figure 4.12b shows R_g as a function of M_w for P(DMA-*stat*-PEGMA) and P(QDMA-*stat*-PEGMA) at pH 10, with $M_{w,abs}$ values of less than

700 kg·mol⁻¹ and R_g values greater than 20 nm. A $R_g \sim M_w^\nu$ scaling relationship was observed, where the Flory exponent $\nu = 0.45$ is related to the solvent quality and the scaling of polymer size,⁸² hence the inherent flexibility of the copolymer chain. According to the polymer physics literature, unperturbed flexible random walk chains scale as $R_g \sim M_w^{0.5}$,^{83,103,104} which corresponds to a typical Gaussian coil under θ -conditions. In contrast, $R_g \sim M_w^{0.588}$ for flexible self-avoiding random walk chains dissolved in a good solvent,^{84,103,105} while $R_g \sim M_w^{0.33}$ is characteristic behaviour for collapsed coils in a poor solvent.¹⁰⁶ This parameter is also reflected in the scaling law exponent in form factor. The lower ν value indicated by MALLS analysis is attributed to the reduced solubility of the copolymer chains in the presence of added salt.¹⁰⁷ However, the observed trend is consistent with random coils over the whole measurement range accessible by MALLS, as at this polymer concentration and pH 10 GPC buffer condition, electrostatic interactions and the solution structure factor are minimised. And therefore the self-avoiding Gaussian chain model is applicable for both charged and neutral copolymer chains with sufficient long contour length.

A calculation based on the data set shown in Figure 4.12b gives $l_p = 19.9 \text{ \AA}$ ($b = 39.8 \text{ \AA}$) for the neutral and 21.7 \AA ($b = 43.4 \text{ \AA}$) for the quaternised statistical copolymers, respectively. It should be noted that the Kuhn lengths determined by MALLS are slightly larger than those obtained from SAXS, which may be attributed to differences between the two techniques.

4.3.6 Interactions between Poly(ethylene glycol) and Salt

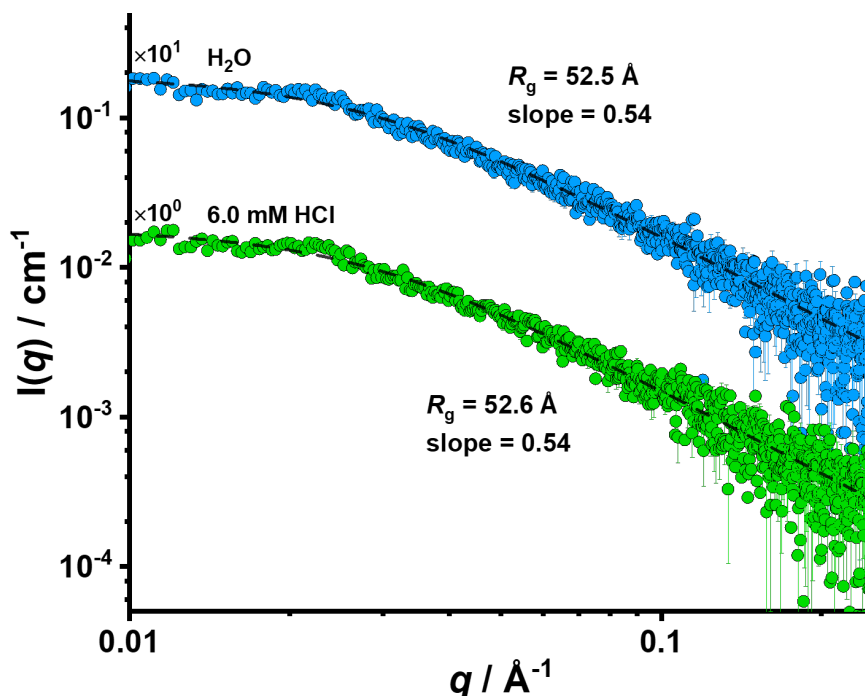


Figure 4.14: SAXS patterns recorded for 1.0% w/w aqueous solutions of P(PEGMA₃₀₀) homopolymer random coils using the Xeuss 2.0 instrument. The flexible polymer chain model accounting for excluded volume was fitted to determine the mean R_g for the random coils formed by this neutral homopolymer in deionised water (blue dots) and in 6 mM HCl aqueous solution (green dots).

In the above discussion, it was assumed that the PEG side chains served only to enhance the aqueous solubility of the copolymer, and that this non-ionic component did not interact with either salt or acid. However, several studies suggest that PEG can interact with various anions and cations.^{108–110} For example, Cao et al. reported that PEG becomes protonated under acidic or weakly basic conditions ($\text{pH} < 9$), thereby forming a super-electrolyte.¹⁰⁹ Moreover, Rogers et al. demonstrated that longer PEG chains interact more strongly with thiocyanate (SCN^-).¹⁰⁸ Similarly, Maltesh and Somasundaran found that various cations influence the conformation of PEG chains.¹¹⁰ In principle, such ions may also affect the copolymer conformation at different solution pH values and salt concentrations. Demonstrating that these effects are negligible for the present P(DMA-*stat*-PEGMA) system is important for validating the WLC-PRISM

model. Accordingly, a P(PEGMA₃₀₀) homopolymer was synthesised for SAXS analysis under identical solution conditions to investigate whether the PEG side chains significantly influence the copolymer chain conformation.

SAXS analysis shows that the scattering patterns recorded for the P(PEGMA₃₀₀) homopolymer in deionised water and in the presence of 6.0 mM HCl are essentially identical, indicating that its chain conformation is independent of the solution pH (Figure 4.14). By modifying the flexible polymer model to account for the effect of excluded volume, the R_g and power law slope were fitted to be 52.5 Å and 0.54 in deionised water, compared with 52.6 Å and 0.54 in the presence of 6.0 mM HCl, respectively. Thus, notwithstanding their role in diluting the cationic charge density, PEGMA₃₀₀ repeat units act solely as a passive non-ionic hydrophilic component when studying the conformation of polyelectrolytes.

4.4 Conclusions

A series of weakly basic statistical copolymers comprising DMA and PEGMA comonomers were synthesised as a model system for investigating the effect of chain flexibility on statistical copolymer surfactant. The statistical nature of the model comonomer distribution was confirmed by determining comonomer reactivity ratio by ^1H NMR spectroscopy studies.

The pH-responsive behaviour of these statistical copolymers was evaluated via acid-base titration and zeta potential measurements. A clear correlation was established between acid addition, mean degree of protonation, and copolymer charge density. DLS and TEM studies indicated changes in size and chain conformation on addition of acid, revealing the role of electrostatic repulsion on the solution behaviours of these statistical copolymers.

SAXS provided useful insight into the chain conformations adopted by such neutral/charged copolymers. Introduction of the WLC-PRISM model enabled the extraction of key structural parameters, including Kuhn length, interchain interaction strength, interaction fuzziness, and effective interaction distance. The fitting results confirmed that the copolymer chains adopt compact coil conformations under neutral conditions, which become more rigid and expanded at low pH due to enhanced intra-chain electrostatic repulsion, with the increasing acid concentration.

Salt screening experiments indicated that electrostatic interactions are significantly attenuated at high ionic strength, resulting in reduced Kuhn length and coil size. Variation of copolymer concentration also suggested the influence of interchain repulsion on coil conformation in the dilute regime. The observed scaling behaviour of the structure factor peak position with concentration was consistent with prior studies of aqueous solutions of polyelectrolytes.^{23,100}

GPC-MALLS measurements were conducted to examine the molecular weight dependence of coil size. Comparison between the precursor P(DMA-*stat*-PEGMA) and its permanently charged analogue P(QDMA-*stat*-PEGMA) revealed a consistent trend of charged coil expansion across the entire molecular weight range, suggesting the generality of charge-induced swelling

in these systems.

Overall, this study demonstrates that the chain conformation of weakly basic statistical copolymers in aqueous solution is governed by charge density, ionic strength, and copolymer concentration. The WLC-PRISM model provides a rigorous and physically grounded framework for analysing SAXS data. In a series of ionisable model copolymers, the stiffness differences arising from the distinct backbone structures of acrylates and methacrylates were simulated through electrostatic interactions, enabling reliable quantification of chain rigidity and electrostatic contributions. Consequently, this modelling approach is expected to be applicable to less complex, non-ionic systems as well, such as the statistical copolymer surfactant system as discussed in Chapter 3.

In principle, SANS experiment could be conducted to investigate the condensed counterion layer that surrounds the charged statistical copolymer coils. The contrast match technique using D_2O/H_2O binary mixture is expected to improve the resolution of the outer layer thickness, thereby refining current fitting models and enabling more reliable characterisation of the electrostatic double layer.⁹⁷

Furthermore, the WLC-PRISM framework could be extended by replacing electrostatic interactions with hydrophobic interactions, enabling the exploration of chain flexibility for non-ionic amphiphilic copolymers in non-aqueous media.

4.5 Appendix

4.5.1 Synthesis

Table 4.7: Summary of reagent quantities required in the synthesis of the statistical copolymers

Sample ID	DMA / g	PEGMA / g	CPDB / g	AIBN / g	Ethanol / g
PD9010:250	0.2406	4.0500			21.5
PD8020:250	0.4813	3.6000	0.0137	0.0025	20.4
PD7030:250	0.7219	3.1500			19.4
PD6040:250	0.9625	2.7000			18.3
PD9010:125	0.2406	4.0500			21.5
PD8020:125	0.4813	3.6000	0.0274	0.0049	20.4
PD7030:125	0.7219	3.1500			19.4
PD6040:125	0.9625	2.7000			18.3
PD9010:FRP	1.5721	12.0000	N/A	0.0014	136.0

4.5.2 NMR Kinetics

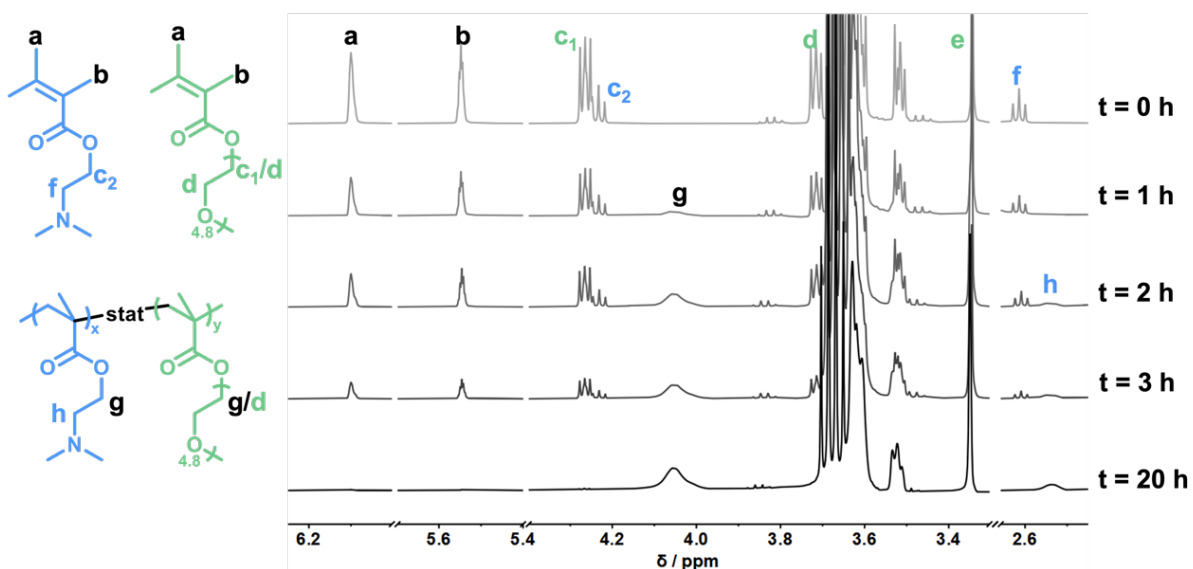
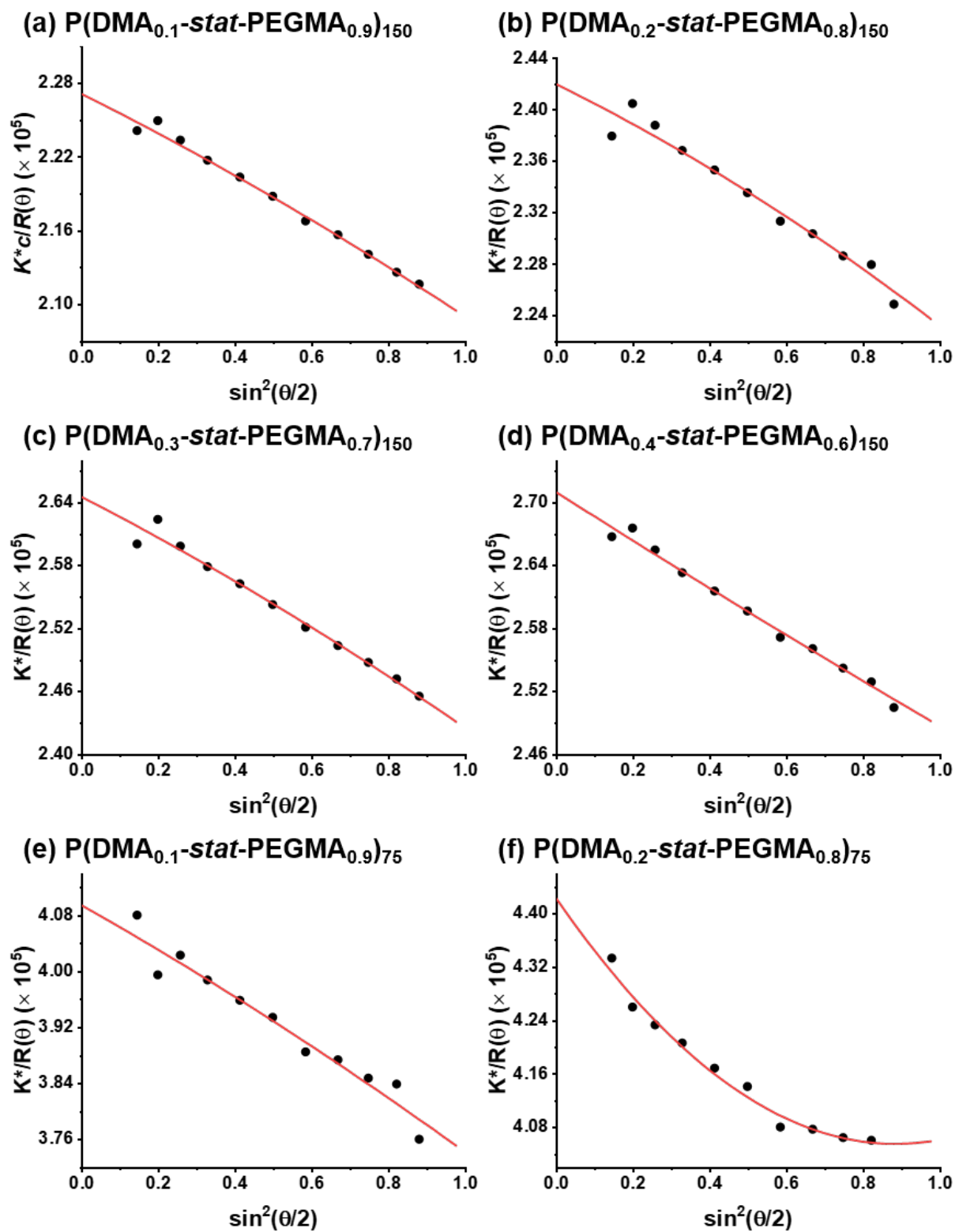


Figure 4.15: Partial ^1H NMR spectra (CDCl_3) recorded during the synthesis of a $\text{P}(\text{DMA}_{0.2}\text{-stat-PEGMA}_{0.8})$ statistical copolymer.

^1H NMR spectra were recorded during the synthesis of $\text{P}(\text{DMA}_{0.2}\text{-stat-PEGMA}_{0.8})$ statistical

copolymer. Both DMA and PEGMA are methacrylic monomers and therefore exhibit several overlapping proton signals (see a, b, c and g). Signals a and b disappeared during the copolymerisation and are assigned to vinyl protons. Conversely, the intensity of signal g increased during the copolymerisation and is assigned to the two oxymethylene protons adjacent to the ester group for the copolymerised DMA and PEGMA repeat units. The corresponding oxymethylene protons adjacent to the ester group for the DMA and PEGMA comonomers are labelled c_1 and c_2 , respectively. The remaining oxymethylene signals arising from the pendent poly(ethylene glycol) groups gave rise to signal d at 3.50 - 3.75 ppm. The methyl group (signal e) at the end of the PEG side chain remained unchanged during the copolymerisation. The overall comonomer conversion was calculated by comparing the integrated vinyl signals at 5.5 and 6.1 ppm to that of the methyl chain end signals on PEG at 3.3 ppm. The initial triplet signal f assigned to the azamethylene protons in DMA monomer at 2.60 ppm was gradually replaced by signal h at 2.54 ppm for the copolymerised DMA repeat units. Integration of these two signals enabled determination of the DMA conversion at any given time. The corresponding PEGMA conversion was calculated from the difference between the overall comonomer conversion and the DMA conversion.

4.5.3 MALLS Measurements



(continued on next page)

(continued from previous page)

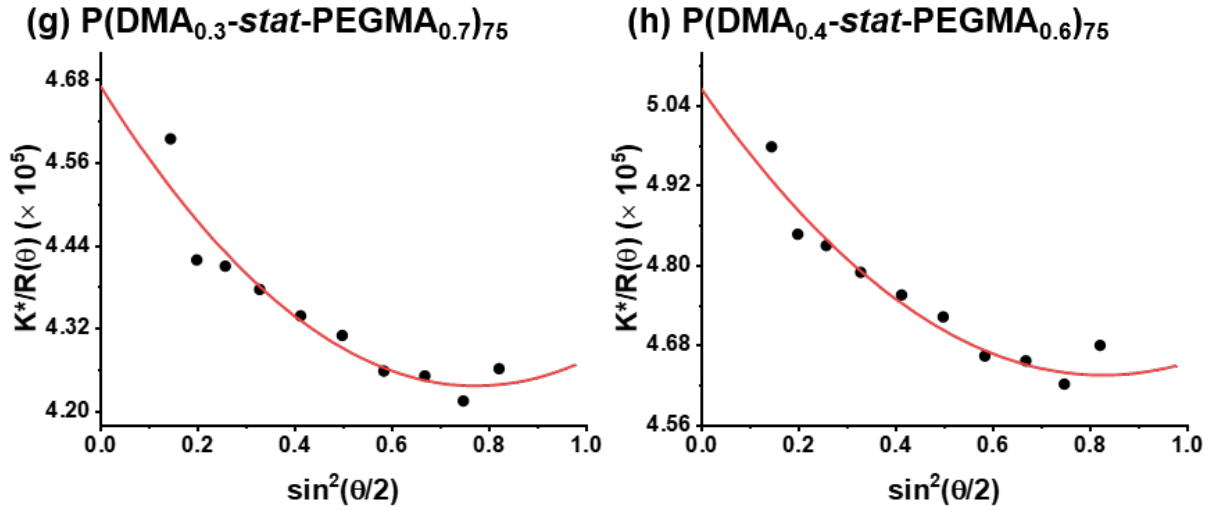


Figure 4.16: MALLS plots obtained using the Zimm formalism for light scattering data collected for eight $P(\text{DMA}_x\text{-stat-PEGMA}_y)$ statistical copolymers dissolved in a pH 10 eluent (a - h).⁵⁵ The absolute weight-average molecular weight, $M_{w,\text{abs}}$, for these eight copolymers are summarised in Table 4.1

4.5.4 SAXS Fitting Functions

Gaussian flexible polymer without excluded volume effect

Polymer chain in an ideal situation conform to a random flight model with Gaussian statistics.^{111,112} The related scattering function has been calculated by Debye:⁸¹

$$P_{\text{Debye}}(q, L, b) = \frac{2(e^{-u} + u - 1)}{u^2} \quad (4.12)$$

with parameter $u = \langle R_g^2 \rangle q^2$, where $\langle R_g^2 \rangle$ is the ensemble-average radius of gyration squared and $\langle R_g^2 \rangle = Nb^2/6$, where b is the Kuhn length and N is the mean number of Kuhn segments. The contour length, L_c , is given by $L_c = Nb$. Hence $\langle R_g^2 \rangle = L_c b/6$.

However, such an expression is only applicable to flexible chains in a theta solvent where the excluded volume effect is precisely cancelled by polymer-solvent interactions.¹¹³ Under such conditions, segment-segment interactions are ignored. In reality, the conformation of a real polymer chain in solution is affected by the solvent quality. A polymer dissolved in a good

solvent forms solvent-swollen random coils and the q dependence of the scattering intensity is not consistent with the Debye Function. In this case, it is necessary to account for the effect of excluded volume.

Self-avoiding flexible chains

The following empirical expression was reported by Hammouda:⁸⁵

$$P_{\text{Hammouda}}(q, R_g, \nu) = \frac{1}{\nu U^{1/(2\nu)}} \gamma\left(\frac{1}{2\nu}, U\right) - \frac{1}{\nu U^{1/\nu}} \gamma\left(\frac{1}{\nu}, U\right) \quad (4.13)$$

where ν is the excluded volume parameter and is defined as the reciprocal of power law exponent $p = 1/\nu$. Parameter U and radius of gyration R_g are defined as:

$$U = \frac{q^2 R_g^2 (2\nu + 1)(2\nu + 2)}{6} \quad (4.14)$$

$$R_g^2 = \frac{b^2 N^{2\nu}}{(2\nu + 1)(2\nu + 2)} \quad (4.15)$$

where R_g is modified by the excluded volume effect parameter ν . The theta condition can only be achieved when $\nu = 0.5$, and $P_{\text{Hammouda}}(q, R_g, \nu)$ is the same as $P_{\text{Debye}}(q, L, b)$ under this condition. The parameter b is the Kuhn length and N is the number of Kuhn segments.

$\gamma(a, b)$ is the lower incomplete gamma function defined as:

$$\gamma(a, b) = \int_0^b t^{a-1} e^{-t} dt \quad (4.16)$$

Worm-Like Chain (WLC) model

To take chain flexibility into account, worm-like chain (WLC) model, also known as Kratky-Porod model, is required to describe local rod-like behaviour of semi-flexible chains.³⁷ A numerical interpolation formula was developed by Yoshizaki and Yamakawa¹¹⁴ and then further

optimised using Monte Carlo simulations to consider excluded volume effect by Pedersen and Schurtenberger.⁴⁷

The overall scattering function for semi-flexible self-avoiding chains consists of the modified Debye function with excluded volume effect, and the expression with local rod-like structure:⁴⁷

$$P_{\text{WLC}}(q, L, b) = P_{\text{sb}}(q, L, b) e^{-\left(\frac{qb}{q_1}\right)^{p_1}} + P_{\text{loc}}(q, L) \left(1 - e^{-\left(\frac{qb}{q_1}\right)^{p_1}}\right) \quad (4.17)$$

where q_1 and p_1 are empirical constants.

The scattering function reported by Sharp and Bloomfield, $P_{\text{sb}}(q, L, b)$ is:¹¹⁵

$$P_{\text{sb}}(q, L, b) = P_{\text{exv}}(q, L, b) + C\left(\frac{L}{b}\right) \left[\frac{4}{15} + \frac{7}{15}u - \left(\frac{11}{15} + \frac{7}{15}u\right) e^{-u} \right] \frac{b}{L} \quad (4.18)$$

The second term, which accounts for the local chain stiffness, is reduced by a factor ($C(L/b)$) that depends on L/b .

For sufficiently long chains where $L/b > 10$, the function $C(L/b)$ can be approximated as:

$$C\left(\frac{L}{b}\right) = \frac{a_4}{\left(\frac{L}{b}\right)^{p_3}} \quad (4.19)$$

where a_4 and p_3 are empirical constants. For shorter chains, where $L/b \leq 10$, the following expression is used:

$$C\left(\frac{L}{b}\right) = 1 \quad (4.20)$$

The first term in $P_{\text{sb}}(q, L, b)$ represents the scattering contribution associated with excluded volume effects:

$$P_{\text{exv}}(q, L, b) = [1 - w(qR_g)] P_{\text{Debye}}(q, L, b) + w(qR_g) [1.220(qR_g)^{-1/\nu} + 0.4288(qR_g)^{-2/\nu} - 1.651(qR_g)^{-3/\nu}] \quad (4.21)$$

where

$$\langle R_g^2 \rangle = a \left(\frac{L}{b} \right)^2 \cdot \frac{bL}{6} \quad (4.22)$$

$$a(x)^2 = \left[1 + \left(\frac{x}{3.12} \right)^2 + \left(\frac{x}{8.67} \right)^3 \right]^{\varepsilon/3} \quad (4.23)$$

with effective $\varepsilon = 0.176$ (or 0.170), and $\nu = (1 + \varepsilon)/2$.

The function $w(qR_g)$ is an empirical crossover function chosen to be:⁴⁷

$$w(x) = \frac{1 + \tan\left(\frac{x-1.523}{0.1477}\right)}{2} \quad (4.24)$$

The parameter u is given by:

$$u = \langle R_g^2 \rangle q^2 = a \left(\frac{L}{b} \right)^2 q^2 \cdot \frac{bL}{6} \quad (4.25)$$

The scattering function at high q reduces to:

$$P_{\text{loc}}(q, L) = \frac{1}{Lbq^2} + \frac{\pi}{Lq} \quad (4.26)$$

Polymer Reference Interaction Site Model (PRISM)

The WLC model has described the scattering pattern well at high q and infinite dilution. The following expression takes into account inter-chain interactions and are based on simulation by Pedersen and Schurtenberger for semi-flexible polymers:^{78,79}

$$I(q) = nM_c^2 \cdot \frac{P(q) P_{\text{cs}}(q)}{1 + v_c(q) P(q)} \quad (4.27)$$

where n is the number density of the polymer coils, v describes the strength of the interaction, M_c is the scattering mass of a single chain. The function $P(q)$ represents the form factor for self-avoiding, semi-flexible polymer chains, $P_{\text{WLC}}(q, L, b)$, based on the WLC model, see Equation (4.17). The function $P_{\text{cs}}(q)$ is an appropriate cross-section form factor of an cylinder

and is given by a first-order Bessel function of the first kind:⁴⁷

$$P_{cs}(q) = \left(\frac{2J_1(qR)}{qR} \right)^2 \quad (4.28)$$

where J_1 is the Bessel function of the first kind of order one:

$$J_1(x) = \frac{1}{\pi} \int_0^\pi \cos(x \sin \theta - \theta) d\theta \quad (4.29)$$

$c(q)$ is the three-dimensional Fourier transform of the direct correlation function in the Ornstein-Zernike (OZ) equation, which describes the interaction between polymer coils. For polyelectrolytes, the empirical form:¹¹⁶

$$c(q) = \frac{\sin(qR_c)}{qR_c} e^{-q^2\sigma^2} \quad (4.30)$$

were found to describe the simulation data, where σ describes the interaction fuzziness and R_c is the effective interaction distance. The two parameters are theoretically subject to the following correlation:

$$\frac{R_c}{b} = 2 \log \left(\frac{\sigma}{b} \right) \quad (4.31)$$

But typically, they are used as fitting parameters.¹¹⁶

v is proportional to the copolymer concentration, copolymer M_w , and to the strength of the excluded volume interaction, which is given by Ohta and Oono:¹¹⁷

$$v = \frac{1}{8} \left(9X - 2 + \frac{2 \ln(1+X)}{X} \right) \exp \left[\frac{1}{4} \left(\frac{1}{X} + \left(1 - \frac{1}{X^2} \right) \ln(1+X) \right) \right] \quad (4.32)$$

with $X = 16A_2cM$, where c is the polymer concentration and M is the polymer mass. Using renormalisation group theory, the second virial coefficient A_2 can be expressed as:¹¹⁷

$$A_2 = 4\pi^{3/2} N_A \frac{R_g^3}{M^2} \Psi \quad (4.33)$$

where N_A is Avogadro's constant, R_g is the ensemble-average radius of gyration of a single chain, and $\Psi \approx 0.21$ is the degree of interpenetration¹¹⁸. It is recommended to use ν as a fitting parameter because the simulations were performed for charged micelles¹¹⁹.

Polydispersity

It is well established that free radical synthesised copolymer chains possess a certain degree of inherent polydispersity.⁶⁵ This arises not only from the statistical nature of the polymerisation process itself but may also be influenced by chain transfer events. The presence of polydispersity has a significant impact on the shape of the SAXS pattern, particular in the Guinier region and at the crossover to the power-law behaviour.¹²⁰ Consequently, molecular weight distribution must be taken into account during data modelling and fitting. The total scattering function for polydisperse copolymer chains can be expressed in the z -average form:⁸⁶

$$\langle P_{\text{WLC}}(q, L, b) \rangle_z = \frac{\int N(L) L^2 P_{\text{WLC}}(q, L, b) dL}{\int N(L) L^2 dL} \quad (4.34)$$

The function $N(L)$ represents the number distribution of copolymer chains with contour length L , while $P_{\text{WLC}}(q, L, b)$ is the form factor for self-avoiding semi-flexible polymer chains, as described in Equation (4.17). To account for polydispersity, a Schulz-Zimm distribution was applied:^{55,87}

$$N(L) = \left(\frac{z+1}{L_{\text{avg}}} \right)^{z+1} \frac{L^z}{\Gamma(z+1)} \exp \left[-(z+1) \frac{L}{L_{\text{avg}}} \right] \quad (4.35)$$

where L_{avg} is the number-average contour length, $\Gamma(z)$ is the Gamma function and z is the distribution parameter:

$$\bar{D} = \frac{1}{z+1} \quad (4.36)$$

The copolymer dispersity was fixed at $\bar{D} = 1.1$, in all cases.

4.5.5 Polydispersity Calculation

Although GPC can be used to evaluate the molecular weight distribution of polymers, the obtained M_w , M_n and \bar{D} values are relative to the calibrants. Due to such systematic errors, the actual distribution cannot be accurately represented. To obtain more reliable absolute molecular weight information, ^1H NMR data were used to determine the number-average molecular weight M_n based on the polymer DP. Meanwhile, the absolute weight-average molecular weight $M_{w,\text{abs}}$ was obtained from MALLS measurements. A more accurate dispersity value \bar{D} was therefore calculated and used for subsequent scattering curve modelling.

The absolute dispersity is given by:

$$\bar{D}_{\text{abs}} = \frac{\text{DP} (x_1 M_1 + x_2 M_2)}{M_{w,\text{abs}}} \quad (4.37)$$

where x and M are the molar fraction and monomer molecular weight, respectively. The calculated value for the PD8020:150 copolymer is 1.1.

4.5.6 Additional SAXS Patterns and Fitting Results

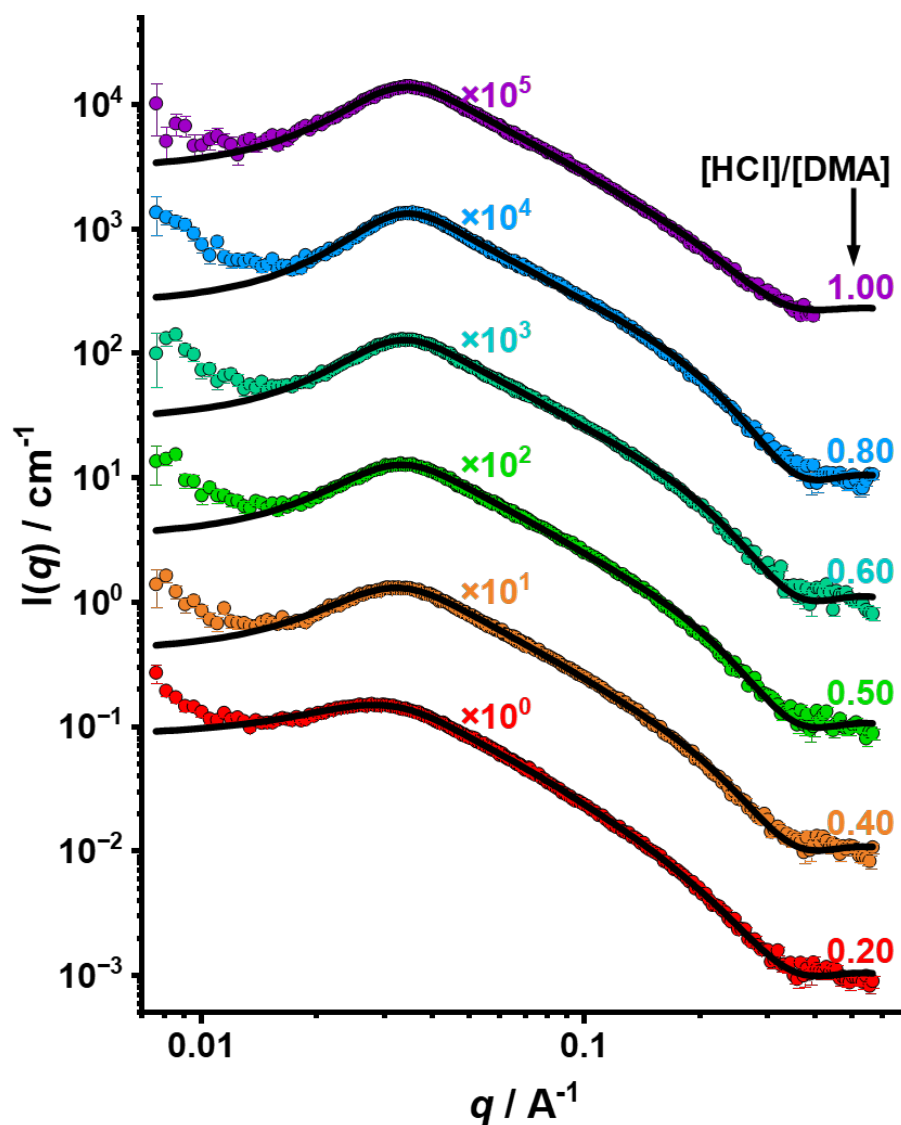


Figure 4.17: Synchrotron SAXS patterns recorded for a 1.0% w/w aqueous solution of PD6040:150 with varying degrees of protonation collected at Diamond Light Source. All scattering data were fitted using the WLC-PRISM model. The $[\text{HCl}]/[\text{DMA}]$ molar ratio is indicated on the righthand side of each curve. For clarity, some curves are vertically shifted by an arbitrary factor.

Table 4.8: Summary of SAXS data fits obtained for 1.0% w/w aqueous solutions of PD6040:150 with varying mean degrees of protonation. All scattering data were fitted using the WLC-PRISM model. The copolymer contour length and cross-sectional cylinder radius were fixed at 378 Å and 9.33 Å, respectively. The b was fitted from WLC form factor. The R_g was calculated using Equation (4.1) rather than fitted. ν , σ and R_c were calculated from the structure factor.

[HCl]/[DMA]	Form factor		Structure factor		
	$b / \text{\AA}$	$R_g / \text{\AA}$	ν	$\sigma / \text{\AA}$	$R_c / \text{\AA}$
H ₂ O	19.2 ± 1.4	41.9	1.8 ± 0.2	25.4 ± 2.5	N/A
0.20	31.0 ± 0.8	50.8	6.8 ± 0.3	39.6 ± 1.7	78.8 ± 2.0
0.40	35.7 ± 0.9	53.6	9.3 ± 0.5	40.1 ± 1.9	76.1 ± 2.5
0.60	40.9 ± 1.1	56.5	12.0 ± 0.7	39.5 ± 1.8	78.5 ± 1.9
0.80	42.5 ± 1.1	57.3	15.0 ± 0.8	38.5 ± 1.4	82.0 ± 1.2
1.00	35.9 ± 0.9	53.7	12.0 ± 0.6	39.4 ± 1.5	78.0 ± 1.6

4.6 References

- (1) B. Bolto and J. Gregory, *Water Research*, 2007, **41**, 2301–2324.
- (2) M. Chen, R. Xu, Y. Wu, J. Xiong, S. Z. Keleş and N. P. Hankins, *Journal of Water Process Engineering*, 2024, **64**, 105528.
- (3) M. Gradzielski, *Langmuir*, 2022, **38**, 13330–13343.
- (4) Q. Yang, S. Wang, P. Fan, L. Wang, Y. Di, K. Lin and F.-S. Xiao, *Chemistry of Materials*, 2005, **17**, 5999–6003.
- (5) M. Semsarilar, V. Ladmiral, A. Blanazs and S. P. Armes, *Langmuir*, 2012, **28**, 914–922.
- (6) E. Pefferkorn, *Advances in Colloid and Interface Science*, 1995, **56**, 33–104.
- (7) C. Tiyaipiboonchaiya, J. M. Pringle, J. Sun, N. Byrne, P. C. Howlett, D. R. MacFarlane and M. Forsyth, *Nature Materials*, 2004, **3**, 29–32.
- (8) X. Hu, H. Dong, N. Gao, T. Wang, H. He, X. Gao, Y. Dai, Y. Liu, D. J. Brett, I. P. Parkin and G. He, *Nature Communications*, 2025, **16**.
- (9) M. Rubinstein and G. A. Papoian, *Soft Matter*, 2012, **8**, 9265–9267.
- (10) A. Katchalsky, *Biophysical Journal*, 1964, **4**, 9–41.
- (11) C. G. Lopez, A. Matsumoto and A. Q. Shen, *Soft Matter*, 2024, **20**, 2635–2687.
- (12) M. Muthukumar, *Macromolecules*, 2017, **50**, 9528–9560.
- (13) L. Nová, F. Uhlík and P. Košovan, *Physical Chemistry Chemical Physics*, 2017, **19**, 14376–14387.
- (14) A. V. Dobrynin and M. Rubinstein, *Progress in Polymer Science*, 2005, **30**, 1049–1118.
- (15) L. Zheng, H. S. Sundaram, Z. Wei, C. Li and Z. Yuan, *Reactive and Functional Polymers*, 2017, **118**, 51–61.
- (16) L. D. Blackman, P. A. Gunatillake, P. Cass and K. E. S. Locock, *Chemical Society Reviews*, 2019, **48**, 757–770.

- (17) E. Kharlampieva and S. A. Sukhishvili, *Macromolecules*, 2003, **36**, 9950–9956.
- (18) L. Li, A. M. Rumyantsev, S. Srivastava, S. Meng, J. J. de Pablo and M. V. Tirrell, *Macromolecules*, 2021, **54**, 105–114.
- (19) A. Takahashi and M. Nagasawa, *Journal of the American Chemical Society*, 1964, **86**, 543–548.
- (20) L. Cannavacciuolo, C. Sommer, J. S. Pedersen and P. Schurtenberger, *Physical Review E*, 2000, **62**, 5409–5419.
- (21) M. Fixman and J. Skolnick, *Macromolecules*, 1978, **11**, 863–867.
- (22) Z.-G. Wang, *Macromolecules*, 2017, **50**, 9073–9114.
- (23) P.-G. de Gennes, P. Pincus, R. M. Velasco and F. Brochard, *J. Phys. France*, 1976, **37**, 1461–1473.
- (24) N. Volk, D. Vollmer, M. Schmidt, W. Oppermann and K. Huber, in *Polyelectrolytes with Defined Molecular Architecture II*, ed. M. Schmidt, Springer, Heidelberg, Germany, 2004, ch. 2, pp. 29–65.
- (25) M. Borkovec, G. J. M. Koper and C. Piguet, *Current Opinion in Colloid & Interface Science*, 2006, **11**, 280–289.
- (26) P. M. Blanco, S. Madurga, F. Mas and J. L. Garcés, *Macromolecules*, 2019, **52**, 8017–8031.
- (27) T. Kitano, A. Taguchi, I. Noda and M. Nagasawa, *Macromolecules*, 1980, **13**, 57–63.
- (28) C. Sommer, J. S. Pedersen, S. U. Egelhaaf, L. Cannavacciuolo, J. Kohlbrecher and P. Schurtenberger, *Langmuir*, 2002, **18**, 2495–2505.
- (29) V. Y. Borue and I. Y. Erukhimovich, *Macromolecules*, 1988, **21**, 3240–3249.
- (30) A. Moussaid, F. Schosseler, J. P. Munch and S. J. Candau, *J. Phys. II France*, 1993, **3**, 573–594.

- (31) C. Svaneborg and J. S. Pedersen, *Current Opinion in Colloid & Interface Science*, 2004, **8**, 507–514.
- (32) M. Ullner, G. Staikos and D. N. Theodorou, *Macromolecules*, 1998, **31**, 7921–7933.
- (33) B. Chu and B. S. Hsiao, *Chemical Reviews*, 2001, **101**, 1727–1762.
- (34) M. Ballauff, *Current Opinion in Colloid & Interface Science*, 2001, **6**, 132–139.
- (35) P. S. Russo, K. A. Streletzky, W. Huberty, X. Zhang and N. Edwin, in *Molecular Characterization of Polymers*, ed. M. I. Malik, J. Mays and M. R. Shah, Elsevier, Amsterdam, Netherlands, 2021, ch. 13, pp. 499–532.
- (36) *6 sample pitfalls to look out for when preparing for SAXS experiments*, <https://www.xenocs.com/saxs-sample-preparation-6-sample-pitfalls-to-look-out-for/>, (accessed May 2025).
- (37) O. Kratky and G. Porod, *Journal of Colloid Science*, 1949, **4**, 35–70.
- (38) A. M. Gupta and S. F. Edwards, *Polymer*, 1993, **34**, 3112–3114.
- (39) S. P. O. Danielsen, C. R. Bridges and R. A. Segalman, *Macromolecules*, 2022, **55**, 437–449.
- (40) B. Kuei and E. D. Gomez, *Soft Matter*, 2017, **13**, 49–67.
- (41) H. K. Murnen, A. M. Rosales, A. V. Dobrynin, R. N. Zuckermann and R. A. Segalman, *Soft Matter*, 2013, **9**, 90–98.
- (42) O. O. Mykhaylyk, in *Neutrons, X-rays, and Light*, ed. P. Lindner and J. Oberdisse, Elsevier, Amsterdam, Netherlands, 2nd edn., 2025, ch. 2, pp. 19–59.
- (43) W. Kuhn, *Kolloid-Zeitschrift*, 1936, **76**, 258–271.
- (44) N. Sherck, T. Webber, D. R. Brown, T. Keller, M. Barry, A. DeStefano, S. Jiao, R. A. Segalman, G. H. Fredrickson, M. S. Shell and S. Han, *Journal of the American Chemical Society*, 2020, **142**, 19631–19641.

- (45) A. J. DeStefano, S. D. Mengel, M. W. Bates, S. Jiao, M. S. Shell, S. Han and R. A. Segalman, *Macromolecules*, 2024, **57**, 1469–1477.
- (46) C. J. Thompson and A. J. Ryan, in *Neutrons, X-rays, and Light*, ed. P. Lindner and J. Oberdisse, Elsevier, Amsterdam, Netherlands, 2nd edn., 2025, ch. 11, pp. 285–310.
- (47) J. S. Pedersen and P. Schurtenberger, *Macromolecules*, 1996, **29**, 7602–7612.
- (48) J. S. Pedersen and M. C. Gerstenberg, *Macromolecules*, 1996, **29**, 1363–1365.
- (49) L. Cannavacciuolo, J. S. Pedersen and P. Schurtenberger, *Langmuir*, 2002, **18**, 2922–2932.
- (50) K. S. Schweizer and J. G. Curro, in *Atomistic Modeling of Physical Properties*, ed. L. Monnerie and U. W. Suter, Springer, Heidelberg, Germany, 1994, ch. 9, pp. 319–377.
- (51) J. S. Pedersen and P. Schurtenberger, *Journal of Polymer Science, Part B: Polymer Physics*, 2004, **42**, 3081–3094.
- (52) J. B. Hayter, Jeff and Penfold, *Molecular Physics*, 1981, **42**, 109–118.
- (53) J. Jennings, R. R. Webster-Aikman, N. Ward-O’Brien, A. Xie, D. L. Beattie, O. J. Deane, S. P. Armes and A. J. Ryan, *ACS Applied Materials & Interfaces*, 2022, **14**, 39548–39559.
- (54) W. Huang, W. Gu, H. Yang, X. Xue, B. Jiang, D. Zhang, J. Fang, J. Chen, Y. Yang and J. Guo, *Polymers*, 2017, **9**, 14.
- (55) B. H. Zimm, *The Journal of Chemical Physics*, 1948, **16**, 1093–1099.
- (56) A. J. Smith, S. G. Alcock, L. S. Davidson, J. H. Emmins, J. C. Hiller Bardsley, P. Holloway, M. Malfois, A. R. Marshall, C. L. Pizzey, S. E. Rogers, O. Shebanova, T. Snow, J. P. Sutter, E. P. Williams and N. J. Terrill, *Journal of Synchrotron Radiation*, 2021, **28**, 939–947.
- (57) SASView, <https://www.sasview.org/>, (accessed May 2025).
- (58) J. S. Pedersen, *Advances in Colloid and Interface Science*, 1997, **70**, 171–210.

- (59) S. U. Egelhaaf and P. N. Pusey, in *Neutrons, X-rays, and Light*, ed. P. Lindner and J. Oberdisse, Elsevier, Amsterdam, Netherlands, 2nd edn., 2025, ch. 8, pp. 211–238.
- (60) S. Perrier, *Macromolecules*, 2017, **50**, 7433–7447.
- (61) J. Chiefari, Y. K. (Bill) Chong, F. Ercole, J. Krstina, J. Jeffery, T. P. T. Le, R. T. A. Mayadunne, G. F. Meijs, C. L. Moad, G. Moad, E. Rizzardo and S. H. Thang, *Macromolecules*, 1998, **31**, 5559–5562.
- (62) N. J. Warren and S. P. Armes, *Journal of the American Chemical Society*, 2014, **136**, 10174–10185.
- (63) D. Fournier, R. Hoogenboom, H. M. L. Thijs, R. M. Paulus and U. S. Schubert, *Macromolecules*, 2007, **40**, 915–920.
- (64) P. Quiñonez-Angulo, J. Ruiz-Villegas, Á. Licea-Claveríe, A. Ramirez-Jiménez, V. Miranda-Soto and I. Zapata-González, *European Polymer Journal*, 2018, **109**, 347–359.
- (65) N. M. Ahmad, F. Heatley and P. A. Lovell, *Macromolecules*, 1998, **31**, 2822–2827.
- (66) M. Fineman and S. D. Ross, *Journal of Polymer Science*, 1950, **5**, 259–262.
- (67) J. P. Kennedy, T. Kelen and F. Tüdös, *Journal of Polymer Science: Polymer Chemistry Edition*, 1975, **13**, 2277–2289.
- (68) V. E. Meyer and G. G. Lowry, *Journal of Polymer Science Part A: General Papers*, 1965, **3**, 2843–2851.
- (69) F. R. Mayo and F. M. Lewis, *Journal of the American Chemical Society*, 1944, **66**, 1594–1601.
- (70) T. Kelen, F. Tüdös, B. Turcsányi and J. P. Kennedy, *Journal of Polymer Science: Polymer Chemistry Edition*, 1977, **15**, 3047–3074.
- (71) A. B. Lowe, N. C. Billingham and S. P. Armes, *Macromolecules*, 1998, **31**, 5991–5998.

- (72) L. Cervera Gontard, D. Ozkaya and R. E. Dunin-Borkowski, *Ultramicroscopy*, 2011, **111**, 101–106.
- (73) K. Chen, A. Kromin, M. P. Ulmer, B. W. Wessels and V. Backman, *Optics Communications*, 2003, **228**, 1–7.
- (74) O. Casse, A. Shkilnyy, J. Linders, C. Mayer, D. Häussinger, A. Völkel, A. F. Thünemann, R. Dimova, H. Cölfen, W. Meier, H. Schlaad and A. Taubert, *Macromolecules*, 2012, **45**, 4772–4777.
- (75) D. Gentili and G. Ori, *Nanoscale*, 2022, **14**, 14385–14432.
- (76) R. Pecora, *Journal of nanoparticle research*, 2000, **2**, 123–131.
- (77) S. Förster, M. Schmidt and M. Antonietti, *Polymer*, 1990, **31**, 781–792.
- (78) J. S. Pedersen and P. Schurtenberger, *Europhysics Letters*, 1999, **45**, 666.
- (79) J. S. Pedersen and P. Schurtenberger, *Journal of Polymer Science Part B: Polymer Physics*, 2004, **42**, 3081–3094.
- (80) S. Förster, N. Hermsdorf, C. Böttcher and P. Lindner, *Macromolecules*, 2002, **35**, 4096–4105.
- (81) P. Debye, *The Journal of Physical and Colloid Chemistry*, 1947, **51**, 18–32.
- (82) R. Everaers, A. Y. Grosberg, M. Rubinstein and A. Rosa, *Soft Matter*, 2017, **13**, 1223–1234.
- (83) P.-G. de Gennes, *J. Physique Lett.*, 1975, **36**, 55–57.
- (84) N. M. Bin Li and A. D. Sokal, *J. Stat. Phys.*, 1995, **80**, 661–754.
- (85) B. Hammouda, in *Polymer Characteristics*, Springer, Heidelberg, Germany, 1993, ch. 3, pp. 87–133.
- (86) G. Jerke, J. S. Pedersen, S. U. Egelhaaf and P. Schurtenberger, *Langmuir*, 1998, **14**, 6013–6024.

- (87) G. Schulz, *Phys. Chem, Abt. B*, 1939, **43**, 25.
- (88) M. Fushiki, *The Journal of Chemical Physics*, 1988, **89**, 7445–7453.
- (89) J. M. Mendez-Alcaraz, B. D’Aguanno and R. Klein, *Langmuir*, 1992, **8**, 2913–2920.
- (90) F. J. Rogers and D. A. Young, *Phys. Rev. A*, 1984, **30**, 999–1007.
- (91) S. L. Perry and C. E. Sing, *Macromolecules*, 2015, **48**, 5040–5053.
- (92) G. S. Manning, *The Journal of Chemical Physics*, 1969, **51**, 924–933.
- (93) R. R. Netz and J.-F. Joanny, *Macromolecules*, 1999, **32**, 9026–9040.
- (94) R. Everaers, A. Milchev and V. Yamakov, *Eur. Phys. J. E*, 2002, **8**, 3–14.
- (95) A. G. Moreira and R. R. Netz, *Europhysics Letters*, 2000, **52**, 705.
- (96) A. Naji, M. Kanduč, J. Forsman and R. Podgornik, *The Journal of Chemical Physics*, 2013, **139**, 150901.
- (97) T. J. Neal, A. J. Parnell, S. M. King, D. L. Beattie, M. W. Murray, N. S. J. Williams, S. N. Emmett, S. P. Armes, S. G. Spain and O. O. Mykhaylyk, *Macromolecules*, 2021, **54**, 1425–1440.
- (98) P.-G. de Gennes, *Scaling concepts in polymer physics*, Cornell University Press, Ithaca, NY, USA, 1979.
- (99) T. Lodge, *Microchim. Acta*, 1994, **116**, 1–31.
- (100) A. V. Dobrynin, R. H. Colby and M. Rubinstein, *Macromolecules*, 1995, **28**, 1859–1871.
- (101) W. Essafi, F. Lafuma and C. E. Williams, *Journal de Physique II*, 1995, **5**, 1269–1275.
- (102) L. N. Andreeva, S. V. Bushin, M. A. Bezrukova, T. N. Nekrasova, R. T. Imanbaev, V. D. Pautov, O. V. Nazarova, Y. I. Zolotova and E. F. Panarin, *Russian Journal of Applied Chemistry*, 2012, **85**, 417–425.

- (103) P. Flory, *Statistical Mechanics of Chain Molecules*, Interscience Publishers, New York, USA, 1969.
- (104) M. Wittkop, S. Kreitmeier and D. Göritz, *The Journal of Chemical Physics*, 1996, **104**, 3373–3385.
- (105) J. C. Le Guillou and J. Zinn-Justin, *Phys. Rev. Lett.*, 1977, **39**, 95–98.
- (106) S. S. Jang, T. Çağın and I. Goddard, William A., *The Journal of Chemical Physics*, 2003, **119**, 1843–1854.
- (107) R. J. McBride, J. F. Miller, A. Blanz, H.-J. Hähnle and S. P. Armes, *Macromolecules*, 2022, **55**, 7380–7391.
- (108) B. A. Rogers, H. I. Okur, C. Yan, T. Yang, J. Heyda and P. S. Cremer, *Nature Chemistry*, 2022, **14**, 40–45.
- (109) N. Cao, Y. Zhao, H. Chen, J. Huang, M. Yu, Y. Bao, D. Wang and S. Cui, *Macromolecules*, 2022, **55**, 4656–4664.
- (110) C. Maltesh and P. Somasundaran, *Langmuir*, 1992, **8**, 1926–1930.
- (111) A. Aksimentiev and R. Hołyst, *Progress in Polymer Science*, 1999, **24**, 1045–1093.
- (112) M. Doi, S. F. Edwards and S. F. Edwards, *The theory of polymer dynamics*, Oxford University Press, Oxford, UK, 1988, vol. 73.
- (113) H. Yamakawa, *Modern theory of polymer solutions*, Harper & Row, New York, USA, 1971.
- (114) T. Yoshizaki and H. Yamakawa, *Macromolecules*, 1980, **13**, 1518–1525.
- (115) P. Sharp and V. A. Bloomfield, *Biopolymers*, 1968, **6**, 1201–1211.
- (116) J. S. Pedersen, in *Neutrons, X-rays, and Light*, ed. P. Lindner and J. Oberdisse, Elsevier, Amsterdam, Netherlands, 2nd edn., 2025, ch. 15, pp. 401–451.
- (117) T. Ohta and Y. Oono, *Physics Letters A*, 1982, **89**, 460–464.

-
- (118) Y. Oono and K. F. Fred, *Journal of Physics A: Mathematical and General*, 1982, **15**, 1931.
- (119) B. Fehér, A. Wacha, B. Jezsó, A. Bóta, J. S. Pedersen and I. Varga, *Journal of Colloid and Interface Science*, 2023, **651**, 992–1007.
- (120) V. Chappa, Y. Smirnova, K. Komorowski, M. Müller and T. Salditt, *Journal of Applied Crystallography*, 2021, **54**, 557–568.

Chapter 5

Synthesis of Amphiphilic Statistical Copolymers with a Highly Flexible Backbone

5.1 Introduction

The chemical structure of the polymer backbone can significantly affect the physical properties of a polymer, including its thermal stability, mechanical strength, solubility and processability.¹ For example, as shown in Figure 5.1, poly(methyl acrylate) (PMA) is composed of highly mobile chains, while poly(methyl methacrylate) (PMMA) chains are much less flexible owing to the additional methyl group within every monomer repeat unit, which increases the steric hindrance.¹ This structural difference is reflected in the glass transition temperatures (T_g) of the two polymers: the T_g of PMA is about 10 °C,² while the T_g of PMMA is about 105 °C,³ indicating that PMA chains exhibit higher segment mobility at room temperature.

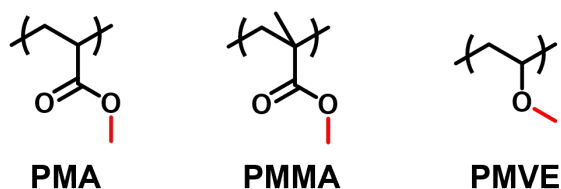


Figure 5.1: Chemical structures of PMA, PMMA and PMVE.

In the previous chapters, acrylic copolymers significantly outperformed their methacrylic counterparts in terms of their foam performance. Thus chain flexibility appears to be an important parameter for surface activity.⁴ In this chapter, vinyl ether-based monomers bearing similar side chains were prepared and polymerised in an attempt to target even more flexible backbones to further optimise the foamability performance of statistical copolymer surfactants.

Compared with the ester side groups contained in PMMA or PMA, the ether side groups in poly(vinyl ethers) (PVE) have lower steric hindrance and higher rotational freedom.⁵ This structural feature should aid the rapid rearrangement of PVE-based amphiphilic copolymer chains at the air-water interface. Taking poly(methyl vinyl ether) (PMVE) as an example (see Figure 5.1), its glass transition temperature is around –31 °C.⁶ Thus, for the same methoxy substituent, PVE < PMA < PMMA, in terms of T_g values, which can be taken as a proxy for chain mobility. In principle, a wide range of vinyl ether monomers can be readily prepared via

transesterification of a suitable commercially available vinyl ether monomer.⁷

Vinyl ether polymers are usually prepared by cationic polymerisation, which involves carbocations as the active chain-end.^{5,8} Due to the high reactivity of such carbocations, cationic polymerisation is extremely sensitive to moisture.¹ Hence low temperature, anhydrous and moisture-free conditions are required to ensure successful syntheses.¹ Commonly used initiators include Lewis acids such as AlCl_3 , TiCl_4 or SnCl_4 combined with a proton source (e.g. alcohols or trace water).^{1,9,10}

Pioneering systematic studies have been reported by Aoshima et al., who designed a series of amphiphilic cationic copolymers.^{8,11,12} In addition, Forder et al. prepared a series of water-soluble poly(vinyl ether)-based block copolymers via living cationic polymerisation.¹³ These latter studies focused on the copolymerisation of various hydrophilic and hydrophobic vinyl ethers such as methyl vinyl ether, tri(ethylene glycol) vinyl ether, iso-butyl vinyl ether, and benzyl vinyl ether.^{14–17} Normally, free radical polymerisation is not considered suitable for vinyl ethers. Nevertheless, Sugihara and co-workers reported the successful copolymerisation of several hydrophilic and hydrophobic vinyl ethers, providing potential for the realisation of free radical copolymerisation.¹⁸

In this chapter, the two desired vinyl ethers, TMHVE and MPEGVE, were prepared via transesterification starting from ethyl vinyl ether (see Figure 5.2). Subsequently, various synthesis conditions were evaluated for the preparation of amphiphilic statistical copolymers based on these two monomers.

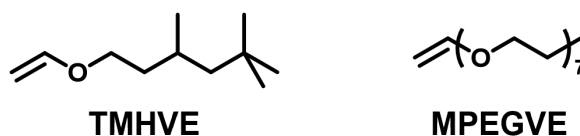


Figure 5.2: Chemical structures of the hydrophobic TMHVE and hydrophilic MPEGVE monomers prepared via transesterification in this chapter.

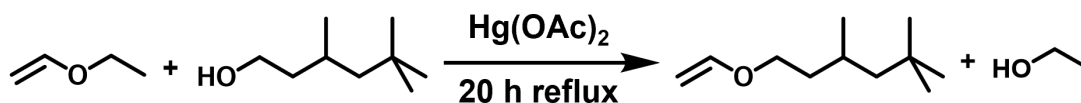
5.2 Experimental

5.2.1 Materials

Ethyl vinyl ether (EVE, > 99%, Sigma-Aldrich, UK) was purified by filtration over basic alumina, followed by drying over anhydrous potassium carbonate (K_2CO_3). The purified EVE was then distilled from freshly cut chunks of sodium metal and then stored in a $-20\text{ }^{\circ}\text{C}$ freezer prior to use. Mercuric acetate ($Hg(OAc)_2$, ACS reagent, $\geq 98.0\%$, Sigma-Aldrich, UK) was recrystallised from absolute ethanol and dried under vacuum prior to use. This compound is light-sensitive, so all operations were performed with glassware wrapped in aluminium foil to minimise light exposure. 3,5,5-Trimethyl-1-hexanol (TMHALC, $\geq 85\%$, Sigma-Aldrich, UK) was freeze-dried and then stored in a $-20\text{ }^{\circ}\text{C}$ freezer before use. Methoxy-capped poly(ethylene glycol) (MPEG₃₅₀) was kindly donated by GEO Specialty Chemicals, UK. This precursor was dried by fractional distillation from a toluene solution to remove water and afford a solution of MPEG₃₅₀ in dry toluene, which was then stored in a $-20\text{ }^{\circ}\text{C}$ freezer before use. Lithium hydroxide (LiOH, 99.9%, Sigma-Aldrich, UK), aluminium chloride ($AlCl_3$, anhydrous, Sigma-Aldrich, UK) and titanium tetrachloride ($TiCl_4$, 99.9%, Sigma-Aldrich, UK) were used as received. Methanol was purchased from Fisher Scientific, UK and used as received. Dry dichloromethane (DCM) was obtained from an in-house Grubbs dry solvent system. MilliQ water was obtained from an Elga Elgastat Option 3A Water Purifier system.

5.2.2 Synthesis of Vinyl Ether Monomers

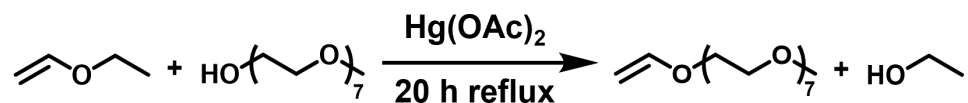
Synthesis of 3,5,5-Trimethylhexyl Vinyl Ether (TMHVE)



Scheme 5.1: Synthesis of 3,5,5-trimethylhexyl vinyl ether (TMHVE) from ethyl vinyl ether by transesterification using a $\text{Hg}(\text{OAc})_2$ catalyst.

The synthesis of 3,5,5-trimethylhexyl vinyl ether (TMHVE) monomer was conducted by transesterification as described by Watanabe et al.⁷ This method was employed to prepare each comonomer for subsequent copolymerisations. Accordingly, recrystallised mercuric acetate (3.00 g) was added to a solution of 3,5,5-trimethyl-1-hexanol (50.0 ml) in purified ethyl vinyl ether (240 ml) in a 500 ml two-neck round-bottom flask. The solution was refluxed for 15 h, followed by addition of a further 1.50 g of mercuric acetate, and refluxing was continued for another 5 h (Scheme 5.1). After cooling, the reaction mixture was washed three times with 10% K_2CO_3 aqueous solution to remove the spent catalyst. The washed solution was then dried over anhydrous K_2CO_3 . The resulting mixture was stirred over freshly cut sodium for three days to remove alcoholic by-products. The filtered mixture was distilled to collect a low-boiling fraction (30 ~ 31 °C), while the crude product remained in the flask. The crude TMHVE was washed several times with deionised water and dried again over K_2CO_3 , followed by an additional treatment with sodium to eliminate any residual alcohol or water impurities. The final filtration yielded a pale yellow, transparent oily liquid identified as 3,5,5-trimethylhexyl vinyl ether (18.86 g, 46%). This monomer was characterised by gas chromatography-mass spectrometry and ^1H NMR spectroscopy and stored in a -20 °C freezer prior to use. ^1H NMR (CDCl_3 , 400 MHz) δ = 6.46 (dd, 1H), 4.16 (dd, 1H), 3.96 (dd, 1H), 3.68 (t, 2H), 1.00 - 1.80(m, 5H), 0.95 (d, 3H), 0.89 (s, 9H).

Synthesis of Methoxy Poly(ethylene glycol) Vinyl Ether (MPEGVE)



Scheme 5.2: Synthesis of methoxy poly(ethylene) vinyl ether (MPEGVE) from ethyl vinyl ether by transesterification using a $\text{Hg}(\text{OAc})_2$ catalyst.

A similar reaction strategy was used to prepare methoxypoly(ethylene glycol) vinyl ether (MPEGVE), as described above. Recrystallised mercuric acetate (2.55 g) was added to a solution of methoxy-capped poly(ethylene glycol) precursor (77.0 ml) in purified ethyl vinyl ether (228.0 ml) in a two-neck round-bottom flask (500 mL). The solution was then refluxed for 20 h, followed by addition of a further charge of mercuric acetate (1.27 g) and then refluxing for another 5 h (Scheme 5.2). After cooling, the solution was purified using the same protocol described above. However, the reaction mixture was first washed and then concentrated by rotary evaporation to remove the majority of unreacted ethyl vinyl ether prior to distillation. The final filtration yielded a colourless transparent oily liquid, methoxy(polyethylene glycol) vinyl ether (5.88 g, 7%). This monomer was characterised by gas chromatography-mass spectrometry and ^1H NMR spectroscopy and stored in a -20°C freezer prior to use. ^1H NMR (CDCl_3 , 400 MHz) δ = 6.46 (dd, 1H), 4.14 (dd, 1H), 3.96 (dd, 1H), 3.61 (m, PEG), 3.34 (s, 3H).

5.2.3 Copolymerisation of TMHVE with MPEGVE

Table 5.1: Summary of statistical copolymerisations of TMHVE with MPEGVE

TMHVE / g	MPEGVE / g	Polymerisation method	Solvent	Initiator	Conversion
0.10	1.00	FRP	Bulk	AIBN	71%
0.10	1.00	FRP	MeOH/LiOH	AIBN	73%
0.50	N/A	Cationic	Dry DCM	TiCl_4	> 99%
0.50	1.00	Cationic	Dry DCM	TiCl_4	Unsuccessful

Synthesis of Poly(TMHE-*stat*-MPEGVE) via Free Radical Copolymerisation

Free radical copolymerisation was evaluated to target the amphiphilic statistical copolymers shown in Table 5.1. AIBN (10.9 mg, 0.07 mmol) was weighed into a 5 ml glass vial, followed by TMHVE (100.5 mg, 0.59 mmol) and MPEGVE (900.0 mg, 2.31 mmol) to target a TMHVE-MPEGVE copolymer with a [TMHVE]:[MPEGVE] mass ratio of 10:90 using 1.0% w/w initiator based on the total mass of comonomer. Polymerisation was performed either in the bulk using AIBN initiator alone or in polymerisation using the same initiator with a catalyst. In the latter case, lithium hydroxide catalyst (7.4 mg, 0.18 mmol) and water co-catalyst (0.10 g) were added to the reaction mixture, followed by 5.00 g of methanol, see Table 5.1. This mixture was vortex-mixed for 30 s and then sealed using a rubber septum after addition of a magnetic stir bar. The solution was degassed with the aid of an ice bath using a stream of nitrogen gas for 30 min and then immersed in an oil bath set at 70 °C with continuous stirring under a nitrogen atmosphere for 16 h. The copolymerisation was quenched by exposing the reaction mixture to air while cooling to room temperature. The overall comonomer conversion and copolymer composition were determined by ^1H NMR spectroscopy (CDCl_3) while molecular weight and dispersity data were obtained by DMF GPC.

Synthesis of PTMHVE via Cationic Polymerisation Using either TiCl_4 as an Initiator.

Dry TMHVE (500.0 mg, 2.95 mmol) was dissolved in dry DCM (2.0 ml) in a 10 ml round bottom flask, which was sealed using a rubber septum after the addition of a magnetic stir bar. This reaction solution was degassed using a stream of nitrogen gas and cooled using a dry ice/acetone bath for 30 min. TiCl_4 (3.5 μL , 0.03 mmol) was added to the mixture under a nitrogen atmosphere using a dry gas-tight glass syringe to initiate the polymerisation, which was quenched by adding methanol after 3 h. The overall monomer conversion was determined by ^1H NMR spectroscopy (CD_2Cl_2) while molecular weight and dispersity were obtained by DMF GPC.

5.2.4 Characterisation Methods

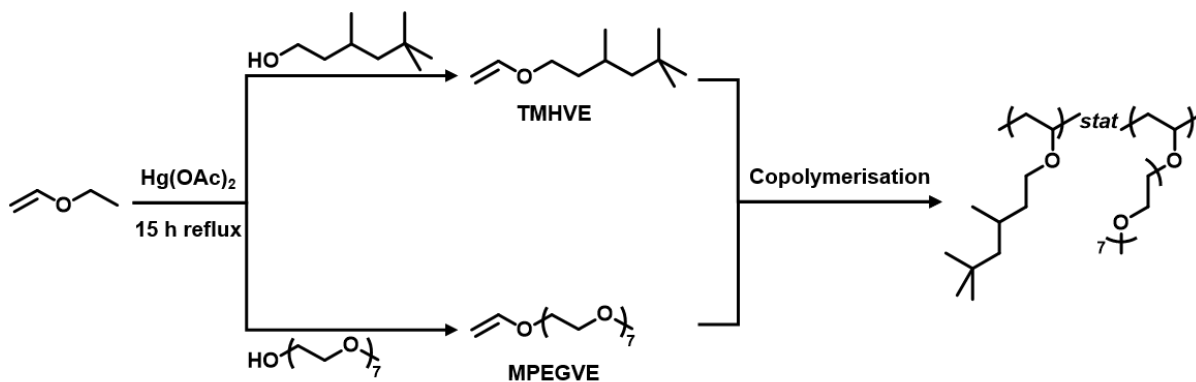
¹H NMR Spectroscopy

Spectra were recorded in either CDCl₃ or CD₂Cl₂ at 25 °C using 400 MHz Bruker Avance-400 spectrometer with 64 scans being averaged per spectrum.

Gel Permeation Chromatography (GPC) with DMF Eluent

Molecular weight data were obtained using an Agilent 1260 Infinity GPC system, which included a pump, degasser, and two PL-gel 5µm Mixed-C columns connected in series, equipped with both UV and refractive index detectors. HPLC-grade DMF containing 0.02% w/w LiBr was used as the eluent, the column and detector temperature was set to 60 °C, and the flow rate was 1.0 mL·min⁻¹. Near-monodisperse poly(methyl methacrylate) standards ranging from 370 to 2,520,000 g·mol⁻¹ were employed for calibration, with data analysed using Agilent Technologies GPC/SEC software.

5.3 Results and Discussion



Scheme 5.3: Overall reaction scheme for the synthesis of statistical copolymers comprising TMHVE and MPEGVE.

As shown in Scheme 5.3, two vinyl ether-based monomers, MPEGVE (hydrophilic) and TMHVE (hydrophobic), were synthesised by transesterification. These two comonomers were selected based on the optimal acrylic copolymer structure indicated by ANOVA analysis in chapter 2. Subsequently, the two comonomers were statistically copolymerised by either free radical or cationic copolymerisation to prepare amphiphilic statistical copolymers comprising highly flexible PVE-based backbones. Such copolymers were anticipated to exhibit enhanced foam stabilisation performance.

5.3.1 Preparation of 3,5,5-Trimethylhexyl Vinyl Ether (TMHVE) Monomer

The TMHVE monomer was prepared by transesterification using 3,5,5-trimethyl-1-hexanol and ethyl vinyl ether. The latter reagent was selected for its affordability and because its corresponding ethanol by-product is relatively volatile, which aids its efficient removal. Mercuric acetate was used as the transesterification catalyst.⁷ The purified target monomer was isolated as an oily pale-yellow liquid and its chemical structure was confirmed by ¹H NMR spectroscopy and GC-MS analysis, see Figure 5.3 and 5.4. Characteristic NMR signals corresponding to the expected

chemical environments were observed. A signal at 6.50 ppm (dd, signal A) was assigned to the vinyl proton adjacent to the ether group. Two doublets between 3.90 - 4.20 ppm (signal B and C) were assigned to the other two non-equivalent vinyl protons located further from the ether group. The remaining signals were consistent with the aliphatic protons of the hydrocarbon chain. However, overlapping chemical shifts and extensive multiplet patterns prevents more detailed proton assignment for this pendant branched alkyl group. During distillation, only one low-boiling fraction was collected at 30 - 31 °C, which was identified by ^1H NMR analysis as unreacted ethyl vinyl ether. In addition, the mass spectrum of the purified monomer exhibited a parent ion signal at $m/z = 170$ Da, which is in good agreement with the calculated molecular weight of TMHVE. These analytical data are consistent with the successful synthesis of the desired compound.

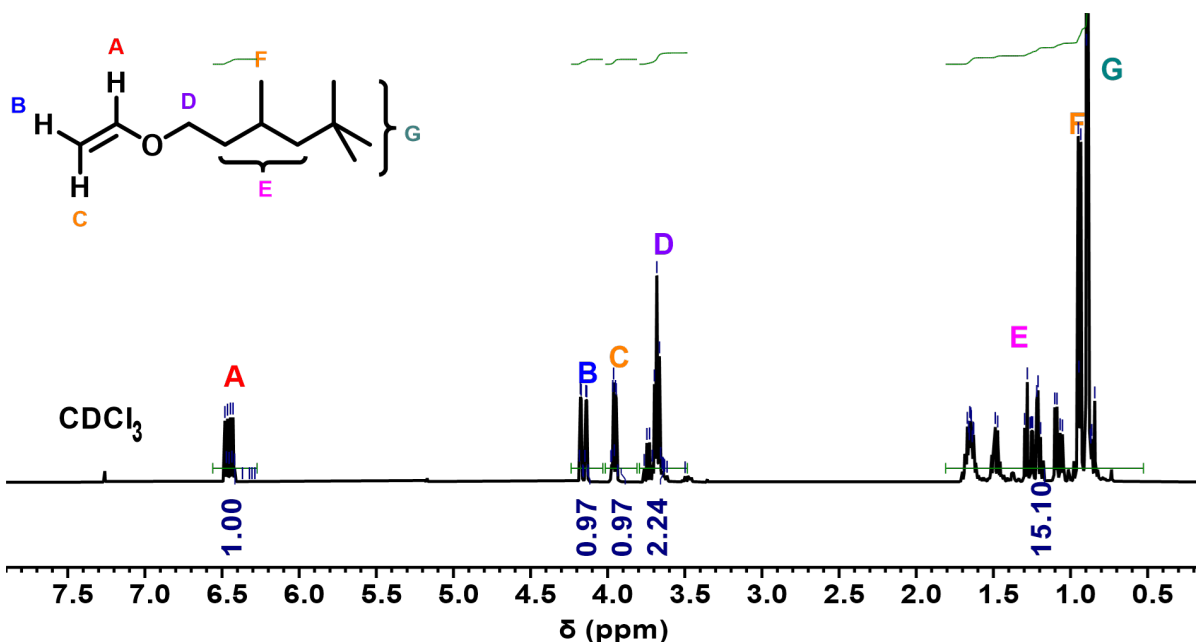


Figure 5.3: Assigned ^1H NMR spectrum (CDCl_3) for the purified TMHVE.

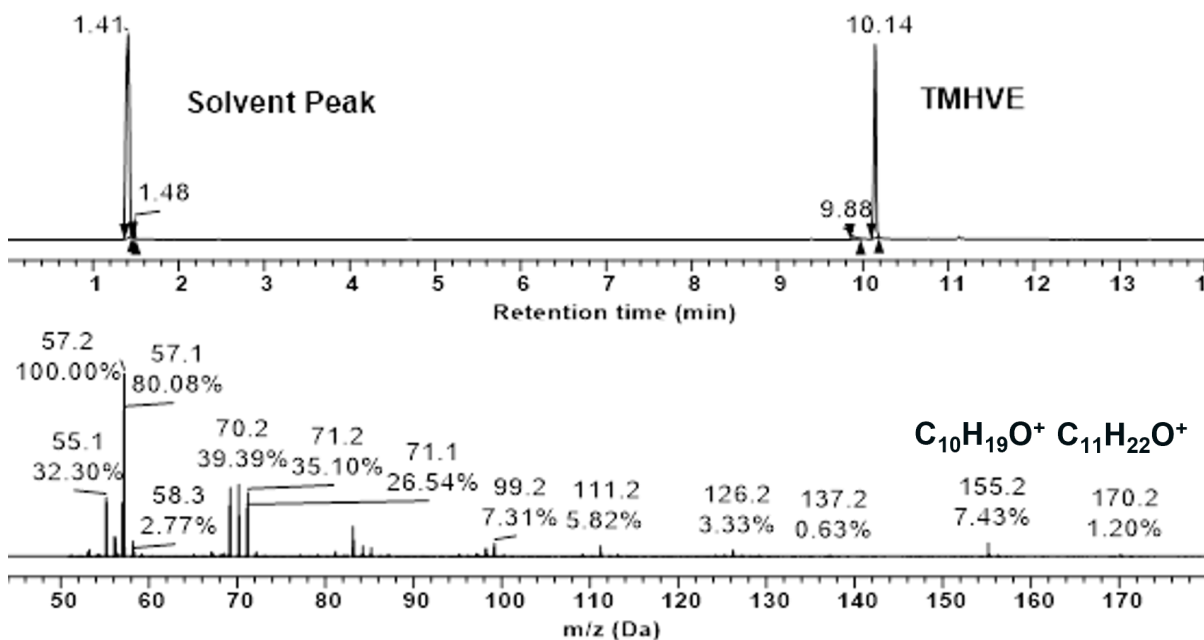


Figure 5.4: GC-MS data for the purified TMHVE.

5.3.2 Preparation of Methoxy Poly(ethylene glycol) Vinyl Ether (MPEGVE) Monomer

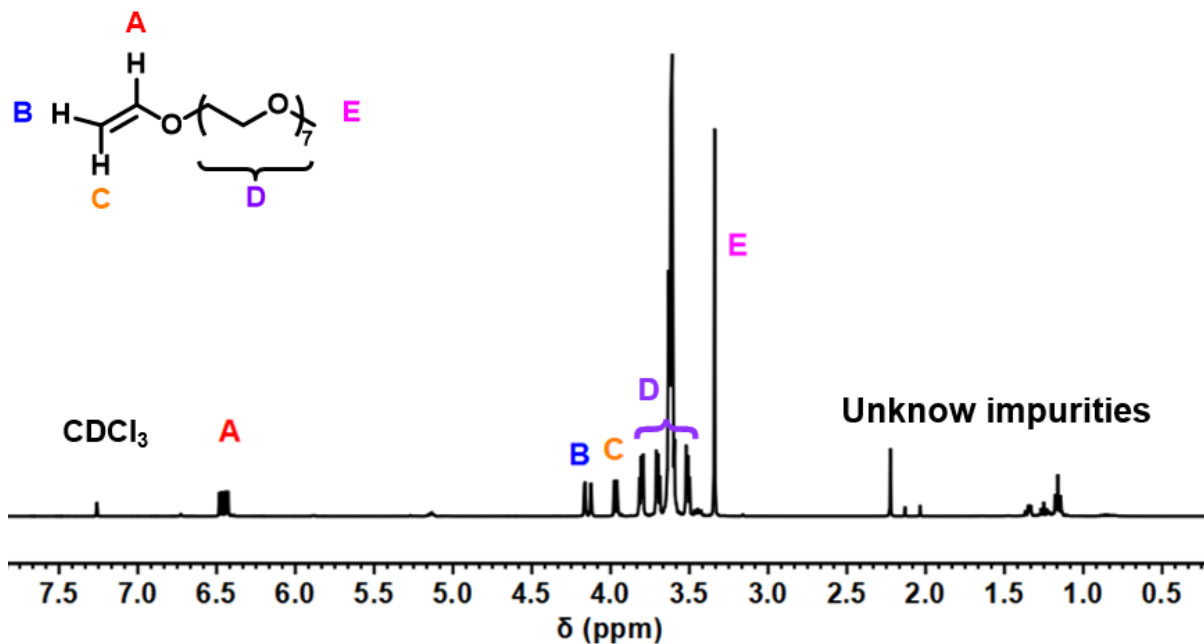


Figure 5.5: Assigned 1H NMR spectrum ($CDCl_3$) for the purified MPEGVE.

The MPEGVE monomer was prepared by transesterification of ethyl vinyl ether using methoxy-capped poly(ethylene glycol). The purified product was isolated as a colourless transparent oily liquid and its chemical structure was confirmed by ^1H NMR spectroscopy and GC-MS analysis. Inspecting the ^1H NMR spectrum, signals A, B and C were assigned to the three vinyl protons. The multiplet signals at 3.61 ppm (signal D) were assigned to the oxyethylene protons within the PEG side-chain. The singlet at 3.34 ppm was assigned to the terminal methoxy group. However, unexpected additional signals were also observed at low chemical shifts. Such signals remained visible even after repeated purification. The combined integrated intensities of these peaks are relatively low compared to those of the expected monomer signals. It is estimated that the monomer purity is approximately 93%. Considering their low chemical shifts, it is plausible that these minor impurity signals arise from hydrocarbon contaminants originating from CDCl_3 . Poly(ethylene glycol) usually appears as a series of characteristic peaks in mass spectrometry analysis, with a spacing of 44 Da between adjacent peaks that corresponds to the mass of the $-\text{CH}_2\text{CH}_2\text{O}-$ repeat unit. This polydispersity effect is problematic for GC-MS analysis of the MPEGVE monomer. Owing to this distribution of PEG chain lengths, there is no unique parent ion, which masks the rather small molecular weight difference between MPEGVE and MPEG.

5.3.3 Free Radical Copolymerisation Synthesis of P(TMHE-*stat*-MPEGVE)

It is well known that vinyl ethers are not normally amenable to free radical polymerisation. This is because vinyl ether radicals are relatively unstable and hence prone to side-reactions such as β -cleavage and hydrogen transfer.¹ However, Sugihara et al. reported a method for preparing poly(vinyl ethers) via free radical polymerisation either in the bulk or in aqueous solution, which opens up new synthetic possibilities.¹⁸ This new approach minimises the reactivity of the growing free radicals through hydrogen bonding, which is sufficient to inhibit the normal side-reactions. Water molecules or hydroxyl groups can act as hydrogen bond donors to form hydrogen bonds with the ether oxygen in the vinyl ether (see Figure 1.6), thereby stabilizing

the intermediate free radicals. In addition, the introduction of Li^+ leads to cation- π interactions which activates vinyl ethers towards initiation. In principle, hydrophilic monomers such as MPEGVE should be suitable for this approach because it can participate in the formation of hydrogen bond networks. Thus good results were anticipated in this case. However, for the hydrophobic TMHVE monomer, modifications are required to facilitate the free radical copolymerisation.

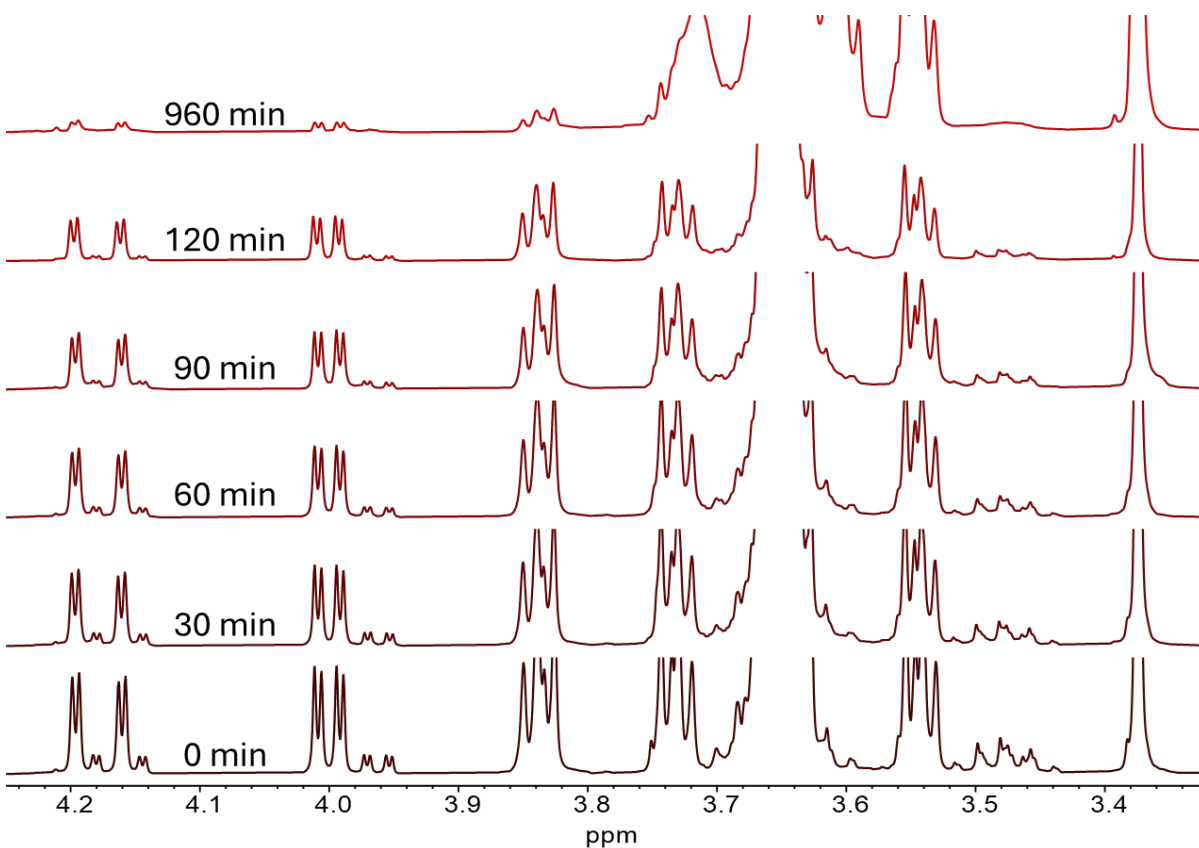


Figure 5.6: NMR spectra (CDCl_3) recorded for the attempted free radical copolymerisation of MPEGVE with TMHVE at 70°C using AIBN initiator in the bulk copolymerisation

Bulk copolymerisation of TMHVE with MPEGVE was attempted initially at 70°C . The progress of this free radical copolymerisation was monitored via ^1H NMR spectroscopy and DMF GPC analysis. The instantaneous comonomer conversion was calculated by comparing the integrated NMR signal assigned to the terminal methoxy chain-end of MPEGVE (singlet at 3.34 ppm) with that of the three vinyl protons at 6.46, 4.14 or 3.96 ppm. The latter signals

gradually disappear as the copolymerisation proceeds, with 90% conversion being achieved within 16 h at 70 °C. However, various side-reactions could also consume the vinyl ether vinyl groups, so in this case NMR analysis does not necessarily prove successful copolymerisation. Indeed, DMF GPC analysis indicates a very modest increase in M_w from 160 to 320 g·mol⁻¹, suggesting merely the formation of dimer only.

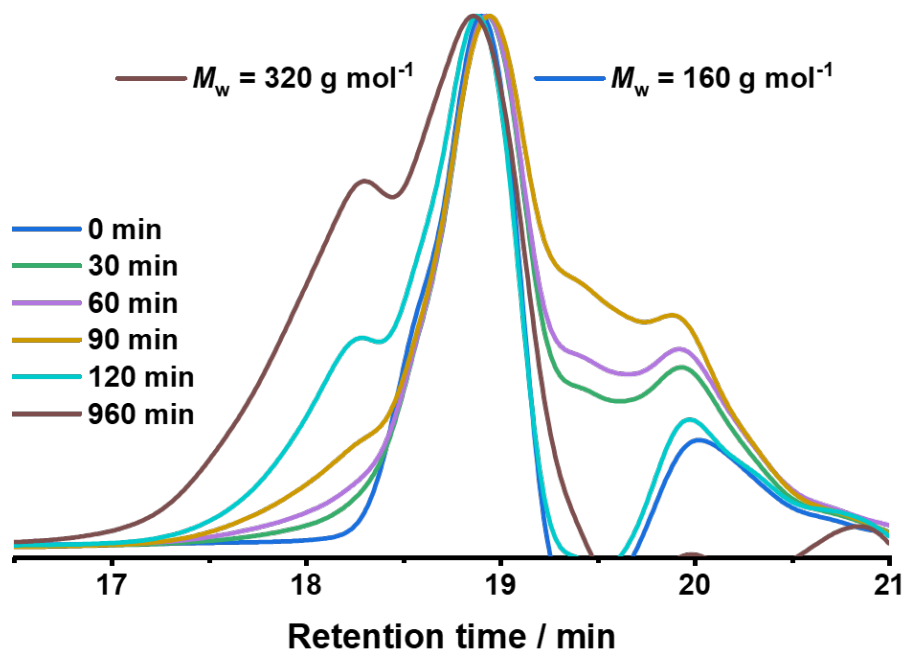


Figure 5.7: DMF GPC recorded for the attempted free radical copolymerisation of MPEGVE with TMHVE at 70 °C using a AIBN initiator in the bulk copolymerisation.

Previous studies by Sugihara et al.¹⁸ indicate that the addition of LiOH to produce a basic aqueous solution can effectively stabilise radical intermediates (see Figure 5.8). In this prior study, M_n of poly(methoxy vinyl ether)¹⁸ was significantly increased from 4,500 to 12,300 g·mol⁻¹ in the presence of LiOH. Inspired by this finding, we investigated the feasibility of applying the same methodology to the free radical copolymerisation of MPEGVE and TMHVE in an aqueous solution of LiOH.



Figure 5.8: Lithium cation - π interactions assisted stabilisation of the vinyl ether, as suggested by Sugihara and co-workers.¹⁸

^1H NMR analysis indicated that the comonomer conversion reached 74% within 15 h at 70 °C. However, GPC analysis again indicated only a marginal increase in M_n , which is inconsistent with the results reported by Sugihara et al.¹⁸ Following email discussions with Prof. Sugihara, we hypothesised that this apparent discrepancy might be attributed to the chemical structure of MPEGVE. More specifically, its PEG side-chains introduce a larger number of potential hydrogen bond sites. Thus, compared to the MOVE monomer used in the prior study, MPEGVE may be more prone to form intramolecular hydrogen bonds within its side-chains. If this is correct, such intramolecular competition would reduce the availability of the ether oxygen to form hydrogen bonds with water, thereby reducing the stabilisation of the propagating radical species and leading to poor polymerisation efficiency.

In view of the consistently low molecular weights obtained under these conditions, further investigation into the radical copolymerisation behaviour of TMHVE and MPEGVE is considered to be of limited practical value.

5.3.4 Cationic Homopolymerisation of PTMHVE

In the TiCl_4 system, the TMHVE monomer conversion was monitored by ^1H NMR. The characteristic vinyl proton signals at 6.5 ppm and 3.9 - 4.2 ppm completely disappeared within 3 h at -78°C , suggesting almost complete conversion. DMF GPC analysis indicated that the peak molecular weight (M_p) of the copolymer increased from 160 $\text{g}\cdot\text{mol}^{-1}$ at the beginning of the reaction up to 820 $\text{g}\cdot\text{mol}^{-1}$, indicating the formation of oligomers, rather than high molecular weight copolymer chains (Figure 5.9). In principle, this might be the result of either water contamination or extensive chain transfer or β -hydride elimination.

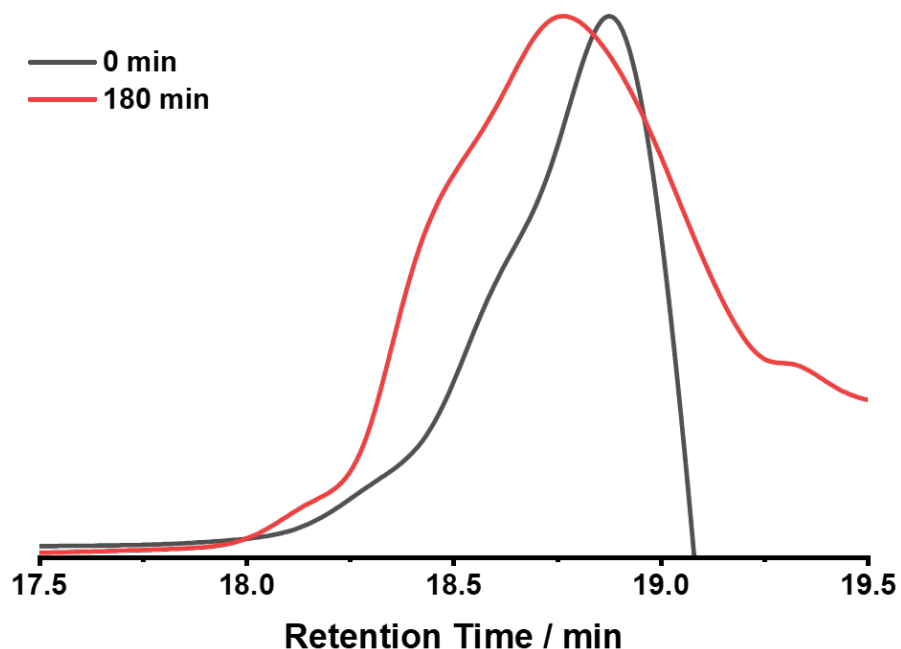


Figure 5.9: DMF GPC recorded for the attempted cationic homopolymerisation of PTMHVE at -78°C using a TiCl_4 initiator in dry DCM.

In addition, the above initiator were also examined for the cationic copolymerisation of MPEGVE with TMHVE. Since residual water associated with the hydrophilic PEG side-chains is difficult to completely remove, the water content of such systems may be relatively high, which in turn could affect the stability and initiation efficiency of the Lewis acid. Unfortunately, no polymerisation was achieved in all experiments.

5.4 Conclusions

Two vinyl ethers were successfully synthesised using transesterification, namely hydrophilic MPEGVE and hydrophobic TMHVE. Either free radical copolymerisation or cationic polymerisation of these two comonomers was explored to produce amphiphilic statistical copolymers for foam stabilisation studies. The rationale here was to target highly flexible backbones compared to the equivalent (meth)acrylic copolymers for optimal surface activity.

Free radical copolymerisation led to the formation of oligomers, which may be attributed to hydrogen-bond stabilisation.¹⁸ Nevertheless, this interpretation requires further verification by infrared spectroscopy. However, the copolymer molecular weight was significantly lower than that desired. In addition, the presence of TMHVE repeat units within the copolymer could not be confirmed by ¹H NMR spectroscopy.

The cationic homopolymerisation of TMHVE was successful when using the TiCl₄ initiator, which produced a low molecular weight product. However, no initiation occurred in the subsequent attempt to copolymerise TMHVE with MPEGVE. This failure is believed to be related to the difficulty of removing of residual water from the hydrophilic MPEGVE monomer: the highly reactive cation chain-ends are readily deactivated in the presence of such a protic impurity. Hence more stringent drying methods such as azeotropic distillation are recommended for future experiments to rigorously dry the MPEGVE monomer prior to copolymerisation.

All attempts to employ the AlCl₃/H₂O system as an initiator system for cationic polymerisation were also unsuccessful.

In summary, the cationic homopolymerisation of the hydrophobic monomer TMHVE can be conducted using the TiCl₄ initiator, whereas the hydrophilic MPEGVE monomer is much more difficult to dry and is hence much less amenable to cationic polymerisation. More rigorous drying and appropriate initiator selection are key problems that need to be addressed for copolymer synthesis via cationic polymerisation. However, RAFT copolymerisation of such vinyl ethers has been successful under certain conditions. There is scope for further examination

of this synthetic protocol in future work.

5.5 References

- (1) G. Odian, *Principles of Polymerization*, Wiley, Hoboken, NJ, USA, 4th edn., 2004.
- (2) B. Metin and F. D. Blum, *The Journal of Chemical Physics*, 2006, **124**, 054908.
- (3) C.-T. Lin, S.-W. Kuo, C.-F. Huang and F.-C. Chang, *Polymer*, 2010, **51**, 883–889.
- (4) J. Jennings, R. R. Webster-Aikman, N. Ward-O'Brien, A. Xie, D. L. Beattie, O. J. Deane, S. P. Armes and A. J. Ryan, *ACS Applied Materials & Interfaces*, 2022, **14**, 39548–39559.
- (5) S. Singha, S. Pan, S. S. Tallury, G. Nguyen, R. Tripathy and P. De, *ACS Polymers Au*, 2024, **4**, 189–207.
- (6) K.-F. Arndt, T. Schmidt and R. Reichelt, *Polymer*, 2001, **42**, 6785–6791.
- (7) W. H. Watanabe and L. E. Conlon, *Journal of the American Chemical Society*, 1957, **79**, 2828–2833.
- (8) S. Aoshima and S. Kanaoka, *Chemical Reviews*, 2009, **109**, 5245–5287.
- (9) S. Zhu, Y. Lu, K. Wang and G. Luo, *RSC Adv.*, 2016, **6**, 97983–97989.
- (10) M. Ouchi, M. Kamigaito and M. Sawamoto, *Macromolecules*, 2001, **34**, 3176–3181.
- (11) S. Sugihara, S.-I. Matsuzono, H. Sakai, M. Abe and S. Aoshima, *Journal of Polymer Science Part A: Polymer Chemistry*, 2001, **39**, 3190–3197.
- (12) S. Aoshima, S. Sugihara, M. Shibayama and S. Kanaoka, *Macromolecular Symposia*, 2004, **215**, 151–164.
- (13) C. Forder, PhD thesis, University of Sussex, 1996.
- (14) C. Forder, C. S. Patrickios, S. P. Armes and N. C. Billingham, *Macromolecules*, 1997, **30**, 5758–5762.
- (15) C. Forder, C. S. Patrickios, S. P. Armes and N. C. Billingham, *Macromolecules*, 1996, **29**, 8160–8169.

-
- (16) C. Forder, C. S. Patrickios, N. C. Billingham and S. P. Armes, *Chem. Commun.*, 1996, 883–884.
- (17) C. Forder, S. P. Armes and N. C. Billingham, *Polymer Bulletin*, 1995, **35**, 291–297.
- (18) S. Sugihara, A. Yoshida, T.-a. Kono, T. Takayama and Y. Maeda, *Journal of the American Chemical Society*, 2019, **141**, 13954–13961.

Chapter 6

Conclusions and Future Work

The structure-property correlations of amphiphilic statistical copolymer surfactants were systematically investigated with a focus on optimising their foaming performance. Appropriate design rules were established by initially screening for important statistical factors, followed by characterisation of amphiphilic (meth)acrylic copolymers and detailed structure-property studies, including evaluation of new polymerisation routes to amphiphilic statistical copolymers with more flexible backbones (e.g. the attempted synthesis of novel vinyl ether-based copolymers). In addition, a fully hydrophilic statistical copolymer was synthesised as a model system for evaluating backbone flexibility from SAXS patterns using the WLC-PRISM model.¹ This approach enabled isolation of conformational effects arising solely from chain stiffness, without interference from chemical composition or molecular weight, providing a useful reference sample for examining chain flexibility.

Primary variables that control foamability for Pluronic-type triblock copolymers and (meth)acrylic copolymers were identified in Chapter 2 using DoE combined with the ANOVA method.^{2–4} For amphiphilic statistical copolymer, the chemical structure of the hydrophobic comonomer emerged as the dominant factor, followed by molecular weight, the [HB]/[HL] ratio and the nature of the copolymer backbone (e.g. acrylic > methacrylic). These findings provided useful guidance for subsequent copolymer syntheses.

Amphiphilic statistical (meth)acrylic copolymers exhibited superior foamability compared to their block counterparts, which is attributed to more efficient interfacial adsorption by the former species.⁵ By connecting dynamic surface tension with foamability, a trade-off was identified between rapid diffusion (which requires shorter copolymer chains) and the formation of stable interfacial films, for which longer copolymer chains are desirable. This highlights the importance of optimising the copolymer molecular weight to achieve a balance between adsorption kinetics and film stability. However, there was no correlation between either foamability or foam stability and the "static" surface tension determined using either the bubble pressure method or the du Noüy ring method. Ideally, such static interfacial properties of the adsorbed copolymer layers require further investigation via neutron reflectometry.^{6–9}

SAXS studies indicated a clear correlation between copolymer composition, micelle morphology and foaming performance. Copolymers with lower hydrophobic character formed relatively loose micellar aggregates which are able to undergo rapid dissociation. This facilitates rapid yet weak surface adsorption. In contrast, more hydrophobic copolymers produced more compact, stable micelles that undergo relatively slow micellar dissociation and interfacial adsorption, which is not desirable for efficient foam formation. Consequently, the hydrophobic comonomer content must be optimised to balance the conflicting requirements of initial fast dissociation/diffusion kinetics with subsequent thermodynamic foam stabilisation. The micelle structure and surface activity can be tuned by varying the nature of the hydrophobic comonomer, with a highly branched alkyl substituent conferring superior foamability.

Although the nature of the copolymer backbone exerted only a mild influence on the micelle structure, it strongly affected the foaming performance. Foam collapse is a dynamic process, which requires a highly flexible copolymer backbone to respond to the continual interfacial deformation. In this context, relatively inflexible methacrylic copolymer surfactants perform poorly. This observation suggested that more mobile/flexible copolymer chains should provide greater foam activity. However, for studies of PEG-based copolymers, differential scanning calorimetry proved to be ineffective for assessing the glass transition temperature, which is a proxy for chain mobility.

The amphiphilic statistical copolymers investigated in this study did not form the desired unimolecular micelles in deionised water, which is attributed to the strongly hydrophobic nature of the THMA comonomer. Accordingly, a series of ethanol-water mixtures could be examined to determine the minimum ethanol content required for unimolecular micelle formation. Likewise, introducing more hydrophilic substituents, such as ionic groups, may also promote the formation of unimolecular micelles. A dedicated systematic study is therefore required to identify the specific solution conditions and copolymer compositions that enable unimolecular micelle formation.

In this study, among the amphiphilic statistical copolymers examined in deionised water, only

the sample with the highest hydrophilic-monomer content (PT95 series) was able to form the expected unimolecular micelles. This is attributed to the strong hydrophobicity of the THMA comonomer. Accordingly, a series of ethanol-water mixtures could be examined to determine the minimum ethanol content required for unimolecular micelle formation. Likewise, introducing more hydrophilic substituents, such as ionic groups, may also promote the formation of unimolecular micelles. A dedicated systematic study is therefore required to identify the specific solution conditions and copolymer compositions that enable unimolecular micelle formation.

To compensate for the limited conformational information reported in Chapter 3, a series of weakly basic P(DMA-*stat*-PEGMA) statistical copolymers was prepared as a model platform for investigating the effect of chain flexibility. For this model system, backbone flexibility can be modulated by introducing intra-chain electrostatic repulsion via reversible protonation of the tertiary amine group on the DMA comonomer repeat units. This strategy simulates the flexibility variations via electrostatic interactions that would otherwise arise from changes in backbone chemical structure, while eliminating compositional bias and enabling direct tuning of chain rigidity. As such, it provides a useful platform for probing structure-property relationships. SAXS analysis using the WLC-PRISM model provided the mean persistence length of the copolymer chains (i.e. intra-chain interactions) while also accounting for electrostatic interactions (inter-chain interactions, interaction fuzziness and the effective interaction distance).¹ Neutral copolymer chains formed compact coils, whereas increasing the degree of protonation at low pH leads to coil expansion and stiffer chains. Salt screening experiments revealed a marked reduction in the mean persistence length and coil dimensions at high ionic strength.^{10,11} Concentration variation produced a structure factor that scaled with classical polyelectrolyte theory.^{12,13} GPC-MALLS studies confirmed that charge-induced coil expansion persisted across a wide range of molecular weight when comparing P(DMA-*stat*-PEGMA) with its permanently charged analogue, P(QDMA-*stat*-PEGMA). Overall, the chain conformation depends on the charge density, ionic strength, and copolymer concentration. This study

has validated the WLC-PRISM scattering model for analysing charged hydrophilic statistical copolymers in aqueous solution. On this basis, the WLC model should also be applicable to less complex, non-ionic systems, such as the statistical copolymer surfactants discussed in Chapter 3. For these systems, the backbone flexibility of acrylic- and methacrylic-based copolymers can be quantified through the Kuhn length derived from the WLC model, enabling a systematic comparison of the chain rigidity of the two backbones and compensating for the limitations of glass-transition measurements obtained by DSC. In the future, the WLC framework should be applied in suitable solution environments to determine the Kuhn lengths of amphiphilic statistical copolymer surfactants and to further evaluate the chain flexibility differences between the two copolymer backbones. Moreover, contrast-match SANS studies should be conducted in D₂O/H₂O mixtures to characterise the condensed counter-ion layer, thereby refining the current data fits to scattering patterns.

Attempts were made to prepare amphiphilic vinyl ether-based statistical copolymers which were expected to exhibit even greater chain flexibility than the best-performing acrylic copolymers. TiCl₄-initiated cationic homopolymerisation of hydrophobic TMHVE was achieved but its statistical copolymerisation with hydrophilic MPEGVE proved to be problematic owing to the presence of residual water. Moreover, alternative syntheses based on free radical copolymerisation yielded only low molecular weight oligomers. Although these syntheses were ultimately unsuccessful, they highlight the critical importance of rigorous monomer drying and initiator selection that is required for successful cationic polymerisation.

Overall, three universal design rules have been identified in this thesis: (i) branched hydrophobic comonomers promote stronger interfacial adsorption compared to their linear counterparts; (ii) moderate molecular weights balance rapid diffusion to the air-water interface with sufficiently resilient adsorbed copolymer layers; and (iii) enhanced copolymer chain flexibility promotes foamability. These useful physical insights suggest design strategies for next-generation non-ionic copolymer surfactants.

Future work should focus on reducing the copolymer molecular weight (e.g. by introducing a

suitable chain transfer agent) and further diversifying the selection of hydrophilic and hydrophobic comonomers. Neutron reflectometry studies should enable the characterisation of adsorbed copolymer layers formed at the planar air-water interface under static conditions (and possibly even dynamic foaming conditions), while contrast match SANS experiments should enable a more refined structural model to be developed to describe the condensed counter-ions associated with charged copolymer chains/micelles.¹⁴ In principle, either longer acquisition times or selecting a shorter camera length should improve the quality of the scattering data recorded in the high q regime, thereby providing greater resolution. Finally, further optimisation of the copolymerisation conditions required for the preparation of amphiphilic vinyl ether-based copolymers remains a key synthetic challenge. A deep practical challenge is to make statistical copolymer surfactants that are not based on a carbon-carbon backbone. Polymers with a heteroatom in the backbone are more intrinsically biodegradable. This is important because polymeric surfactants are ultimately dispersed in the environment in their application and they need to safely degrade into degnin, mineralisable residual rather than becoming persistent "forever chemicals".¹⁵ Such future studies are expected to accelerate the design of next-generation statistical copolymer surfactants.

6.1 References

- (1) J. S. Pedersen, in *Neutrons, X-rays, and Light*, ed. P. Lindner and J. Oberdisse, Elsevier, Amsterdam, Netherlands, 2nd edn., 2025, ch. 15, pp. 401–451.
- (2) D. Montgomery, *Design and Analysis of Experiments*, John Wiley & Sons, Ltd, New York, USA, 8th edn., 2012.
- (3) P. Alexandridis and T. A. Hatton, *Colloids and Surfaces A: Physicochemical and Engineering Aspects*, 1995, **96**, 1–46.
- (4) J. Jennings, R. R. Webster-Aikman, N. Ward-O'Brien, A. Xie, D. L. Beattie, O. J. Deane, S. P. Armes and A. J. Ryan, *ACS Applied Materials & Interfaces*, 2022, **14**, 39548–39559.
- (5) M. Mu, F. A. Leermakers, J. Chen, M. Holmes and R. Ettelaie, *Journal of Colloid and Interface Science*, 2023, **644**, 333–345.
- (6) S. W. An, T. J. Su, R. K. Thomas, F. L. Baines, N. C. Billingham, S. P. Armes and J. Penfold, *The Journal of Physical Chemistry B*, 1998, **102**, 387–393.
- (7) S. W. An, R. K. Thomas, C. Forder, N. C. Billingham, S. P. Armes and J. Penfold, *Langmuir*, 2002, **18**, 5064–5073.
- (8) Q. S. Mu, J. R. Lu, Y. H. Ma, M. V. Paz de Banez, K. L. Robinson, S. P. Armes, A. L. Lewis and R. K. Thomas, *Langmuir*, 2006, **22**, 6153–6160.
- (9) S. W. An, P. N. Thirtle, R. K. Thomas, F. L. Baines, N. C. Billingham, S. P. Armes and J. Penfold, *Macromolecules*, 1999, **32**, 2731–2738.
- (10) N. Volk, D. Vollmer, M. Schmidt, W. Oppermann and K. Huber, in *Polyelectrolytes with Defined Molecular Architecture II*, ed. M. Schmidt, Springer, Heidelberg, Germany, 2004, ch. 2, pp. 29–65.

-
- (11) M. Borkovec, G. J. M. Koper and C. Piguet, *Current Opinion in Colloid & Interface Science*, 2006, **11**, 280–289.
 - (12) P.-G. de Gennes, P. Pincus, R. M. Velasco and F. Brochard, *J. Phys. France*, 1976, **37**, 1461–1473.
 - (13) A. V. Dobrynin, R. H. Colby and M. Rubinstein, *Macromolecules*, 1995, **28**, 1859–1871.
 - (14) H. B. Stuhmann, *Journal of Applied Crystallography*, 2007, **40**, 23–27.
 - (15) R. Rothman and A. J. Ryan, in *Plastic Pollution in the Global Ocean*, ed. A. A. Horton, World Scientific Publishing Co Pte Ltd, Singapore, 2023, ch. 1, pp. 21–46.